PGE–Cu–Ni Sulfide Mineralization of the Mesoproterozoic Escape Intrusion, Northwestern Ontario

Connor Caglioti

A thesis presented to Lakehead University in partial fulfillment

of the requirements for the degree of

Master of Science in Geology

Department of Geology

Thunder Bay, Ontario, Canada, 2023

Abstract

The Escape intrusion is a tabular to bladed, mafic–ultramafic chonolith that hosts economic concentrations of PGE–Cu–Ni magmatic sulfide mineralization. The Mesoproterozoic intrusion is located about 50 km northeast of Thunder Bay, Ontario, and with the Current intrusion makes up the Thunder Bay North Intrusive Complex (TBNIC). The intrusive rocks of the TBNIC are part of the 1.1 Ga Midcontinent Rift System (MRS) of North America and were emplaced into the Quetico Basins during early stages of rift development. The fractionated HREE (Gd/Yb_{cn} = 3.18–4.96) signature of the Escape rocks suggests magma derivation from a deep mantle source. Primitive mantle-normalized trace element patterns of the Escape intrusive rocks are similar to ocean-island basalt, as well as multiple MRS-related mafic–ultramafic intrusions (e.g., Hele, Disraeli, Kitto), which is consistent with the mantle-plume hypothesis of MRS formation.

The high-grade zone occurs within the (mostly wehrlitic) peridotite unit of the Escape intrusion, which lies below the weakly mineralized gabbro and hybrid units. The high-grade zone within the Escape intrusion is characterized by intercumulus sulfide mineralization that is net-textured at the core and disseminated at the margins. The primary sulfide mineralization within the net-textured ore is characterized by an assemblage which consists predominantly of pyrrhotite + chalcopyrite + pentlandite + platinum-group minerals (PGMs). The disseminated sulfides of the high-grade zone are composed of a variable assemblage that includes the primary sulfides as well as some or all of the following: native Cu, mackinawite, cubanite, native Ag/electrum, sugakiite, pyrite, and valleriite. In addition to interstitial sulfide mineralization at Escape, numerous centimetre-sized sulfide (± carbonate) veinlets crosscut the groundmass. The sulfide veinlets exhibit complex intergrowths often with mottled textures and variable composition. Phases

commonly identified within the sulfide veinlets include cubanite, pyrrhotite, pyrite, pentlandite, chalcopyrite, and mackinawite.

Sulfide trace element compositions obtained via in situ laser ablation inductively coupled plasma mass spectrometry (LA–ICP–MS) indicate that Pd is concentrated in pentlandite (around 100 ppm) and IPGE (Ir, Os, Ru) are concentrated in pyrrhotite within the net-textured ores. Sulfide minerals from the interstitial–primary assemblage exhibit S/Se ratios within the mantle domain (2850–4350). The high-grade PGE tenors of the deposit were likely the result of moderate magmatic enrichment of the Escape segregated sulfide liquid at R factors of ~7,500, based on numerical models derived from whole-rock, major and trace element geochemistry. Sulfide minerals within the disseminated style are depleted in PGE and S/Se (as low as 668) relative to the net-textured sulfides. These trace element signatures and the distinct sulfide assemblage identified in the disseminated ores are attributed to desulfurization and remobilization of metals during hydrothermal alteration. Sulfide minerals measured within veinlets from the crosscutting assemblage are depleted in PGE and strongly enriched in As (e.g., up to ~900 ppm in pentlandite) relative to the primary–interstitial assemblage, as well as elevated in S/Se (ranging up to 27,896), considerably outside of the mantle range. Various As-bearing PGM were identified within the sulfide veinlets but were not found within the net-textured ores. These features suggest that remobilized metals from the interstitial ores were transported as As-rich bisulfide complexes and emplaced as veinlets within small fractures between cumulus olivine during the later stages of hydrothermal activity.

In situ S-isotopes of Escape sulfides obtained via secondary ion mass spectrometry (SIMS) show that $\delta^{34}S$ values range from -3.07 to -0.97‰, and all values for $\Delta^{33}S$ and $\Delta^{36}S$ fall within a range produced by mass-dependent fractionation (MDF). S-isotopes were also measured in pyrite from Quetico metasedimentary country rocks. There is overlap between Escape and Quetico S-isotopes both in and outside the mantle range. Results from numerical modelling of

equilibration between the Escape sulfide liquid and pulses of fresh, uncontaminated melt suggest that the mass-independent fractionation (IDF) signal was erased due to isotopic exchange. It is inconclusive what drove the Escape parental magma to S-saturation, however, the origin of sulfur is likely to be a mixture of mantle source and country rock contamination.

Acknowledgements

There are many people and groups that supported me in writing this thesis that I wish to thank. Firstly, I am incredibly grateful to my supervisor Dr. Pete Hollings for taking a chance on me as a graduate student and guiding me throughout the program. Thank you for your mentorship and unwavering support. My success in this research would not have been possible without the exceptional support of Dr. Matthew Brzozowski. His dedication, patience, and instruction were invaluable to my understanding of magmatic sulfide deposits; thank you for everything. I would like to extend my sincere thanks to Al MacTavish, Dr. Geoff Heggie, and all the talented people at Clean Air Metals Inc. I am greatly appreciative for the practical support in learning about the geology of the Thunder Bay North Intrusive Complex, professional development, and access to samples. I am thankful to Kristi Tavener and Dr. Jonas Valiunas for their services in creating thin sections used in this thesis, and for their interest and encouragement in my research success. Thank you to Jean Claude Barrette, and the Great Lakes Institute for Environmental Research (GLIER) at the University of Windsor for use of LA–ICP–MS instrumentation. I am grateful to Dr. Laure Martin and the team at the University of Western Australia's Centre for Microscopy, Characterisation and Analysis for their work in providing sulfur isotope compositions. I am also very appreciative of the MLA work done by Dr. Derek Wilton at the Core Research Equipment & Instrument Training Network at Memorial University. I am thankful for the reviews from the Department of Geology and Dr. Joel Gagnon. I am profoundly grateful for funding support from NSERC/Clean Air Metals Inc. (Alliance Grant), Lakehead University and Barrick Gold (Graduate Scholarship), the Society of Economic Geologists Canada Foundation (Student Research Grant and Ronald E. Seavoy SFT Grant), the Institute on Lake Superior Geology (Eisenbrey Student Travel Award), and to Equinox Gold/Young Mining Professionals (NW Ontario Mining Scholarship). Last but certainly not least, I would like to thank my dear friends, family, and Maya Saggar for their love, support, and encouragement.

Table of Contents

List of Figures

List of Tables

List of Abbreviations

Act	Actinolite
Alt	Alteration
Amp	Amphibole
(Au,Ag)	Electrum
BSE	Back-scattered electron
Bt	Biotite
CAM	Clean Air Metals Inc.
Cb	Carbonate
Cbl	Cobaltite
Cbn	Cubanite
Ccp	Chalcopyrite
Chl	Chlorite
Chr	Chromite
Cla	Clay minerals
Cpx	Clinopyroxene
D	Disseminated
EDS/EDX	Energy-dispersive X-ray spectroscopy
EWC	East–West Connector
Gn	Galena
GV	Gangue veinlet (with sulfide blebs)
HFSE	High field-strength element
HGZ	High-grade zone
HREE	Heavy rare earth element
ICPS	Integrated counts per second
Ilm	Ilmenite
IPGE	Iridium-platinum-group element
ISS	Intermediate solid solution
LA–ICP–MS	Laser ablation inductively coupled plasma mass spectrometry
LIP	Large igneous province
LOI	Loss on ignition
LREE	Light rare earth element
Mag	Magnetite
Mch	Michenerite
MDF	Mass-dependent fractionation
Mfv	Mitrofanovite
MIF	Mass-independent fractionation
Mkw	Mackinawite
MLA	Mineral liberation analyzer/analysis
MLA	Mineral liberation analyzer/analysis
MRS	Midcontinent Rift System
MS	Massive sulfide
MSS	Monosulfide solid solution
Msl	Maslovite
Npl	Nipalarsite

NT	Net-textured
OIB	Ocean island basalt
Ol	Olivine
PEA	Preliminary economic assessment
PGE	Platinum-group element
PGM	Platinum-group mineral
PPGE	Palladium-platinum-group element
Pl	Plagioclase
Pn	Pentlandite
Po	Pyrrhotite
PPL	Plane polarized light
Py	Pyrite
REE	Rare earth element
SD	Strongly disseminated
SEM	Scanning electron microscopy
Ser	Sericite
Sg	Sugakiite
SIMS	Secondary ion mass spectrometry
Spy	Sperrylite
Srp	Serpentine
Sst	Saussurite
SV	Sulfide veinlet
T	Trace mineralization
TABS	Te, As, Bi, Sn, Sb
TBNIC	Thunder Bay North Intrusive Complex
Tlc	Talc
Tro	Troilite
Val	Valleriite
WD	Weakly disseminated
XPL	Cross polarized light

1 Introduction

1.1 Background

Global demand for "critical minerals" has dramatically increased within the past decade, as nation states race to develop and implement critical mineral strategies to bring these materials into the supply chain (Government of Canada, 2022). This effort is being undertaken to reduce emissions of greenhouse gases into the atmosphere through the adoption of green-energy solutions to decrease reliance on, and eventually phase out, the use of fossil fuels. Whether it is the nickel required for production of lithium-ion batteries, copper required for electrical infrastructure, or palladium for the manufacture of catalytic converters and aerospace technology, metals are necessary to bring about the decarbonization of society.

The Midcontinent Rift System (MRS) formed 1.1 billion years ago when the North American Craton failed to split apart. During the development of the MRS, voluminous flood basalts, mafic–ultramafic intrusions, and related sedimentary basin units were deposited in the area that is now the Lake Superior region. Numerous magmatic Ni–Cu–platinum-group element (PGE) sulfide deposits of economic significance have been identified within various intrusive units of the MRS, including the Tamarack deposit (Minnesota, USA; Taranovic et al., 2015), Eagle deposit (Michigan, USA; Ding et al., 2010), and the Marathon and Sally deposits (Marathon, Ontario; Brzozowski et al., 2020). The Thunder Bay North Intrusive Complex (TBNIC) is another suite of rocks that hosts economic concentrations of base and precious metals in the form of the Current and Escape deposits. These twinned intrusive bodies are examples of conduit or chonolith deposits, being characterized by a tabular to bladed shape in cross-section and an elongated, tadpole-like shape in plan view (Barnes et al., 2015; Clark, 2020). The intrusions were emplaced into the metasedimentary rocks of the Quetico Basin of the Superior Province and do not outcrop at surface. As a result, characterization of these intrusions is restricted to drill core. The Current deposit has been dated at 1106.6 ± 1.6 Ma (Bleeker et al.,

2020), and the Escape deposit dated at 1107.6 ± 0.9 Ma (Yahia, 2023) indicating that the TBNIC formed during the early stages of MRS development (Woodruff et al., 2020).

Exploration in the region initially started with investigation of a uranium showing to the east of Current Lake, Ontario (Clark, 2020). In 2001, activity in the area led to the discovery of Ni–Cu–PGE-mineralized peridotite boulders on the west shore of Current Lake. By 2006, all claims in the area of the TBNIC were staked and exploration efforts continued at both the Current and Escape deposits; mineral claims encompassing both deposits were consolidated under the company Clean Air Metals Inc. (CAM) in 2020. To date, over 260,000 metres of diamond drilling has been completed across the two deposits. Previous mineral estimates for the Current deposit include an Indicated Resource of 8,460,000 tonnes at 2.13 g/t platinum equivalent, whereas a representative intercept for the Escape deposit through the high-grade zone included 10.9m at 2.35 g/t Pt + Pd + Au (Thomas et al., 2011; Clark, 2020). Given the high-grade concentration of PGE–Cu–Ni sulfide mineralization and existence of favourable external factors (e.g., proximity to transportation and energy infrastructure), the resources contained within the TBNIC constitute an important and viable source for critical minerals. Therefore, to facilitate and enhance exploration, extraction and processing of these ores, characterization of the mineralization in these deposits is paramount.

1.2 Magmatic sulfide deposits

Economic concentrations of Ni and Cu occur within a wide variety of settings and deposit types worldwide (e.g., Ni laterite deposits, porphyry Cu deposits). One of the foremost deposit types that contributes greatly to the global resource of these metals, as well as the PGE, is the family of magmatic sulfide deposits. In particular, these deposits account for approximately 40.5% of Ni resources and almost all PGE resources worldwide (Mudd and Jowitt, 2014; Mudd et al., 2018). Naldrett (2004) divided Ni–Cu deposits into six different subtypes based on their petrogenetic setting and nature of magmatism — komatiite, flood basalt, picrite, anorthosite–

granite–troctolite, miscellaneous picrite–tholeiite, and impact melt magmatism. Although magmatic PGE deposits are related to Ni–Cu magmatic sulfide deposits, they differ in that they generally contain notably less sulfide, and their major component of economic value constitute the PGEs (Naldrett, 1998). The compositional variability of the Ni–Cu subtypes and PGE deposits is illustrated in Figure 1.1, along with the composition of select deposits in the MRS, including the Escape deposit. Conduit-style magmatic sulfide deposits plot within multiple petrogenetic fields, but are often compositionally similar to deposits associated with miscellaneous picrite–tholeiite magmatism (e.g., Tamarack, Eagle, and the Coldwell Complex).

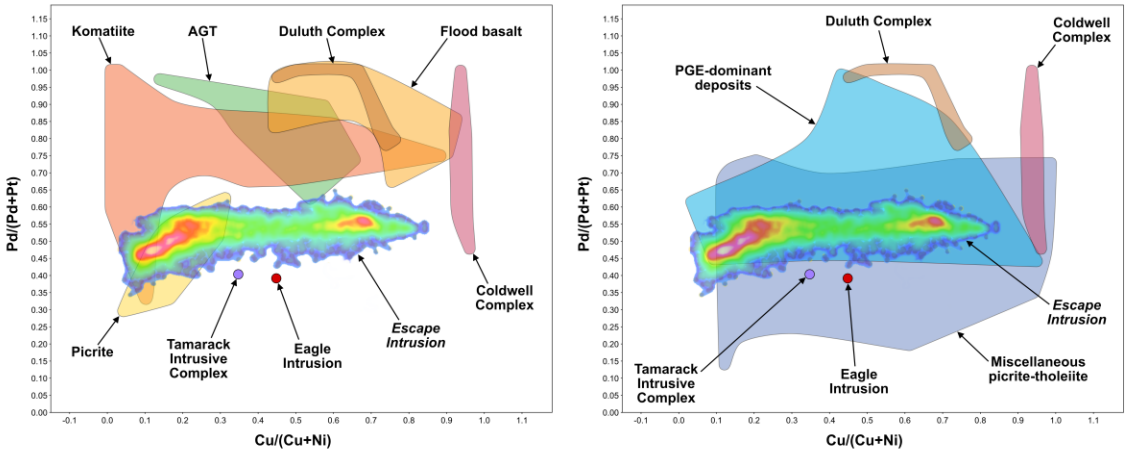

Figure 1.1: Binary diagram illustrating the Cu, Ni, Pd, and Pt concentrations of magmatic sulfide deposit subtypes. The density field in the centre of both plots corresponds to mineralization from the Escape intrusion, with warm colours indicating a higher abundance of points. For clarity, deposit fields have been split into two diagrams and the field for impact melt magmatism has been omitted. AGT = anorthosite–granite–troctolite. Diagrams were produced with assay data from Clean Air Metals Inc., Ding et al. (2010), Queffurus and Barnes (2015), Taranovic et al. (2015), and Brzozowski et al. (2020).

In general, magmatic Ni–Cu–PGE deposits form as a result of the segregation and concentration of sulfide liquid droplets from mafic–ultramafic magma, with chalcophile elements in the parental silicate magma partitioning into the sulfide liquid (Naldrett, 2004). To concentrate base and precious metals into small volumes of rock to form a magmatic sulfide deposit, several geologic processes must occur in addition to sulfide segregation. It can be helpful to consider the formation of magmatic sulfide deposits using the mineral system approach, which divides these geologic processes into four components — source, fluids, transport, and trap (Barnes et al.,

2015). Each of these components plays a critical role in controlling the genesis of the mineralization, including the mechanisms of metal concentration, and the size, location, and preservation potential of the orebodies. The melts that feed these mineralized intrusions are typically sourced from a hot, upwelling mantle plume (Fig. 1.2; Barnes et al., 2015). These plumes are anomalously hotter and less dense than the surrounding mantle; this density contrast initially drives its ascent through the asthenosphere. Once the plume impinges on the lithospheric boundary, the head of the plume spreads laterally and partially melts. In order for a Ni–Cu–PGE deposit to form from this parental magma, it must represent a high-degree partial melt from PGE-undepleted mantle; this ensures that all sulfide and olivine in the source gets dissolved, which are the primary hosts of the base and precious metals in the mantle (Fig. 1.2; Mungall, 2014). These partial melts reflect the characteristics of the mantle which restricts them to mafic–ultramafic compositions. For these melts to form deposits that are accessible, they need to be emplaced into relatively shallow levels in the crust. Initial movement of the partial melt is typically achieved via magma buoyancy (Barnes et al., 2015). Movement within the crust typically occurs along major crustal structures, with the final location of emplacement often localized by dilations or traps created by cross-linking structures in strike-slip fault zones (Fig. 1.2; Lightfoot and Evans-Lamswood, 2014). Finally, at the tectonic or cratonic-scale, magmatic sulfide deposits are commonly emplaced within rift basins or the margins of ancient cratons (Fig. 1.2; Barnes et al., 2015). This is because within these settings, the head of the mantle plume is deflected to zones of thin lithosphere which is permissive to bulk melting (Barnes et al., 2015). Plume-derived magmas are focused through the crust by lithospheric architecture which guides their ascent.

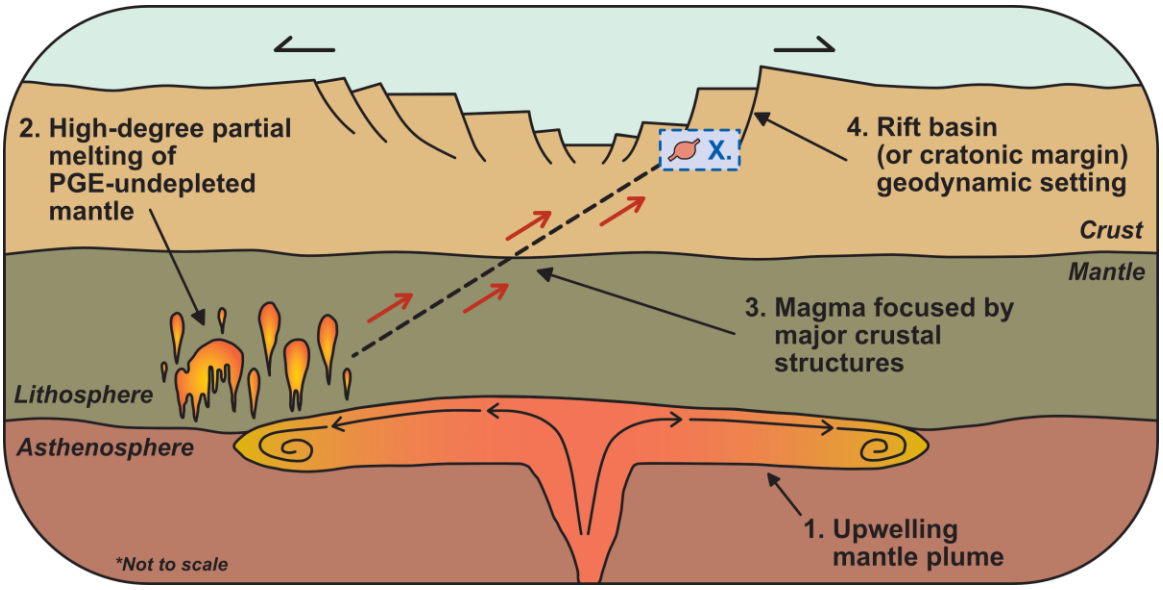

Figure 1.2: Tectonic-scale processes that contribute to the formation of magmatic sulfide deposits. The dashed box inset depicts the setting of Figure 1.3. Sources: 1,4 – Barnes et al. (2015); 2 – Mungall (2014); 3 – Lightfoot and Evans-Lamswood (2014).

Once the mantle-derived, mafic–ultramafic magma arrives in the crust, several critical processes must occur to generate the necessary sulfide liquid and enrich it with metals. Within the magmatic plumbing system, mafic–ultramafic magma is transported through dynamic environments characterized by low- and high-energy regions (Naldrett, 2011; Barnes et al., 2015). Repetitive interaction with the wallrock can cause fracturing, thermal erosion, and detachment of material into the magma. This detached material can be completely or partially assimilated into the magma, and may contribute additional sulfur (and/or silica) to the system (Fig. 1.3).

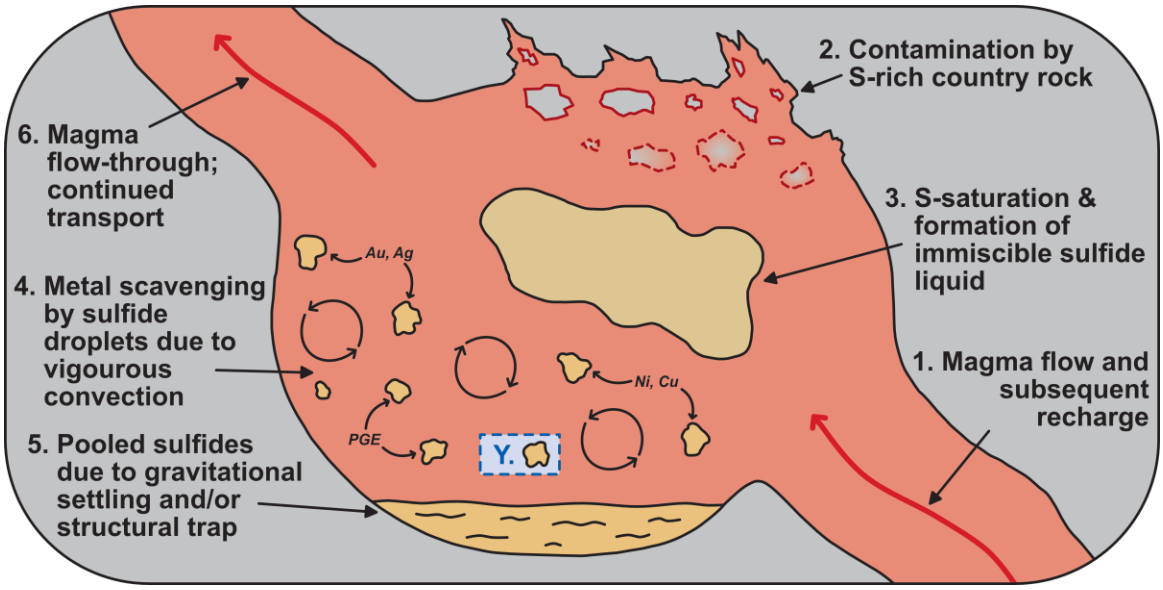

Figure 1.3: Regional-scale processes that contribute to the formation of magmatic sulfide deposits. The dashed box inset depicts the setting of Figure 1.4. Sources: 1,2 – Barnes and Lightfoot (2005), Mungall (2014), Barnes et al. (2015); 3 – Barnes and Lightfoot (2005), Holwell and McDonald (2010), Mungall (2014), Barnes et al. (2015); 4,5 – Barnes and Lightfoot (2005); 6 – Barnes et al. (2015).

The addition of these external elements affects the equilibrium of the system, driving the magma to sulfur saturation. Upon saturation, the system reaches a critical point where an immiscible sulfide liquid segregates and remains entrained in the magma as it flows through the system (Fig. 1.3). The highly siderophile and strongly chalcophile elements (e.g., Fe, Cu, Pt, Pd, Bi, and Te) will partition into the sulfide liquid from the PGE-undepleted magma. As the magma is transported and/or when the magma chamber/conduit is recharged with pulses of undepleted magma, the sulfide droplets undergo vigorous convection, continuously scavenging PGE and base metals from the silicate magma. This enrichment of the sulfide liquid in metals via interaction with silicate melt is quantified using the R factor, which, in its simplest form, is the mass ratio of silicate melt to sulfide liquid (Fig. 1.3). Sulfide liquids which have been exposed to greater volumes of silicate magma will obtain higher R factors, resulting in a greater degree of upgrading and enrichment of the sulfide liquid, which ultimately translates to higher metal tenors in the resulting deposit (Naldrett, 2011; Barnes et al., 2015).

The magmatic system may continue to behave in this manner until the magma cools at a shallower level in the crust and crystallizes in situ and/or the magma encounters a structural trap or dramatic change in conduit morphology (Lightfoot and Evans-Lamswood, 2014; Barnes et al., 2015). In the case where the sulfide droplets become physically trapped or can no longer be suspended in the magma due to a decrease in velocity (e.g., at the widening of a conduit), they will settle through the magma column because of their high density and concentrate near the base, which can lead to the formation of massive sulfide orebodies (Fig. 1.3). Lastly, given that these magmatic systems may pass through multiple staging chambers at various depths within the Earth's crust, the magmas can continue to move through the system, regardless of whether or not sulfides are trapped and lost along the way (Fig. 1.3).

Once the system begins to lose energy and the segregated sulfide liquid cools, sulfide minerals begin to crystallize through a defined sequence (Fig. 1.4). At 1200°C, the metal-rich sulfide liquid is trapped between cumulus silicate minerals (Holwell and McDonald, 2010). As the temperature within the system decreases to approximately 1000°C, a monosulfide solid solution (MSS) containing Ni, Fe, IPGE (Ir, Os, Ru), and Rh crystallizes, with the residual liquid being Cu rich. Upon further cooling to around 900°C, the Cu-rich residual liquid crystallizes to intermediate solid solution (ISS); this fractionation leaves behind the remaining PGE and semimetals (e.g., Te, As, Bi, Sn, Se) in the system in a residual liquid (Holwell and McDonald, 2010). Between 650-250°C, discrete platinum-group minerals (PGMs) crystallize from semimetal-rich liquid, while MSS and ISS recrystallize to pyrrhotite–pentlandite, and chalcopyrite, respectively. The flux of deuteric, meteoric, or metamorphic fluids through the system post-crystallization has the potential to alter the primary sulfide (and PGM) assemblage by low–temperature, hydrothermal processes (Prichard et al., 2013; Holwell et al., 2017). Post-magmatic alteration of sulfide minerals has the potential to contribute to further concentration, or removal, of metals in the system, simply by reconfiguring the mineralization in the system, or by

remobilization of PGE and base metals leading to depletion in the deposit (Hinchey and Hattori, 2005; Song et al., 2009; Prichard et al., 2013; Holwell et al., 2017; Wang et al., 2021).

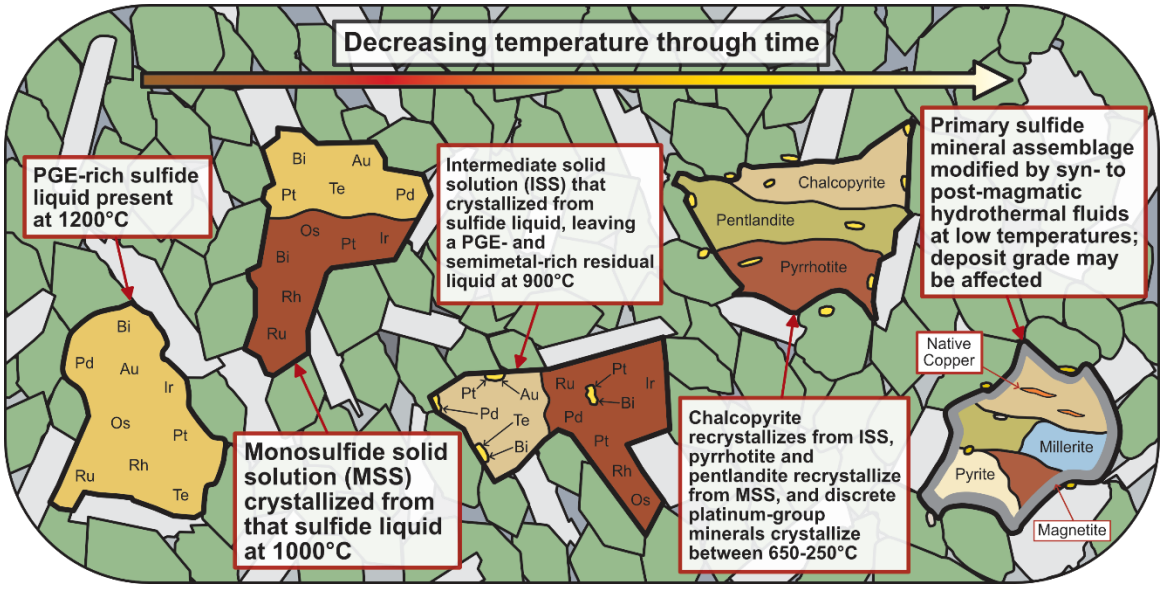

Figure 1.4: Deposit- or local-scale processes that contribute to the formation of magmatic sulfide deposits. Modified after Holwell and McDonald (2010, and Holwell et al. (2017).

1.3 Objective

The primary objective of this thesis was to investigate and characterize the mineralogy, chemistry, and isotope systematics of sulfide and platinum-group minerals within and around the high-grade zone of the Escape intrusion. To achieve this, characterization of the textures and relationships of these minerals has been used to delineate the paragenesis and fractionation history of mineralization in the deposit. Process mineralogy and data obtained from mineral liberation analysis (MLA) has been integrated with petrographic observations to assess potential challenges of ore beneficiation during metallurgical processing. The multiple S isotope composition of sulfide minerals has been utilized to examine the contribution of externally derived S on the sulfur saturation history of the magma. These data are complimented by bulk-rock geochemical data to further investigate the effects of crustal contamination on the mineralized system. The trace-element chemistry of sulfides obtained via laser ablation ICP–MS was used to characterize the

location of metals within the system (i.e., are the PGE hosted by sulfides?), quantify their concentrations, and assess the degree of magmatic enrichment experienced by the sulfide liquid (i.e., R factor). In addition, these data, combined with mineral textures, were used to assess the effects of post-magmatic (i.e., hydrothermal) processes on the distribution of metals and characterize whether these processes affected the metal tenor of the deposit. Lastly, these mineralogical, textural, and geochemical features were integrated into a genetic model for the Escape mineralizing system.

2 Regional Geology

2.1 Superior Province

2.1.1 Subdivisions and Formation

The Superior Province is one of the world's largest intact Archean cratons and forms the majority of the Canadian Shield (Percival et al., 2006a). It extends from eastern Manitoba and northern Minnesota, through Northern Ontario, and into western–northwestern Quebec. Figure 2.1 illustrates the extent of the Superior Province through Northwestern Ontario.

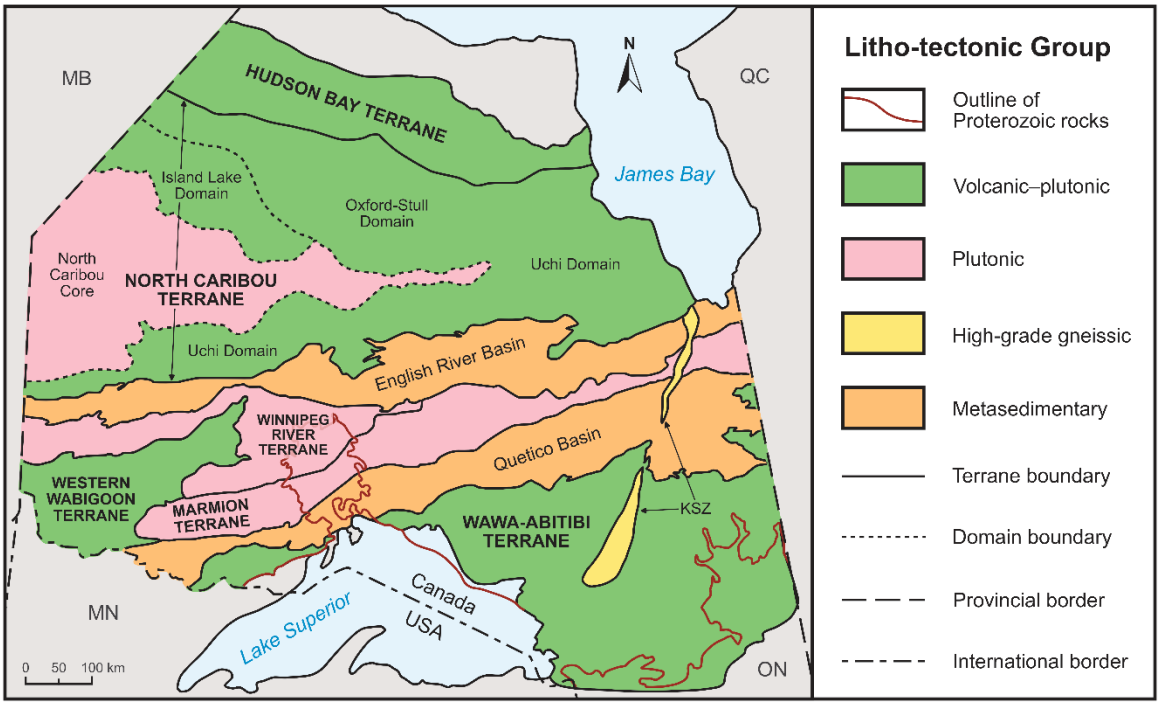

Figure 2.1: Terrane and domain boundaries of the various subprovinces of the Superior Province in Northwestern Ontario (modified from Stott, 2011).

Card & Ciesielski (1986) subdivided the Superior Province into four litho-tectonic groups, namely volcanic–plutonic, plutonic, high-grade gneissic, and metasedimentary subprovinces. Definitions of subdivisions have evolved over time, such that the term "subprovince" now refers to any major subdivision of the Superior Province. Modern revisions to the nomenclature for the terrane boundaries of the Superior Province include "terrane", which is defined by Stott et al. (2010) as a tectonically bounded region with internal characteristics distinct

from those in adjacent regions that existed prior to the Neoarchean assembly of the Superior Province, and "domain", which is a typically younger, lithologically distinct portion of a terrane, but with either juvenile crust or sharing a common basement. The terrane subdivision includes metasedimentary basins, which are interpreted by Stott et al. (2010) to have formed on the margin of the larger terranes during the assembly of the Superior Province. Initial and revised subdivisions of the Superior Province are based on interpretations derived from analysis of major fault zones and structures, seismic reflection and refraction profiles, aerial geophysical surveys, geochemical signatures, metamorphic grades and assemblages, geochronology, and lithological units (Card and Ciesielski, 1986; Stott et al., 2010). The volcanic–plutonic subprovinces typically consist of long linear assemblages of supracrustal metavolcanic rocks. These metavolcanic rocks are commonly referred to as greenstone belts due to their sub-greenschist to greenschist metamorphic grade (Card and Ciesielski, 1986). The granite–greenstone subprovinces of the Superior Province include the North Caribou, Wabigoon, and Wawa–Abitibi terranes, respectively (Fig. 2.1). The metavolcanic rocks occur alongside numerous felsic intrusive rocks, including earlier synvolcanic plutons and gneisses, as well as later foliated to massive quartz diorite–granite plutons and syenite (Card and Ciesielski, 1986). The plutonic subprovinces, such as the Winnipeg River terrane, the Marmion terrane, and the North Caribou Core of the North Caribou Terrane, are highly metamorphosed and variably deformed. Although the plutons in the granite–greenstone provinces are largely indistinguishable from those in the predominantly plutonic subprovinces, the defining feature that demarcates the two types of terranes is the presence of supracrustal greenstone rocks in the former (Williams et al., 1992; Card and Ciesielski, 1986). The metasedimentary belts comprise turbiditic sediments, migmatites, and granitic equivalents, and are believed to have formed from rapidly deposited detritus from nearby granite–greenstone terranes (Williams et al., 1992; Card and Ciesielski, 1986). The metasedimentary subprovinces of the Superior Province include the English River, Quetico, and Pontiac basins (Fig. 2.1).

Over the past 80 years, a significant amount of work has been done towards developing an understanding of the formation of the Superior Province, with initial paradigms invoking autochthonous cyclicity to explain the preponderance of different rock assemblages throughout the province (Williams et al., 1992). With more detailed studies and the application of new technologies, juxtaposition of allochthonous terranes by way of accretionary processes has become the generally accepted mechanism for the formation of the craton (Angus et al., 2009; Percival et al., 2006b; White et al., 2003; Williams et al., 1992). Evidence that supports an accretionary origin includes the presence of large-scale linear collections of diverse rock types, which have structural and metamorphic transition zones at their boundaries. Moreover, the application of high-precision U–Pb dating has led to the recognition of a progressive younging of the subprovinces southward (Corfu and Davis, 1992). This is complemented by seismic reflection and refraction surveys (e.g. the Lithoprobe and NATMAP transects) which have demonstrated the presence of continuous north-dipping features interpreted as a series of stacked accreted terranes (Percival and Helmstaedt, 2006; White et al., 2003).

The formation of the Superior Province may be divided into two main stages. The first stage involves the assembly of the individual subprovinces (Mesoarchean tectonism), and the second stage sees their accretion and amalgamation as a result of a series of tectonic collisions, collectively known as the 2.7 Ga Kenoran Orogeny (Percival, 2007; Williams et al., 1992; Percival et al., 2006a). The North Caribou Terrane has been interpreted by Percival et al. (2006a) as the nucleus or protocontinent around which the core of the Superior Province formed. The onset of subprovince aggregation took place in the north, with the collision of the Hudson Bay and the North Caribou terranes at 2.72 Ga, in an event known as the Northern Superior Orogeny (Percival et al., 2006a). The Uchian Orogeny occurred at 2.72–2.70 Ga, with the collision of the Winnipeg River Terrane with the Uchi Domain of the North Caribou Terrane. During this collision, turbidite sequences were deposited between the converging terranes and subsequently

deformed, leading to the formation of the English River Basin (Corfu et al., 1995). The Central Superior Orogen occurred at the south margin of the composite Superior Province between 2.71–2.70 Ga; with the Western Wabigoon Terrane accreted onto the Winnipeg River Terrane (Percival et al., 2006a; Sanborn-Barrie and Skulski, 2006). The Wawa–Abitibi Terrane impacted the composite Superior craton from the south during the Shebandowanian Orogeny at 2.695 Ga. Prior to and during this collision, volcanic–plutonic detritus was rapidly deposited in a deep-water delta fan environment, which was subsequently scaped off by the down-going slab and trapped in the collision zone. This tectonic stacking of turbiditic sedimentary sequences produced the accretionary wedge that is the Quetico Basin (Fralick et al., 2006). Lastly, the Minnesotan Orogeny at ~2.68 Ga marked the accretion of the Minnesota River Valley terrane onto the southernmost margin of the Superior Province. Similar to the creation of the previous metasedimentary subprovinces, the Pontiac Basin was formed during this event from the confining of synorogenic turbidite deposits within the fore-arc basin (Percival, 2007; Percival et al., 2006a).

2.1.2 Quetico Basin

The country rocks surrounding the Escape intrusion, the focus of this study, constitute rocks of the metasedimentary Quetico Basin. The Quetico Basin (Fig. 2.1) forms a roughly 1,000 km long linear belt running from the edge of northern Minnesota and into Ontario, through the Kapuskasing Structural Zone (KSZ) and into Quebec, with an approximate width of 70 km (Williams, 1991).

In the north, the Quetico Basin borders the Wabigoon terrane, with the major transcurrent Quetico and Gravel River faults marking the boundary. In the south, the Basin borders the Wawa–Abitibi terrane, with the boundary marked by thrust faults (Williams, 1991; Percival and Williams, 1989). The majority of rocks within the Quetico Basin are metamorphosed wacke (Williams, 1991), with other minor metasedimentary rocks (e.g., siltstones, iron formation,

conglomerate, and ultramafic wackes), both I-type and S-type granitoid suites, widely scattered mafic-ultramafic intrusions, thin swarms of mafic sheets near the southern margin of the subprovince, and paragneisses and migmatites derived from a combination of these rock types (Williams, 1991; Percival et al., 2006a). The sedimentary sequences of the Quetico Basin are thought to be synorogenic based on the overlap of their depositional ages (2.71–2.699 Ga dated from detrital zircons), and the ages obtained for the regional deformation and late magmatism (2.70–2.696 Ga and 2.71–2.70 Ga, respectively) of the Wabigoon subprovince (Davis, 1998). Within the accretionary tectonic framework, the Quetico sediments would have formed in a forearc setting as rapidly deposited clastic sediments in deep-water turbidite sequences (Percival and Williams, 1989). These sedimentary successions (where preserved near the margins of the subprovince) record stratigraphic younging directions to the north, in spite of being subjected to four deformation events and metamorphic recrystallization over a period of 40 million years (Williams, 1991; Percival and Williams, 1989). Almost all of the rock types in the Quetico Basin are metamorphosed, with low metamorphic grades (greenschist) occurring near the boundaries of the subprovince, whereas the highest grades (upper amphibolite and local granulite) are recorded at the central axis of the subprovince (Percival and Williams, 1989; Williams, 1991).

The various granitoid units within the Quetico Basin can be broadly divided into early (~2.688-2.680 Ga) “I-type” granitoids (those which are predominantly derived from mantle or lower crust sources) and later (~2.67-2.653 Ga) “S-type” granitoids (those which are predominantly derived from metasedimentary sources; Wang, et al., 2020; Williams, 1991; White and Chappell, 1983). The earlier “I-type” granitoids consist of hornblendites, diorites, syenites, and tonalites, and are often foliated due to their emplacement being coincident with the deformational events associated with the formation of the Quetico Basin (Williams, 1991). The later “S-type” granitoids are one- to two-mica leucogranitoids, often peraluminous to

metaluminous, and constitute the most abundant granitoid rocks in the Quetico Basin. The leucogranitoids are often present as leucosomes in the migmatites (Williams, 1991).

2.2 Geology of the Lake Superior Region, Ontario

2.2.1 Paleo-Mesoproterozoic Sedimentary Rocks

Prior to MRS magmatism, two distinct Paleo- to Mesoproterozoic sedimentary rock sequences — the Animikie and Sibley groups — were deposited in the Lake Superior region (Fig. 2.2).

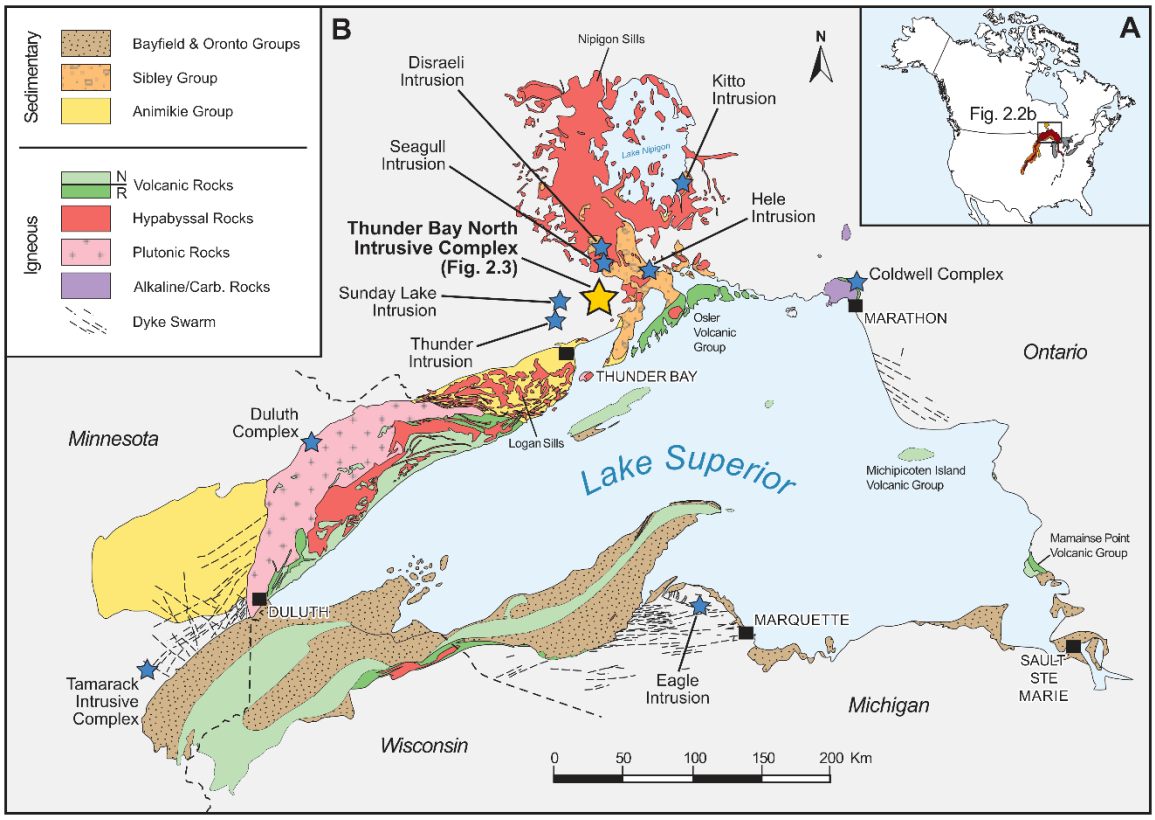

Figure 2.2: Map of Lake Superior Region geology (modified after Bleeker et al., 2020; Hinze and Chandler, 2020; and Jirsa et al., 2011). A – Extent of MRS rocks within North America; B – Rock units and associated mineral deposits.

In the Thunder Bay area, the Animikie Group represents a homoclinal structure of Paleoproterozoic sedimentary rocks, deposited on Archean basement (Sutcliffe, 1991). The Animikie rocks are present in Ontario, Minnesota, Wisconsin, and Michigan, with different names used in Canada and the United States. In Ontario, the Animikie Group consists of the lower

Gunflint Formation and the upper Rove Formation. The 1878.3 ± 1.3 Ma Gunflint Formation consists of iron formation, chert, and argillite, while the 1836 ± 5 Ma Rove Formation comprises shales and greywackes (Fralick et al., 2002; Addison et al., 2005). These two formations are separated by a 25 to 70cm-thick layer consisting of hypervelocity impact ejecta, which is interpreted to be produced from the 1850 ± 1 Ma Sudbury impact event (Addison et al., 2005).

In the area west of Lake Nipigon extending to the northern shore of Lake Superior, the Sibley Group is exposed and consists of five chemical and siliciclastic sedimentary formations — the Pass Lake, Rossport, Kama Hill, Outan Island, and Nipigon Bay formations (Rogala et al., 2007). The Pass Lake Formation consists of two members: the conglomerates of the Loon Lake Member unconformably overlie the basement rocks in this area, with the plane-bedded sandstone of the Fork Bay Member deposited on top (Rogala et al., 2007).

The sedimentary environment in which the Sibley Group formed is interpreted as a change from a lacustrine system (Pass Lake Formation) through to more arid conditions, culminating in an aeolian environment (Nipigon Bay Formation; Heaman et al., 2007; Rogala et al., 2007). The deposition of sedimentary rocks of the Sibley Group predates the Keweenawan magmatic activity of the Midcontinent Rift; the maximum depositional age for these rocks is bracketed by the youngest U-Pb detrital zircon of the Outan Island Formation at ~1400 Ma (Rogala et al., 2007).

2.2.2 Midcontinent Rift System

2.2.2.1 Formation and Lithology

During the Mesoproterozoic to early Neoproterozoic, a series of tectonic and magmatic events produced the North American Midcontinent Rift System (MRS). The MRS is arcuate in shape and spans approximately 2,000 km through the axis of Lake Superior, with its limbs extending southward into the United States of America (Fig. 2.2a; Sutcliffe, 1991). Various

geophysical studies have been implemented to image the size and structure of the rift system, including seismic reflection and refraction, gravity, and aeromagnetic surveys. Profiles of the MRS have been created using data collected from seismic surveys, such as GLIMPCE (Great Lakes International Multidisciplinary Program on Crustal Evolution; Behrendt et al., 1988) and recently the SPREE project (Superior Province Rifting EarthScope Experiment; Bollmann et al., 2019). These profiles have been used to suggest that the MRS may extend up to 32 km below the surface, and that significant underplating beneath the rift is supportive of initiation by a mantle plume (Zhang et al., 2016; Behrendt et al., 1988). Gravity surveys (and the resultant residual Bouguer gravity anomaly maps), in conjunction with total magnetic intensity maps have been used to define the overall shape of the MRS and its projected extent at surface (Hinze and Chandler, 2020).

Rocks of the MRS were emplaced into and on the rocks of the Superior Province and the sedimentary rocks of the Animikie and Sibley groups (Cannon, 1992), and generally comprise voluminous flood basalts and minor felsic volcanic rocks that occupy the center of the rift; syn- and post-tectonic sedimentary units; mafic–ultramafic intrusions (e.g., sills, dyke swarms, discordant conduits, and layered intrusive complexes such as the Duluth Complex in Minnesota, USA) that are contemporaneous with volcanism; and alkaline complexes (e.g., the Coldwell Complex). The duration of MRS magmatism and the corresponding emplacement of these rocks spanned from 1.15-1.094 Ga (Heaman et al., 2007). The formation of the MRS can be divided into three main events — i) regional extension and wide-spread magmatism, ii) termination of rifting followed by subsidence, sedimentation, and thermal sag basin development, and iii) inversion of rift-related structures due to regional compression (Hinze and Chandler, 2020). Most of the magmatic activity occurred during the first event between ca. 1112–1083 Ma, and can be split into an Early Plateau Stage, a Rift Stage, and a Late-Rift Stage (Woodruff et al., 2020). There are two competing theories that attempt to explain the mechanism that initiated continental

rifting. The first, more widely accepted hypothesis, is that of an active rifting model, which involves crustal thinning and eventual extension produced by the upwelling of a mantle plume (Cannon and Hinze, 1992). The head of the mantle plume spread laterally beneath the lithosphere, dissipating its mechanical energy, and causing crustal extension above. Support for this theory includes the abundant magmatic rocks associated with the rift, and primitive isotopic signatures that characterize the rift-fill flood basalts (Cannon and Hinze, 1992). The alternative hypothesis invokes a passive rifting model initiated by far-field forces that caused regional extension due to collision and subduction of the Grenville Orogeny (Cannon and Hinze, 1992; Sutcliffe, 1991). Recently, the debate regarding the applicability of the plume model has resurfaced due to questions concerning the extended period of magmatic activity when compared to other large igneous provinces (LIPs), the absence of a radiating dyke swarm that typically results from mantle plume impaction, and the fact that magmatic rocks of the MRS display heterogeneous mantle source characteristics (Hollings and Cundari, 2020). Swanson-Hysell et al. (2019) suggested that the 25 million years of magmatism of the MRS may be explained by slab avalanche. By analyzing the apparent polar wander path (APWP) of Laurentia, Swanson-Hysell et al. (2019) concluded that the plates were moving very rapidly prior to and during the formation of the Midcontinent Rift. This movement was interpreted to be the result of rapid subduction at the margin of Laurentia, which contributed downwelling material to the mantle, affecting its mass-balance. The deposition of this slab in the mantle in effect drove the upwelling of the mantle plume and has been evoked to explain for the lengthy duration of MRS magmatism.

The onset of voluminous magmatism occurred during the Plateau Stage (ca. 1111–1105 Ma), with the formation of a ~10 km thick volcanic plateau in the Lake Superior region comprising hundreds of subaerial basalt flows (Green, 1989; Woodruff et al., 2020). Contemporaneous intrusive activity occurred during this period, and due to the abundance of newly accumulated volcanic material, a thermal sag basin developed with subordinate normal

faulting (Sutcliffe, 1991; Woodruff et al., 2020). Following a brief three-million-year period of latent magmatic activity, the Rift Stage occurred from ca. 1102–1090 Ma, during which time crustal thinning and extension of the rift took place. This produced a series of alternating, asymmetric grabens, with accompanying normal faults along the central axis of the rift. At this point, the rapidly subsiding rift basins were infilled with large volumes of successive subaerial basalt flows (Woodruff et al., 2020). Interflow sedimentary units commonly mark breaks in these successive basalt flows. Similar to the Plateau stage, intrusion of mafic–ultramafic rocks (e.g., the Duluth Complex) accompanied this volcanism. The Late-Rift Stage occurred between ca. 1090–1083 Ma and marked a turning point in the evolution of the MRS; heat of the mantle plume began to dissipate (thermal collapse of the mechanism driving rift development), magmatism diminished, subsidence continued, and sedimentary processes dominated. During the period between ca. 1083–1060 Ma, known as the Post-Rift Stage, massive volcanism abruptly ceased, subsidence continued at a slower rate, and sedimentation increased broadly beyond the central axis and basins of the MRS (Sutcliffe, 1991; Cannon, 1992; Woodruff et al., 2020). Finally, the Compressional Stage occurred between ca. 1060–1040 Ma, during which time normal faults bounding the central grabens were inverted due to the transformation of regional tectonism to a compressional regime (Sutcliffe, 1991; Hinze and Chandler, 2020; Woodruff et al., 2020). This resulted in the juxtaposition of older volcanic rocks upon younger sedimentary units, as well as regional folding. The nearby Grenville Orogeny is often credited with the cessation of rifting and compression of rift structures (Hinze and Chandler, 2020). As the thermal and mechanical energy of the upwelling mantle plume decreased, the concurrent events of the Grenville Orogeny to the east became the dominant regional stress, terminating the rifting and eventually inverting the central basins of the MRS (Hinze and Chandler, 2020; Woodruff et al., 2020).

The rocks associated with the Midcontinent Rift can be separated into two main groups: the extrusive and sedimentary rocks of the Keweenawan Supergroup, and the intrusive rocks of

the Logan igneous suite (Heaman et al., 2007). The Keweenawan Supergroup constitutes a >35 km-thick supracrustal sequence of rocks (Sutcliffe, 1991; Heaman et al., 2007). Its generalized stratigraphic sequence includes a lower, relatively thin (~100 m-thick) fluvial and lacustrine sandstone unit, followed stratigraphically by a (up to 25 km-thick) dominantly basaltic, bimodal (mafic–felsic) volcanic unit, with interflow sedimentary units of conglomerate and synvolcanic sandstone; these igneous rocks are unconformably overlain by up to 8 km of sedimentary rocks deposited after rifting (Sutcliffe, 1991; Heaman et al., 2007). In Ontario, the volcanic rocks are mostly exposed in the Black Bay Peninsula–St. Ignace Island area (Osler Volcanic Group), Michipicoten Island (Michipicoten Island Formation), and Mamainse Point (Mamainse Point Formation; Sutcliffe, 1991; Heaman et al., 2007). The overlying unconformable clastic sedimentary rocks comprise the Oronto, Bayfield, and Jacobsville groups (Heaman et al., 2007). The second group of significant rocks produced by the events of Midcontinent Rift formation include the intrusive rocks of the Logan igneous suite, which in turn form the Nipigon Embayment (Heaman et al., 2007). The Logan igneous suite is divided into two main groupings: diabase to gabbro sills and mafic-ultramafic intrusions (and/or sills). The diabase to gabbro sills may be subdivided into the Logan sills, Nipigon sills, McIntyre sills, Inspiration sills, and the Shillabeer sill, all of which intrude all other rock types in the area (Hollings et al., 2007). While the Logan sills are located south of Thunder Bay, the remaining sills are located in and around the Nipigon Embayment (Fig. 2.2; Heaman et al., 2007). The mafic–ultramafic intrusions include the Seagull, Disraeli, Hele, and Kitto intrusions, with the first three located between Lake Nipigon and Lake Superior, and the latter intrusion located on the east shore of Lake Nipigon (Heaman et al., 2007).

2.2.2.2 Magmatic Sulfide Mineralization of the Midcontinent Rift

Of relevance to this study are the intrusive rocks which host economic to subeconomic Ni-Cu-PGE mineralization. Within the Nipigon Embayment, examples of such mineralization

include occurrences within the Kitto and Seagull intrusions (Fig. 2.2). These intrusions (as well as the unmineralized Disraeli and Hele intrusions) have been dated by Heaman et al. (2007) and correspond to the Plateau Stage and Early Rift Stage of MRS development, and were emplaced into the Animikie and Sibley groups, as well as several Archean subprovinces (Woodruff et al., 2020). These intrusions exhibit sill-like to lopolithic geometry, with the emplacement of ultramafic members interpreted to have been controlled by multiple north- and northwest-trending faults of the Black Sturgeon Fault Zone (Heaman et al., 2007; Hart and MacDonald, 2007; Hart et al., 2005). In general, these mafic–ultramafic intrusions comprise a cumulate peridotite core, with irregular olivine gabbro to olivine melagabbro margins. They are geochemically similar in terms of composition, and their uniform rare-earth element (REE) as well as high field-strength element (HFSE) ratios (2.32–5.24 Gd/Yb and 4.07–30.07 La/Yb) are comparable to ratios found in ocean-island basalts (OIBs; Hart, 2005; Heaman et al. 2007). In addition, the Seagull, Disraeli, Hele, and Kitto intrusions host zones of orthomagmatic base- and precious-metal sulfide mineralization similar to that found at the Escape deposit (Smyk and Franklin, 2007; Heaman et al., 2007; Hart, 2005). Other MRS-related intrusions that host Ni-Cu-PGE sulfide mineralization include the Thunder, Sunday Lake, and Eagle intrusions (Fig. 2.2). MRS-related complexes that are host to multiple mineralized intrusions include the Tamarack Intrusive Complex, Duluth Complex, the Coldwell Complex, and the Thunder Bay North Intrusive Complex (TBNIC).

In the case of the Seagull intrusion, Heggie (2005) interpreted the basal Pt, Pd, Ni, and Cu sulfide mineralization to be the result of in situ sulfur saturation during initial emplacement of the ultramafic magma. The second zone of mineralization within the upper RGB Horizon was interpreted to be the result of individual events from magma replenishment from subsequent injections. Sm-Nd and Rb-Sr isotopic evidence suggests that the Seagull intrusion was variably contaminated by continental crust, which is consistent with the incorporation of crustal sulfur contributing or driving the magma to sulfur saturation (Heggie, 2005).

The mafic-ultramafic Thunder intrusion is located about 10 km north-northwest of Thunder Bay (Fig. 2.2) and was emplaced into the metavolcanic and metasedimentary assemblages of the Archean Shebandowan greenstone belt at 1108 ± 1.0 Ma (Trevisan, 2015). The intrusion can be subdivided into a lower mafic to ultramafic basal unit and an upper gabbroic unit based on major textural and geochemical differences; the trace and rare earth element ratios indicate that the units were the result of crystal fractionation and cumulate mineral layering from a single magmatic pulse (Trevisan, 2015). The Thunder intrusion contains magmatic Ni-Cu-PGE sulfide mineralization with grade intercepts including 20 m of 0.22 wt. % Cu, 0.06 wt. % Ni, 0.25 ppm Pt, and 0.29 ppm Pd. The main sulfide assemblage includes pyrrhotite and chalcopyrite; marcasite-pyrite replacing pentlandite occurs rarely in addition to a variety of trace PGM (e.g., michenerite, kotulskite, merenskyite). The mineralization is usually 1 to 5% in abundance, and rarely accounts for 30% of the feldspathic peridotite modally. The sulfide habit ranges from medium- to fine-grained disseminated to globular, with rare net-texture. Sulfide mineralization occurs in the lower mafic-ultramafic unit which is adjacent to the greenstone footwall (Trevisan, 2015).

The Sunday Lake intrusion is located approximately 25 km north of Thunder Bay (Fig. 2.2) and is host to PGE-Cu-Ni sulfide mineralization with the highest grade intersections showing 42.9 m of 3.43 g/t combined Pt+Pd+Au, 0.44% Cu, and 0.17% Ni found at a starting depth of 849.7 m within drillhole SL-15-013 (Flank, 2018). This mafic-ultramafic intrusion has been subdivided into four main units: the Upper Gabbro Series (UGS), Lower Gabbroic Series (LGS), Ultramafic Series (UMS), and Marginal Zone (MZ). Sulfide mineralization styles include disseminated ‘reef style’, blebby, and veinlets, with mineral assemblages dominated by pyrrhotite, chalcopyrite, pyrite, and magnetite (Flank, 2018).

The Eagle intrusion is located on the south shore of Lake Superior in the northern peninsula of Michigan, USA (Fig. 2.2). The intrusion exhibits a subvertical dike-like morphology

and was emplaced into the sedimentary rocks of the Paleoproterozoic Baraga Group around 1107.2 ± 5.7 Ma (Ding et al., 2010). This crystallization age obtained from U-Pb baddeleyite dating indicates that the Eagle intrusion formed during the Early Plateau Stage of MRS development, and was emplaced contemporaneously with the picritic basalts which mark the base of the volcanic rocks of the MRS. The Eagle intrusion is host to a magmatic Ni-Cu-PGE deposit; sulfide mineralization ranges from disseminated to semimassive to massive and is present within olivine cumulates, such as feldspathic peridotites, melatroctolites, and olivine melagabbros (Ding et al., 2010). It has been suggested by Ding et al. (2010) that at least three pulses of magma contributed to the formation of the Eagle intrusion based on mineral composition variation and ratios of incompatible trace elements. The Eagle deposit is an example of a conduit-style magmatic sulfide deposit; the concentration of ore within the intrusion has been interpreted as the result of settling of cumulus olivine and sulfide droplets at widened parts of the magmatic conduit (Ding et al., 2010).

The rocks of the Tamarack Intrusive Complex were emplaced into the Paleoproterozoic Thomson Formation (sulfide-bearing, metasedimentary black shales of the Animikie Group) in northeastern Minnesota, USA during the Early Plateau Stage of MRS development at around 1105.6 ± 1.2 Ma (Fig. 2.2; Taranovic et al., 2015). Within the complex, the “dike” area intrusions to the north are host to magmatic Ni-Cu-PGE mineralization within olivine cumulate, mafic-ultramafic rocks. Sulfide mineralization grades range up to 2.33% Ni, 1.24% Cu, 0.34 g/t Pt, 0.23 g/t Pd, and 0.18 g/t Au, with sulfides occurring mainly with net-textures within the core of the intrusion surrounded by a halo of disseminated sulfides (Taranovic et al., 2015). Massive sulfides are volumetrically minor within the intrusions and occur as lenses within the country rocks. Taranovic et al. (2015) concluded that the mineralization within the Tamarack Intrusive Complex formed by at least two unique sulfide saturated pulses of magma, in which sulfur saturation within the silicate magma was brought about by significant crustal contamination from the Thomson

Formation country rocks. Their results demonstrated that the mineralization at the Tamarack Intrusive Complex was the product of processes related to typical conduit-style magmatic sulfide deposits associated with large continental basaltic provinces (Taranovic et al., 2015).

The Duluth Complex represents a nearly continuous mass of intrusive rock found along the west axis of the MRS in northeastern Minnesota, USA (Fig. 2.2; Miller et al., 2002). The rocks of the Duluth Complex have been subdivided into four main rock series (distinguished based on age, lithology, and structure), all of which were emplaced into the metasedimentary country rocks of the Virginia Formation during the Rift Stage of MRS development (emplacement ages range from ~1108-1099 Ma). The Felsic series occurs as a semicontinuous mass along the eastern and central roof zone of the complex and consist of massive granophyric granite with lesser amounts of intermediate rocks. The Early gabbro series was emplaced along the northeastern contact of the complex and consist of layered sequences of gabbroic cumulate rocks. The Anorthositic series was emplaced throughout the complex and consists of plagioclase-rich gabbroic cumulates which constitute a structurally complex suite of foliated (but not commonly layered) rocks. The Layered series was emplaced along the base of the complex and consist of variably differentiated mafic layered intrusions in a stratiform suite that is troctolitic to ferrogabbroic in cumulate composition. Both disseminated and massive sulfide mineralization occur within the Duluth Complex in the basal contact zones of the intrusions and with the latter style of mineralization also occurring within footwall country rocks (Miller et al., 2002). Two predominant intrusions host magmatic sulfide mineralization within the complex, namely the South Kawishiwi and Partridge River intrusions. The disseminated sulfide deposits within these intrusions occur within taxitic troctolitic to gabbroic rocks and contain abundant inclusions of various footwall rocks; in addition to this textural evidence, sulfur isotopic studies indicate that the pelitic country-rocks of the Virginia Formation provided the source of sulfur for these systems (Ripley, 1986). The disseminated sulfide mineralization in these intrusions is dominantly

composed of an interstitial assemblage of pyrrhotite, chalcopyrite, pentlandite, and cubanite, with average modal abundances of sulfides ranging from 1-5% (Miller et al., 2002). In aggregate, these deposits contain more than 4.4 billion tonnes of ore, with an average content of 0.66% Cu and 0.2% Ni; local anomalous concentrations of PGE are found within the basal zones of these intrusions as well (Listerud and Meineke, 1977). Locally, semi-massive to massive sulfide mineralization occurs along the basal zones of these intrusions in the Duluth Complex.

The Coldwell Complex was emplaced into the Archean Schreiber-Hemlo greenstone belt on the northeastern shore of Lake Superior (Fig. 2.2) around 1108 ± 1 to 1105.3 ± 0.6 Ma, placing it within the Early Plateau Stage of MRS development (Heaman and Machado, 1992; Good and Dunning, 2018). The complex is a composite pluton of tholeiitic-alkaline affinity and is composed of three intrusive centers (Walker et al., 1993). The Marathon Cu-PGE deposit (and numerous other Cu-PGE deposits) occurs within the Eastern Gabbro Suite of Center I of the Coldwell Complex (Brzozowski et al., 2020). The Marathon deposit is in development and contains 179 Mt of ore with grades up to 0.20% Cu, 0.56 ppm Pd, 0.18 ppm Pt, and 0.07 ppm Au (Bradfield et al., 2020). The sulfide assemblage amongst the various mineralized horizons in the deposit consists of disseminated to semimassive chalcopyrite, and pyrrhotite, with lesser pentlandite, bornite, and cubanite (Brzozowski et al., 2020). Brzozowski et al. (2020) concluded that the mineralized magma that produced the Marathon deposit was subjected to high R factors and contamination by high S/Se Archean metasedimentary rocks; chalcophile elements were also interpreted to have been remobilized from chalcopyrite and reprecipitated by late-stage hydrothermal fluids.

2.3 Thunder Bay North Intrusive Complex

2.3.1 Overview

The Thunder Bay North Igneous Complex (TBNIC) is located approximately 50 km northeast of Thunder Bay, Ontario, and comprises a series of genetically related, physically interconnected, weakly to undeformed, and unmetamorphosed mafic–ultramafic chonoliths (Fig.

2.3; Clark, 2020). This network of intrusions comprises the Current, Escape, and Lone Island intrusions, which are orthogonally joined by the East–West Connector (EWC). The EWC is bound by the Escape Lake Fault Zone, which is the southernmost structural corridor of the Quetico Fault System (Fig. 2.3). The complex also contains the 025 and Greenwich intrusions, which are located ~3 km north-northwest and ~ 3 km north-northeast of the Current Intrusion, respectively (Fig. 2.3). All these intrusions were emplaced into rocks of the Quetico Subprovince. Although the Current and Escape intrusions are separated by several kilometres, their lithostratigraphy is comparable, with both being characterized by a mineralized peridotite core, an overlying altered olivine gabbro to melagabbro, and an upper Hybrid unit. The zones of mineralization in both the Current and Escape intrusions have been interpreted to be the result of long-term magma flow through active, dynamic conduit systems (i.e., a flow-through system; Thomas et al., 2011; Heggie et al. 2014; Clark, 2020).

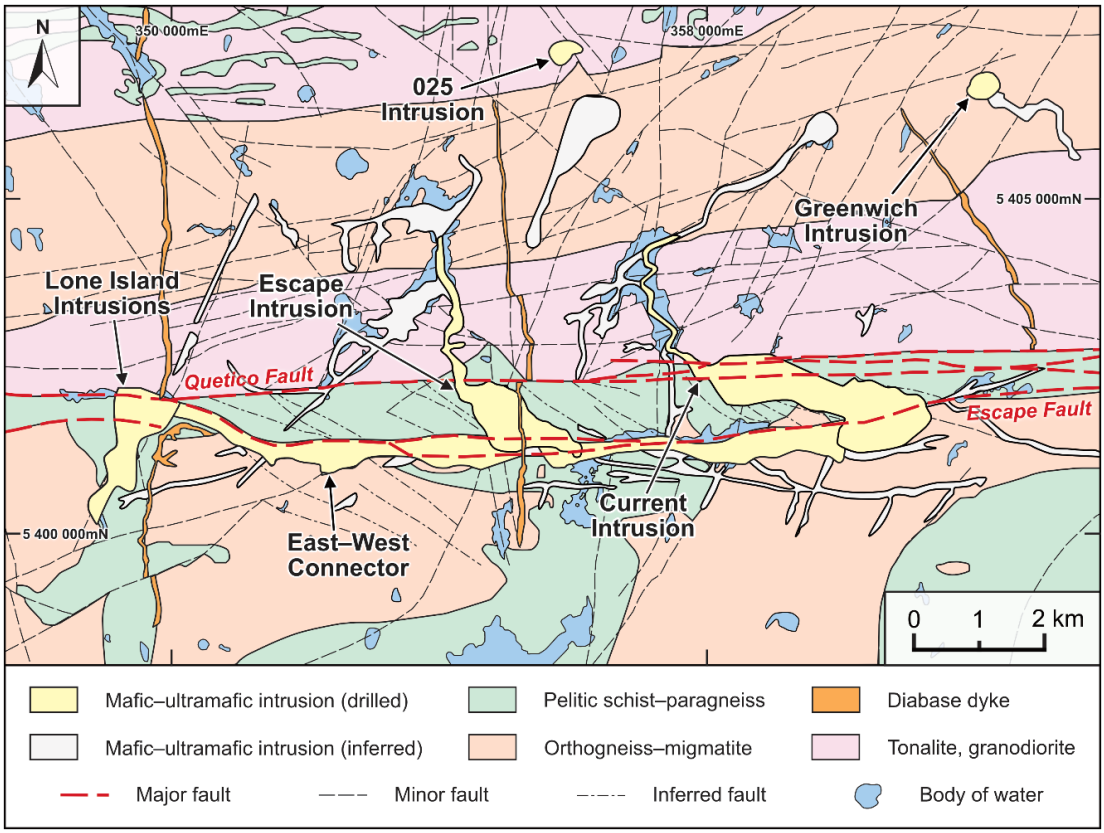

Figure 2.3: Map of the Thunder Bay North Intrusive Complex geology (modified after Thomas et al., 2011). Coordinate system: NAD83, UTM Zone 16N.

The main lithologies of the Escape intrusion comprise peridotite (both lherzolite and wehrlite), feldspathic peridotite, olivine melagabbro, and varitextured and layered gabbro. Atypical mafic intrusions — which are termed "Hybrid" by Clean Air Metals Inc. — are spatially related and frequently overlie these mafic–ultramafic intrusions. These units contain abundant cavities, structures interpreted as infilled gas bubbles (amygdules) or calcium carbonate ocellae (immiscible liquid droplets), and provide evidence for assimilation of country rock (e.g., rounded siliceous xenoliths; D'Angelo, 2013; Chaffee, 2015). The Hybrid consists of upper and lower varieties; the upper red Hybrid has been strongly hematized, is amphibole-bearing, and exhibits an ophitic to subophitic texture, whereas the lower grey Hybrid exhibits weak to no hematization and is subophitic to equigranular. In the case of the Current Intrusion, the Hybrids have been characterized as a variable mixture of altered leucogabbro, leucotroctolite, and monzonite. The Hybrid sequences are unmineralized, in sharp contact with the underlying intrusions (in the case of the upper Hybrid) and are interpreted by Clean Air Metals Inc. (CAM) geologists as products of fractional crystallization.

The TBNIC is interpreted as a component of the Keweenawan Supergroup. Based on U-Pb geochronology on zircon, the age of the Current Intrusion has been reported as 1106.6 ± 1.6 Ma (Bleeker, 2020) which corresponds to the Plateau Stage of MRS development.

2.3.2 Exploration History

Since 2001, extensive mineral exploration has been completed throughout the TBNIC. Dr. Graham Wilson and Dr. Gerald Harper discovered mineralized peridotite boulders along the western shore of Current Lake, with elevated concentrations of platinum-group elements (PGE) and base metals. Subsequently, extensive drilling, geophysical surveying, mapping campaigns, and multiple desktop studies were completed by various exploration companies during the 2000s to 2010s. Exploration efforts have continued over the years following the discovery of abundant orthomagmatic sulfide mineralization in the Current and Escape intrusions (and locally minor

disseminated sulfide mineralization in the Lone Island and 025 intrusions). Recent activities include development of combined mineral resources for the Current and Escape deposits by the present claim holder CAM. To date, combined drilling includes 896 drill holes totaling over 212,320 m between the two deposits, the majority of which having been conducted on the Current deposit. The deposits are polymetallic in nature, and contain elevated concentrations of Pt, Pd, Au, Ag, Rh, Co, Cu, and Ni. While the Current deposit constitutes a significant component of the TBNIC, the focus of this thesis is the Escape intrusion.

2.3.3 Escape Intrusion

The Escape intrusion is located ~3 km west of the Current intrusion, adjacent to the EWC, and approximately in the center of the TBNIC (Fig. 2.3). It is volumetrically larger than the Current intrusion, and is sub-horizontal, with a south- to southeast plunge (Clark, 2020). The shape of the intrusion has been interpreted from aeromagnetic data and when observed in plan view can broadly be described as a "tadpole" which widens substantially from north to south. In three dimensions, the Escape intrusion is described as a "chonolith", which is defined by Daly (1905) as an irregularly injected body of magma that does not conform to conventional sill or dyke geometries. These irregular intrusions are often tube-shaped, and as is the case at Noril'sk-Talnakh, display margins which truncate the layering in host sedimentary rocks (Barnes et al., 2015). Chonoliths are often associated with major crustal structures, with magma localized by dilations and traps created by cross-linking (transtensional) structures in strike-slip fault zones (Lightfoot and Evans-Lamswood, 2014). The Escape intrusion has been subdivided into four mineralized zones, which are connected sequentially along the length of the intrusion; these are, from north to south, Steepledge North, Steepledge South, and Escape South (Fig. 2.4).

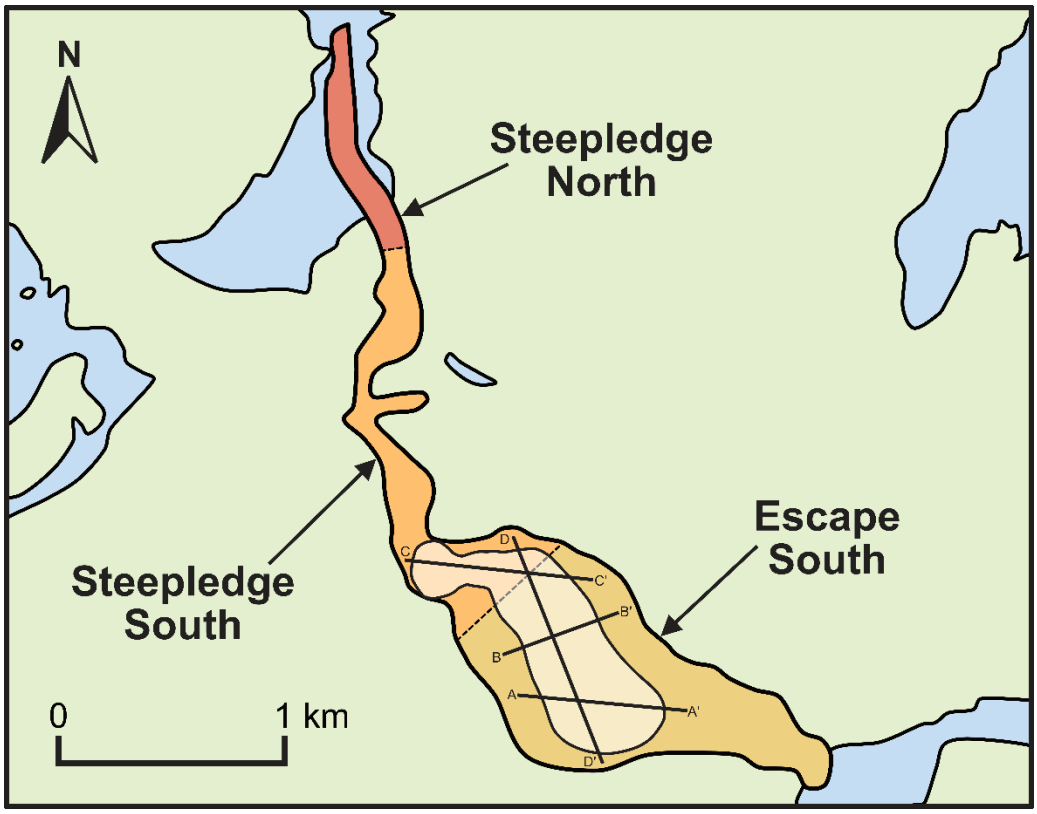

Figure 2.4: Generalized map outlining the different mineralized zones of Escape. White outline and cross section lines correspond to sections shown in Figure 2.5 (modified after Thomas et al., 2011 and Clark, 2020). Central lake coordinates are 354,688.98 mE, 5,402,602.19 mN (NAD83, UTM Zone 16N).

The Steepledge zones occur north of the Quetico Fault and exhibit a shape similar to a tall, hourglass-like tube; these zones occur at different stratigraphic levels and results from diamond drilling indicate the merging of two or three separate magma conduits (Clark, 2020). The Escape South Zone is larger than the Steepledge zones, and is tabular in form, with a flow-channeled top and bottom (Fig. 2.5). The majority of mineralization in the Escape Intrusion occurs in the Escape South Zone. This zone has been further subdivided into the Escape South High-Grade Zone (HGZ) and the Escape South Perimeter, with the latter surrounding the former, and lacking net-textured sulfide mineralization. This thesis is focused on the sulfide mineralization contained in Escape South. The overlying rocks within the Escape intrusion constitute the hybrid units. Below the hybrids, the mafic rocks of the Escape intrusion comprise fine-grained oxide gabbros, olivine gabbros/melagabbros, which are in sharp contact with each other and, in particular, the lower ultramafic rocks.

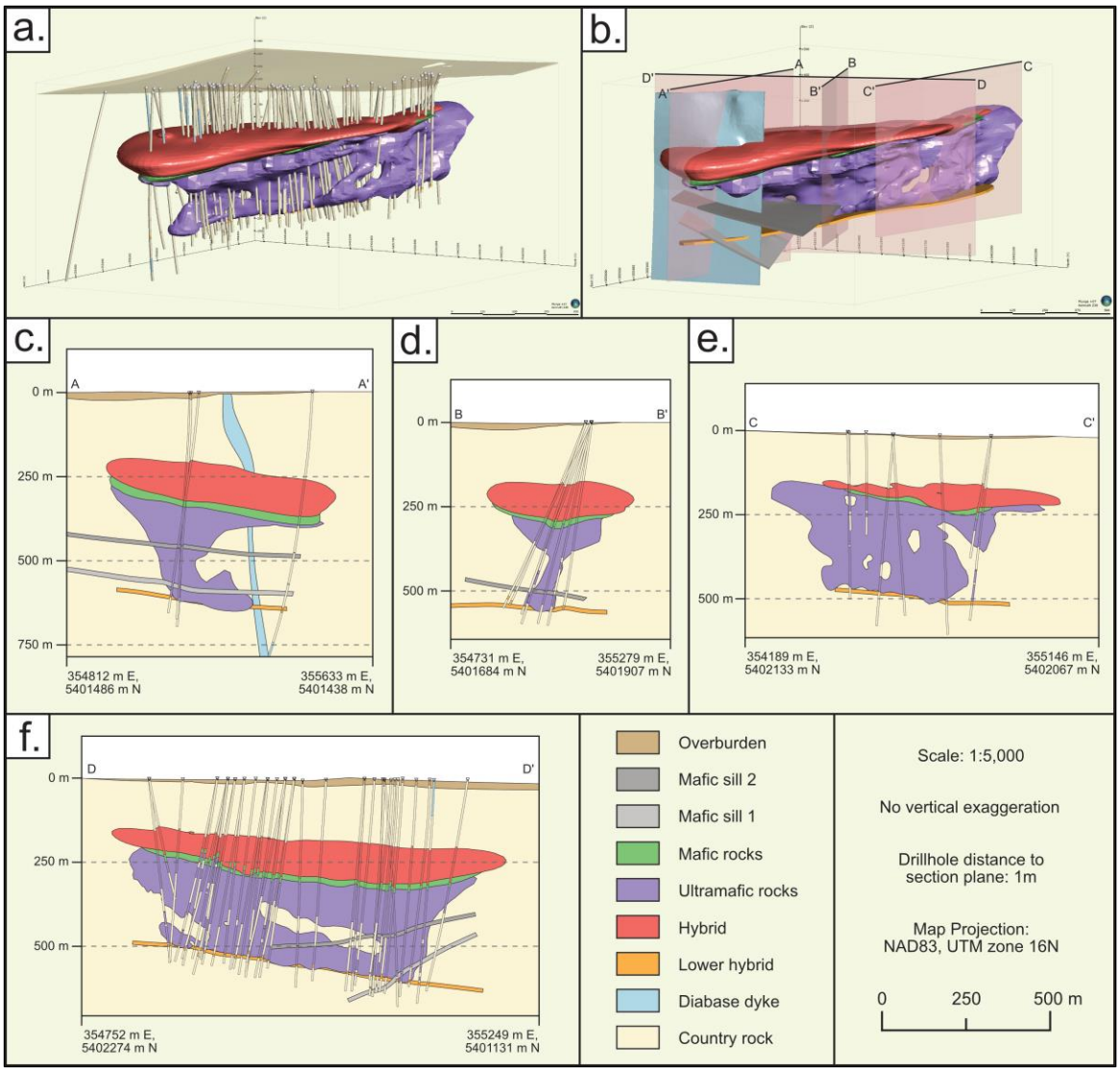

Figure 2.5: 3D geological model of the Escape intrusion and corresponding cross-sections : a. Illustrates the extent of the intrusion from Escape South to approximately Steepledge South – drillholes used to produce the model are shown as traces; b. Same view without drillhole traces and with cross section planes shown in pink; c. Cross-section A—A' through the high-grade zone; d. Cross-section B—B' across the middle of the conduit; e. Cross-section C—C' through the Ribbon Zone/Steepledge South; f. Cross-section D—D' showing the length of the Escape intrusion along strike. This model was produced from drillhole logs provided by CAM using Leapfrog Geo software.

The Hybrid lithologies include the red and grey hybrid varieties described earlier. The Lower Hybrid group occurs below the main intrusion and is fine-grained to aphanitic and gabbroic in composition. CAM has interpreted this unit to be related to the upper Hybrid units due to geochemical similarities (Heggie et al., 2015). The mafic rocks in the upper portion (between the Hybrid and Peridotite units) of the Escape intrusion are locally vari-textured and/or rhythmically layered (D'Angelo, 2013). The ultramafic rocks consist of fine- to medium-grained

peridotite, with modal layering of plagioclase occurring sporadically throughout the intrusion (i.e., a feldspathic peridotite). There is also a thin unit of olivine clinopyroxenite that always occurs between the mafic rocks and the peridotites. Miller (2020) completed a petrographic study on 32 samples collected from diamond drillhole ELR20-004, which intersected mineralization in the Escape HGZ. Miller (2020) divided the drillhole into several units, which are (from top to bottom) — oxide gabbro, <20 m of olivine clinopyroxenite; upper, middle, and lower wehrlite units (with several crosscutting leuco- and oxide-rich gabbroic dykes in between); and a 7 m-thick basal chill zone, resulting from chilling of the Escape intrusion against the Archean metasedimentary rocks.

Sulfide mineralization within the Escape South HGZ has previously been characterized as mainly consisting of strongly disseminated to net-textured (ranging from 15-40% modally) pyrrhotite, chalcopyrite, and pentlandite host within the previously mentioned medium-grained feldspathic peridotite (Clark, 2020). The sulfide mineralization present within the Escape South Perimeter is effectively the same as mineralization within the Escape South HGZ, albeit in lesser abundance with sulfides making up to 15% of the ultramafic cumulates.

3 Methods

3.1 Planning, Sampling, and Core Logging

Exploration data comprising historical core logs, drill collar locations, downhole surveys, and laboratory assays were provided by Clean Air Metals Inc. (CAM) to identify intervals for sampling. Drillhole data was imported into Leapfrog Geo where drillholes were visualized in 3D. Drillholes of interest were selected based on intersection with the mineralized body, with samples covering a range of sulfide abundance and metal grade. The mineralized body of the Escape intrusion can be divided into the high-grade zone (that contains the ore horizon) and lower mineralized zone which are depicted in Figure 3.1.

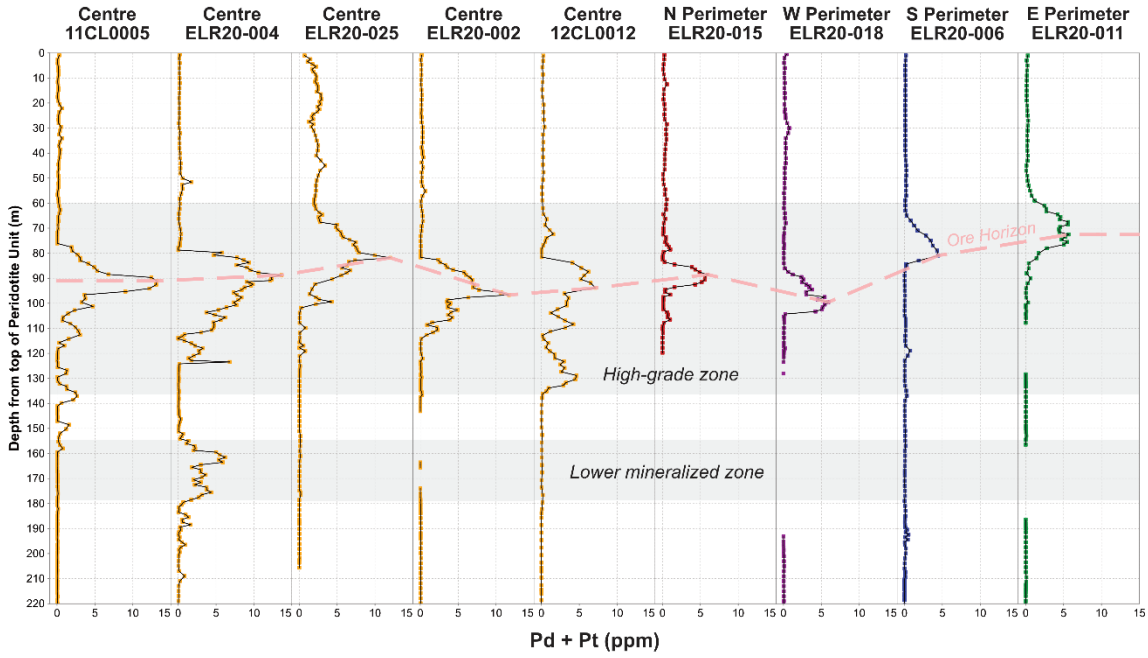

Figure 3.1: Correlated downhole plots for drillholes sampled in this study, illustrating the mineralized portions of the Escape intrusion. Depth is normalized to the top of the peridotite unit (contact with the overlying gabbro unit). The grey areas represent the range of mineralization based on the extents of PGE grade amongst the sampled drillholes. The pink dashed line represents the ore horizon which marks the highest metal grade through the sampled drillholes.

Three drillholes intersecting the main body of the high-grade zone (ELR20-025, ELR20-002, and ELR20-004) and four drillholes encompassing the perimeter of the main body (ELR20-015, ELR20-006, ELR20-018, and ELR20-011) were sampled. In total, 117 samples were collected from the seven drill holes. Initial sampling was conducted over a week in May 2021 at

Clean Air Metals' core yard west of Current Lake and Escape Lake in the Unorganized Thunder Bay District. Samples were collected every few metres down the length of the drillholes, ensuring sampling above, below, and through the mineralized horizons. In addition to sampling of the mineralized ultramafic unit, the overlying gabbroic and hybrid units, as well as metasedimentary and granitoid country rocks were also sampled.

During the summer of 2021, a relogging program of historical drill core from Rio Tinto Exploration now in possession by CAM was conducted. Detailed geological, alteration, and mineralization logs were produced for rocks at Escape, and seven mineralized drill core samples were collected from diamond drill holes 11CL0005 and 12CL0012, to capture a thorough representation of mineralization from the high-grade zone.

Maps were produced using ArcGIS to illustrate the location of sampled drillholes within the Thunder Bay North Intrusive Complex. In addition to visualization of mineralization in Leapfrog to inform sampling, a 3D geologic model of the Escape chonolith was produced. Lithologies from CAM core logs were grouped into simplified units to construct a geologically reasonable morphological model of the Escape intrusion. This helped to refine the understanding of the intrusion lithostratigraphy, and allowed creation of cross-sections to illustrate sample locations through the mineralized body.

3.2 Analytical Methods

3.2.1 Optical Microscopy

Thin section analysis was conducted using an Olympus BX2M Microscope at the Microanalytical Facility in the Department of Geology at Lakehead University. A total of 81 polished thin sections and 10 polished resin thick pucks were produced at the Department of Geology Lapidary Facility of Lakehead University for petrographic and elemental–isotopic analysis. Using transmitted- and reflected-light microscopy, the polished sections were described

in terms of modal mineralogy, textural associations, alteration, and ore assemblages. Optical microscopy was performed to identify and map out suitable sulfide grains in thin section for laser ablation microsampling, and in pucks for secondary ion mass spectrometry (SIMS).

3.2.2 Scanning Electron Microscopy and Energy Dispersive X-ray Spectroscopy

Determination of the major-element chemistry of sulfide minerals was conducted at the Lakehead University Instrumentation Laboratory (LUIL) using a Hitachi SU-70 Schottky Field Emission Scanning Electron Microscope (SEM) outfitted with an Oxford Aztec 80mm/124eV Energy-dispersive X-ray spectrometer (EDS). The electron gun filament was operated at a voltage of 20 kV, working distance between the sample surface and detector was set to 15 mm, and the Z value (effectively stage height) was adjusted for each analysis. Polished thin sections were carbon coated using an Edwards Auto 306 Carbon Coater prior to analysis.

At the start of each session, the amperage was adjusted to around 300 pA by measuring at 50k magnification within a Faraday Cup, and either increasing or decreasing the condenser lens accordingly. Following this, the EDS was calibrated using a nickel sulfide standard to ensure accuracy in measuring the energy of characteristic x-ray peaks. After calibration, the EDS was tested on a "FeS_2-Pyrite" standard (produced by Micro-Analysis Consultants Ltd.) for accuracy. If the result from this test produced a total within ±0.5% of 100%, analyses were commenced; if this total was not obtained, the calibration procedure was repeated until the check produced acceptable results. X-ray spectra obtained were converted to concentrations using the instrument's accompanying Aztec EDS analysis software. The software used various standards for analyzing the characteristic x-ray peaks of different elements, which included: "Ni Sulphide" GL Standard (produced by the Carnegie Science Geophysical Laboratory in Washington, DC, USA) for measuring S and Ni, "CuFeS2-Chalcopyrite" standard (produced by Micro-Analysis Consultants Ltd.) for measuring Fe and Cu, and the default database standards were used for measuring all other elements.

3.2.3 Whole-rock Geochemistry

Twenty-two unmineralized rock samples from Escape were submitted to ALS Canada Ltd. to characterize their bulk-rock geochemistry using their complete characterization package CCP-PKG01. Sample preparation was performed at ALS Thunder Bay. Samples were first crushed fine to 70% of particles passing 2 mm (package CRU-31) and then split using a riffle splitter (package SPL-21); each split was then pulverized to 85% of particles passing 75 μm. The prepared samples were then shipped to ALS Vancouver for chemical analysis. Major-element oxides were obtained using fusion decomposition with inductively coupled plasma atomic emission spectroscopy (ICP–AES), total carbon and sulfur using LECO infrared spectroscopy, trace elements using lithium borate fusion and aqua regia digestion paired with inductively coupled plasma mass spectroscopy (ICP-MS), and base metals by four-acid digestion in conjunction with ICP–AES. Loss on ignition was performed at 1000°C. Of the 22 samples, six were from the ultramafic unit, seven from the overlying gabbroic unit, one from the overlying hybrid unit, six from the metasedimentary country rock, and two from the granitoid country rock. All whole-rock data were recalculated to a volatile-free (anhydrous) basis prior to plotting and interpretation.

3.2.4 Sulfide Mineral Chemistry

Two hundred and eighty-five sulfide mineral grains were analyzed for major and trace element geochemistry using an Agilent 7900 inductively coupled plasma mass spectrometer coupled with a 193 nm excimer laser at the Element and Heavy Isotope Analytical Laboratories of the University of Windsor. Fluence, or the radiant exposure of the beam ablating the mineral surface, was set to 2.24 J/cm^2 for all analyses except native copper, where beam energy was set to 100% (2.36 J/cm^2). The laser was operated at a repetition rate of 20 Hz, a transect speed of 5 um/s, and a spot size of 20 um. Sampling comprised 30 seconds of combined instrument and gas

background collection, followed by up to 90 seconds of sample ablation and signal acquisition (transect lengths up to 300 um).

Ablated material was transported from the ablation cell to the ICP via helium gas. The ionized material was then fed to a mass spectrometer, which measured the signal intensity (integrated counts per second – ICPS) for each isotope of interest. Exported data (ICPS) were converted to concentration units (ppm) using Iolite 4 software, which allowed for manual selection within the spectra of specific regions of interest to be integrated. Regions of interest were sections of the spectra which represented the purest composition of the sulfide mineral being analyzed. For example, integration regions were systematically selected to minimize the contamination by mineral inclusions. Comparison of Si and S within the spectra enabled selection of purely sulfide material by avoiding silicate mineral grains. For pyrrhotite grains, coincident spikes in Ni-Co were avoided because they were representative of pentlandite exsolution "flames" in pyrrhotite. For chalcopyrite and cubanite spectra, coincident spikes of Zn and Cd were avoided because they represent sphalerite "stars". Spikes in the spectra of Pb were avoided in all sulfide analyses to not contaminate the calculated concentrations with possible inclusions of galena. Pyrite appeared to be the only mineral with appreciable zonation, with separate high and low Ni-Co regions; this zonation was integrated separately where present. Lastly, coincident spikes between platinum-group elements and semi-metals (e.g., Bi, Te, Sn) were avoided in all analyses, because they likely represented discrete platinum-group minerals (Fig. 3.2).

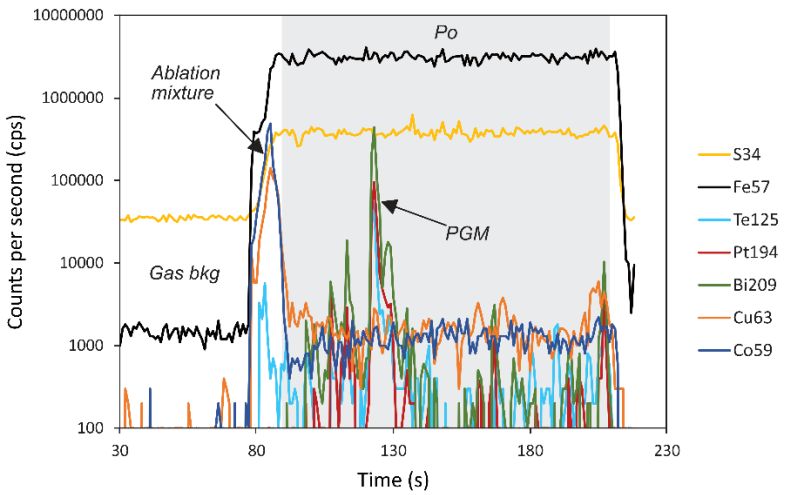

Figure 3.2: Laser ablation spectra from analysis Po 156, illustrating a Pt-Bi-Te mineral inclusion in pyrrhotite.

By adhering to this selection procedure, contamination with undesired elements in ablated material was minimized, ensuring that trace-element concentrations were representative of the sulfide minerals of interest exclusively. These selection rules were modified or disregarded when spectra were processed for native metals and for one discrete PGM analysis.

Six standards were used for various quality assurance and quality control measures throughout the experiments. This amounted to correcting for instrument drift across the analytical session, and for converting measured integrated counts per second (ICPS) to parts per million (ppm) concentrations during data reduction. The MASS-1 standard reference material is a pressed powder pellet of amorphous sulfides precipitated from solution and is composed of a suite of chalcophilic trace elements in a Fe-Zn-Cu-S matrix (Wilson et al., 2002). The composition of MASS-1 made it suitable as an external calibration standard for determining the concentrations of base and trace metals, not including the platinum-group elements and gold. It was used for most spectra to determine concentrations of analytes ^{33}S, ^{34}S, ^{51}V, ^{57}Fe, ^{59}Co, ^{61}Ni, ^{63}Cu, ^{65}Cu, ^{66}Zn, ^{68}Zn, ^{75}As, ^{77}Se, ^{78}Se, ^{82}Se, ^{109}Ag, ^{111}Cd, ^{118}Sn, ^{120}Sn, ^{121}Sb, ^{123}Sb, ^{125}Te, ^{185}Re, ^{208}Pb, and ^{209}Bi. The Po725 standard reference material is a synthetic pyrrhotite containing ~30ppm of each platinum-group element and gold (Sylvester et al., 2005), which made it suitable as an external

calibration standard for determining concentrations of these elements. It was used for most spectra to determine concentrations of analytes ^{101}Ru, ^{103}Rh, ^{105}Pd, ^{106}Pd, ^{108}Pd, ^{189}Os, ^{193}Ir, ^{194}Pt, ^{195}Pt, and ^{197}Au.

Iron was used as an internal standard during data processing for most analyses to compensate for difference in ablation rate between samples because Fe is present in significant proportions in the main sulfide minerals analyzed (i.e., pyrrhotite, pentlandite, chalcopyrite, pyrite, and cubanite). Some analyzed phases did not contain Fe as a major element, which rendered Po725 unusable for these analyses. In these cases, MASS-1 was used to determine concentrations for all analytes. While MASS-1 does contain PGE and Au, it was not developed for this purpose; as such, results for these elements from the Fe-barren phases are not considered robust. For the Fe-barren phases, the internal standards used were Cu for native copper and chalcocite, Ag for native silver, and Pb for galena.

UQAC FeS-1 (iron sulfide produced by D. Savard and S.-J. Barnes at LabMaTer of the University of Quebec in Chicoutimi, Canada) and MSS1 (synthetic pyrrhotite from University of Windsor), which were treated as unknown samples, were used as verification standards, whereby their calculated concentrations were compared with published values (provided by the respective labs) to assess the accuracy of the instrument during each experiment. The measured values are in good agreement with the published values within analytical uncertainty (Appendix D).

During laser ablation, ^{63}Cu, ^{65}Cu, ^{66}Zn, and ^{68}Zn can combine with ^{40}Ar to form metal-argides (e.g., ^{63}Cu^{40}Ar), which can interfere with measurement of ^{103}Rh, ^{105}Pd, ^{106}Pd, and ^{108}Pd, respectively. Pure Cu and Zn metal standards (produced by Alfa Aesar) where measured at the start of each session using LA-ICP-MS to obtain the concentrations of Cu and Zn argide interferences, which were used to calculate quantitative correction factors for the interfered PGE prior to processing in Iolite 4 (*cf*, Brzozowski et al., 2020).

Like the metal-argide interferences, ^{106}Cd and ^{108}Cd can cause isobaric interferences with ^{106}Pd and ^{108}Pd, respectively. The similarities in the mass-to-charge ratios make it impossible for the quadrupole mass spectrometer to resolve these isotopes. Post Iolite export, Cd corrections, which were calculated based on the natural abundances of Pd isotopes, were applied to account for isobaric interferences between ^{106}Cd and ^{108}Cd, and ^{106}Pd and ^{108}Pd, respectively (*cf*, Brzozowski et al., 2020).

3.2.5 In Situ Stable Isotope Chemistry

To conduct multiple sulfur isotopic analysis using secondary ion mass spectrometry (SIMS), six composite resin mounts containing two polished samples each were submitted to the Centre for Microscopy, Characterisation and Analysis at the University of Western Australia. Major element chemistry for sulfide minerals to be analyzed by SIMS was obtained beforehand using SEM-EDS and the compositional data were submitted to the lab for accurate phase characterization. Resin mounts were trimmed 1cm from the side of the puck to allow for addition of a standard block with accompanying matrix-matched standards. To prevent charging during analysis, the resin mounts were cleaned with ethanol and deionized water before being covered with an approximately 20 nm thick gold coating. A CAMECA IMS1280 ion microprobe was used to simultaneously collect in situ quadruple sulfur isotope ratios. Sulfur isotopes ^{32}S, ^{33}S and ^{34}S were measured using Faraday cup detectors fitted with 10^{10} Ω (L'2, ^{32}S) and 10^{11} Ω (L1, ^{33}S and H1, ^{34}S) resistors, and ^{36}S was measured using an electron multiplier (H2), all of which operated at a mass resolution of ~2500. A 10 kV Gaussian Cs^+ beam with intensity of ~2.5 nA and total impact energy of 20 keV was used to sputter the sample surface over a 10 x 10 µm area. The secondary ions produced were channeled in the double focusing mass spectrometer within a 75µm entrance slit and focused within the center of a 3000 µm field aperture (at 130 times magnification). The analysis procedure included a pre-sputtering over a 15 x 15 µm area within 30 seconds, followed by the automatic centering of the secondary ions in the field aperture. This

was followed by 30 four-second cycles of data acquisition. Instrument drift was accounted for during the analytical session by using two bracketing standards every 5-6 sample analyses. Instrumental mass fractionation (IMF) was corrected using the matrix-matched reference material for pyrrhotite (Alexo), pyrite (Sierra), chalcopyrite (Nifty-b), and pentlandite (VMSO) (Laflamme et al., 2016). The magnetic field used to focus the ions was offset slightly to the low-mass side to avoid interference from $^{32}S^{1}H$ on the ^{33}S peak and enable resolution between the isotopes. Each S isotope composition represents the average of up to seven spot analyses within a sulfide grain with internal precision represented as two standard deviations from this average. Data processing followed the procedure described in Laflamme et al. (2016). Sulfur isotope values are reported in delta notation as per mil deviations relative to Vienna Canyon Diablo troilite:

$$\delta^{3x}S = \left[\frac{(^{3x}S/^{32}S)_{sample}}{(^{3x}S/^{32}S)_{standard}} - 1\right] \times 1{,}000 \qquad eq.\,3.1$$

$$where\ x = 3, 4, or\ 6$$

Mass-independent fractionation was assessed by calculating the deviation of the measured values from the mass-dependent fractionation lines:

$$\Delta^{33}S = \delta^{33}S - 1{,}000 \times [(1 - \delta^{34}S)^{0.515} - 1] \qquad eq.\,3.2$$

$$\Delta^{36}S = \delta^{36}S - 1{,}000 \times [(1 - \delta^{34}S)^{1.91} - 1] \qquad eq.\,3.3$$

Accuracy of the sample measurements was assessed by measuring the isotopic composition of the standards described above. The measured compositions and standard errors are in good agreement with the reference values provided by LaFlamme et al. (2016; Appendix E).

3.2.6 Mineral Liberation Analysis

To characterize the abundance and types of platinum-group minerals (PGM) present at Escape, 17 polished thin sections were submitted to the CREAIT (Core Research Equipment and Instrument Training) Network at Memorial University in St. John's, NL, for Mineral Liberation

Analyzer-Scanning Electron Microscope (MLA-SEM) analysis. The instrument utilized was an FEI MLA 650 FEG (2011 model) SEM with a Bruker EDS Detector. The SEM is augmented with Mineral Liberation Analyser (MLA) software developed at the University of Queensland Julius Kruttschnitt Mineral Research Centre (JKTech) in Australia. The FEI MLA 650 FEG SEM electron gun uses a filament at an operating voltage of 25 Kv and a beam current of 10 nA. The working distance between sample and detector is 13.5 mm, and the spot size is ~5 µm. The imaging scan speed was 16 microseconds, with frame resolution of 800 dpi, and X-ray collection at 12 microseconds.

The integration of the energy dispersive X-ray (EDX) component of the SEM with the sophisticated MLA software package allows for the automated quantification of the abundance, size, and shape of minerals within a sample. The analysis of a given polished thin section results in a map of mineral phases in the sample, which is akin to providing a digital point count of mineralogy. Specifically, an energy dispersive spectrum is obtained for each mineral, with each spectrum being matched against a database of stored EDX spectra, which are indexed as Species Identification Protocols (SIPs; also known as 'fingerprints'). The CREAIT network has developed a sophisticated library of SIPs, which can identify almost all minerals present within a given sample, down to < 0.3% detected unknowns, using a matching threshold of 70% in the MLA software.

Following the automated MLA-SEM analysis, each sample was post-processed on live SEM to evaluate any unknowns detected, with the technician identifying the location and/or form of unknown particles. Moreover, in most samples, inclusions of PGMs were too small (i.e., < 10 µm in diameter) to be detected by the MLA software. However, PGM location, and identification was aided with the use of the back-scattered electron (BSE) scans produced by the MLA, insofar as PGM appear considerably brighter than other phases (e.g., sulfide minerals) in the images. The instrument was engaged to re-analyze sections of interest where the technician examined particles

in detail, up to, and including, conducting real-time EDX analyses of unknown phases. At this point, higher resolution BSE imagery was obtained alongside EDX spectra for species of interest. Following the post-processing review, the data for each sample were re-calculated using a 70% fit parameter. The technician 'cleaned-up' the section scans at this stage, with un-mapped objects such as holes and edges of the section removed from both the maps and the MLA quantification database. The MLA does not provide crystallographic data or trace element compositions of individual minerals. Thus, any elements identified in a mineral are generally significant (>1%) components of the given mineral phase.

4 Results

4.1 Petrography

4.1.1 Introduction

Petrographic descriptions for the gabbroic and ultramafic units (Fig. 2.5) were produced from polished thin sections. Transmitted- and reflected-light microscopy was utilized to characterize the mineralogy and texture of silicate, oxide, and sulfide minerals, and modal percentages were visually estimated. Grain sizes are reported as ultra fine-grained (<0.01 mm), very fine-grained (0.1 to 0.01 mm), fine-grained (1 to 0.1 mm), medium-grained (1 to 4-5 mm), coarse-grained (4-5 to 16 mm), and very coarse-grained (>16 mm). Detailed petrographic descriptions of each sample are presented in Appendix B.

4.1.2 Rock types

4.1.2.1 Gabbro unit

The upper gabbroic unit of the Escape intrusion is characterized by fine- to medium-grained, subhedral to elongate clinopyroxene phenocrysts and medium-grained interstitial plagioclase, with minor olivine phenocrysts that have been pseudomorphed to possible clay minerals (± serpentine; Fig. 4.1).

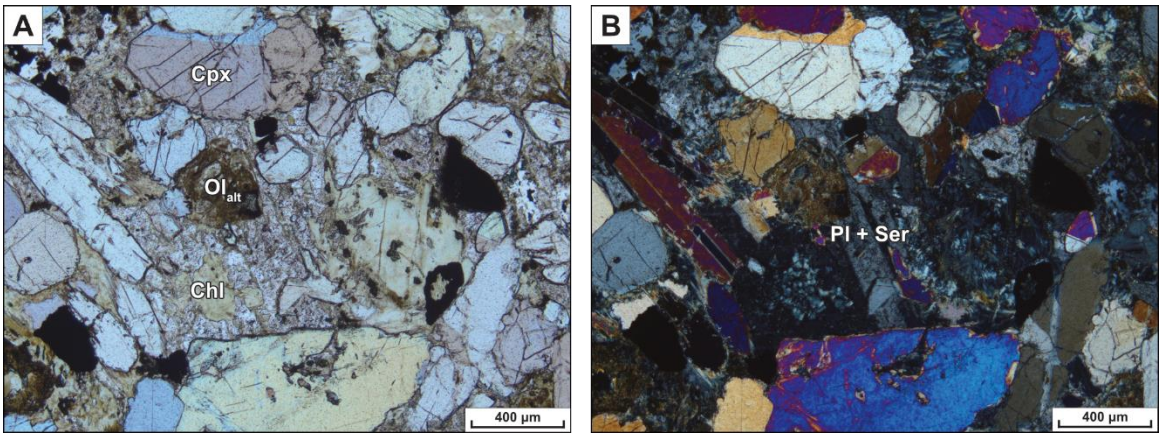

Figure 4.1: Transmitted light photomicrographs from the upper gabbro unit . The sample is a strongly altered, homogeneous, fine-grained, weakly foliated, poikilitic, oxide- and sulfide-bearing gabbro. Sample CAM-21-CC-003 from drillhole ELR20-025 at a depth of 315.7m (A – PPL; B – XPL). Abbreviations: Pl – plagioclase, Ser – sericite.

Alteration is variable throughout the unit and ranges from strong to pervasive. Olivine phenocrysts, where present, are brown in plane-polarized light, with dull interference colours under cross polars. Olivine is typically completely replaced by an ultra fine-grained assemblage of talc, serpentine, and clay minerals. Plagioclase is variably altered, ranging from relatively fresh to completely replaced by fine-grained chlorite aggregates, and ultra fine-grained sericite. Clinopyroxene phenocrysts are fresh compared to other phases, but often exhibit irregular grain boundaries; locally rims are replaced by serpentine.

Under reflected light, oxide minerals are more abundant than sulfide minerals (e.g., 5%:1% oxides to sulfides). Ilmenite is a common accessory phase and occurs as fine- to medium-grained interstitial crystals, and as fine- to ultra fine-grained reticular lamellae in (pseudomorphed) magnetite (Fig. 4.2).

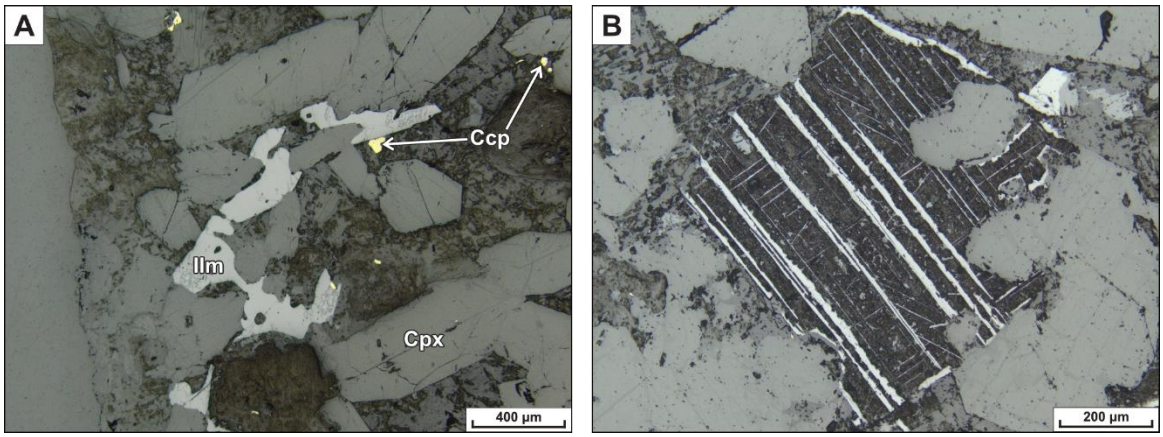

Figure 4.2: Reflected light photomicrographs from the upper gabbro unit depicting habits of Fe-Ti oxides. A – fine-grained ilmenite occupies the interstitial space between clinopyroxene and plagioclase grains, PPL. B – relict boxwork ilmenite lamellae remain in Fe-chlorite–pseudomorphed magnetite, PPL. Sample CAM-21-CC-003 from drillhole ERL20-025 at a depth of 315.7m. Abbreviations: Ccp – chalcopyrite, Cpx – clinopyroxene.

Sulfide minerals never exceed a few percent in modal abundance and occur interstitially to silicate and oxide minerals as anhedral disseminations in the groundmass. Chalcopyrite is the most common sulfide mineral present, but lesser pyrite and trace pentlandite, pyrrhotite, mackinawite, and galena also occur.

4.1.2.2 Mafic–ultramafic (peridotite) unit

The majority of petrographic characterization was completed on rocks within the lower peridotite unit (n = 39), which contains the high-grade zone of PGE–Cu–Ni sulfide mineralization. Based on estimated mineral proportions and mineral liberation analyzer area percentages, the most common rock type identified within and around the high-grade zone of the Escape intrusion is wehrlite (Fig. 4.3b).

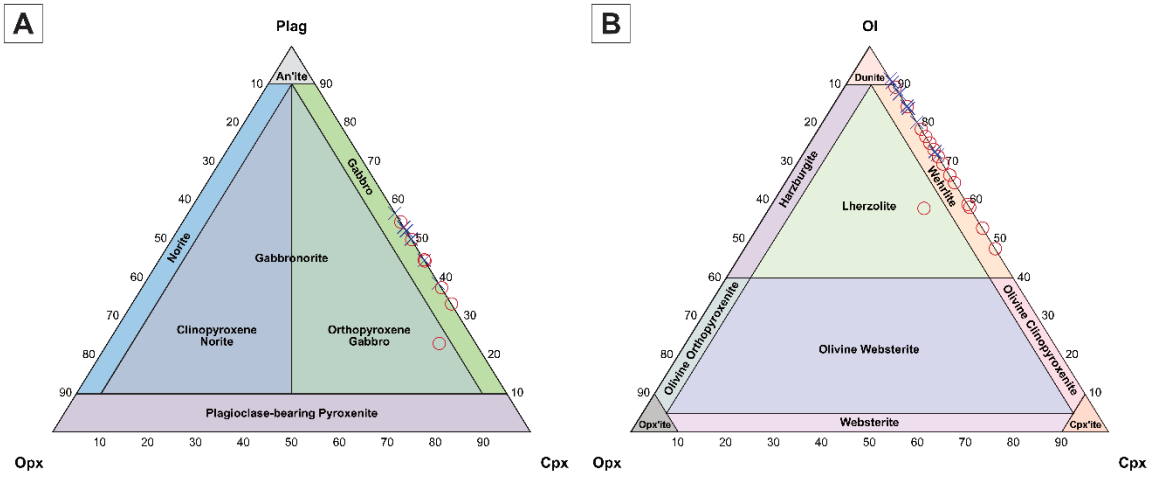

Figure 4.3: IUGS ternary diagrams for classification of mafic (A) and ultramafic (B) plutonic rocks. Red circles indicate samples where modal abundances were estimated visually from thin sections, and blue X's indicate modal abundances as determined by MLA. Selection of the appropriate ternary diagram was based on a cutoff of greater than or equal to 10% plagioclase (i.e., when there is ≤10% plagioclase, the ultramafic ternary is used). Modified after Le Maitre et al. (2002).

The main minerals that comprise the unit are olivine, clinopyroxene, and plagioclase, however, considerable variation in mineral mode, grain size, and alteration was observed. Figure 4.4 depicts this mineralogy with a representative thin section MLA scan of a typical mineralized wehrlite that is homogeneous, non-foliated, fine-grained, and poikilitic.

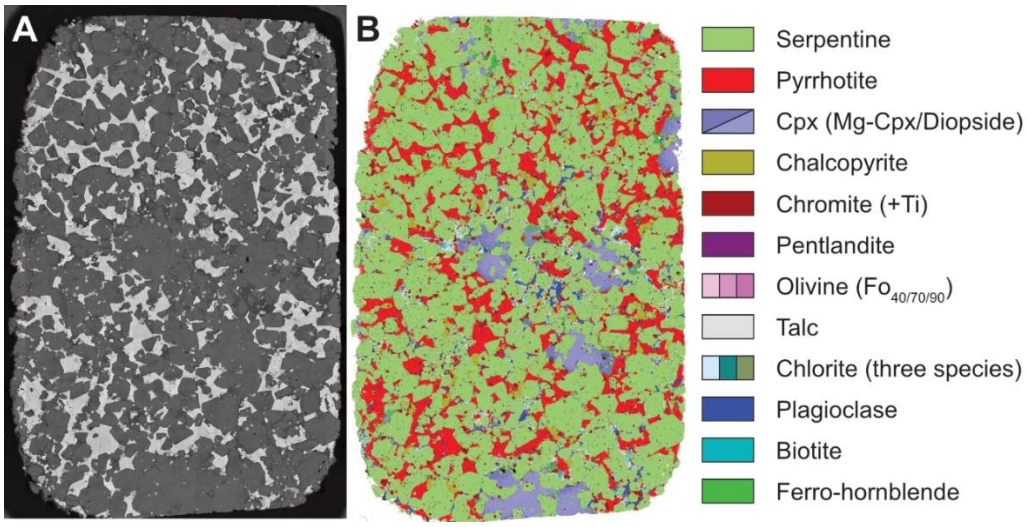

Figure 4.4: MLA scans of polished thin section CAM-21-CC-044 from drillhole ELR20-004, illustrating mineral abundances by area % for the interstitial–primary sulfide assemblage. A – back-scattered electron image. B – False colour EDS library-matched minerals mapped to BSE image. Minerals are listed in order of decreasing abundance in the legend. Minerals representing <1% of the area are omitted.

The unit is characterized by 45% to >60% olivine chadacrysts, which range in size from very fine- to coarse-grained (average being fine-grained). Moreover, olivine is typically fine-grained throughout the unit, but occasionally occurs as a range of grain sizes. Olivine crystals display habits that range from euhedral to anhedral and are locally prismatic, but are generally rounded (Figs. 4.4; 4.5).

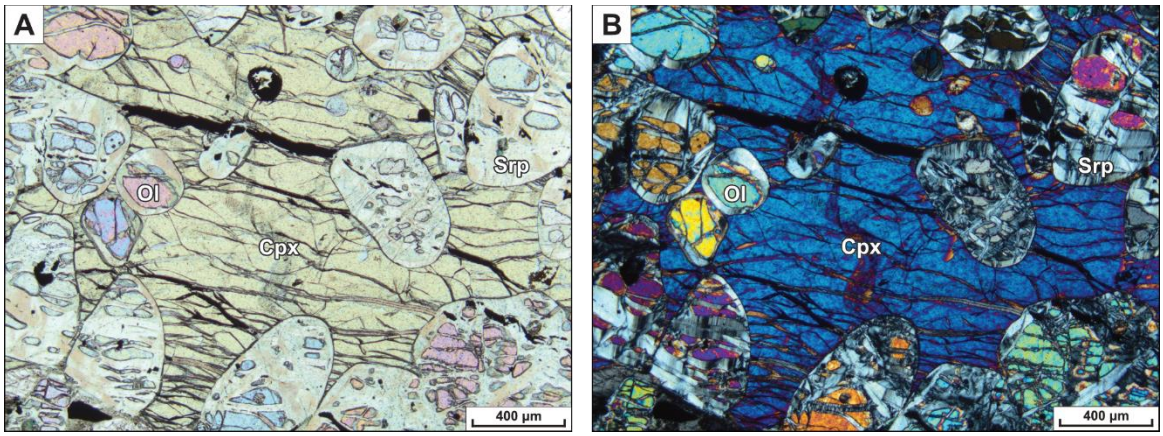

Figure 4.5: Representative photomicrographs of wehrlite from the peridotite unit. The wehrlite is intensely serpentinized, homogeneous, medium-grained, moderately foliated, and poikilitic. Sample CAM-21-CC-026 from drillhole ELR20-002 at a depth of 331.4m (A – PPL; B – XPL). Abbreviations: Cpx – clinopyroxene; Ol – olivine; Srp – serpentine.

Olivine rarely occurs in a fresh state and is typically partially to completely replaced. Weakly altered olivine crystals are altered to serpentine along fractures, while more strongly altered grains are characterized by pervasive alteration. Ultra fine-grained, anhedral, linear aggregates of magnetite often occur along the fractures of serpentinized olivine. Talc alteration of olivine is common, and typically occurs along grain boundaries (rims) of olivine, and locally as complete replacement. A less common form of alteration exhibited by olivine in the Escape intrusion is to indeterminate clay minerals, potentially iddingsite (Fig. 4.6).

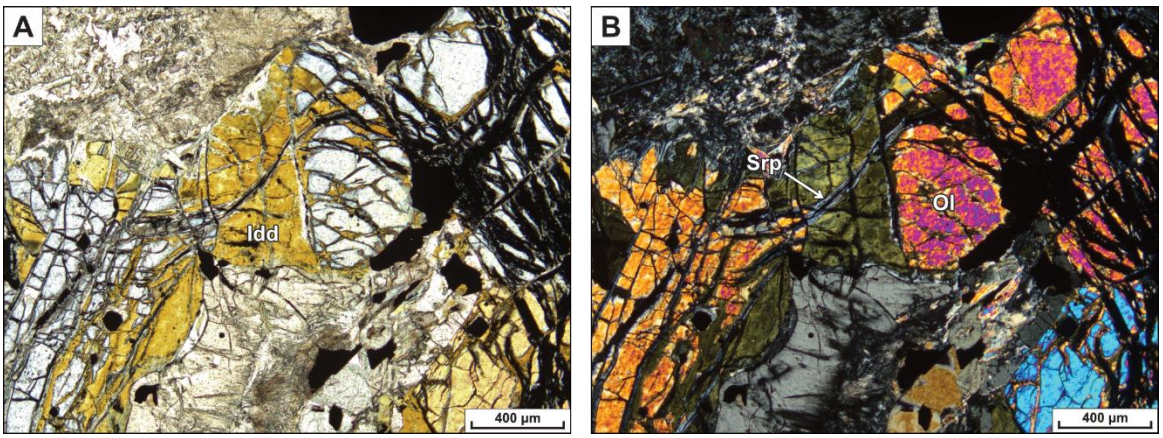

Figure 4.6: Representative photomicrographs of clay alteration in olivine. Images depict clay-altered (iddingsite?) olivine cores within a poikilitic feldspathic wehrlite. Sample CAM-21-CC-101 from drillhole ELR20-011 at a depth of 403.6m (A – PPL; B – XPL). Abbreviations: Idd – iddingsite; Ol – olivine; Srp – serpentine.

Clinopyroxene occurs as a solid solution between Mg-clinopyroxene (augite) and diopside and is the second most abundant silicate rock-forming mineral in the peridotite unit, ranging in modal abundance from <5% to 40%. It typically occurs as medium- to coarse-grained oikocrysts that enclose olivine chadacrysts (Figs. 4.4; 4.5). Clinopyroxene exhibits greater resistance to alteration than olivine and plagioclase and is often unaltered in thin section. The most common form of alteration exhibited by clinopyroxene is weak serpentinization along fractures. It is also not uncommon to find chlorite (with or without associated talc) having altered clinopyroxene along grain boundaries when it is proximal to altered plagioclase. Rarely, clinopyroxene is altered to amphibole (Figs. 4.4; 4.7). In this scenario, clinopyroxene is grey-brown in plane-polarized light and exhibits characteristic ~87–93° cleavage planes, whilst

amphibole is brown-orange in plane-polarized light and exhibits characteristic ~56–124° cleavage planes.

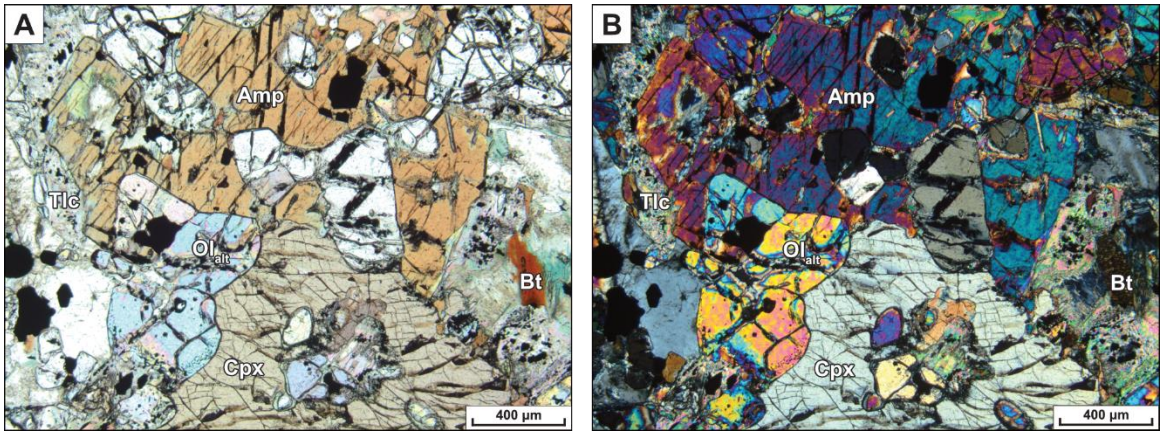

Figure 4.7: Representative photomicrographs of clinopyroxene alteration. The sample is a strongly altered, homogeneous, fine- to medium-grained, non-foliated, poikilitic, sulfide-bearing, olivine melagabbro. Sample CAM-21-CC-035 from drillhole ELR20-002 at a depth of 426m (A – PPL; B – XPL). Abbreviations: Amp – amphibole; Bt – biotite; Cpx – clinopyroxene; Ol_{alt} – altered olivine; Tlc – talc.

The modal abundance of plagioclase within and around the high-grade zone ranges from a few percent up to ~20%. Due to this wide range in abundance, rock types within the peridotite unit constitute a spectrum that ranges from wehrlite (little to no plagioclase) to feldspathic wehrlite (<10% plagioclase) to melanocratic gabbro (~10–20% plagioclase). Moreover, where net-textured sulfides occur within the peridotite unit, the rock type may constitute dunite, with minimal to no clinopyroxene or plagioclase present. Figure 4.8 provides an example of a melanocratic gabbro with ~20% plagioclase that is relatively fresh, exhibiting characteristic polysynthetic twinning, and occurring interstitial to olivine crystals.

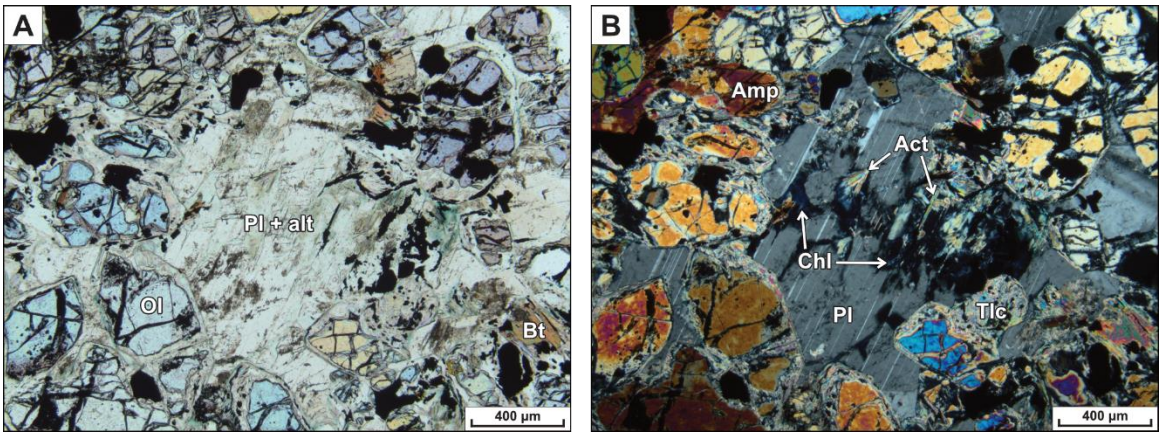

Figure 4.8: Representative photomicrographs of patchy alteration in plagioclase. The images depict interstitial plagioclase altered to a mixture of chlorite and actinolite. Sample CAM-21-CC-035 from drillhole ELR20-002 at a depth of 426m (A – PPL; B – XPL). Abbreviations: Act – actinolite; Amp – amphibole; Bt – biotite; Chl – chlorite; Ol – olivine; Pl + alt – plagioclase plus alteration; Tlc – talc.

On the mafic ternary diagram in Figure 4.3a, three samples contain >30% olivine, but have plagioclase abundances greater than 10%, and as such are melanocratic gabbros. Plagioclase exhibits a wide variety of alteration phases, styles, and assemblages. Plagioclase alteration is often only represented by an ultra fine-grained phase, possibly sericite, which, when coarser, appears to be a combination of sericite, epidote, and possibly saussurite. Another common alteration style of plagioclase is to patchy, anhedral to fibrous aggregates of chlorite (which can be intergrown with actinolite and/or talc; Fig. 4.8). In other sections where the intensity of alteration is high, interstitial phases (i.e., plagioclase and sometimes clinopyroxene) exhibit complex intergrowths with multiple phases. It is difficult to assess the paragenesis of alteration as the original grain boundaries are often obliterated, with primary mineralogy destroyed. For example, the boundary of clinopyroxene appears to be replaced, but the serpentine, biotite, carbonate, chlorite, actinolite, and talc assemblage continues throughout the interstitial space (Fig. 4.9).

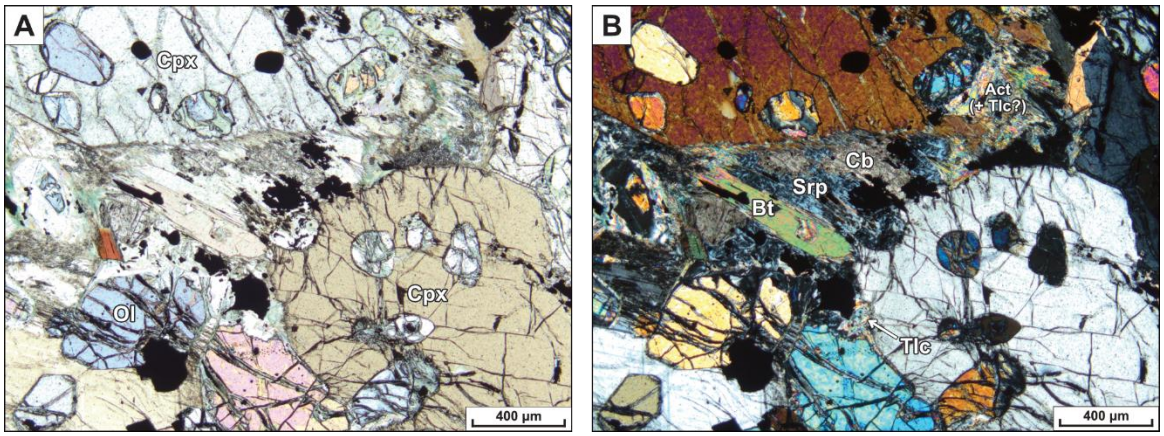

Figure 4.9: Representative photomicrographs illustrating the complexity and range of alteration in the peridotite unit of the Escape intrusion. Sample CAM-21-CC-013 from drillhole ELR20-025 from a depth of 521.5m (A – PPL; B – XPL). Abbreviations: Act – actinolite; Bt – biotite; Cb – carbonate; Cpx – clinopyroxene; Ol – olivine; Srp – serpentine; Tlc – talc.

Biotite occurs with a platy (micaceous) habit, serpentine and talc are anhedral to fibrous, and carbonate is anhedral, all of which are chaotically intergrown. Biotite constitutes a minor component of the mineral mode within the peridotite unit. Its modal abundance ranges from absent (or trace, <1%) up to around 3%. Where present, platy biotite commonly occurs at the silicate–sulfide interface, marking the rims of sulfides (Fig. 4.10).

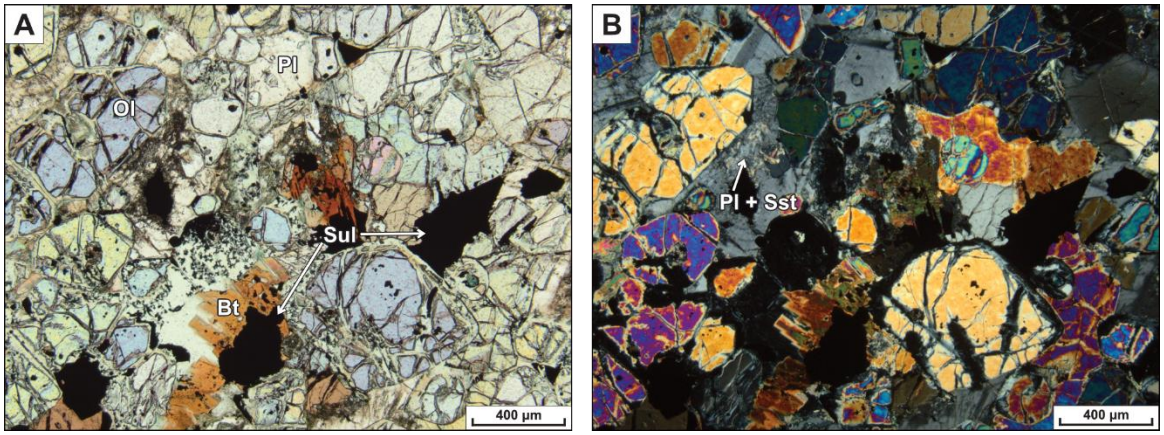

Figure 4.10: Representative photomicrographs depicting platy biotite occurring along the boundary of sulfides (opaque). Sample CAM-21-CC-089 from drillhole ELR20-018 at a depth of 399.6m (A – PPL; B – XPL with light condenser). Abbreviations: Bt – biotite; Ol – olivine; Pl – plagioclase; Sst – saussurite; Sul – sulfides.

The last feature of note regarding alteration within the peridotite unit of the Escape intrusion is the presence of crosscutting veinlets/stringers. There are various types of veinlets that crosscut the poikilitic minerals, including serpentine–carbonate–chlorite–magnetite, carbonate–

amphibole, feldspathic, and sulfide veinlets (described in the following sections). While the compositions of these veinlets are all markedly different, they all have intensely altered selvages. Alteration intensity is proportional to proximity to the crosscutting veinlet. In the example in Figure 4.11, the groundmass proximal to a carbonate veinlet crosscutting the sample is completely replaced by variable amounts of clay minerals, serpentine, and calcite. This type of veinlet (carbonate ± serpentine) is commonly found within the shallower levels of the intrusion, often below the contact with the overlying gabbroic unit and above the sulfide-mineralized high-grade zone.

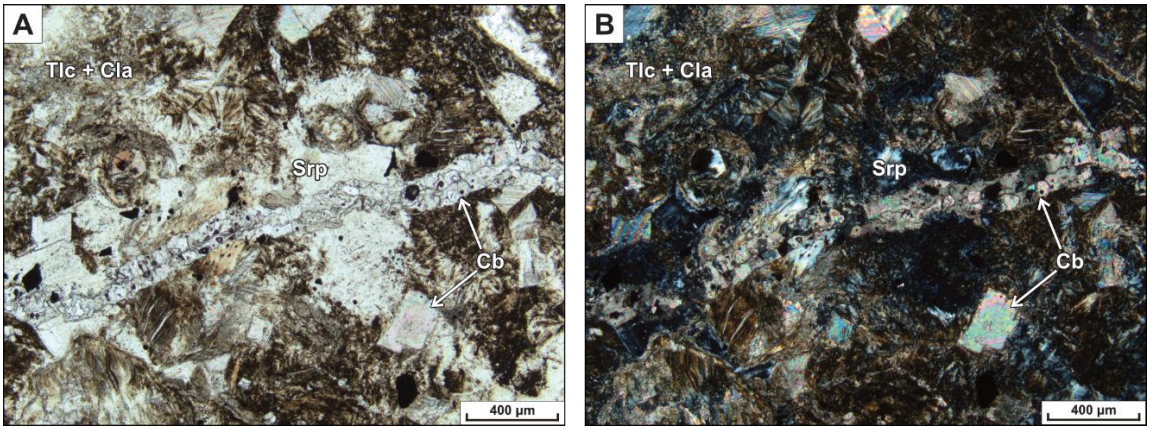

Figure 4.11: Representative photomicrographs of a carbonate stringer crosscutting the groundmass in sample CAM-21-CC-030 from drillhole ELR20-002 at a depth of 371.5m (A – PPL; B – XPL). Abbreviations: Cb – carbonate; Cla – clay mineral(s); Srp – serpentine; Tlc – talc.

4.1.3 Sulfide mineralization

The sulfide minerals have been categorized into groups based on their mode of occurrence and overall composition; these are outlined in Figure 4.12.

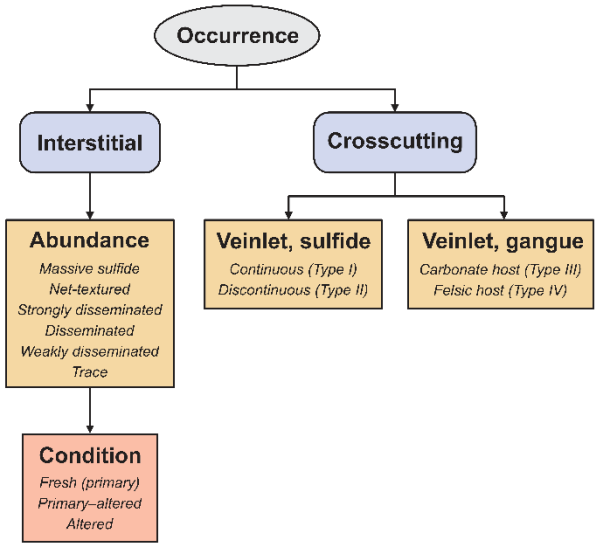

Figure 4.12: Schematic diagram for classification of sulfide mineralization within and around the high-grade zone of the Escape intrusion.

The following sections describe representative samples from each of these mineralization styles and are followed by a summary of results from quantitative mineralogy of the sulfide assemblages.

4.1.3.1 Interstitial–Primary Mineralization

The highest concentration of base- and precious-metal mineralization within the Escape intrusion corresponds to the interstitial sulfides located within the ore horizon of the high-grade zone (Fig. 3.1). The abundance of interstitial mineralization changes systematically downhole; from top to bottom through the ore horizon, sulfide abundance ranges from trace to disseminated, to net-textured, back to disseminated, and trace. The distinction between interstitial sulfide abundance is made qualitatively by visual estimation in hand samples. The range in modal abundance for each interstitial sulfide category are trace (<1%), disseminated (1–30%, ranging

from weak to strong), and net-textured (30–70%). Within net-textured mineralization, sulfides occupy most of the interstitial space between olivine (Figs. 4.4 and 4.13a).

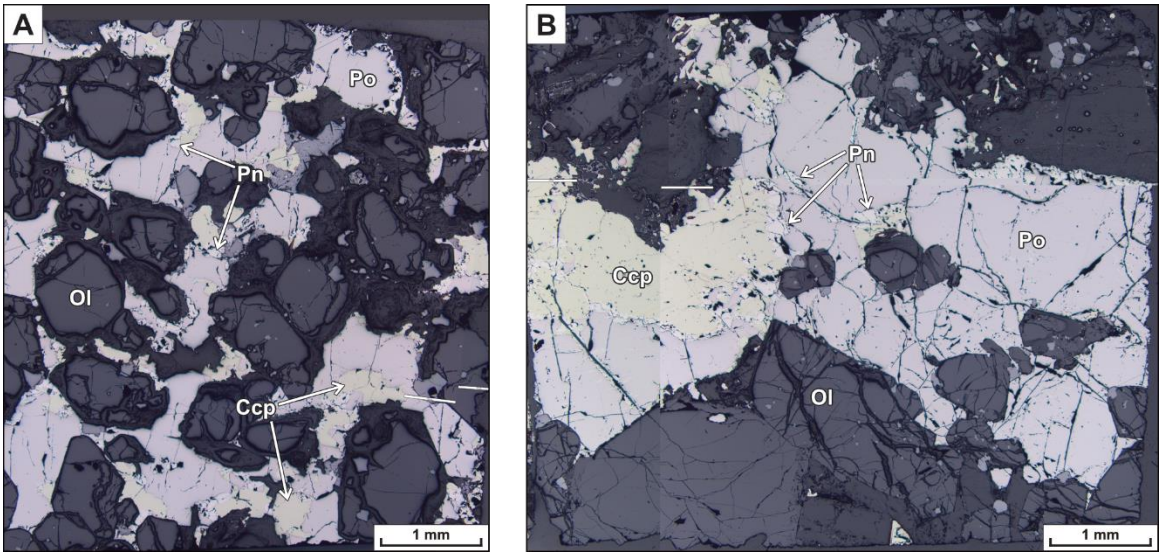

Figure 4.13: Composite-stitched, reflected light photomicrographs of net-textured (A) and massive sulfide (B) mineralization. Samples CAM-21-CC-045 and CAM-21-CC-048 from drillhole ELR20-004 at depths of 404.3m and 475.1m respectively; plane polarized light. Abbreviations: Ccp – chalcopyrite; Ol – olivine; Pn – pentlandite; Po – pyrrhotite.

When sulfides comprise >70% of the groundmass, the mineralization is characterized as massive. Massive sulfide accumulations have seldom been intersected within footwall country rock by drilling and only found in minor accumulations within the peridotite unit. Figure 4.13b is a reflected-light image of a thin (~2.5 mm wide) accumulation of massive sulfide in wehrlite from the lower mineralized zone.

In order of abundance, the primary, interstitial sulfide assemblage consists of pyrrhotite (non-stoichiometric and troilite varieties; confirmed by EDS element compositions), chalcopyrite, pentlandite, and lesser to trace cubanite and pyrite. Pyrrhotite occurs with a massive (anhedral) habit, is fine- to medium-grained, often fractured, and is rimmed by pentlandite, chalcopyrite, and silicates (Fig. 4.14). Locally, troilite occurs as wispy exsolution lamellae within pyrrhotite.

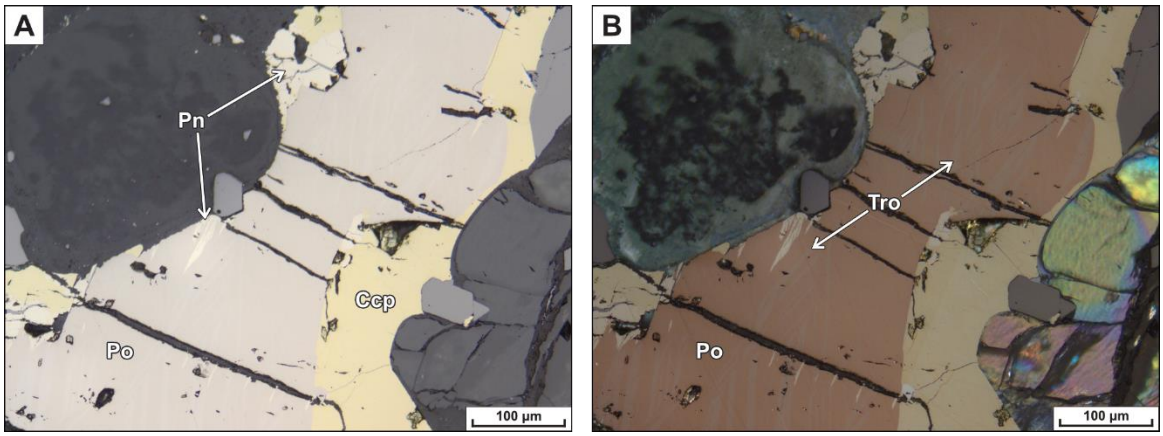

Figure 4.14: Representative photomicrographs of net-textured, primary–interstitial assemblage containing pyrrhotite (+ troilite), chalcopyrite, and pentlandite. Sample CAM-21-CC-120 from drillhole 11CL0005 at a depth of 401.1m within the ore horizon (A – PPL; B – XPL). Abbreviations: Ccp – chalcopyrite; Pn – pentlandite; Po – pyrrhotite; Tro – troilite.

Chalcopyrite occurs within the primary, interstitial assemblage as a fine- to very fine-grained phase, with an anhedral habit, often in equilibrium with pyrrhotite (Fig. 4.15). Chalcopyrite may also exhibit polysynthetic twinning, which is only apparent under cross-polarized light. Locally, fine-grained, cubanite exsolution laths occur within chalcopyrite, which appear greenish yellow in colour and exhibit more distinct anisotropy compared to chalcopyrite. Cubanite also occurs with massive habit in equilibrium with chalcopyrite and pyrrhotite.

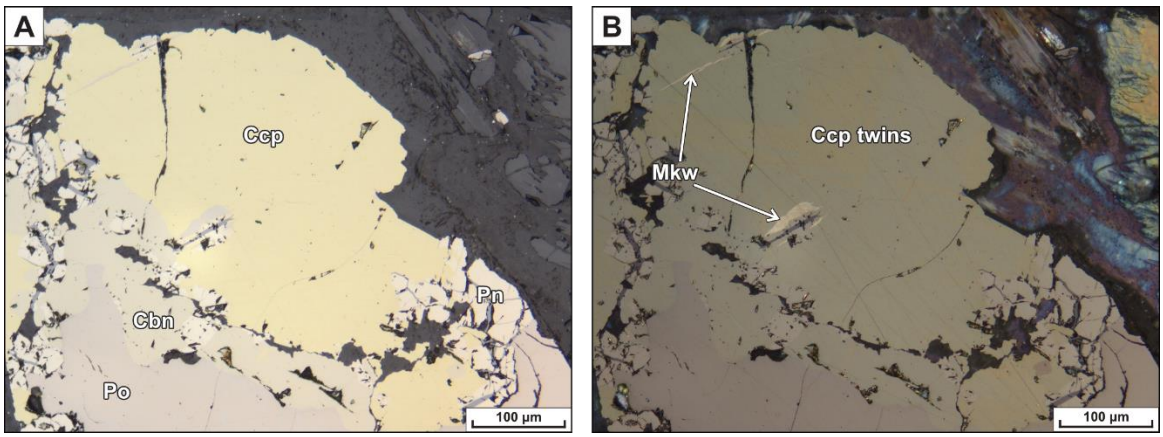

Figure 4.15: Representative photomicrographs of chalcopyrite within the net-textured, primary–interstitial assemblage associated with cubanite, pyrrhotite, pentlandite, and worm-like mackinawite exsolutions. Sample CAM-21-CC-120 from drillhole 11CL0005 at a depth of 401.1m within the ore horizon (A – PPL; B – XPL). Abbreviations: Cbn – cubanite; Ccp – chalcopyrite; Mkw – mackinawite; Pn – pentlandite; Po – pyrrhotite.

Pentlandite most often occurs with a fine- to very fine-grained, granular habit, forming clusters and chain aggregates (Fig. 4.16a). Pentlandite aggregates often occur along fractures in pyrrhotite, and commonly mark the interface between pyrrhotite and chalcopyrite. Pentlandite also frequently occurs as exsolution 'flames' in pyrrhotite, which are oriented perpendicular to grain boundaries and fractures (Fig. 4.16b).

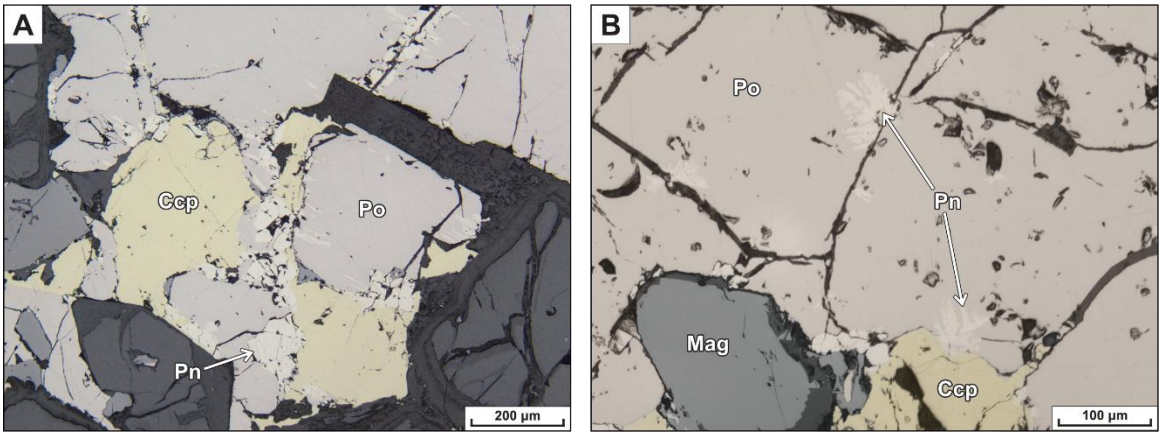

Figure 4.16: Representative photomicrographs of pentlandite within the net-textured, interstitial–primary assemblage associated with pyrrhotite, chalcopyrite, and magnetite. A – sample CAM-21-CC-116 from drillhole ERL20-002 at depth of 392.12m within the ore horizon, showing granular pentlandite in the centre of the image; PPL. B – sample CAM-21-CC-008 from drillhole ELR20-025 at a depth of 393.9m within the ore horizon, showing pentlandite dendrites in pyrrhotite; PPL. Abbreviations: Ccp – chalcopyrite; Mag – magnetite; Pn – pentlandite; Po – pyrrhotite.

Pyrite is uncommon within the primary sulfide assemblage, locally accounting for <1% of the sulfides. It is fine-grained, subhedral to euhedral (with cubic cleavage), and is associated with the other sulfide phases (Fig. 4.17).

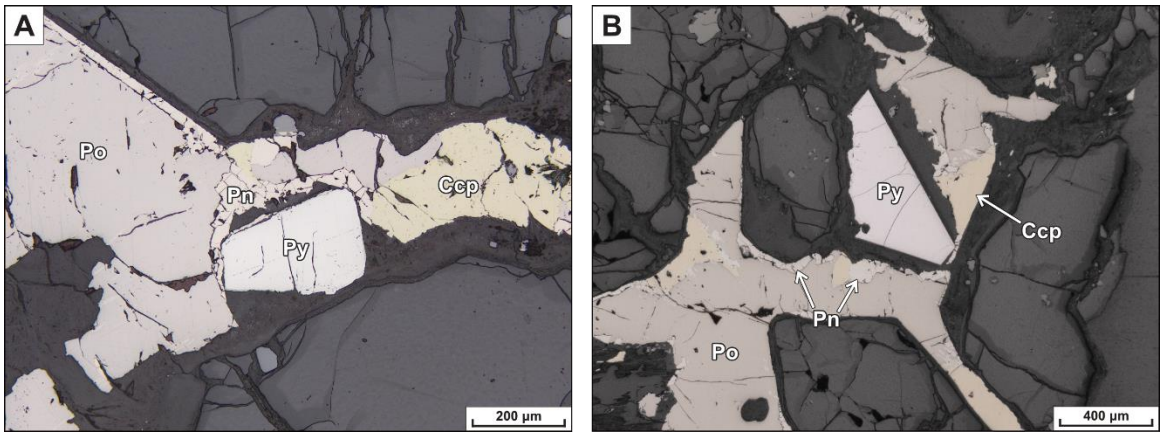

Figure 4.17: Representative photomicrographs of pyrite within the net-textured, interstitial–primary assemblage associated with pyrrhotite, chalcopyrite, and pentlandite. Sample CAM-21-CC-045 from drillhole ELR20-004 at a depth of 404.3m within the ore horizon; PPL. Abbreviations: Ccp – chalcopyrite; Pn – pentlandite; Po – pyrrhotite; Py – pyrite.

Fine- to ultra fine-grained, anhedral galena (composition confirmed via SEM-EDS analysis) was identified only in samples from intervals corresponding to the highest metal grades within the ore horizon. Where present, galena occurs in trace abundance and is in equilibrium with the primary sulfide assemblage. Moreover, discrete, ultra fine-grained platinum-group minerals also occur in this assemblage and will be described in the following sections.

Under reflected light, three oxide minerals have been identified throughout the groundmass, and may be associated with the primary sulfide assemblage: chromite, magnetite, and ilmenite. Very fine- to ultra fine-grained, rounded to subhedral chromite chadacrysts occur throughout the groundmass, most often within olivine phenocrysts. Chromite also occurs within clinopyroxene, plagioclase, and sulfides, and along their grain boundaries (Fig. 4.18a,b).

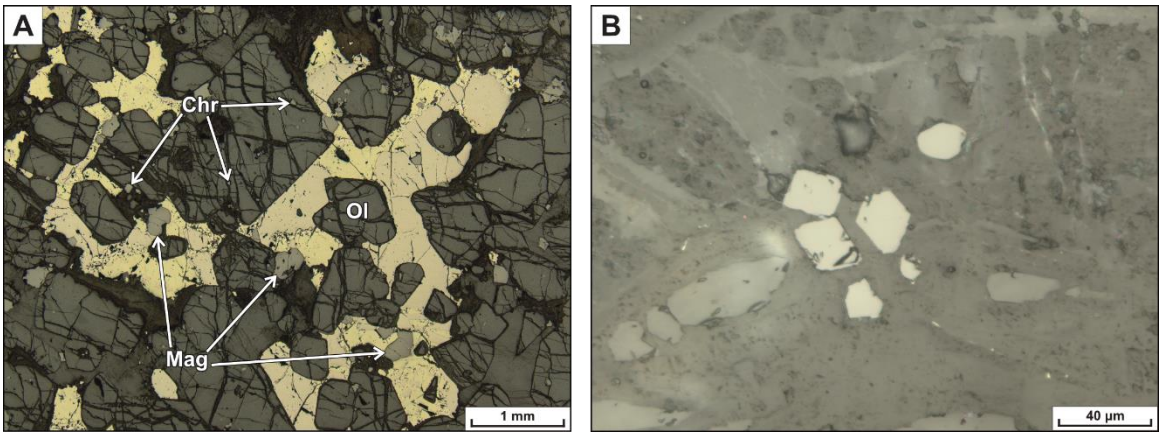

Figure 4.18: Representative photomicrographs of oxide minerals within the Escape peridotite unit. A – intergrown magnetite and chromite chadacrysts within the net-textured, interstitial–primary assemblage (Sample CAM-21-CC-011 from drillhole ELR20-025 at a depth of 403.6m within the ore horizon; PPL). B – very fine-grained chromite chadacrysts within wehrlite groundmass (Sample CAM-21-CC-027 from drillhole ELR20-002 at a depth of 336m well above the ore horizon; PPL). Abbreviations: Chr – chromite; Mag – magnetite; Ol – olivine.

Chromite ranges in size from ultra fine- to fine-grained, is grey in colour, and isotropic. Magnetite occurs within the primary assemblage in two styles. It occurs as discrete, rounded phenocrysts that display clear grain boundaries. In this habit, magnetite may contain thin (very fine- to ultra fine-grained) ilmenite exsolution lamellae in an oriented, reticular pattern. They can also occur as intergrowths with pyrrhotite and/or chalcopyrite, with no ilmenite lamellae (Fig. 4.18a). Magnetite is grey in colour and isotropic, which can render it difficult to distinguish from chromite, however, the chromite is often disseminated, generally more euhedral, and never contains ilmenite lamellae. Ilmenite is much less common than the previous two oxide minerals and, where present, is fine-grained and occurs interstitially to silicate minerals. Ilmenite is grey with a slight brownish tint when compared to magnetite and chromite, and exhibits strong, grey to reddish anisotropy under cross polars.

4.1.3.2 Interstitial–Altered Mineralization

Relative to the primary mineralization, interstitial–altered sulfide minerals exhibit varying degrees of alteration, which include minor oxidation to magnetite, exsolution, and complete replacement of chalcopyrite and pentlandite. In general, the amount of alteration in sulfide minerals is proportional to the distance from the net-textured mineralization; this is true for depths

above and below the high-grade zone, as well as laterally along the perimeters of the high-grade zone. Unlike the net-texture common to the interstitial–primary mineralization, alteration of sulfide minerals is almost exclusively restricted to disseminated occurrences (Fig. 4.19).

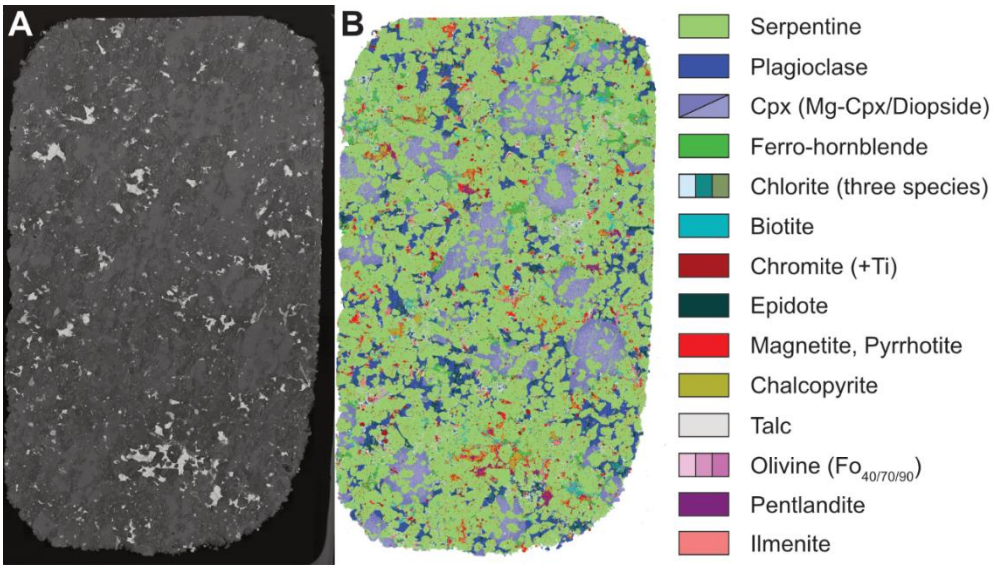

Figure 4.19: MLA scans of polished thin section CAM-21-CC-061 from drillhole ELR20-015, illustrating mineral abundances by area % for the disseminated interstitial–altered assemblage. A – back-scattered electron image. B – false colour EDS library-matched minerals mapped to BSE image. Minerals are listed in order of decreasing abundance in the legend. Minerals representing <<1% of the area are omitted.

Moreover, alteration of silicate minerals is more intense and exhibits greater variability — evidenced by a greater proportion of Fe-hornblende, chlorite, biotite, and epidote — than silicate minerals associated with primary mineralization (Fig. 4.19). Mineralization textures found in this assemblage exhibit complex intergrowths and exsolution relationships; locally, individual sulfide minerals do not have distinct grain boundaries and one phase blends into another. It is also common to find replacement of original sulfide boundaries by silicate alteration; this is visible where sulfide minerals do not extend to the edge of the interstitial space, and silicate minerals, such as biotite and serpentine, occupy the area between irregular sulfide grain boundaries and olivine (and/or clinopyroxene). This section summarizes the range of sulfide alteration by describing key features of mineralization above and below the ore horizon.

Just under the ore horizon (~10 m below) occurs the least altered assemblage of interstitial–altered sulfides. Overall, the primary assemblage of pyrrhotite, chalcopyrite, and pentlandite is preserved, and sulfides generally preserve original equilibrium grain boundaries, but with a few modifications. Fine-grained, cubanite occurs in greater frequency than the primary mineralization, occurring within chalcopyrite as oriented exsolution laths and/or with irregular mottled habit (Fig. 4.20).

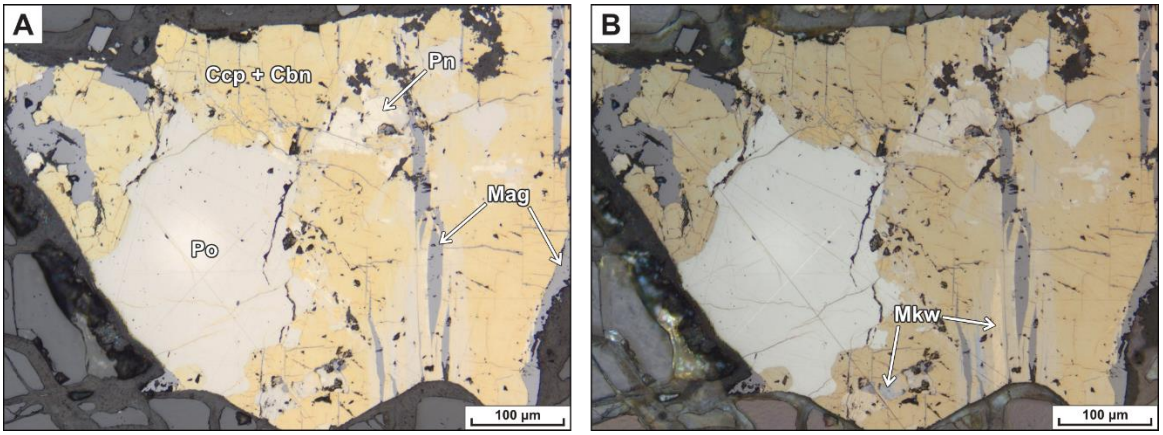

Figure 4.20: Representative photomicrographs of weakly altered, disseminated to weakly disseminated ore with pyrrhotite, chalcopyrite, pentlandite, cubanite, mackinawite, and magnetite. Sample CAM-21-CC-122 from drillhole 11CL0005, taken below the ore horizon at 411.4m depth corresponding to mid metal grade (A – PPL; B – XPL). Abbreviations: Cbn – cubanite; Ccp – chalcopyrite; Mag – magnetite; Mkw – mackinawite; Pn – pentlandite; Po – pyrrhotite.

Fine- to ultra fine-grained mackinawite occurs in greater abundance as worm-like, elongate to tabular exsolutions within chalcopyrite and pyrrhotite (Fig. 4.20). Fine-grained magnetite occurs in greater abundance relative to primary mineralization and is often irregularly intergrown with sulfides and occurs also with lenticular to elongate habit between sulfides, possibly exploiting cleavage planes in pentlandite (and pyrrhotite; Fig. 4.20).

From ~20 to 70 m above the ore horizon, mineralization exhibits strong to intense alteration of the primary sulfide assemblage. The interstitial–altered mineralization assemblage consists of a variable mixture of pyrrhotite, magnetite, native copper, cubanite, chalcopyrite, mackinawite, pentlandite, and valleriite. Like the primary mineralization assemblage, pyrrhotite is present as the most abundant phase in all the thin sections analysed. Pyrrhotite is fine-grained and

occurs with a massive, anhedral habit. Locally, pyrrhotite occurs with subgrains that exhibit undulatory extinction and triple junctions under cross polars. A common feature of pyrrhotite within the altered assemblage is the presence of fractures that contain any or all of magnetite, native copper, and Cu–Fe-bearing sulfide minerals (Fig. 4.21a).

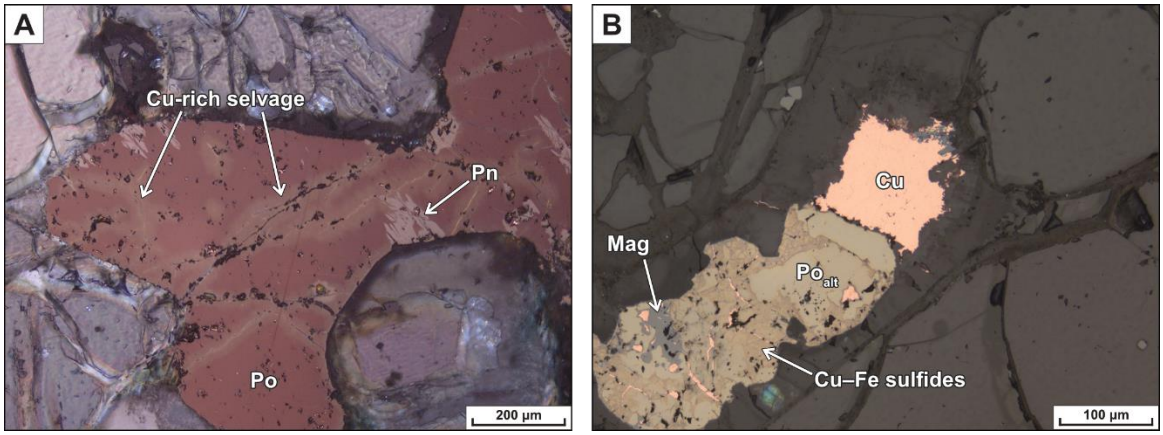

Figure 4.21: Representative photomicrographs of Cu-rich altered, disseminated mineralization with pyrrhotite, native copper, pentlandite, magnetite, and trace Cu–Fe sulfides. A – sample CAM-21-CC-006 from drillhole ELR20-025 taken above the ore horizon at 368.9m depth, depicting Cu-diffuse fracture selvages in pyrrhotite, with minor pentlandite flames; XPL. B – sample CAM-21-CC-042 from drillhole ELR20-004 taken above the ore horizon at 363.7m depth, depicting a lone native copper grain and native copper within altered sulfides; PPL. Both samples correspond to intervals in the intrusion with low metal grade. Abbreviations: Cu – native copper; Mag – magnetite; Pn – pentlandite; Po_{alt} – altered pyrrhotite.

The fracture selvages are commonly discoloured yellow, which dissipates away from the fracture towards the centre of pyrrhotite grains. LA–ICP–MS results indicate that these selvages are Cu-rich, whereas SEM–EDS analyses indicate that the pyrrhotite can contain up to a percent copper within the crystal, even distal to the fractures and discoloured selvages. Native copper is easily recognized within the altered mineralization assemblages due to its orange/pink colour and high reflectance. Under crossed polars, native copper is isotropic, but fine scratches exhibit bright anisotropy. Moreover, the light reflected from native copper can produce fiery-red internal reflections in adjacent silicate minerals. Native copper is typically fine- to ultra fine-grained and occurs with a variety of habits, most commonly as fracture fill within sulfide minerals, where it is intimately associated with magnetite (Fig. 4.22c, d). This occurrence of native copper is locally observed spreading out from the sulfide fractures into adjacent silicate minerals. Native copper

also occurs with altered Cu–Fe sulfides as rim replacement and irregular to emulsoid habits (the latter shown in Fig. 4.21b). Chalcopyrite and cubanite occur with anhedral habits, and are commonly irregularly intergrown with native copper, magnetite, mackinawite, valleriite, and relict pentlandite. Chalcopyrite is often strongly tarnished to peacock-colours, which requires a good polish to remove.

Pentlandite, where present, occurs as very fine-grained, anhedral aggregates that are often fractured, with fractures filled by chalcopyrite/cubanite, magnetite, sugakiite, and/or mackinawite. Pentlandite is often altered to mackinawite, where less-altered grains show anastomosing replacement along fractures in pentlandite (vermicular to 'flame'-like exsolutions), whereas advanced alteration occurs with complete replacement by tabular to anhedral mackinawite (Fig. 4.22).

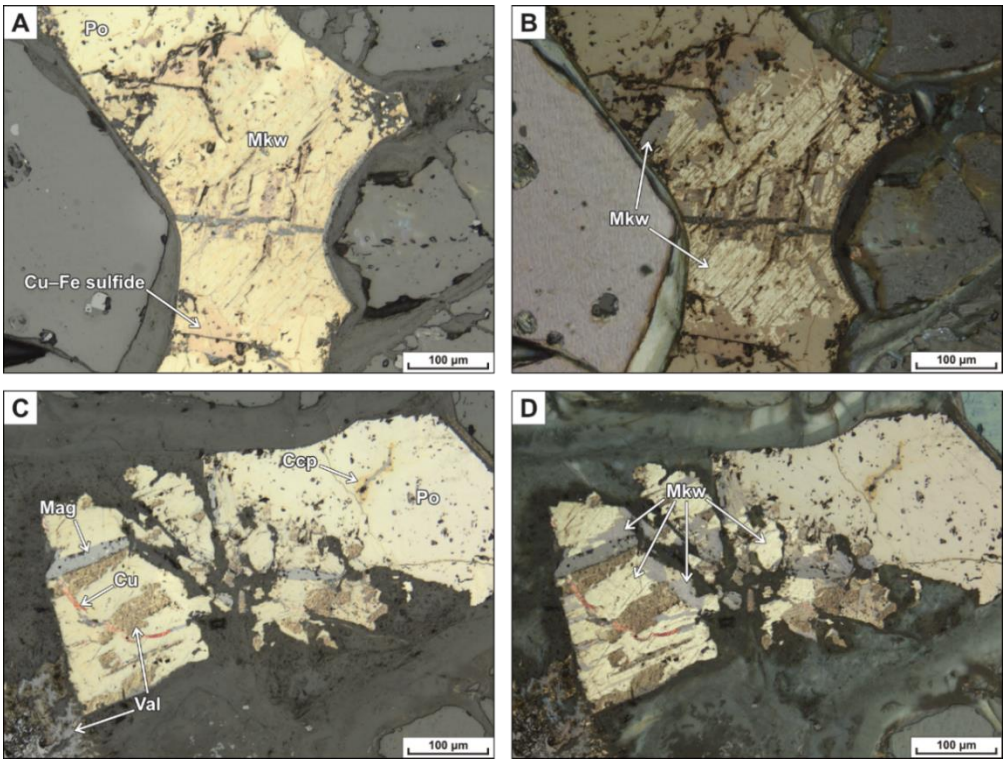

Figure 4.22: Representative photomicrographs of mackinawite within altered, disseminated mineralization associated with pyrrhotite, magnetite, native copper, valleriite, and trace chalcopyrite. A,B – sample CAM-21-CC-042 from drillhole ELR20-004, taken above the ore horizon at 363.7m depth corresponding to low metal grade. C,D – sample CAM-21-CC-005 from drillhole ELR20-025, taken above the ore horizon at 358.1m depth corresponding to low metal grade. A,C – PPL; B,D – XPL. Abbreviations: Ccp – chalcopyrite; Cu – native copper; Mag – magnetite; Mkw – mackinawite; Po – pyrrhotite; Val – valleriite.

Mackinawite is inconspicuous in plane-polarized light, with a blueish-grey to greyish-brown colour and weak pleochroism. However, under crossed polars, mackinawite exhibits strong to very strong anisotropy, with blue-grey to yellow-beige anisotropic colours (Fig. 4.22).

Sugakiite is unassuming in thin section; its identification was verified by LA–ICP–MS and SEM–EDS compositional data indicating a homogeneous composition of Fe, Cu, Ni, and S. Sugakiite is cream coloured, with a pinkish to reddish tint, is not pleochroic, and is isotropic to weakly isotropic, with shades of grey, under crossed polars. It has low relief, relatively low reflectivity, and does not have cleavage planes. Sugakiite occurs with an exsolution relationship with both pentlandite and mackinawite (Fig. 4.23).

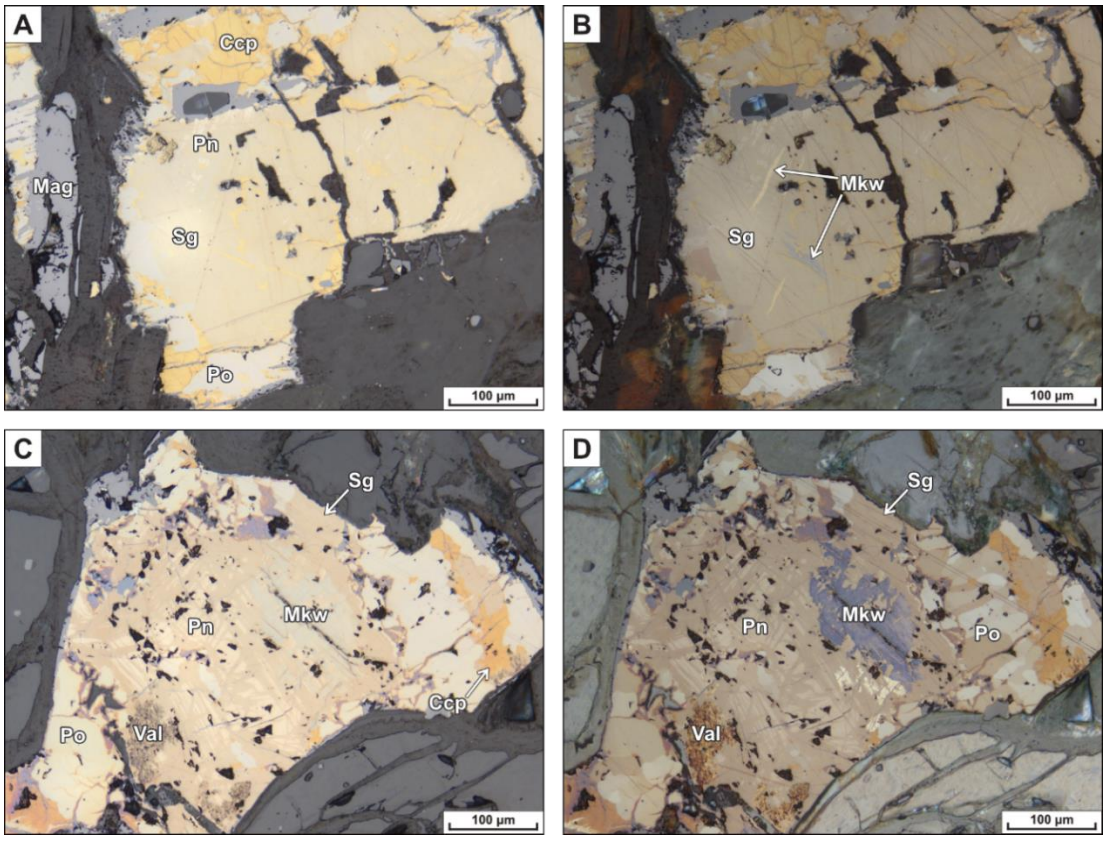

Figure 4.23: Representative photomicrographs of sugakiite within the altered, disseminated mineralization assemblage. A,B – sample CAM-21-CC-061 from drillhole ELR20-015, taken around the ore horizon from the N perimeter of the HGZ at 399.33m depth, corresponding to mid metal grades. The assemblage contains sugakiite, chalcopyrite, magnetite, pyrrhotite, mackinawite, and trace pentlandite. C,D – sample CAM-21-CC-071 from drillhole ELR20-006, taken above the ore horizon from the S perimeter of the HGZ at 378.7m depth, corresponding to mid metal grades. The assemblage contains sugakiite, pyrrhotite, pentlandite, mackinawite, chalcopyrite, magnetite, and valleriite. A,C – PPL; B,D – XPL. Abbreviations: Ccp – chalcopyrite; Mag – magnetite; Mkw – mackinawite; Pn – pentlandite; Po – pyrrhotite; Sg – sugakiite; Val – valleriite.

Valleriite occurs within the disseminated ores that experienced higher degrees of alteration than assemblages proximal to net-textured sulfides in the ore horizon. It typically occurs with bladed to leaf-like habits and is fine- to ultra fine-grained. Valleriite is constrained to the interstitial space between primary silicate minerals and may follow the original sulfide boundaries (Fig. 4.24).

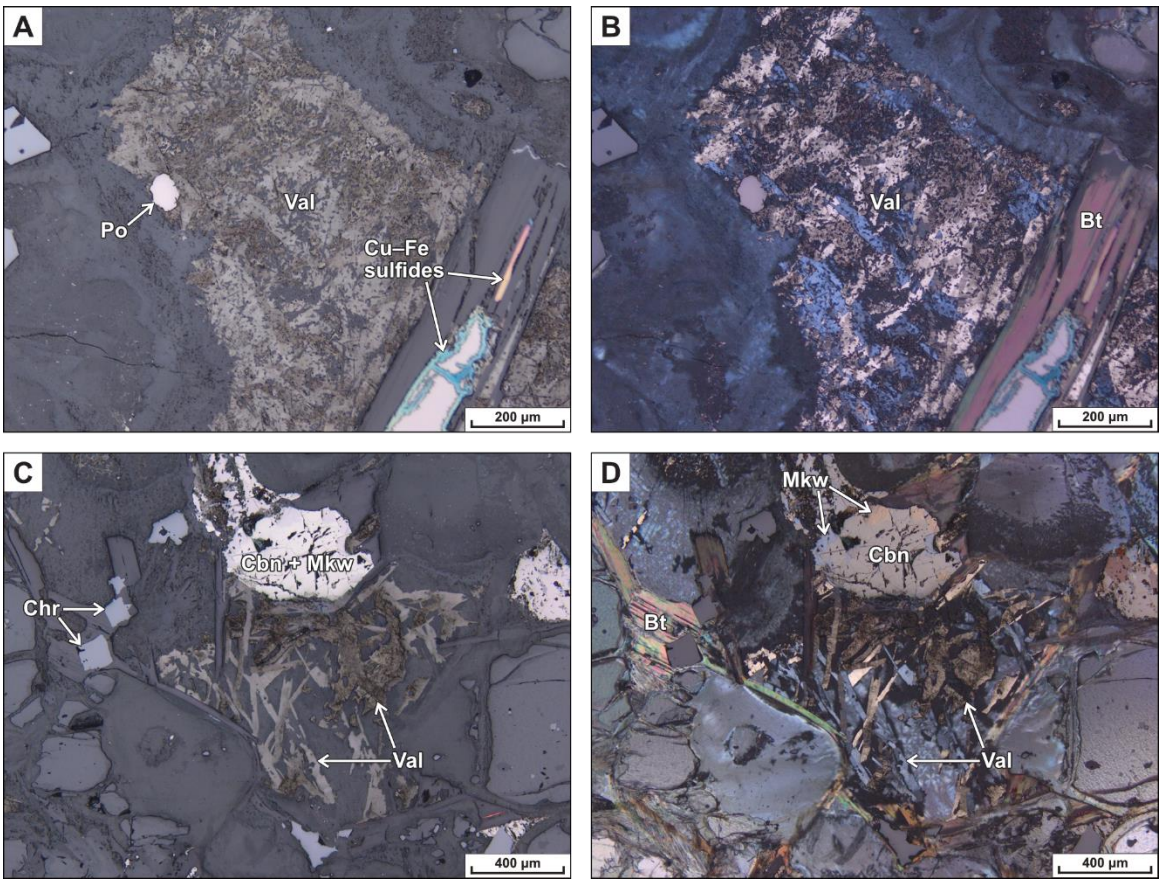

Figure 4.24: Representative photomicrographs of valleriite within altered, weakly disseminated mineralization associated with relict pyrrhotite, mackinawite, Cu-Fe-sulfides, serpentine and biotite. A,B – sample CAM-21-CC-028 from drillhole ELR20-002, taken well above the ore horizon at 349.4m depth, corresponding to very low metal grade (A – PPL; B – XPL). C,D – sample CAM-21-CC-029 from drillhole ELR20-002, taken well above the ore horizon at 359.1m depth, corresponding to very low metal grade (C – PPL; D – XPL). Abbreviations: Bt – biotite; Cbn – cubanite; Chr – chromite; Mkw – mackinawite; Po – pyrrhotite; Val – valleriite.

Valleriite exhibits a dull brown colouration in plane polarized light and is easily overlooked in thin section. Like mackinawite, under crossed polars, valleriite exhibits extreme brown-beige to blue-grey anisotropy (Fig. 4.24). Valleriite is intimately associated with fibrous serpentine and tabular biotite, and always occurs at the edge of relict sulfides. Moreover, sulfides

may be partially altered to valleriite, which presents as a unique decomposition texture that is ultra fine-grained and brown (e.g., Figs. 4.22c–d and 4.23c–d). When viewed with secondary electron (SE) imagery, this occurrence of valleriite is characterized by abundant surface irregularities and pitting, and chemical composition determined via SEM–EDS produced variable results. This is due to valleriite's poor polish, and the effect of underlying sulfides on the analysis.

At depths below the ore horizon (~90 m below the primary net-textured assemblage), disseminated sulfides are present within the peridotite unit. These interstitial sulfides contain little to no metal grade, and are almost exclusively composed of pyrite and pyrrhotite. Figure 4.25 illustrates an intergrowth with variable abundances of pyrite and pyrrhotite, with associated magnetite.

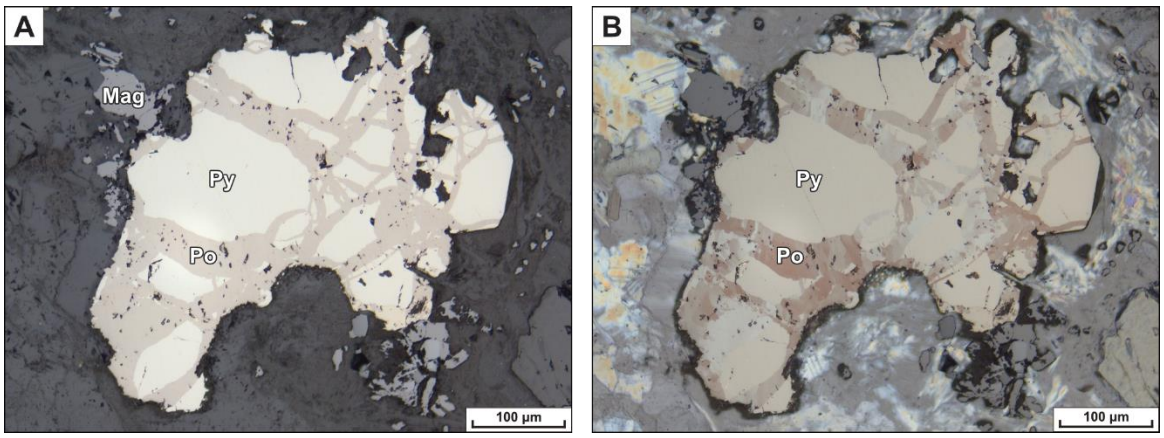

Figure 4.25: Representative photomicrographs altered, trace disseminated mineralization with pyrite, pyrrhotite, magnetite, and chromite. Sample CAM-21-CC-019 from drillhole ELR20-025, taken well below the ore horizon at 489.2m, corresponding to very low metal grades (A – PPL; B – XPL). Abbreviations: Mag – magnetite; Po – pyrrhotite; Py – pyrite.

Both sulfides are fine- to ultra fine-grained, with anhedral pyrrhotite anastomosing through fractured (angular) pyrite, with an 'island–ocean' texture (Fig. 4.25). Under crossed polars, the anastomosing pyrrhotite is anisotropic, exhibits undulatory extinction, and local triple junctions.

In summary, the main differences between sulfides from the primary assemblages and those from the altered assemblages (above, below, and around the ore horizon) is the occurrence of some or all of the following within the altered assemblage: loss of original sulfide boundaries

(volume), native copper, lenticular (gash-like) magnetite, replacement of pentlandite by mackinawite, Cu-rich pyrrhotite (particularly in fracture selvages), sugakiite, and replacement of interstitial sulfides by valleriite.

4.1.3.3 Crosscutting Mineralization

The following section outlines the representative mineralization styles observed in the crosscutting sulfide assemblage; sulfide veinlets (continuous and discontinuous; Type I and II, respectively) and gangue veinlets (which contain sulfide blebs in carbonate and felsic hosts; Type III and IV, respectively; Fig. 4.12).

4.1.3.3.1 Sulfide veinlets

The Type I veinlets share common characteristics: they crosscut the groundmass, lack silicate phenocrysts, and are effectively coherent across the length of the veinlet in a fashion that resembles primary, massive sulfide mineralization. What distinguishes the Type I veinlets (and all of the sulfide veinlets, for that matter) from the massive sulfide lenses (Fig. 4.13b) is that sulfides in the former are mineralogically and texturally distinct. Rather than the orderly layering of pyrrhotite, pentlandite, and chalcopyrite found within the massive sulfide lens, the sulfide veinlets typically show entire sections composed of a single mineral (e.g., Fig. 4.26) or an irregular mixture of multiple sulfide minerals (e.g., Fig. 4.27).

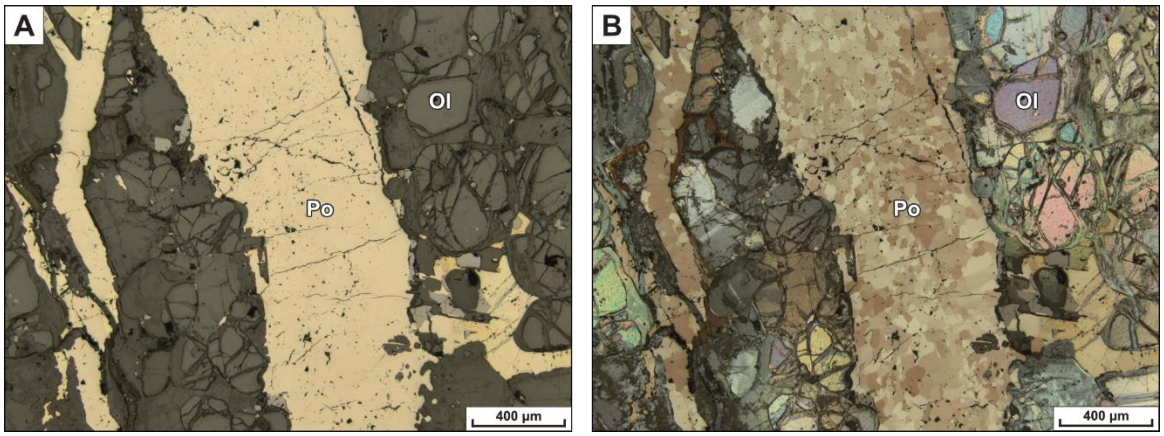

Figure 4.26: Representative photomicrographs of a segment of a continuous sulfide (Type I) veinlet dominated by pyrrhotite. Sample CAM-21-CC-089 from drillhole ELR20-018 taken near the ore horizon from the W perimeter of the HGZ at 396.4m depth, corresponding to mid metal grades (A – PPL; B – XPL). Abbreviations: Ol – olivine; Po – pyrrhotite.

In plane-polarized light, minerals, such as pyrrhotite, chalcopyrite, and cubanite, commonly exhibit massive textures, with no distinct grain boundaries. However, under cross-polarized light, the pyrrhotite often exhibits sub-grains, with triple junctions (Figs. 4.26b and 4.27b).

Within Type I and II sulfide veinlets, the distribution of sulfides is similar to that of the primary mineralization insofar as pyrrhotite is the most abundant sulfide phase. However, unlike the primary sulfide ores, cubanite occurs as the dominant Cu–Fe sulfide mineral, with chalcopyrite being less common (Fig. 4.27).

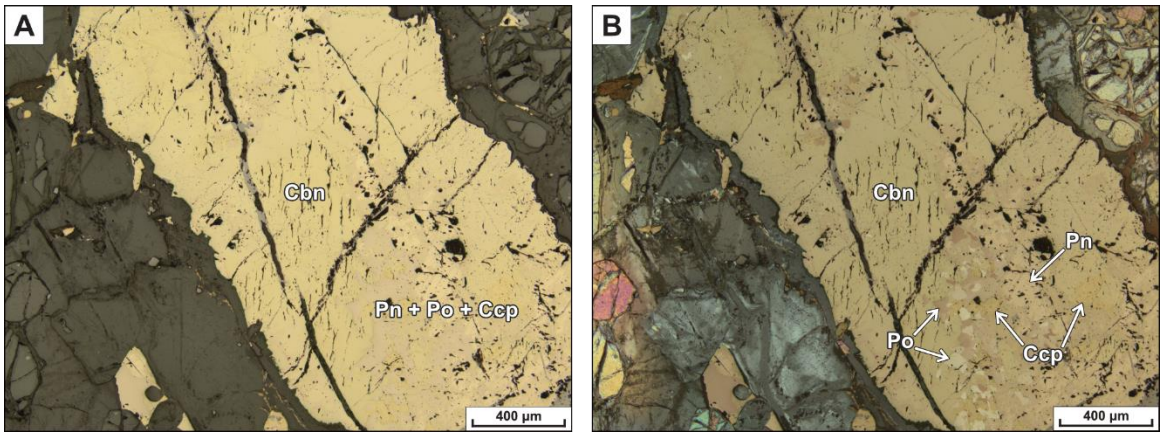

Figure 4.27: Representative photomicrograph of cubanite within a segment of a continuous sulfide (Type I) veinlet associated with a mixture of chalcopyrite, pyrrhotite, and pentlandite. Sample CAM-21-CC-089 from drillhole ELR20-018 taken near the ore horizon from the W perimeter of the HGZ at 396.4m depth, corresponding to mid metal grades (A – PPL; B – XPL). Abbreviations: Cbn – cubanite; Ccp – chalcopyrite; Pn – pentlandite; Po – pyrrhotite.

Pentlandite occurs as anhedral, granular aggregates that either form clusters/linear aggregates that can run along the length of the veinlet, and/or networks between pyrrhotite and the Cu–Fe sulfides (Figs. 4.27; 4.28a). Pentlandite also commonly occurs as exsolution 'flames' within pyrrhotite, which usually emanate perpendicularly from fractures within the sulfide veinlets. Pyrite and mackinawite are rare within the sulfide veinlets. Pyrite occurs as very fine-grained, discrete disseminations throughout the veinlet groundmass, often occurring at the edges of sulfide veinlets (Fig. 4.31a), and mackinawite occurs within fractures in pentlandite.

Type I veinlet selvages are marked by strong alteration along the length of the veinlets, with serpentine, talc, biotite, and chlorite rimming the edge of the veinlet, and oriented sub-normal to the length of the veinlet (Fig. 4.28).

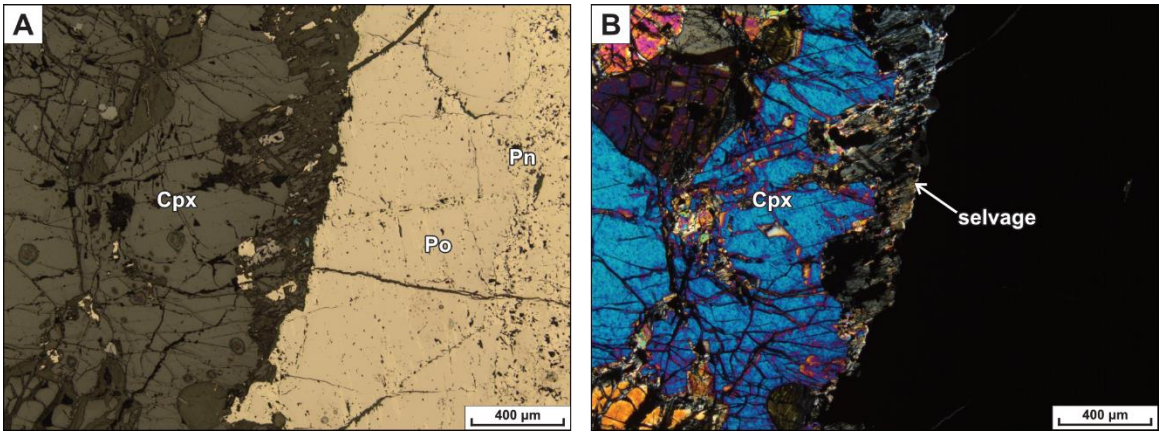

Figure 4.28: Representative photomicrographs depicting the altered selvage of a continuous sulfide veinlet composed of pyrrhotite and pentlandite. Sample CAM-21-CC-101 from drillhole ELR20-002 taken around the ore horizon from the E perimeter of the HGZ at 403.61m depth, corresponding to mid metal grades (A – reflected PPL; B – transmitted XPL). Abbreviations: Cpx – clinopyroxene; Pn – pentlandite; Po – pyrrhotite.

Selvages of the Type II sulfide veinlets are also marked by strong alteration of the silicate groundmass and are dominated by talc and serpentine after olivine. Moreover, breaks in the Type II sulfide veinlets are typically occupied by carbonates, chlorite, and silicate minerals pseudomorphed by serpentine and talc (Fig. 4.29).

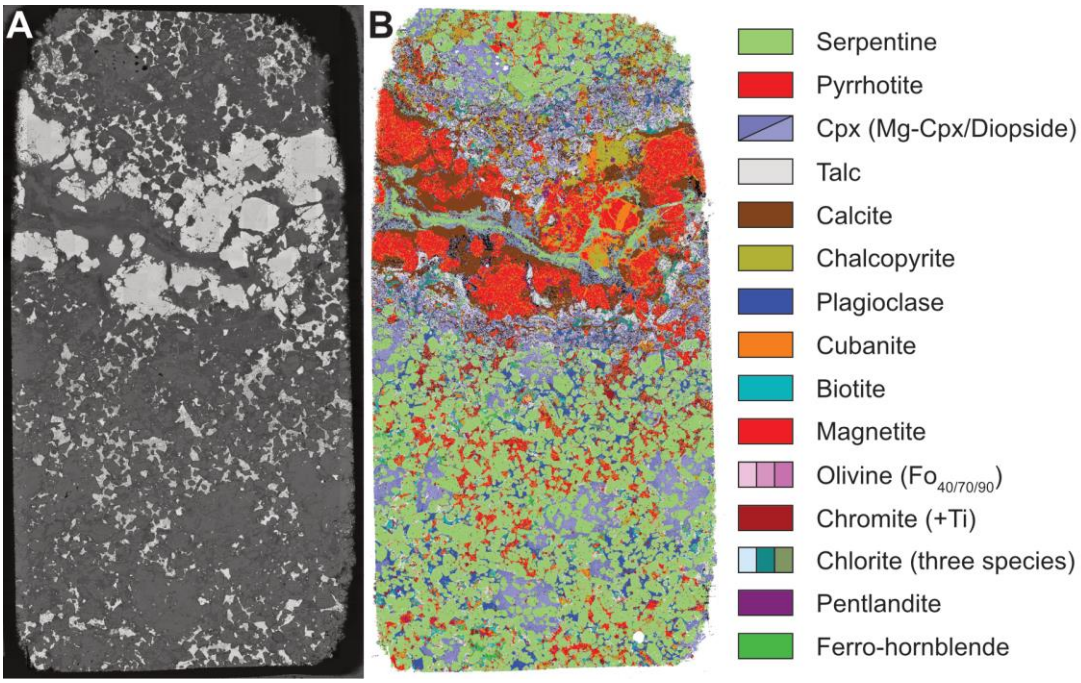

Figure 4.29: MLA scans of polished thin section CAM-21-CC-117 from drillhole ELR20-002, illustrating mineral abundances by area % for a discontinuous sulfide (Type II) veinlet. A – back-scattered electron image. B – false colour EDS library-matched minerals mapped to BSE image. Minerals are listed in order of decreasing abundance in the legend. Minerals representing <1% of the area are omitted.

The mineralogy and textural relationships in the Type II sulfide veinlets are similar to those exhibited by the Type I sulfide veinlets insofar as sulfides may be complexly intergrown (Fig. 4.30a) or largely separated within sections of the veinlet (Fig. 4.30b).

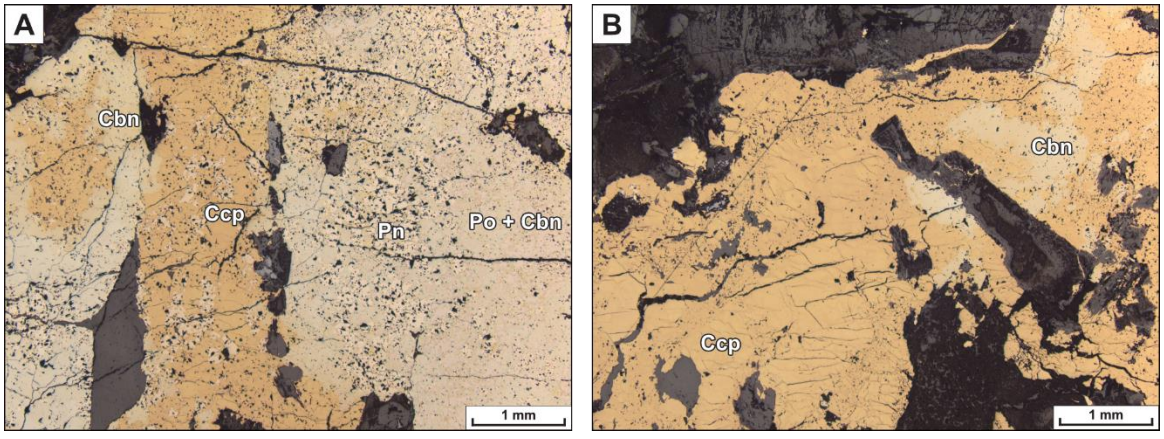

Figure 4.30: Representative photomicrographs of segments of a discontinuous sulfide (Type II) veinlet composed of irregular intergrowths of chalcopyrite, pyrrhotite, granular pentlandite, cubanite, and trace pyrite. Sample CAM-21-CC-060 from drillhole ELR20-015 taken just above the ore horizon from the N perimeter of the HGZ at 396.3m depth, corresponding to mid metal grades; PPL. Abbreviations: Cbn – cubanite; Ccp – chalcopyrite; Pn – pentlandite; Po – pyrrhotite.

Where a massive habit is not the dominant texture within the sulfide veinlets and there is a mixture of pyrrhotite and Cu–Fe sulfides, the assemblage may occur with two main styles. In one, Cu–Fe sulfides (typically chalcopyrite) occur as subveinlets (or ribbons) that wrap around subgrains of pyrrhotite (Fig. 4.31a). In the other, sulfides in the veinlet exhibit a mottled, blotchy, or patchy texture (Fig. 4.31b).

Pentlandite aggregates form linear arrangements as is common in the Type I sulfide veinlets, or random arrangements disseminated throughout pyrrhotite and Cu–Fe sulfides (Fig. 4.30a). A habit of pentlandite that is not observed within the Type I sulfide veinlets, but is common to the Type II sulfide veinlets, are rounded clusters, or glomerocrysts (Fig. 4.31). The pentlandite clusters occur within any portion of the sulfide veinlet and are not limited in their mineral associations.

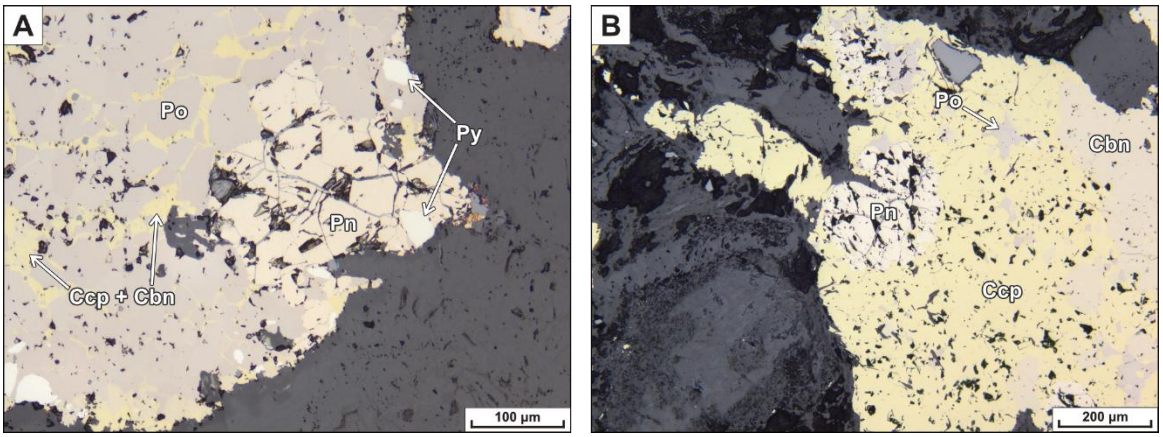

Figure 4.31: Representative photomicrographs of pentlandite within a segment of a discontinuous sulfide (Type II) veinlet associated with pyrrhotite, chalcopyrite, trace cubanite, and trace pyrite. Sample CAM-21-CC-117 from drillhole ELR20-002 taken at the ore horizon of the high-grade zone at 399.3m depth. A – area showing close-up of pentlandite cluster within pyrrhotite, PPL; B – a different area showing two pentlandite clusters within chalcopyrite, PPL. Abbreviations: Cbn – cubanite; Ccp – chalcopyrite; Pn – pentlandite; Po – pyrrhotite; Py – pyrite.

4.1.3.3.2 Sulfide blebs in gangue veinlets

Two types of sulfide bleb-hosting veinlets have been identified — those which are predominantly composed of carbonate minerals (Type III) and those that are predominantly composed of felsic minerals (Type IV). Type III veinlets account for the majority of sulfide bleb-

hosting veinlets analyzed in this study. Within both categories, the entrained sulfide blebs are mineralogically and texturally variable; and may contain any or all of pyrrhotite, chalcopyrite, cubanite, and pentlandite. As with the pure sulfide veinlets, the mineralogy may be segregated or irregularly intergrown. Figure 4.32a depicts an example of a pyrrhotite and pentlandite bleb within a Type III (carbonate ± talc ± chlorite ± serpentine) veinlet, whereas Figure 4.32b depicts an example of a medium-grained, rounded sulfide bleb that is almost entirely composed of anhedral chalcopyrite and cubanite within a Type IV (felsic) veinlet.

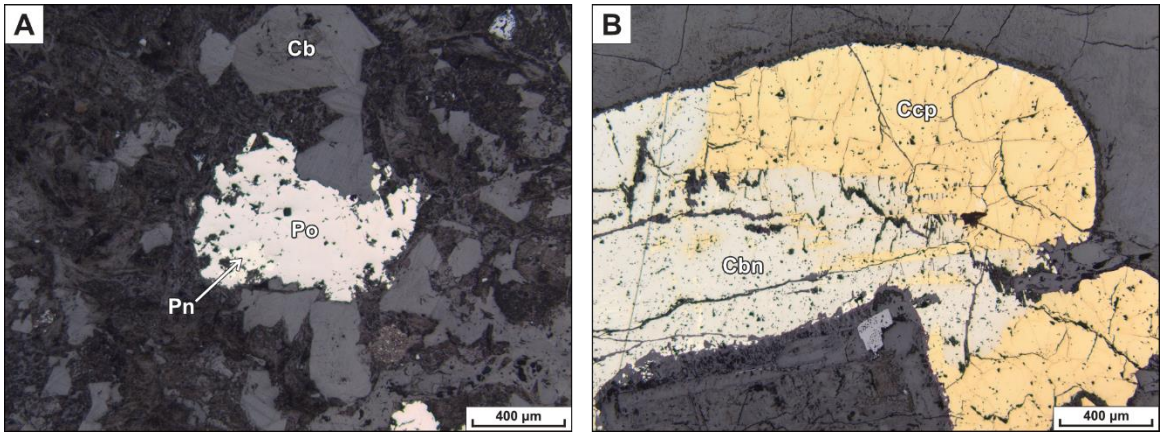

Figure 4.32: Representative photomicrographs of sulfide blebs within gangue veinlets . A – a pyrrhotite, pentlandite and trace cubanite sulfide bleb in a (Type III) carbonate veinlet; sample CAM-21-CC-030 from drillhole ELR20-002 taken above the ore horizon of the HGZ at 371.5m depth, corresponding to very low metal grades; PPL. B – medium-grained, rounded bleb composed of chalcopyrite and cubanite in a (Type IV) felsic veinlet; sample CAM-21-CC-072 from drillhole ELR20-006 taken above the ore horizon from the S perimeter of the HGZ at 383m depth, corresponding mid metal grades; PPL. Abbreviations: Cb – carbonate; Cbn – cubanite; Ccp – chalcopyrite; Pn – pentlandite; Po – pyrrhotite.

The pyrrhotite-pentlandite-cubanite sulfide bleb is fine-grained and exhibits jagged to cuspate grain boundaries. Under cross polars, pyrrhotite contains subgrains which exhibit triple junctions, while pentlandite is isotropic. Typically, Type III carbonate veinlets crosscut the wehrlite groundmass and are devoid of mafic phenocrysts. The Cu-Fe sulfide bleb is surrounded by a felsic assemblage that is dominated by plagioclase, minor wollastonite, and orthoclase. Type IV gangue veinlets also crosscut the wehrlite groundmass and do not contain mafic phenocrysts.

4.1.4 Platinum-group minerals and related species

Twenty-two platinum-group minerals (PGM), tellurides, sulfosalts, sulfides, and native metals were identified using SEM–EDS. These minerals have been organized based on the mineralization style in which they occur (Table 4.1).

Table 4.1: Summary table of platinum-group, precious-metal minerals, sulfides, and native elements identified during post-processing of MLA sections.

Interstitial–Primary		**Crosscutting**	
Species	**Formula**	**Species**	**Formula**
Sperrylite	$PtAs_2$	Mitrofanovite	Pt_3Te_4
Michenerite	PdBiTe	Maslovite	PtBiTe
Mitrofanovite	Pt_3Te_4	Merenskyite	$PdTe_2$
Sopcheite	$Ag_4Pd_3Te_4$	Hessite	Ag_2Te
Native Silver	Ag	Altaite	PbTe
Electrum	(Au,Ag)	Sperrylite	$PtAs_2$
Galena	PbS	Palladoarsenide	Pd_2As
unknown	Pt-Bi-Pd-Te	Nipalarsite	$Ni_8Pd_3As_4$
Interstitial–Altered		Ni-cobaltite	(Co,Ni)AsS
Species	**Formula**	Co-gersdorffite	(Ni,Co)AsS
Native gold	Au	Alloclasite	$Co_{1-x}Fe_xAsS$
Native silver	Ag	Native silver	Ag
Electrum	(Au,Ag)	Galena (± Se)	Pb(S,Se)
Native copper	Cu	Greenockite	CdS
Galena	PbS	Sphalerite	ZnS
unknown	Pt-Bi-Pd-Te	*unknown*	PbTeS

Sperrylite, michenerite, and mitrofanovite were the most frequently identified PGMs in the primary, net-textured mineralization. Sperrylite occurs as ultra fine-grained, anhedral to subhedral (blade-like, poor cubic habit) grains within primary pyrrhotite, chalcopyrite, and pentlandite (Fig. 4.33a, b). It is found both as inclusions directly within sulfides and between fractures/cleavage planes in sulfides (Fig. 4.33a, b).

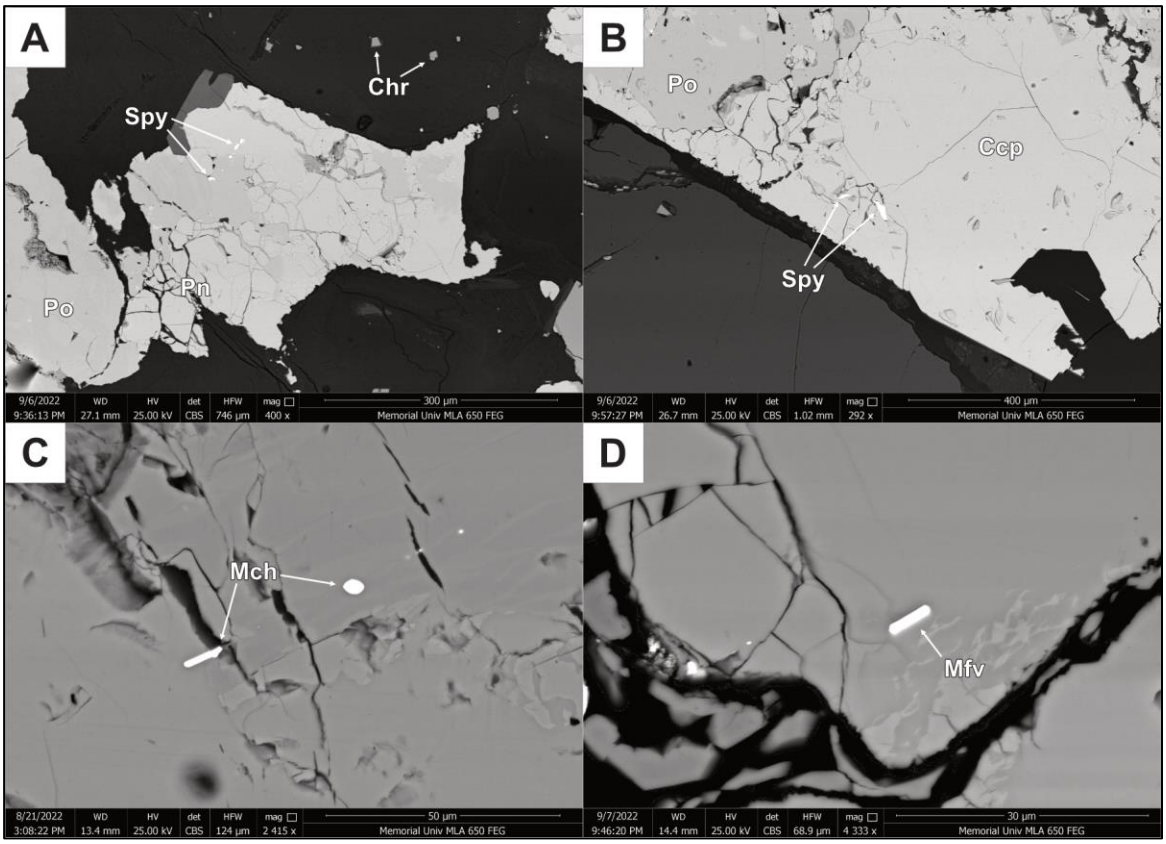

Figure 4.33: Back-scattered electron images of platinum group minerals within interstitial–primary sulfide mineralization. A – ultra fine-grained, anhedral sperrylite grains within pyrrhotite (sample CAM-21-CC-011). B – ultra fine-grained, sperrylite blades within chalcopyrite (sample CAM-21-CC-044). C – ultra fine-grained, elongate, and round michenerite inclusions in chalcopyrite and pyrrhotite (sample CAM-21-CC-009). D – ultra fine-grained, elongate mitrofanovite in pyrrhotite, and ultra fine-grained, anhedral specs of michenerite in chalcopyrite (sample CAM-21-CC-048). Abbreviations: Ccp – chalcopyrite; Chr – chromite; Mch – michenerite; Mfv – mitrofanovite; Pn – pentlandite; Po – pyrrhotite; Spy – sperrylite.

Michenerite and mitrofanovite occur in the same fashion, typically as inclusions within the base-metal sulfides. Inclusions of these PGMs often occur as anhedral to rounded specs, however, the coarser inclusions commonly exhibit elongate habits (Fig. 4.33c, d).

The only PGM identified in the interstitial–altered sulfide mineralization was an unidentified Pt–Pd bismuth–telluride. However, native metals and altaite (a Pb-telluride) were repeatedly identified (>10 occurrences) amongst four thin sections from this mineralization style. These minerals occur in two textures. The first texture is as ultra fine-grained inclusions that range from anhedral to angular to emulsoid in habit, and are present directly within sulfides, but also intergrown with magnetite in fractures (Fig. 4.34a,b).

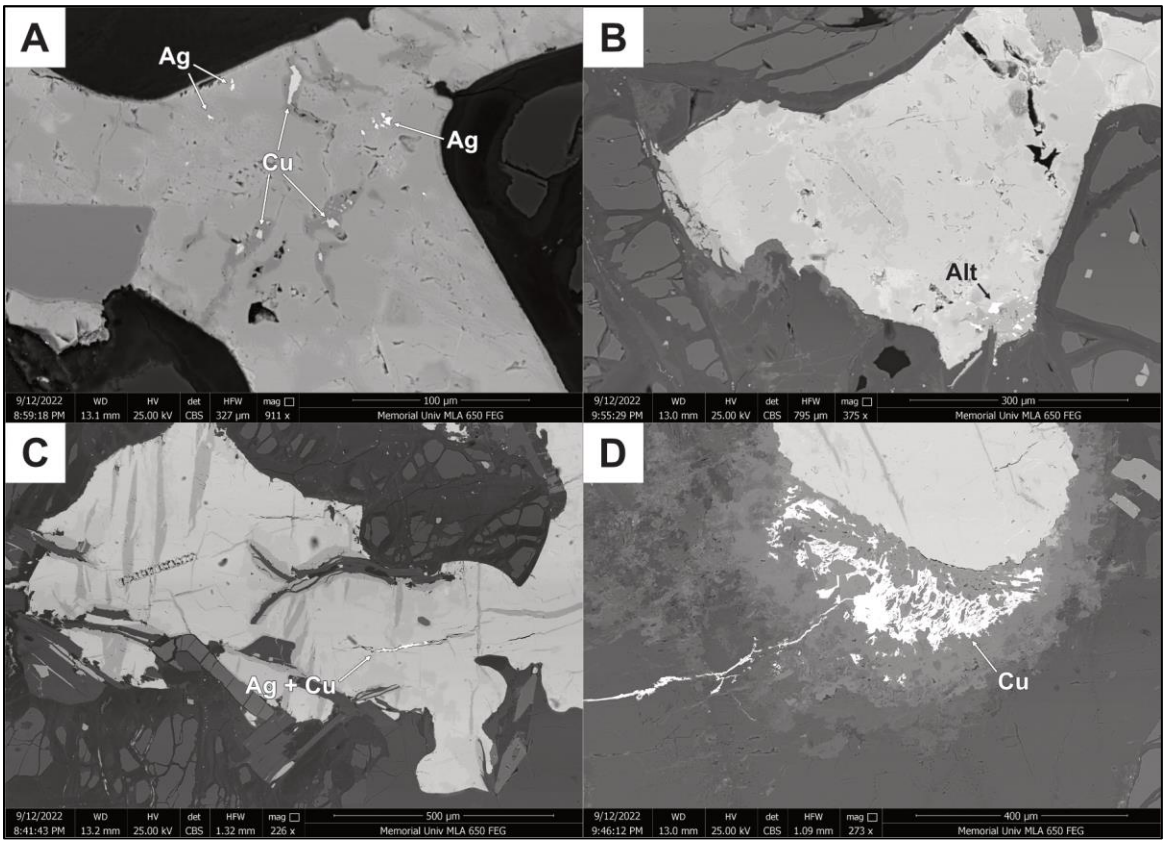

Figure 4.34: Back-scattered electron images of native metals and altaite within interstitial–altered sulfide mineralization. A – ultra fine-grained, anhedral to emulsoid inclusions of native silver (brighter) and native copper associated with magnetite in chalcopyrite (sample CAM-21-CC-061). B – ultra fine-grained, anhedral inclusions of altaite in magnetite, associated with sugakiite, pyrrhotite, pentlandite, mackinawite, and Cu-Fe-sulfides (sample CAM-21-CC-071). C – very fine-grained microveinlet of native silver and native copper associated with magnetite, running through chalcopyrite; note the laser ablation track to the upper left (sample CAM-21-CC-061). D – fine-grained, anhedral to wiry mass of native copper within Fe-Al-silicate, and chalcopyrite to the north (sample CAM-21-CC-087). Abbreviations: Ag – native silver; Alt – altaite; Cu – native copper.

Where there is a greater abundance of native metals, they present as fracture fill or vermicular veinlets that are present between sulfides (Fig. 4.34c). This style is most often represented by native copper and magnetite, but may also include native silver. The second style of native metals found in the altered mineralization assemblage is largely restricted to native copper present within silicate minerals; native metals of this style range from thin, wiry habits that permeate through silicate fractures to anhedral masses that may be intergrown with silicates (Fig. 4.34d).

The greatest variety of PGMs and related minerals were identified within the crosscutting sulfide assemblages. These include the PGMs that were identified within the interstitial–primary mineralization style (e.g., sperrylite and mitrofanovite), but also multiple Pd-bearing arsenides

(e.g., palladoarsenide), sulfarsenides (e.g., Co-gersdorffite), and sulfides (e.g., greenockite, sphalerite). The habit of the PGMs within this mineralization is similar as those present in the interstitial–primary assemblage. For example, mitrofanovite and maslovite occur as very fine-grained, elongate grains, as well as rounded to anhedral inclusions within sulfides (Fig. 4.35b,c).

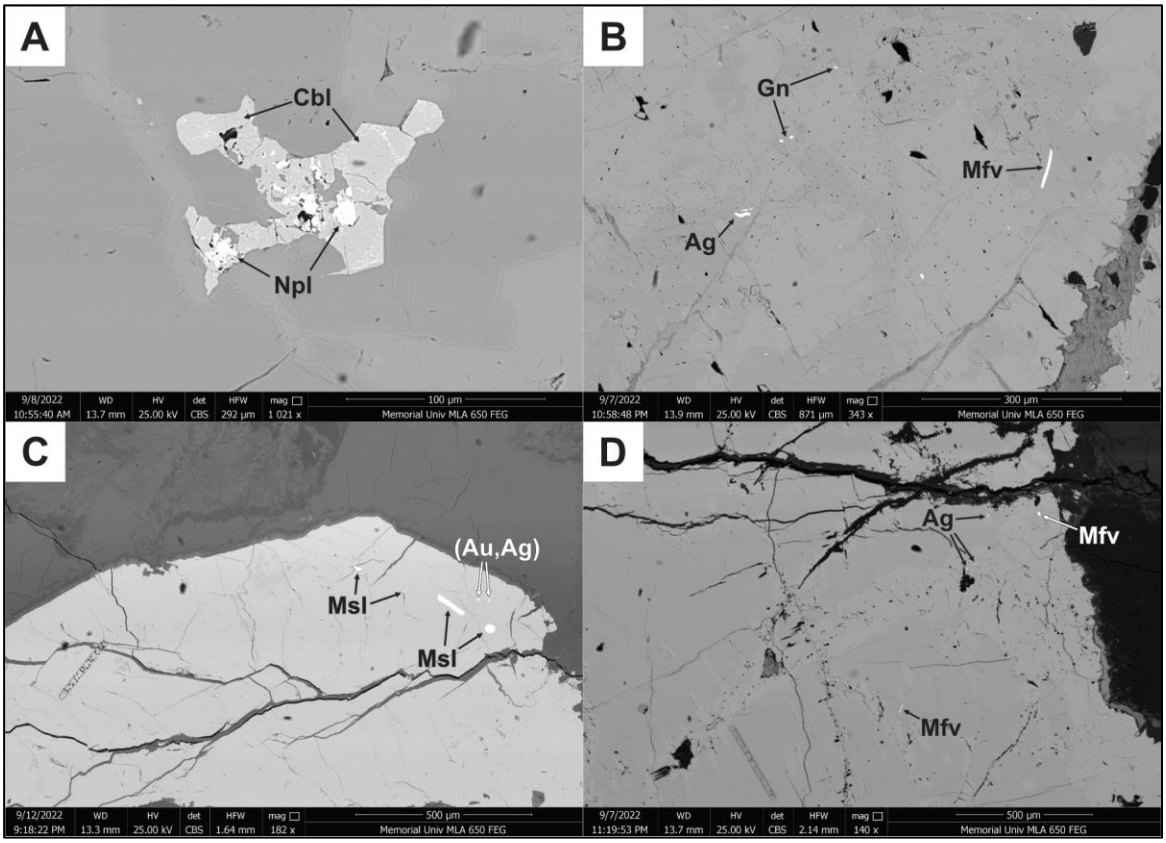

Figure 4.35: Back-scattered electron images of platinum-group minerals, sulfarsenides, sulfides, and native metals within crosscutting sulfide mineralization. A – fine-grained intergrowth of nipalarsite and cobaltite interstitial to pyrrhotite and chalcopyrite within a discontinuous sulfide veinlet (sample CAM-21-CC-117). B – ultra fine-grained inclusions of elongate mitrofanovite, anhedral native silver, and rounded galena within intergrown chalcopyrite and cubanite in a continuous sulfide veinlet (sample CAM-21-CC-089). C – very fine-grained, elongate, rounded and anhedral inclusions of maslovite and ultra fine-grained specs of native electrum within chalcopyrite occurring within a sulfide bleb in felsic veinlet; note the laser ablation track to the left (sample CAM-21-CC-072). D – ultra fine-grained, elongate, and rounded inclusions of mitrofanovite and ultra fine-grained, rounded specs of native silver within cubanite and pyrrhotite from a continuous sulfide veinlet (sample CAM-21-CC-101). Abbreviations: Ag – native silver; (Au,Ag) – electrum; Cbl – cobaltite; Gn – galena; Mfv – mitrofanovite; Msl – maslovite; Npl – nipalarsite.

There is a preponderance of As-rich minerals within the crosscutting sulfide assemblages. Figure 4.35a provides an example of a fine-grained intergrowth of nipalarsite and Ni-cobaltite occurring interstitial to base-metal sulfides. Galena (locally Se-rich) commonly occurs as ultra fine-grained, anhedral disseminations throughout continuous crosscutting sulfide assemblages, and is most

often present within pyrrhotite, cubanite, and chalcopyrite (Fig. 4.35b). Native metals, such as Ag, were also found within the crosscutting sulfide veinlets and, where present, occur as ultra fine-grained, anhedral inclusions within sulfides.

4.1.3.4 Ore Mineral Distributions

Each of the 17 thin sections that were analyzed via MLA were categorized by the three main sulfide mineralization styles: interstitial (primary), interstitial (altered), and interstitial with crosscutting veinlets. The average distribution of opaques for the interstitial–primary mineralization shows that the majority of the assemblage comprises pyrrhotite > chalcopyrite > pentlandite > magnetite > cubanite (Fig. 4.36).

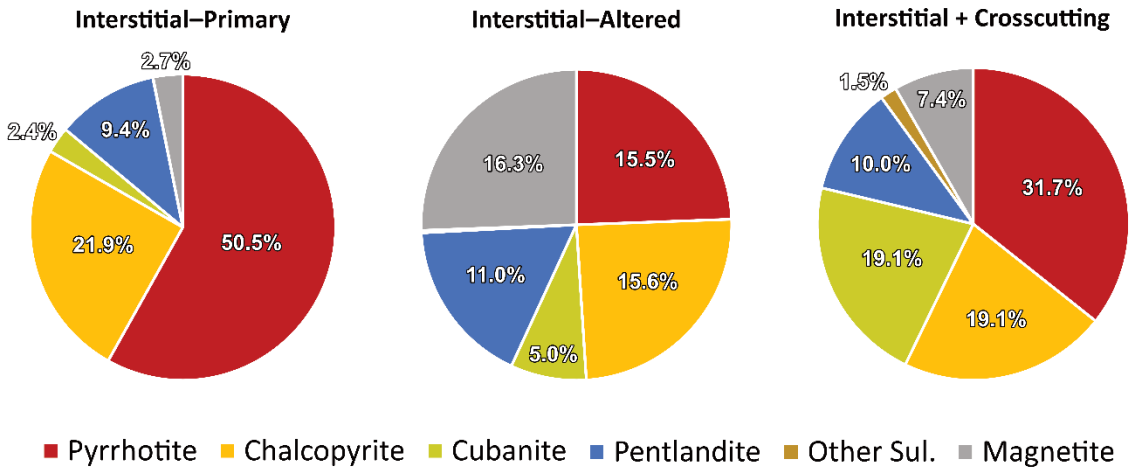

Figure 4.36: Pie charts summarizing average sulfide mineral and magnetite distributions determined by MLA for each mineralization category.

The interstitial–altered assemblage shows a clear change in the distribution of sulfides and magnetite. The assemblage is magnetite > chalcopyrite > pyrrhotite > pentlandite > cubanite (Fig. 4.36). The greater relative abundance of magnetite results in magnetite commonly occurring intergrown with sulfides. For the distribution of interstitial sulfides with crosscutting veinlets, the assemblage comprises pyrrhotite > cubanite > chalcopyrite > pentlandite > magnetite > other sulfides (pyrite ± galena, sphalerite, and chalcocite). Within this assemblage there is greater

proportion of cubanite, lower proportions of pyrrhotite, greater proportions of magnetite, and similar proportions of chalcopyrite and pentlandite compared to the primary–interstitial assemblage. The silicate alteration assemblage between the three mineralization styles is relatively similar, comprising serpentine > clinopyroxene > plagioclase > olivine (Fig. 4.37). The interstitial–crosscutting mineralization shows a higher proportion of talc alteration; this is likely attributed to the abundance of talc that occurs within the veinlet selvages. The altered and crosscutting styles show little to no scapolite alteration when compared to the primary style.

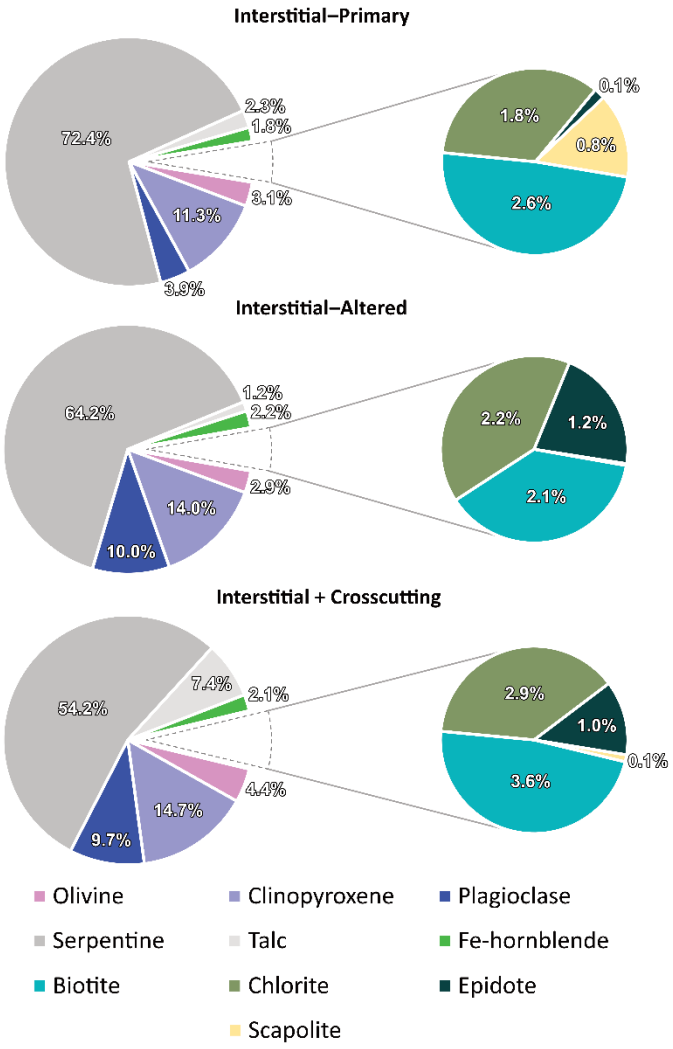

Figure 4.37: Pie charts summarizing average silicate and alteration mineral distributions determined by MLA for each mineralization category.

4.2 Whole-rock characterization

Lithogeochemical analysis was undertaken on unmineralized samples from the upper hybrid and gabbroic units (n = 1 and n = 7, respectively), the main mafic–ultramafic peridotite unit (n = 6), and country rocks of schistose and granitic composition (n = 6 and n = 2, respectively). The complete major- and trace-element dataset for these samples is provided in Appendix C.

4.2.1 Major elements

Rocks within the upper gabbroic unit from multiple drillholes between depths of 296.9 to 323.4 m contain anhydrous concentrations of 49.8–51.5 wt. % SiO_2, 1.3–1.7 wt. % TiO_2, and 13.9–15.0 wt. % MgO; the loss on ignition (LOI) for the gabbroic rocks ranges from 2.24–3.44 wt. %. Peridotites within the main mafic–ultramafic unit from multiple drillholes between depths of 313.9 to 343.5 m contain anhydrous concentrations of 41.1–41.8 wt. % SiO_2, 0.7–0.8 wt. % TiO_2, and 31.6–32.9 wt. % MgO; the LOI for the peridotitic rocks ranges from 7.70–8.46 wt. %.

Metasedimentary country rocks from multiple drillholes between depths of 425.1 to 558.05 m contain anhydrous concentrations of 59.7–65.3 wt. % SiO_2, 0.5–0.6 wt. % TiO_2, and 2.5–9.0 wt. % MgO; the LOI for the metasedimentary rocks ranges from 2.20–4.19 wt.%.

Granitoid country rocks contain anhydrous concentrations of 74.14–74.79 wt. % SiO_2, 0.01–0.02 wt. % TiO_2, and 0.16–0.17 wt. % MgO; the LOI for granitoid country rocks is 1.44–1.99 wt. %. The granitoid rocks are strongly peraluminous based on their saturation in alumina relative to alkali metals and calcium; ($Al_2O_3 >> CaO + Na_2O + K_2O$; Winter, 2001).

4.2.2 Trace elements

Rocks within the upper gabbroic unit from multiple drillholes between depths of 296.9 to 323.4 m are characterized by La/Sm_{cn} values ranging from 1.43–1.72, and Gd/Yb_n values ranging from 3.29–4.08 (Fig. 4.38). Peridotites within the main mafic–ultramafic unit from multiple

drillholes between depths of 313.9 to 343.5 m are characterized by La/Sm_n values ranging from 1.87–2.14, and Gd/Yb_n values ranging from 3.18–4.96. Metasedimentary country rocks from multiple drillholes between depths of 425.1 to 558.05 m are characterized by La/Sm_n values ranging from 2.97–4.03, and Gd/Yb_n values ranging from 1.74–2.95. Granitoid country rocks are characterized by La/Sm_n values ranging from 1.08–2.08, and Gd/Yb_n values ranging from 0.61–0.73.

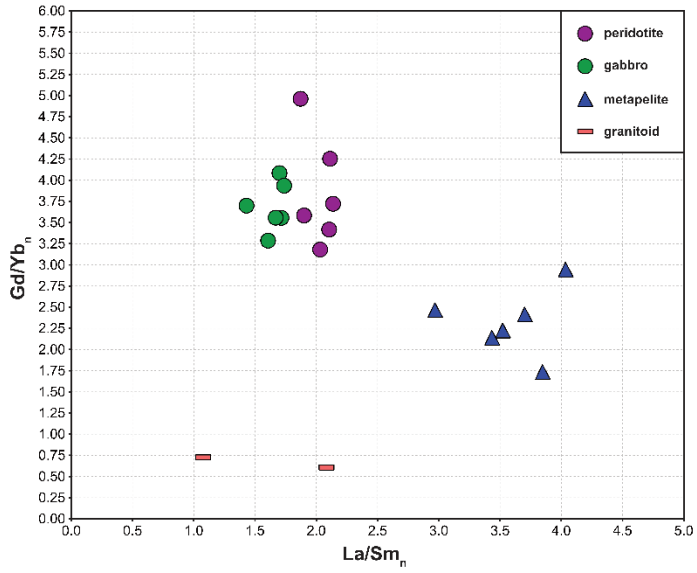

Figure 4.38: Chondrite-normalized, whole-rock trace-element variation diagram for Escape intrusive and country rocks. Normalizing values from Sun and McDonough (1989).

To further characterize the intrusive and country rocks at Escape, bulk-rock trace-element data were plotted on multiple primitive mantle-normalized extended trace-element diagrams. Both the gabbro and peridotite units depict a gently negative-sloping pattern that resembles ocean island basalt (OIB; Sun and McDonough, 1989; Fig. 4.39). The upper gabbroic rocks follow a similar pattern as the peridotites, apart from a few features. The main difference being that the gabbros show a greater enrichment in trace elements compared to the peridotite.

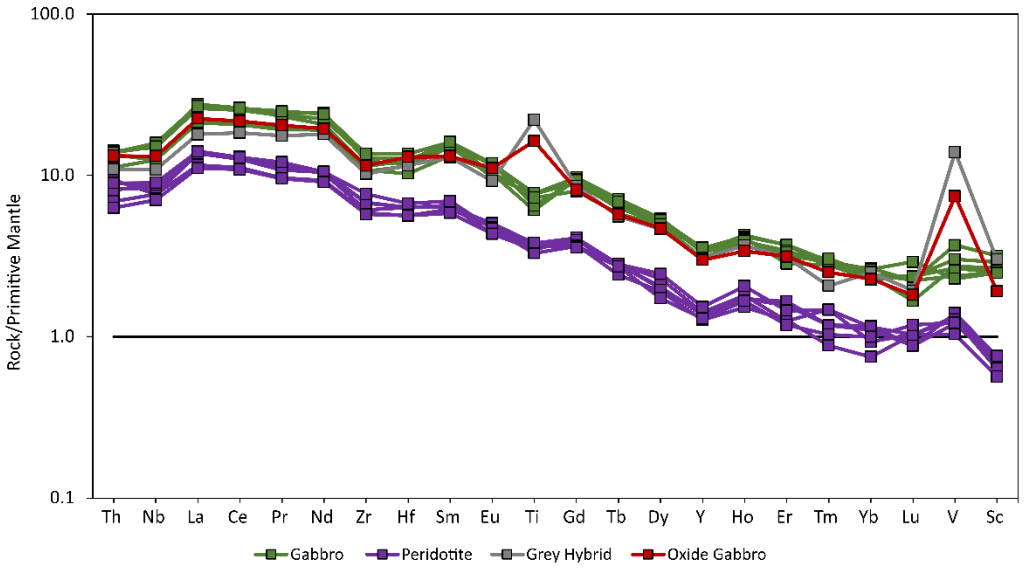

Figure 4.39: Primitive mantle-normalized spidergram for Escape intrusive rocks. Normalizing values from Sun and McDonough (1989).

The second difference being that the peridotites exhibit a greater variability in their Tm and Yb concentrations. The final key difference between the intrusive units is that the peridotites exhibit a higher V/Sc_{PM} ratio than the gabbros (where values range from 1.61–2.02 and 0.92–1.16, respectively). The grey hybrid and oxide gabbro rocks exhibit trace-element patterns that follow the gabbros almost identically, save for pronounced positive Ti and V anomalies (Fig. 4.39).

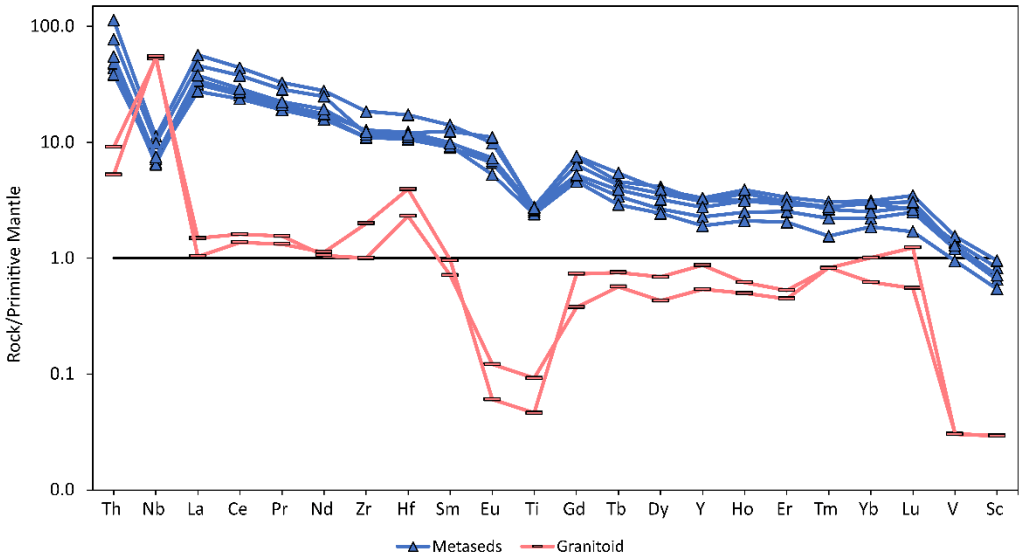

Figure 4.40: Primitive mantle-normalized spidergram for Escape country rocks. Normalizing values from Sun and McDonough, 1989.

Figure 4.40 illustrates the trace-element patterns for the metasedimentary and granitoid country rocks at Escape. The schistose country rocks exhibit a gently sloping negative trend similar to the Escape intrusive units. Pronounced differences exhibited by the metasedimentary rocks relative to the mafic–ultramafic rocks include elevated Th concentrations and a negative Ti anomaly. Both the Escape intrusive rocks and the metasedimentary country rocks exhibit a negative Nb anomaly relative to OIB, albeit the anomaly for the Escape rocks is less pronounced. Negative Nb and Ti anomalies are features common to continental crust (Wedepohl, 1995). Conversely, the granitoid country rocks exhibit a markedly different trace-element signature, with a low Th/Nb ratio, a positive Hf anomaly, and significant depletions in Eu, Ti, V, and Sc.

4.3 Sulfide chemistry

4.3.1 Major element chemistry

The most abundant sulfide minerals identified by SEM–EDS in this study were pyrrhotite (and troilite), chalcopyrite, cubanite, and pentlandite. Pyrite, mackinawite (with and without Cu impurities), and sugakiite constitute lesser sulfide phases within the Escape intrusion. The complete data set for sulfide compositions is provided in Appendix C. Figure 4.41 illustrates the variation in major-element composition of these sulfides on ternary diagrams.

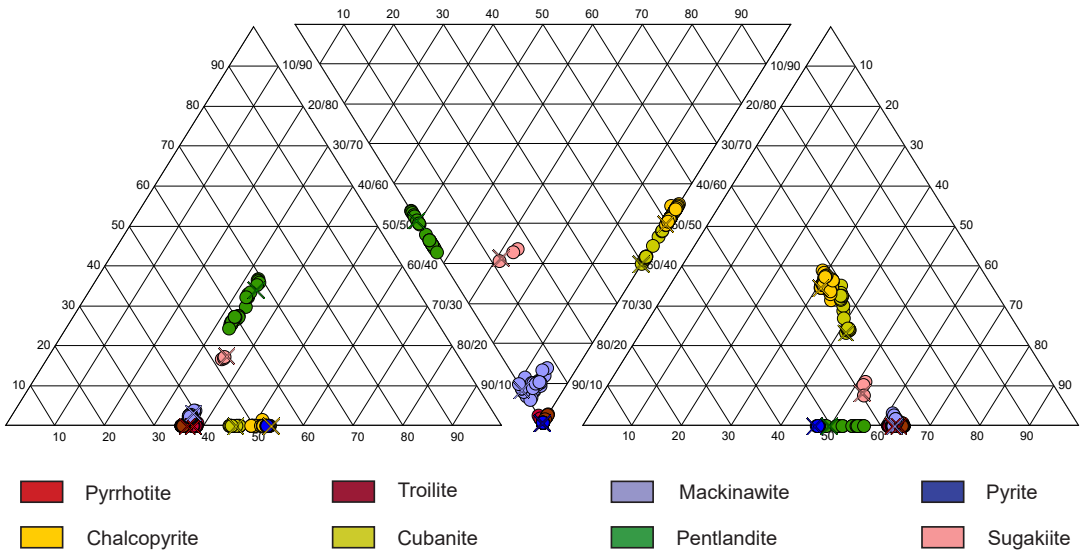

Figure 4.41: Escape sulfide major element compositions plotted on ternary diagrams for the Ni+Co–Fe–S, S–Cu–Ni+Co, and Cu–S–Fe systems. Stoichiometric compositions are plotted as Xs on the diagrams. Note — chalcopyrite and pyrite reference standards overlap in Ni+Co–Fe–S space, while pyrite, pyrrhotite, and troilite reference standards overlap in S–Cu–Ni+Co space. Reference standard data from Bathelmy (2022) and Mücke (2017).

All sulfide minerals plot close to their reference standards, except for pentlandite and cubanite which exhibit spreads which trend towards Fe (Fig. 4.41). Mackinawite also deviates from the reference standard due to some samples containing <3% Cu. Sugakiite plots between all of the other sulfide minerals, in a location that is consistent with its published composition (Kitakaze, 2008).

4.3.2 Trace-element chemistry

Trace-element data were collected for 298 unique mineral grains of pyrrhotite, chalcopyrite, pentlandite, cubanite, pyrite, mackinawite, native copper, and sugakiite. Data were obtained for minerals present within primary, altered, and crosscutting mineralization assemblages. The complete dataset for all analyses is provided in Appendix D.

The platinum-group elements (PGEs) occur within each sulfide (across all mineralization assemblages) in concentrations ranging from ~0.01–10 ppm, with the PPGE (Pt, Pd, Rh) and

IPGE (Ir, Os, Ru) exhibiting similar mineral affinities, respectively (Fig. 4.42). Palladium occurs in the greatest concentration in sulfides out of all the PGE, with the highest concentrations occurring in pentlandite (average of ~150 ppm in primary pentlandite; Fig. 4.42); the remainder of the PGE occur in concentrations ≤10 ppm in pentlandite. Platinum and Pd occur in concentrations of up to 10 ppm in chalcopyrite and pyrrhotite, whilst Ir and Os are preferentially enriched in pyrrhotite (up to 10 ppm; Fig. 4.42). Ruthenium and Rh occur in the lowest concentrations in sulfides out of all of the PGE, albeit Rh values are not reported for chalcopyrite and cubanite due to a molecular ion interference by CuAr in the mass spectrometer. Pyrite is consistently depleted in PGE relative to the other sulfide minerals and is often undetectable (Fig. 4.42). Like the PGE, silver exhibits similar concentrations in the sulfides, where it occurs up to and exceeding 10 ppm in each of the sulfides (except for pyrite), while Au occurs in consistently low concentrations amongst all the sulfides (always <1 ppm; Fig. 4.42).

Pentlandite in both the altered and crosscutting assemblages contains Pd concentrations that are depleted relative to pentlandite from primary, net-textured mineralization (Fig. 4.42). The other PGE do not show much variability in the secondary sulfide assemblages relative to primary sulfides, but do exhibit minor variations in Co concentrations (e.g., an additional ~0.2–0.6 ppm Co in chalcopyrite from the secondary assemblage).

The TABS (Te, As, Bi, Sn, and Sb) group of semimetals occur with consistently low concentrations in all the sulfide phases, with averages typically <10 ppm. The TABS element with the highest concentration in sulfides is Te, with concentrations of up to 100 ppm (Fig. 4.42). Tellurium, Bi, and Sb in chalcopyrite, pyrrhotite, and pentlandite within secondary assemblages exhibit minor enrichments relative to primary mineralization, albeit there is still significant overlap between primary and secondary assemblage concentrations (Fig. 4.42).

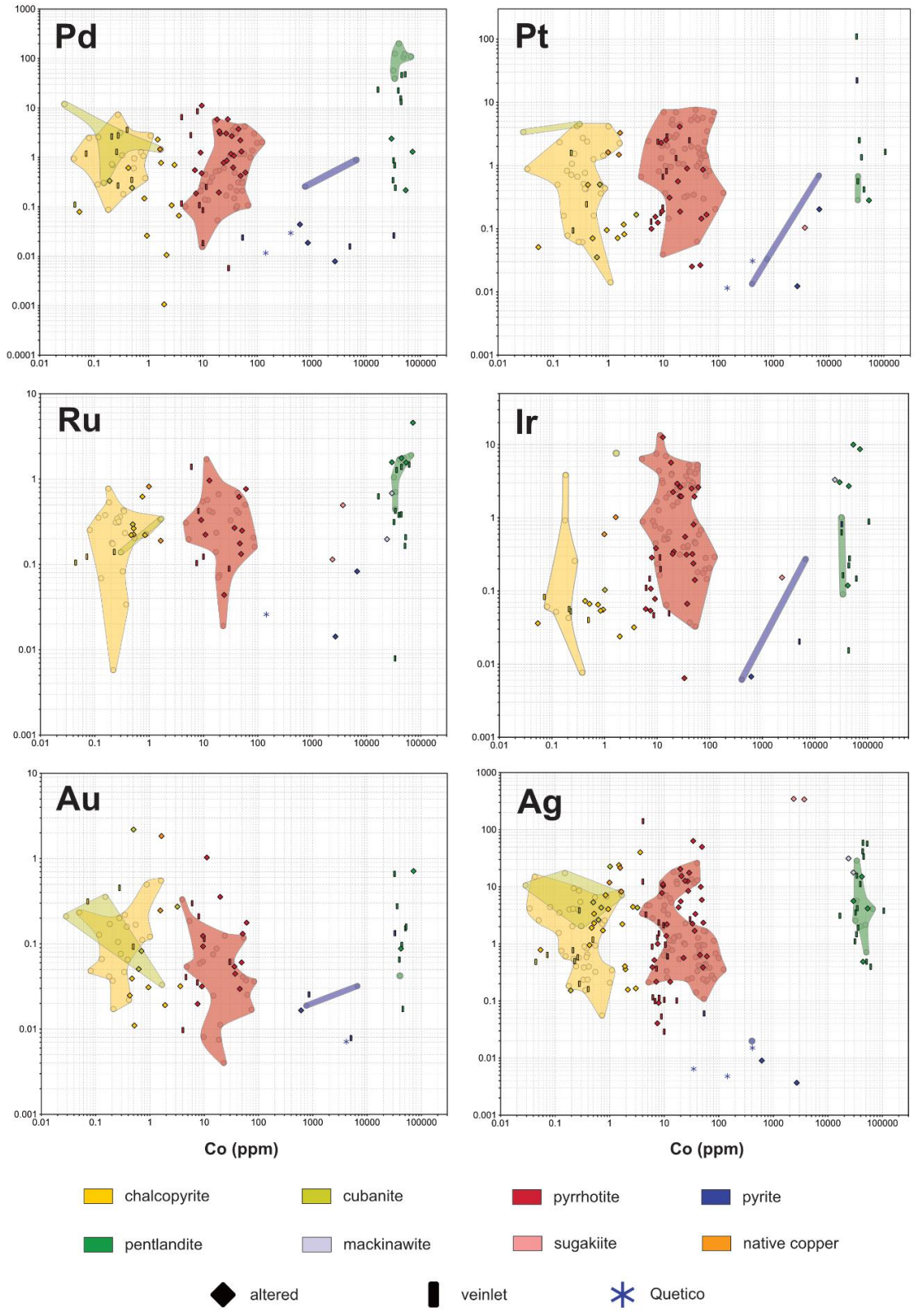
Pd
Pt
Ru
Ir
Au
Ag
Co (ppm)
Co (ppm)
chalcopyrite
cubanite
pyrrhotite
pyrite
pentlandite
mackinawite
sugakiite
native copper
altered
veinlet
Quetico

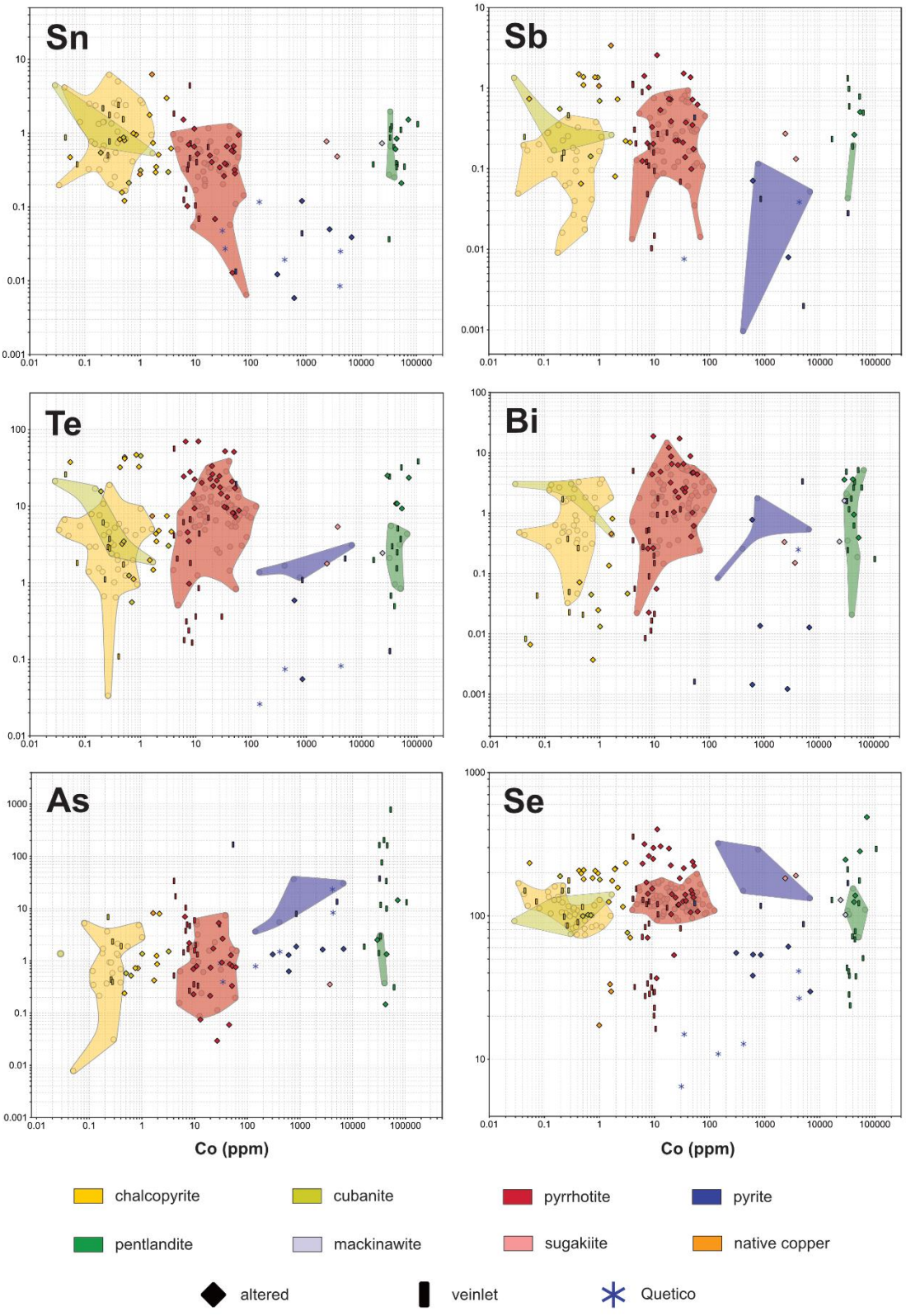

Figure 4.42: Sulfide trace-element binary variation diagrams for elements with representative concentrations and key metal deportments. Diagrams in the left column depict analyses from minerals within the primary assemblage. Data from sulfides in the primary mineralization assemblage are underlain as fields.

Moreover, arsenic contained within pentlandite and pyrrhotite from the crosscutting assemblages is significantly enriched relative to its concentration found in those minerals from the primary mineralization (Fig. 4.42). Selenium occurs within chalcopyrite, cubanite, pyrrhotite, and pentlandite from the primary mineralization assemblage with comparable concentrations around 70 to 180 ppm, while primary pyrite may range to >300 ppm (Fig. 4.42). Sulfides from the altered mineralization assemblage contain Se concentrations that range up to several hundred ppm greater than concentrations in the primary mineralization. This is true except for pyrite, which contains Se concentrations ~50 ppm in the altered assemblage. Selenium concentrations within veinlet sulfides overlap with primary mineralization fields, and occur with lower values in pyrrhotite, pyrite, and pentlandite. However, a few veinlet pentlandite values show slightly higher Se values (~20-100 ppm greater) than pentlandite in the primary mineralization. Pyrite from Quetico metasedimentary country rocks contain on average the lowest Se concentrations of the sulfides analyzed, reaching ~11 ppm (Fig. 4.42).

Pentlandite contains higher concentrations of PGE than the other sulfide minerals. The total TABS and PGE data in pentlandite from Escape are compared to the compositional fields for Ni–Cu and PGE deposits highlighted in Mansur et al. (2021; Fig. 4.43).

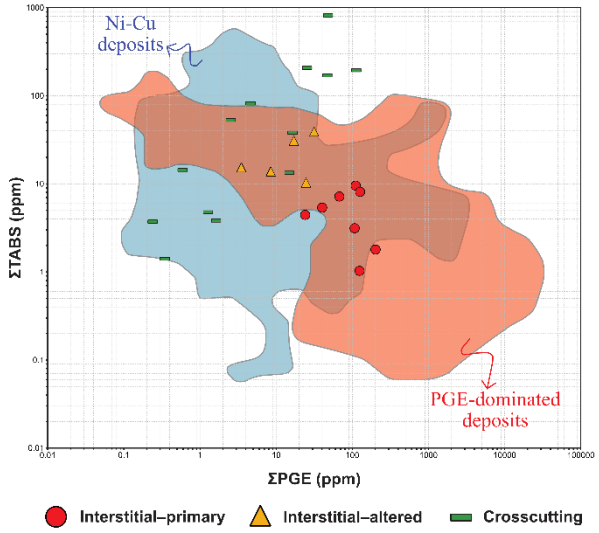

Figure 4.43: Sulfide trace-element binary variation diagram illustrating the sum of platinum-group elements against the sum of TABS (Te, As, Bi, Sn, Sb) elements. Diagram and deposit fields modified after Mansur et al. (2021).

Two trends are illustrated by the Escape data. Compositional data for crosscutting pentlandite exhibit a positive, linear correlation that overlaps significantly with the compositional field for Ni–Cu-dominant magmatic sulfide deposits. Compositional data for interstitial (primary + altered) pentlandite exhibit a negative, linear correlation that overlaps with both the Ni–Cu and PGE-dominated magmatic sulfide deposits (Fig. 4.43).

Primary sulfide mineralization is characterized by Cu/Pd ratios that plot within the mantle range, with the majority of sulfides having S/Se ratios also within the range of mantle values (Fig. 4.44a).

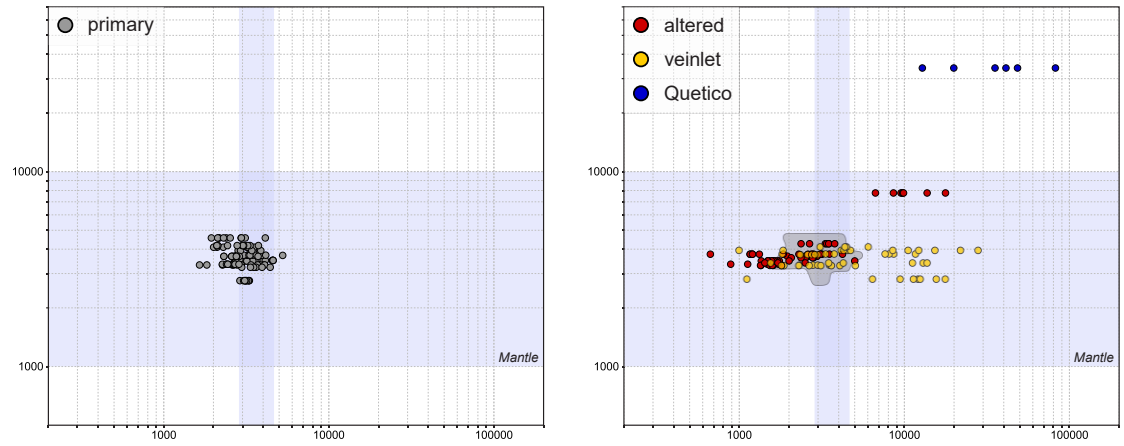

Figure 4.44: Binary variation diagrams illustrating S/Se values of sulfides and whole-rock Cu/Pd values of their corresponding host rocks from Escape. The fields represent the range of mantle values for Cu/Pd (1,000-10,000) and S/Se (2,632-4,350).

Although the mineralization containing altered and crosscutting sulfide assemblages also has mantle-like Cu/Pd ratios, the sulfides are characterized by highly variable S/Se ratios that extend higher and lower than the mantle range (Fig. 4.44b). Most sulfides from the altered assemblage have depleted S/Se values (relative to primary sulfides and mantle), albeit there is a small group of altered sulfides that have elevated S/Se values. The latter group corresponds to sulfides ~90 m below the ore horizon, and lacks chalcopyrite, pentlandite, and PGMs (Fig. 4.44). Sulfides in the crosscutting assemblage have highly variable S/Se that extend to values notably higher than primary sulfides and mantle values (up to 30,000; Fig. 4.44b). Lastly, pyrite within

metasedimentary country rocks has Cu/Pd and S/Se ratios that are systematically greater than mantle values (Fig. 4.44b).

4.4 Sulfur isotopes

The S isotope composition of sulfides in 57 samples were characterized. $\delta^{33}S$, $\delta^{34}S$, $\delta^{36}S$, $\Delta^{33}S$, and $\Delta^{36}S$ values were obtained for pyrrhotite, pentlandite, and chalcopyrite in Escape peridotites, and for pyrite in Quetico schists. The full data set containing each analysis is provided in Appendix E. Variations in $\delta^{34}S$ and $\Delta^{33}S$ are illustrated in Figure 4.45a.

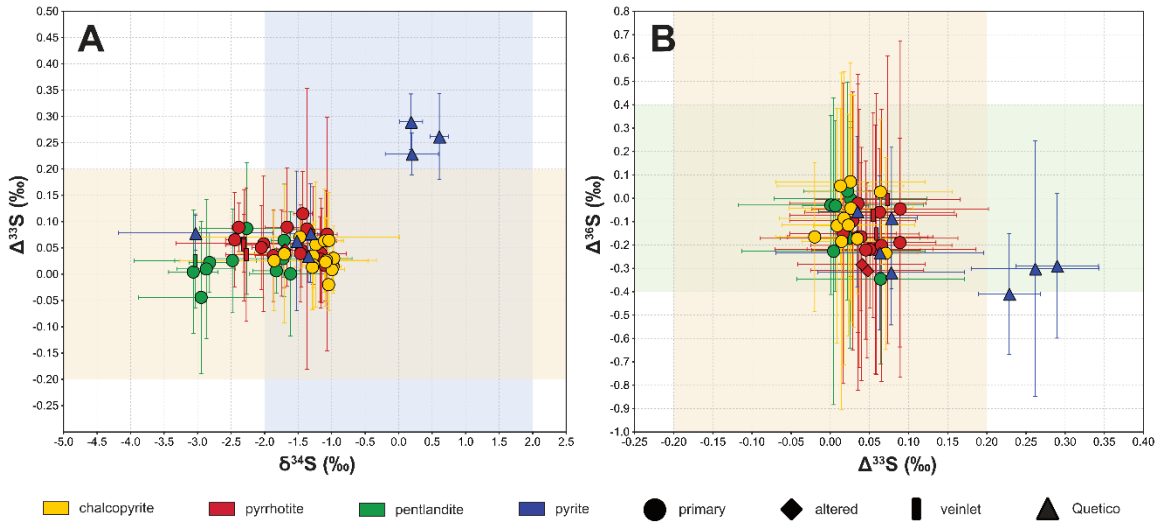

Figure 4.45: S isotope binary variation diagrams for Escape and Quetico sulfides. Error bars are two standard deviations from the mean (2σ). Coloured fields represent mantle ranges for each isotope, with values from Farquhar and Wing (2003) and Ripley and Li (2003).

The Escape sulfides have $\delta^{34}S$ values that range from -3.07 to -0.97‰, while pyrite from the country rocks exhibit a wider range of $\delta^{34}S$ values from around -3.0 to 0.6‰. Most $\delta^{34}S$ values for Escape sulfides fall within the mantle range of 0 ± 2‰ (Fig. 4.45a). The average $\delta^{34}S$ composition of Escape pyrrhotite (n = 23), chalcopyrite (n = 15), and pentlandite (n = 11) is -1.68 ± 0.95‰, -1.23 ± 0.53‰, and -2.40 ± 1.17‰, respectively. The average $\delta^{34}S$ composition of Quetico pyrite (n = 8) is -0.95 ± 2.41‰.

The average $\Delta^{33}S$ composition of Escape pyrrhotite (n = 23), chalcopyrite (n = 15), and pentlandite (n = 11) is 0.05 ± 0.05‰, 0.03 ± 0.05‰, and 0.02 ± 0.07‰, respectively. The $\Delta^{33}S$ values for Escape sulfides fall within mantle range of 0 ± 0.2‰ (Fig. 4.45). The average $\Delta^{33}S$ composition of Quetico pyrite (n = 8) is 0.13 ± 0.22 ‰. Three pyrite samples from the metasedimentary country rocks fall outside the mantle range for $\Delta^{33}S$.

The average $\Delta^{36}S$ composition of Escape pyrrhotite (n = 19), chalcopyrite (n = 12), and pentlandite (n = 7) is -0.17 ± 0.22‰, -0.09 ± 0.20‰, and -0.11 ± 0.28‰, respectively. The $\Delta^{36}S$ values for Escape sulfides fall within mantle range of 0 ± 0.4‰, albeit some error bars extend out of this range (Fig. 4.45b). The average $\Delta^{36}S$ composition of Quetico pyrite (n = 8) is -0.28 ± 0.31‰, and only one value falls outside of the $\Delta^{36}S$ mantle range.

There is a horizontal trend between $\delta^{34}S$ and $\Delta^{33}S$ for Escape sulfides, where the variation in $\delta^{34}S$ is independent of $\Delta^{33}S$. However, metasedimentary $\delta^{34}S$ varies with $\Delta^{33}S$, exhibited by a positive linear trend in the data (Fig. 4.45a). For the Escape sulfides, there is no appreciable trend between $\Delta^{33}S$ and $\Delta^{36}S$ (Fig. 4.45b). However, there is a slight horizontal to negative trend between $\Delta^{33}S$ and $\Delta^{36}S$ for Quetico pyrite, where $\Delta^{33}S$ varies out of mantle range, independently of $\Delta^{36}S$ (Fig. 4.45b).

5 Discussion

5.1 Fractionation history, hydrothermal alteration, and remobilization

The mafic-ultramafic rock-forming minerals and accompanying sulfide mineralization of the peridotite unit of the Escape intrusion exhibit complex textural relationships that record processes related to primary magmatic crystal fractionation/deposit formation, and at least one hydrothermal alteration event with associated secondary sulfide veinlet emplacement. Using petrographic observations of mineral associations and crosscutting relationships, and integrating geochemical data, a general paragenesis of the Escape intrusion was produced, with the sequence divided into three main phases: the primary, mineralization, and hydrothermal phases (Table 5.1).

Table 5.1: Simplified paragenetic sequence of crystallization for the Escape intrusion.

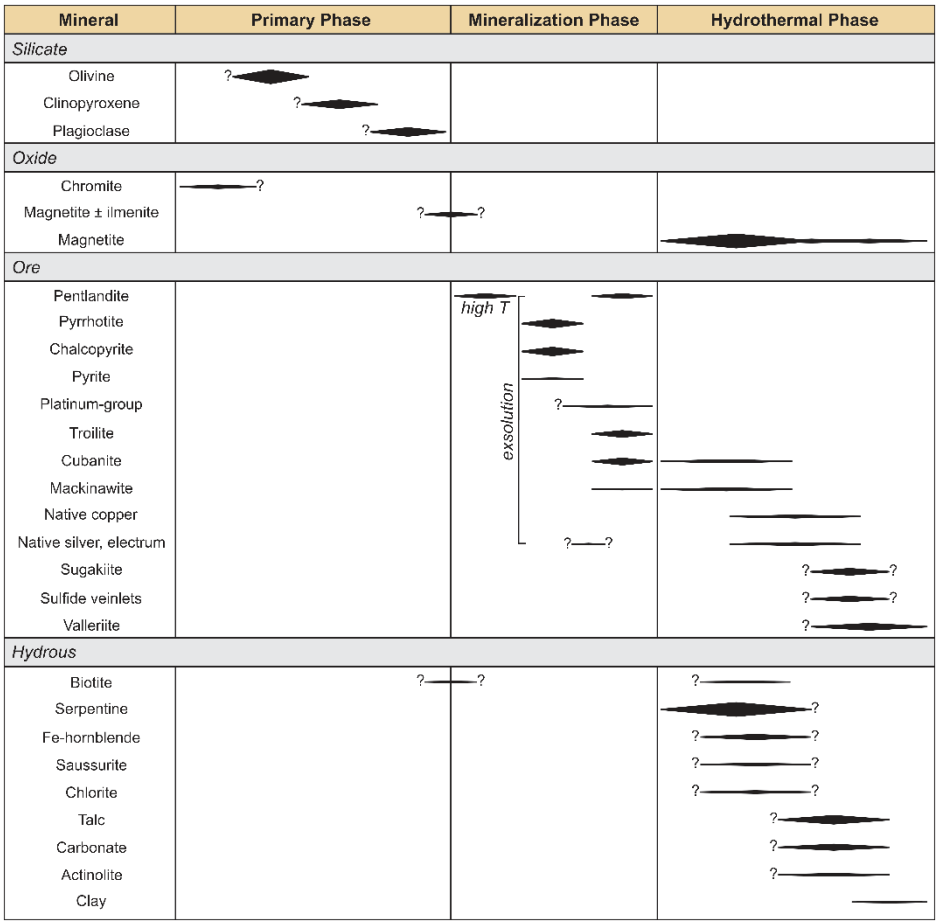

5.1.1 The Primary Phase

The primary phase encompasses the crystallization and accumulation of the primary minerals from the parental magma. The occurrence of chromite as fine-grained chadacrysts, present in almost every phase is indicative of it being the earliest mineral formed during the primary phase. The enclosure of olivine by clinopyroxene is indicative of its later crystallization as the second mineral to fractionate from the silicate melt. Primary olivine ranges from ~85 to 95% of the mode, meaning that the peridotite rocks range from ortho- to mesocumulate in character. The occurrence of plagioclase (and minor Fe-Ti oxides) interstitial to the early formed minerals indicates it was the final mineral(s) to crystallize during this phase. Petrographic evidence of wide size variation in cumulus olivine (e.g., Fig. 4.4 versus Fig. 4.19), and the variable abundance of interstitial plagioclase (i.e., the feldspathic versus non-feldspathic rock types in Fig. 4.3) is consistent with the repeated injection of fractionated crystal mushes within the Escape conduit.

5.1.2 The Mineralization Phase

Upon S-saturation and segregation from the silicate melt, an immiscible sulfide liquid can coexist in the magma chamber at high temperatures (Naldrett, 2011). This segregated sulfide liquid would behave according to phase relations of the Fe–Ni–Cu–S system as determined by experimental studies (Li et al., 1995; Mungall et al., 2005; Liu and Brenan, 2015; Duran et al., 2017). Upon cooling, the sulfide liquid follows a defined fractionation and exsolution sequence, with the first phase to crystallize around 1000°C being monosulfide solid solution (MSS), a "pyrrhotite-like" sulfide mineral (Craig and Vaughan, 1994; Holwell and McDonald, 2010). Various base metals, PGE, and semimetals partition into this newly formed phase, with the remaining elements in the system remaining in the residual Cu-rich sulfide liquid. As the system continues to cool, another high-temperature sulfide mineral crystallizes from the residual liquid around 900°C — intermediate sulfide solution (ISS). This leaves behind a PGE and semimetal

rich residual liquid, which will eventually form discrete platinum-group minerals (PGM) once the system fully cools and reaches equilibrium. In some natural systems, MSS and ISS phases may be preserved at low temperature in situ, but most often they recrystallize to the stable sulfides pyrrhotite + pentlandite in the case of MSS, and chalcopyrite (and then ± cubanite) in the case of ISS (Holwell and McDonald, 2010; Mansur et al., 2021). Monosulfide solid solution and ISS have not been identified within the Escape intrusion, however, it is likely that the segregated sulfide liquid fractionated these phases at some point near the end of the primary phase and into the start of the mineralization phase, given that the main sulfide assemblage consists of pyrrhotite, pentlandite, and chalcopyrite (Holwell and McDonald, 2010; Mansur et al., 2021). The occurrence of sulfides interstitial to the silicate minerals suggests that their crystallization postdates the host silicate minerals. Therefore, the mineralization phase mostly constitutes the exsolution of sulfide minerals from the earlier formed high-temperature MSS and ISS minerals (Table 5.1). The fact that pentlandite is commonly found at the interface between pyrrhotite and chalcopyrite supports its formation at high temperature via peritectic reaction between MSS and Cu-rich residual liquid (Mansur et al., 2021). This type of pentlandite is clearly visible in Figure 4.13b within the massive sulfide lens. Thus, pentlandite was likely the first sulfide mineral to reach equilibrium within the interstitial sulfide assemblage.

Between 650-350°C (Mansur et al., 2021), crystallization of high-T pentlandite was followed by the exsolution of massive pyrrhotite and flame pentlandite (with minor euhedral pyrite) from MSS, and chalcopyrite from ISS. At this point, composite grains of platinum-group minerals (PGM) also crystallized from the residual sulfide liquid that was present between the interstices of earlier formed sulfide crystals, forming angular to subhedral phases such as sperrylite (Fig. 4.33a-b). The elongate habit of PGMs, such as michenerite and mitrofanovite (Fig. 4.33c-d), may be evidence of their exsolution from MSS/pyrrhotite in a cooling magmatic sulfide system, as suggested by Mansur et al. (2021). Moreover, it has been suggested by Mansur et al.

(2021) that high concentrations of PGE and TABS (the group of chalcophile semimetals Te, As, Bi, Sb, and Sn) in pentlandite can create a chemical potential for exsolution of discrete PGM. Figure 5.1 illustrates the resulting trace element signature from this process in pentlandite analyses from Escape peridotites.

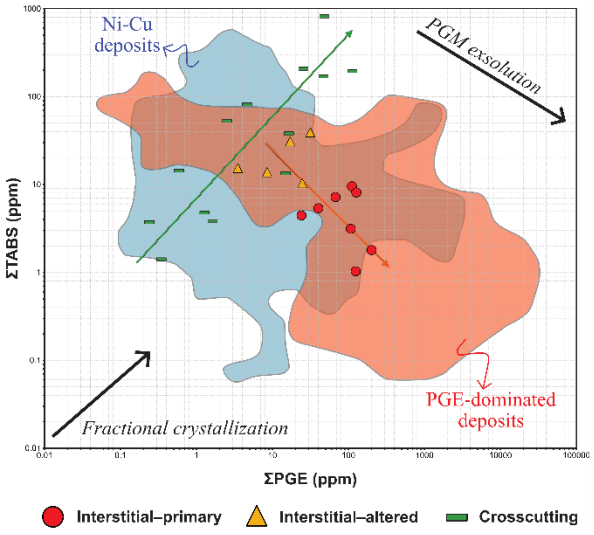

Figure 5.1: Annotated sulfide trace element binary variation diagram illustrating the sum of platinum-group elements against the sum of TABS (Te, As, Bi, Sn, Sb) elements in pentlandite. Explanation: circles — interstitial–primary; triangles — interstitial–altered; rectangles — crosscutting veinlets. Diagram modified after Mansur et al. (2021).

The negative trend shown by pentlandite from the primary and altered interstitial assemblages on Figure 5.1 can be explained by the partitioning of abundant PGE into sulfides. With a high concentration of PGE and TABS (the group of chalcogen semimetals Te, As, Bi, Sb, and Sn) in pentlandite (more than the mineral can accommodate in its crystal lattice), the elements will exsolve as discrete PGMs, depleting pentlandite of TABS as they are more readily exhausted than PGE when forming PGM, leaving Pd enriched within pentlandite (typically ≥100 ppm; Mansur et al., 2021). The positive trend shown by veinlet pentlandite may be explained by fractional crystallization of a separate sulfide liquid, such that PGE and TABS are effectively enriched as the sulfides crystallize, albeit there is never a large enough concentration of PGE to begin with to drive chemical potential for PGM exsolution in these sulfide veinlets, and Ni-Cu sulfide deposits in general (Mansur et al., 2021). The separation of these two trends suggests that the two styles of

mineralization (interstitial versus crosscutting) formed via different processes and at separate times. Moreover, the sulfides within the veinlets do not exhibit equilibrium textures characteristic of primary magmatic sulfide deposits, consistent with a distinct origin to the event that produced the interstitial sulfides.

During fractionation of the sulfide liquid, Ag typically partitions into the Cu-rich liquid after the formation of MSS (Mansur et al., 2021). Therefore, it is possible that native silver found enclosed in chalcopyrite at Escape crystallized (or exsolved) as a discrete phase at the same time as composite grain PGM crystallization. Lastly, upon further cooling (at temperatures of >210°C – a temperature range synthesized from various experimental data on the cooling behaviour of magmatic sulfides presented in Mansur et al., 2021), multiple mineral exsolutions occurred. Troilite exsolved from pyrrhotite, cubanite exsolved from chalcopyrite, and trace mackinawite worms exsolved from chalcopyrite and pyrrhotite.

5.1.3 The Hydrothermal Phase

The hydrothermal phase constituted a period (or likely periods) of alteration of the Escape intrusion. Following crystallization of the cumulate pile and sulfide mineralization, low-temperature, percolating deuteric (with the possible addition of external) fluids reacted with olivine to produce serpentine-group minerals, typically resulting in mesh-textures through fractures in olivine. Serpentine is replaced by several other minerals which suggests that it is one of the first, if not the first hydrous mineral to form during the hydrothermal phase. This reaction also produced abundant, very to ultra fine-grained, anhedral magnetite that occupies olivine fractures, as the ferrous iron from olivine cannot be accommodated due to low silica activity lowering the stability of the $Fe_3Si_2O_5(OH)_4$ component in serpentine (Frost and Beard, 2007). Concurrent with serpentinization, the formation of amphibole after clinopyroxene and saussuritization occurred. The serpentinization of olivine likely proceeded according to the following reaction (after Andreani et al., 2007):

$$6(Mg,Fe)_2SiO_4 + 7H_2O \rightarrow 3(Mg,Fe)_3Si_2O_5(OH)_4 + Fe_3O_4 + H_2 \qquad eq.5.1$$

$$olivine + hydrothermal\ fluid \rightarrow serpentine + magnetite + hydrogen$$

It is proposed that the alteration of plagioclase to chlorite also occurred during the hydrothermal phase; previous workers have documented chlorite alteration of plagioclase to be associated with progressive serpentinization of peridotites (Beard et al., 2009). Biotite occurring at the interface between primary silicate and sulfide minerals may be the result of hydrothermal fluids circulating between fractures in these minerals. However, the possibility of primary biotite forming from the silicate melt within the remaining interstitial space during the later stages of crystallization remains. A possible explanation for the formation of native copper found in the deposit is that the infiltrating hydrothermal fluids were able to react with the recently produced aqueous hydrogen from serpentinization to bring about the desulfurization of chalcopyrite (based on a similar reaction in pentlandite from Schwarzenbach et al., 2014; 2021):

$$3CuFeS_2 + 4H_2O + 2H_2, aq \rightarrow 3Cu + Fe_3O_4 + 6H_2S, aq \qquad eq.5.2$$

$$chalcopyrite + hydrothermal\ fluids + hydrogen \rightarrow native\ copper + magnetite + hydrogen\ sulfide$$

This reaction is consistent with the intimate association & intergrowth of native copper with magnetite within the interstitial–altered assemblage (Fig. 5.2).

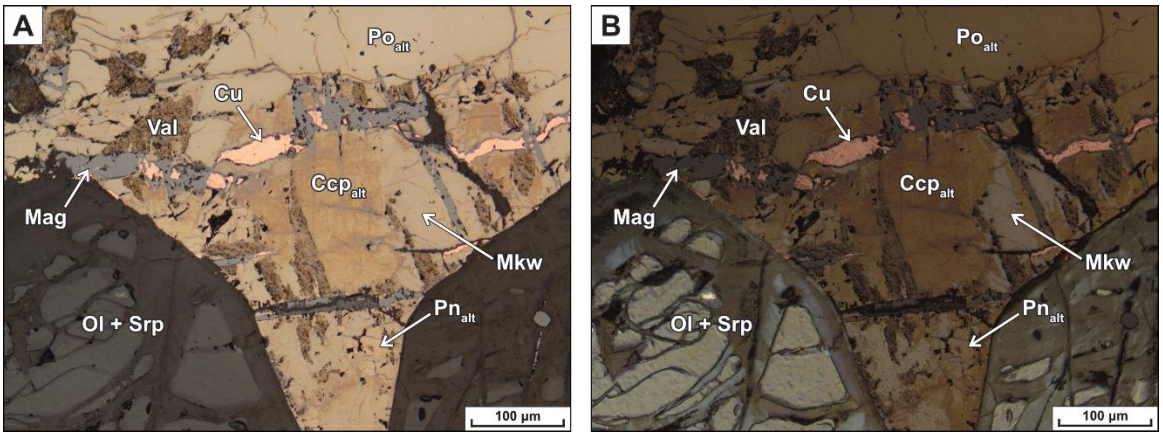

Figure 5.2: Representative photomicrographs of native Cu intergrown with magnetite within fractures/veins in sulfides from the interstitial–altered (disseminated) sulfide assemblage. Sample CAM-21-CC-005 from drillhole ELR20-025, taken above the ore horizon at 358.1m depth corresponding to low metal grade (A – PPL; B – XPL). Abbreviations: Ccp_{alt} – altered chalcopyrite; Cu – native copper; Mag – magnetite; Mkw – mackinawite; Ol – olivine; Pn_{alt} – altered pentlandite; Po_{alt} – altered pyrrhotite; Srp – serpentine; Val – valleriite.

This possibly explains why the proportion of magnetite within the interstitial–altered assemblage is much greater than in the preserved interstitial–primary assemblage (Fig. 4.36). Moreover, the magnetite and the fractures in sulfides consistently align with fractures/serpentine infill found within altered silicate minerals. This may suggest that serpentine-producing fluids passed through the groundmass and sulfides continuously, reacting with the different minerals as the system progressed. A similar process has been invoked for hydrothermal fluids that migrated through cracks in sulfides from serpentine veins in the Huangshandong magmatic Ni–Cu sulfide deposit (Wang et al., 2021). This reaction may also explain the association between native copper and silver seen in Figure 4.34a,c. The Ag concentrated in Cu-Fe sulfides (as illustrated in Fig. 4.42) could have also been liberated during desulfurization, producing intergrowths of Ag, Cu and magnetite (Fig. 4.34). Copper was likely particularly mobile during the hydrothermal phase given the presence of several other Cu-bearing secondary phases within the interstitial–altered assemblage in addition to the native Cu, including sugakiite, Cu-bearing mackinawite and pyrrhotite, and valleriite. The occurrence of these various Cu-bearing secondary sulfides suggests that the hydrothermal fluids present during this phase were significantly reducing to allow for breakdown of chalcopyrite (e.g., Schwarzenbach et al., 2014; Evans et al., 2023). In particular,

after native Cu was liberated from chalcopyrite, it subsequently could have reacted with existing sulfides to produce the secondary Cu-bearing sulfide minerals, such as sugakiite (e.g., Ikehata and Hirata, 2012; Schwarzenbach et al., 2014). It has been shown that mackinawite may form during serpentinization by the replacement of pentlandite or desulfurization of pyrrhotite due to late circulating low-temperature fluids through brittle faults, at low fO_2 and increasing fS_2 conditions (Delacour et al., 2008). The alteration of pentlandite to mackinawite at Escape likely occurred at a similar time as the remobilization of Cu as several SEM analyses of mackinawite indicate substitutions of Cu in the crystal lattice (as was also the case for altered pyrrhotite with Cu-rich zones; Fig. 4.21a).

To account for the range of alteration minerals present in the Escape intrusion, requires generation of a redox gradient that caused the prevailing conditions to transition from reducing serpentinization to oxidizing conditions over time, promoting talc–carbonation of the Escape rocks (e.g., Schwarzenbach et al., 2014). At this time, serpentine was replaced by talc + carbonate, chlorite by actinolite, and the intermittent sulfide (± carbonate) veinlets were possibly emplaced (Fig. 4.11). Figure 4.24c-d shows valleriite which is pseudomorphed after biotite suggesting that valleriite formed as one of, if not the last ore mineral in the paragenesis of the deposit. Valleriite is commonly formed by the reaction of hydrothermal fluids with serpentine and biotite in the presence of chalcopyrite (Mücke, 2017). The exact timing of sulfide alteration in the interstitial–altered mineralization is difficult to resolve, but it is possible that multiple replacements/modifications occurred during the hydrothermal phase, as conditions changed from reducing to more oxidizing.

Within the Escape intrusion, different locations exhibit different alteration assemblages (i.e., above the ore horizon as in Fig. 5.2, lateral from the ore horizon as in Fig. 4.23, well below the ore horizon as in Fig. 4.25). Within the ore horizon and net-textured mineralization, little to no alteration of sulfides occurred, with the intensity of sulfide alteration increasing with distance

away from the high-grade zone. For example, the occurrence of sugakiite laterally distal from the net-textured sulfides is indicative of metasomatic adjustment of pentlandite and chalcopyrite (Kitakaze, 2008), whereas sulfides in the strongly disseminated assemblages proximal to the net-textured sulfides record only minor alteration of chalcopyrite to cubanite, magnetite from desulfurization of sulfides, and minor mackinawite worms (e.g., Fig. 4.20). It is possible that the low relative abundance of cumulus olivine in the net-textured ores meant that there were limited fracture pathways for migration of hydrothermal fluids which acted to insulate the net-textured sulfides, protecting them from the downgrading of metal tenor apparent in some of the interstitial–altered disseminated assemblage (e.g., Pd in Pn illustrated in Fig. 4.42).

5.1.4 Whole-rock and sulfide geochemistry

The elemental ratios of Cu/Pd and S/Se are important tools for identifying the conditions of formation of magmatic sulfide mineralization and their subsequent modification. The Cu/Pd ratio may be used as a proxy for the ratio between the segregated sulfide liquid and silicate melt (R factor) in which the mineralization formed, but also as an exploration tool for the presence of significant PGE-mineralization (Barnes et al., 1993; Barnes and Ripley, 2016). In particular, Cu/Pd ratios in whole-rock data that are greater than mantle values may be indicative of magmas depleted in Pd, potentially due to removal of sulfides that have already scavenged PGE from the parental magma (Barnes et al., 1993). This implies that PGE-enriched sulfide mineralization may be present either at greater depths, or upstream from the sampling area, in the case of magmatic sulfide deposits generally. In contrast, Cu/Pd ratios near mantle values may be indicative that the sampled magmatic sulfide mineralization has potential for PGE as a by-product of deposit extraction, and Cu/Pd ratios lower than mantle values may indicate significant economic concentrations of PGE mineralization due to metal upgrading at high R factors (Barnes et al., 1993). The S/Se ratio may be used to interpret R factor changes, S loss from oxidation, contamination by external S/Se source with non-mantle values, and remobilization of primary

sulfides (Brzozowski et al., 2020). This is possible for the following reasons: mantle S/Se values are well constrained, S and Se behave similarly during partial melting of the mantle, Se readily partitions into the sulfide liquid, and Se tends to behave differently than S during hydrothermal alteration (e.g., S is more readily mobile; Brzozowski et al., 2020). Therefore, by utilizing these two ratios, we can investigate the processes that influenced the formation and post-magmatic modification of magmatic sulfide mineralization at Escape. Figure 5.3 illustrates the difference between interstitial–altered, crosscutting, and interstitial–primary mineralization styles in S/Se versus Cu/Pd space for all sulfide species.

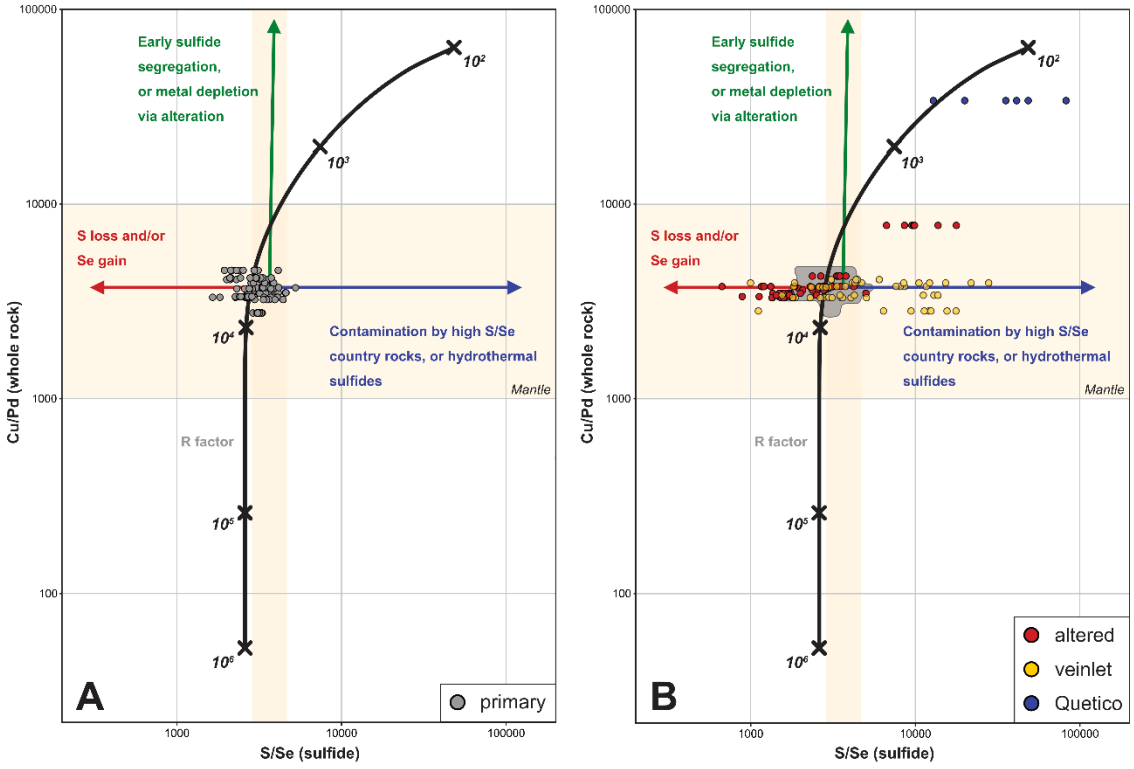

Figure 5.3: Annotated binary variation diagrams illustrating the S/Se values of Escape sulfides and whole-rock Cu/Pd values of their corresponding host rocks with model curves of these element ratios as a function of R factor variations. The beige fields represent the range of mantle values for Cu/Pd (Barnes et al., 2015) and S/Se (Eckstrand and Hulbert, 1987; Palme and O'Neil, 2014). The grey field in B represents the primary sulfide values shown in A. The green arrow indicates possible variations due to sulfide segregation or metal depletion from hydrothermal alteration. The red arrow indicates possible variations due to S loss, or Se gain through hydrothermal processes. The blue arrow indicates possible variation due to contamination by high S/Se rocks, or formation of sulfides by hydrothermal fluids. Model calculations after Ripley and Li (2003), and diagram after Brzozowski et al. (2020).

The two trends of decreased S/Se (red – altered) and elevated S/Se (yellow – veinlet) relative to primary sulfides may be explained via hydrothermal activity post-magmatism and/or localized crustal contamination in the Escape conduit. Whereas the trend seen in the interstitial–altered sulfides, may be explained by subsolidus S loss during alteration. The desulfurization of sulfides is responsible for the ubiquity of magnetite in the interstitial–altered assemblage, as was partly outlined regarding the breakdown of chalcopyrite in *Equation 5.2* above. Sulfur is commonly believed to be more mobile than Se during alteration under hydrothermal conditions (Prichard et al., 2013; Queffurus and Barnes, 2015). Moreover, it is commonly understood that Se readily substitutes for S in the base-metal sulfide structure (Prichard et al., 2013). Therefore, combining these assumptions with the evidence that sulfur was removed, the increase in Se relative to primary sulfides is likely the result of Se being retained in the remaining sulfides, while S was preferentially mobilized. While the total volume of sulfide decreases, the mass of Se remains the same. This would create a trace-element signature that shows elevated Se concentrations in the altered sulfides relative to primary (Fig. 5.4), as the sulfides have effectively concentrated Se over S during hydrothermal modification.

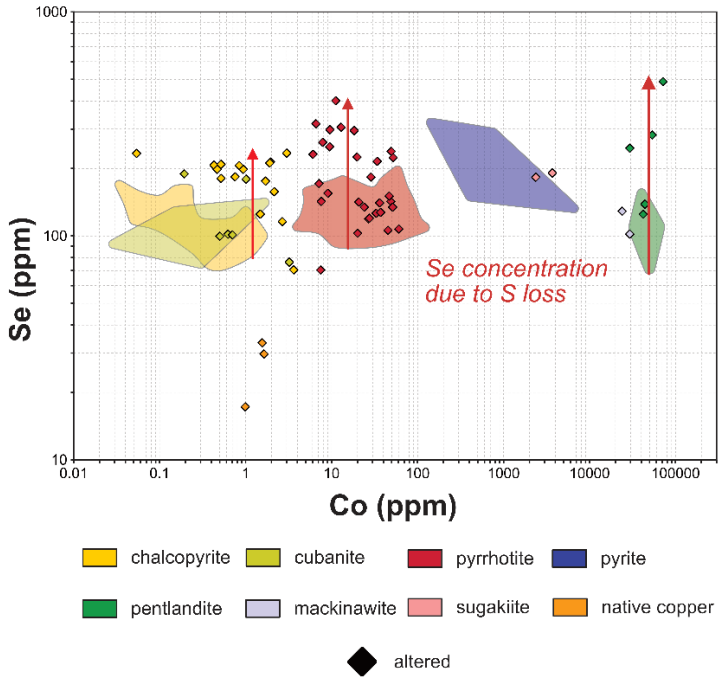

Figure 5.4: Annotated sulfide trace element binary variation diagram illustrating difference in Se concentration between the primary mineralization (underlain fields) and sulfides within the altered assemblage. The red arrows illustrate the trend of Se concentration resulting from S loss during alteration of the primary mineral assemblage.

An alternative explanation for the elevated Se concentrations in altered sulfides would be that Se was released during the desulfurization process, remobilized within the hydrothermal fluid, and subsequently diffused into the adjacent preserved sulfides. This is similar to the remobilization process proposed by Prichard et al. (2013) to explain the occurrence of Se-bearing platinum-group minerals within the altered mineralization in the Jinchuan intrusion.

There are two possible explanations for the sulfide veinlet S/Se trend that extends to the right of primary sulfides (Fig. 5.3b). It is possible that S/Se signature in these sulfides were derived from pyrite in the metasedimentary country rock. High S/Se values can be indicative of addition of significant crustal S, as this would change the mantle S/Se signature (Queffurus and Barnes, 2015). Thus, there is the possibility that sulfur saturation due to local crustal contamination generated a secondary sulfide melt. The formation of a secondary segregated sulfide liquid late in the life of the magma conduit could explain the fact that the crosscutting veinlets show a trend consistent with minimal metal upgrading, as PGE would have already been

scrubbed from the chamber, and also there would be less magma to interact with. This lack of enrichment is consistent with the pure fractional crystallization trend shown by veinlet sulfides in Figure 5.1. Moreover, it has been shown that during compaction of partially molten cumulate piles that interstitial liquid can be squeezed out and permeate through the cumulate pile (Meurer and Boudreau, 1996), and that sulfide liquids can infiltrate and travel hundreds of metres upwards within the cumulate pile (Mungall, 2002). Thus, the emplacement of a secondary sulfide melt as a result of late S saturation at the base of the Escape intrusion may have occurred. This model would mean that the crosscutting sulfides did not form during the hydrothermal phase, but rather during late stages of magmatism and concurrent with the primary mineralization phase.

The second scenario that may explain the formation of these crosscutting sulfides is due to hydrothermal fluids. The fact that the sulfide veinlets crosscut the cumulate groundmass and do not record extensive alteration like the interstitial–altered assemblage (e.g., lack of native Cu), suggests that they were emplaced after the silicate minerals crystallized when reducing conditions during serpentinization were prevalent. Moreover, their frequent association with talc and carbonate mineralogy (e.g., Fig. 5.5) suggests that these sulfide veinlets were produced after the redox change during talc–carbonation of the peridotites in the hydrothermal phase.

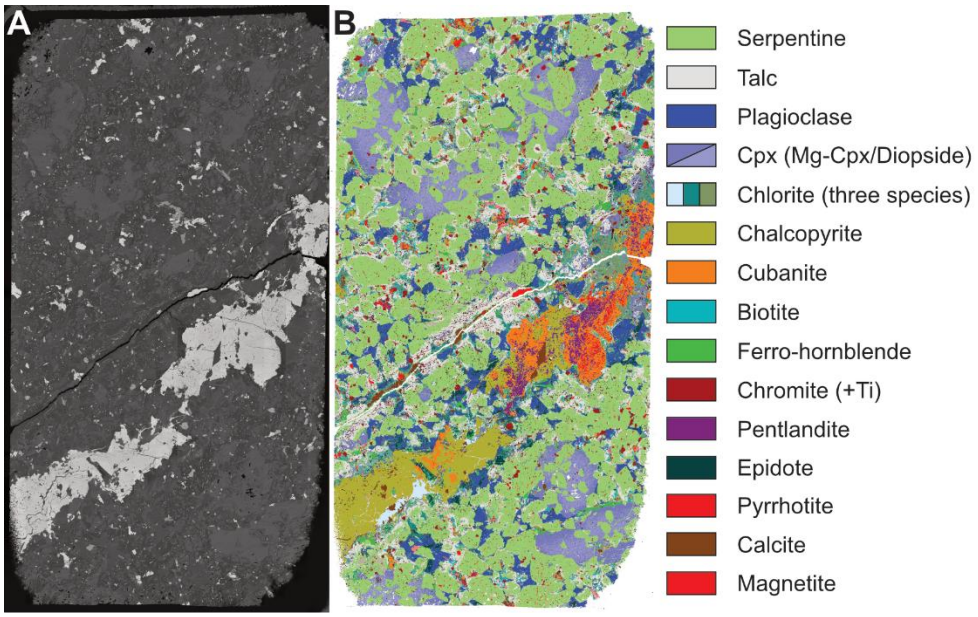

Figure 5.5: MLA scans of polished thin section CAM-21-CC-060 from drillhole ELR20-015, illustrating mineral abundances by area % for a discontinuous sulfide (Type II) veinlet. A – back-scattered electron image. B – false colour EDS library-matched minerals mapped to BSE image. Minerals are listed in order of decreasing abundance in the legend. Minerals representing <1% of the area are omitted. Note the intimate association of sulfide minerals with calcite and talc.

Another line of evidence that supports these veinlets being the result of hydrothermal fluids is the arsenic present within the sulfide veinlets. Arsenic is a slightly chalcophile element that is less readily available in silicate magmas than crustal rocks (Mansur et al., 2021). Primary PGM formed from the crystallization of a magmatic sulfide liquid are commonly As-bearing (Barnes and Ripley, 2016). However, magmatic sulfide deposits tend only to be abundant or enriched in arsenic when the parental melt has assimilated As-rich country rock, which influences the types and amount of PGMs that form (Barnes and Ripley, 2016). At Escape, there are elevated As concentrations in base-metal sulfides found within the veinlets compared to primary sulfides (see As in Fig. 5.6), and multiple unique arsenides and sulfarsenides (e.g., palladoarsenide, nipalarsite, and cobaltite–gersdorffite) were identified within several crosscutting sulfide veinlets, but not within the interstitial–primary or altered sulfide assemblages. This is suggestive of late-stage addition of As to the system, as the primary sulfides contain orders of magnitude lower As than the sulfides within the crosscutting assemblage. Tabelin et al. (2012) experimentally determined that hydrothermal fluids can effectively leach As from pyrite in metasediments via

oxidation. It is possible that the As within the Escape sulfide veinlets was sourced from pyrite in the Quetico metasedimentary rocks by interaction with fluids during the hydrothermal phase. This possibility is similar to the model proposed for the Cliff chromitites of the Shetland Ophiolite Complex, Scotland, where hydrothermal fluids leached As from nearby metasediments (O'Driscoll et al., 2018).

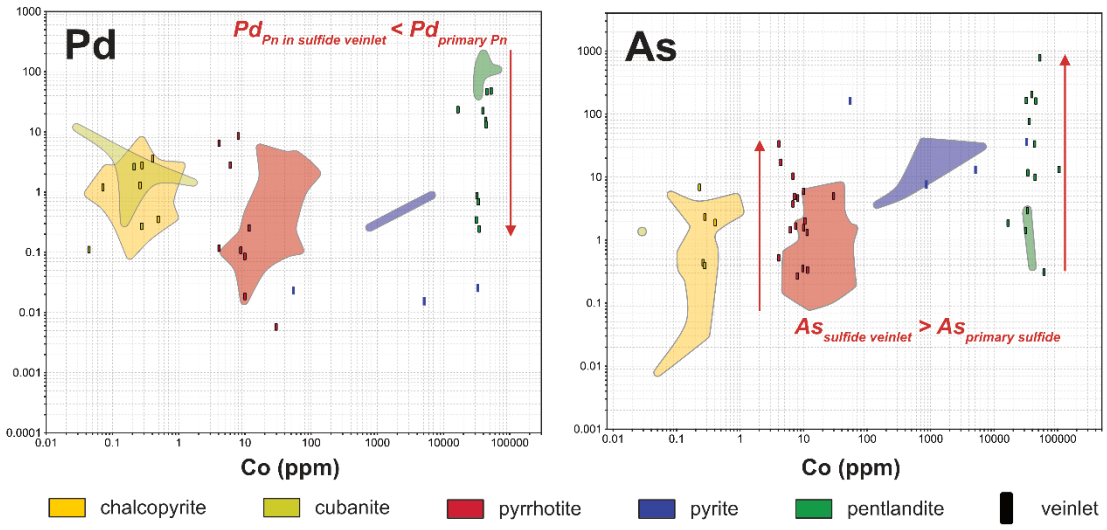

Figure 5.6: Annotated sulfide trace element binary variation diagram illustrating the difference in Pd and As concentration in ppm between primary sulfides (underlain as fields) and sulfide minerals within the crosscutting assemblage.

Whatever the amount of Pd present within the proposed hydrothermal fluids that formed these sulfide veinlets, it did not partition into the sulfide minerals as was the case in the sulfide liquid that segregated from the Escape parental magma. Palladium illustrates this, as pentlandite from the crosscutting assemblage contains significantly less Pd than pentlandite present within the primary mineralization (Fig. 5.6). This suggests that Pd did not preferentially partition into base-metal sulfides within the veinlets, as it did for the interstitial–primary sulfide mineralization at Escape. Experimental studies have determined that Pt and Pd can be remobilized through bisulfide complexation, under reducing conditions (such as during serpentinization of ultramafic rocks), at low to high temperatures for geologically reasonable sulfide concentrations (Wood and Mountain, 1989; Wood et al., 1994). Therefore, it is possible PGE were dissolved in hydrothermal

solution during breakdown of sulfide minerals in the Escape deposit. This provides a plausible explanation for the transportation and source of metals within the crosscutting sulfide veinlets. Hydrothermal remobilization of primary magmatic PGE to form As-rich PGMs is uncommon but has been proposed for other deposits. Almeida et al. (2007) determined that the Ni–Cu–PGE sulfide mineralization from the Fortaleza de Minas deposit was remobilized by reduced, neutral to alkaline pH, carbonic fluids, which precipitated PGE tellurides and arsenides in veins. Kiseleva et al. (2019) suggested that base metals and PGE were remobilized and deposited as nickel arsenides and As-Sb PGMs during serpentinization, due to an inversion from reducing to oxidizing conditions within chromitites. Lastly, Raič et al. (2015) suggested remobilization and re-deposition of PGE as As-rich PGM occurred due to a late-stage hydrothermal event in which bisulfide complexes carried the PGE into veins in the footwall of the Wetlegs deposit within the Partridge River intrusion (Duluth Complex). In summary, it is possible that as the hydrothermal system at Escape moved to more oxidizing conditions and shifted toward talc–carbonation of the host rocks, that a metal- and As-rich, bisulfide-complexed hydrothermal fluid deposited sulfide veinlets within mm-scale fractures throughout the intrusion, but in particular proximal to the ore horizon.

5.2 Source, contamination, and enrichment

To generate a magmatic sulfide deposit, sulfur saturation of a parental mafic–ultramafic magma sourced from a high-degree PGE-undepleted partial melt of the mantle is required (Barnes and Lightfoot, 2005; Mungall, 2014). The introduction of, and contamination by, crustal material (Quetico metasedimentary and granitoid country rocks in the case of the Escape intrusion) into the silicate magma is a common mechanism invoked for initiating sulfur saturation (Naldrett, 1997; Naldrett, 1998; Naldrett, 2011; Barnes and Lightfoot, 2005; Barnes et al., 2015; Barnes and Ripley, 2016). The addition of S-rich or silica-rich rocks may bring about saturation by increasing

the overall abundance (and ratio) of sulfur in the silicate magma, such that it is no longer soluble in the melt, or may lower its ability to dissolve sulfur in the melt, respectively (Ripley and Li, 2003; Naldrett, 2011). The source of the Escape parental magma, its relation to other Midcontinent Rift-related intrusions in the area, and the effect of potential crustal contamination on the Escape parental magmas can be investigated using whole-rock trace element and sulfide S-isotope signatures.

5.2.1 Whole-rock geochemistry

When compared to other MRS-associated Ni–Cu–PGE-mineralized mafic–ultramafic intrusions (e.g., the Disraeli, Hele, and Kitto intrusions), the intrusive units at Escape display an enriched LREE and fractionated HREE trace-element signature similar to these intrusions (Fig. 5.7).

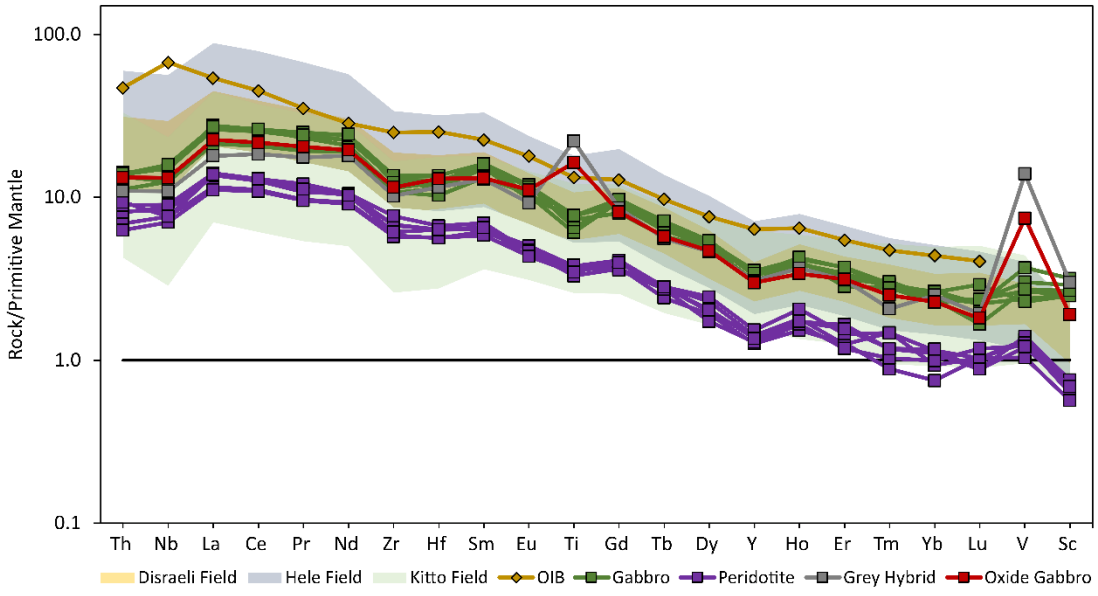

Figure 5.7: Primitive mantle-normalized spidergrams for Escape intrusive rocks, with fields from select MRS intrusions. Intrusive field data from Cundari et al. (2021) and OIB + normalizing values from Sun and McDonough (1989).

The gently sloping negative pattern (similar to ocean island basalt, OIB; Fig. 5.7; Sun and McDonough, 1989) is shared amongst all of the intrusions and is consistent with the model that the Midcontinent Rift System (MRS) and associated magmatism formed via an upwelling mantle

plume (Cannon and Hinze, 1992; Nicholson et al., 1997; Hollings et al., 2007; 2010; 2021). Although recent Os isotope data has suggested that not all MRS-related magmatism was derived from a mantle plume, and that some of the ultramafic intrusions and sills were derived from an enriched subcontinental lithospheric mantle (SCLM; Brzozowski et al., 2023). Regarding the similarities between the Escape intrusive rocks, the overlying gabbro unit (as well as oxide gabbro and grey hybrid) has a similar pattern to the peridotite unit although it has higher overall trace element abundance, which can be explained by crystal fractionation of the parental melt to form the gabbro unit. A feature of note within the trace-element signature of the overlying Escape intrusive units are the positive Ti and V anomalies in the oxide gabbro and grey hybrid. Both anomalies may be explained by strong partitioning of these elements into Fe–Ti oxides, which occur in greater abundance in the grey hybrid and oxide gabbro relative to the gabbros and peridotites that they overlie (e.g., Fig. 4.2).

Heavy rare earth elements (HREE) have very high distribution coefficients with respect to garnet (Kato et al., 1988; Ohtani et al., 1989). At approximate depths greater than 70 km in Earth's mantle, garnet and clinopyroxene are key minerals that resist partial melting. The Gd/Yb_n ratio represents the slope of the HREE on a normalized trace element diagram, with a negative slope (high ratio) indicative of HREE depletion (fractionation). As previously suggested by Jayananda et al. (2008) and Wang et al. (2019), the elevated Gd/Yb_n values shown in the trace-element signature of the Escape mafic–ultramafic rocks is supportive of a deep mantle source in the garnet stability field for these rocks (Fig. 5.8).

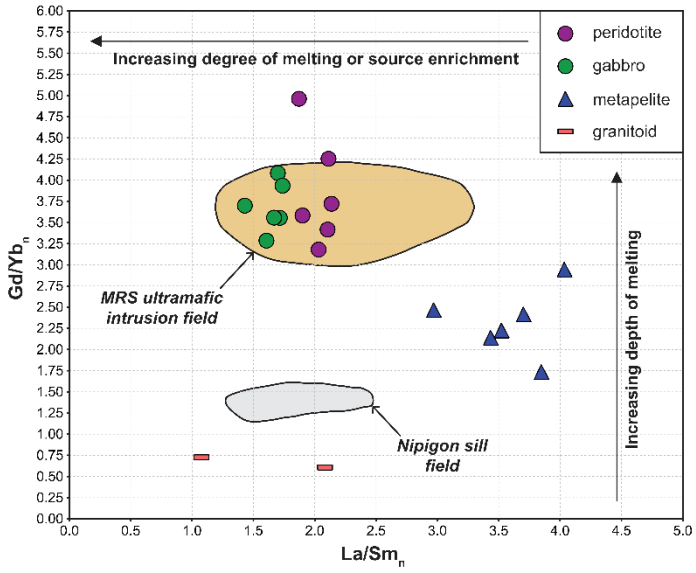

Figure 5.8: Annotated, chondrite-normalized, whole-rock trace-element binary variation diagram for Escape intrusive and country rocks with overlain annotations. Normalizing values from Sun and McDonough (1989). Arrow interpretations from Dasgupta et al. (2019). Midcontinent Rift System (MRS) fields from Hollings et al. (2021).

The possibility of contamination of the Escape parental magma by bulk assimilation of Quetico country rock may be assessed by comparison of their LREE signatures. Given that LREE are relatively incompatible and prefer the liquid phase, it follows that they will be preferentially enriched in partial melts. Therefore, a partial melt generated from Quetico country rocks will be enriched in LREE, which would then be reflected in the magma it was assimilated by (i.e., Escape). Hollings et al. (2007) demonstrated that most MRS-related magmas underwent contamination, with the ultramafic intrusions exhibiting the least amount of crustal assimilation and the closest trace-element signatures to OIB. The main markers of crustal contamination amongst the trace elements in the MRS intrusions were enriched LREE and a pronounced negative Nb anomaly; this signature is clear in the pattern for Quetico metasedimentary rocks (Fig. 5.9).

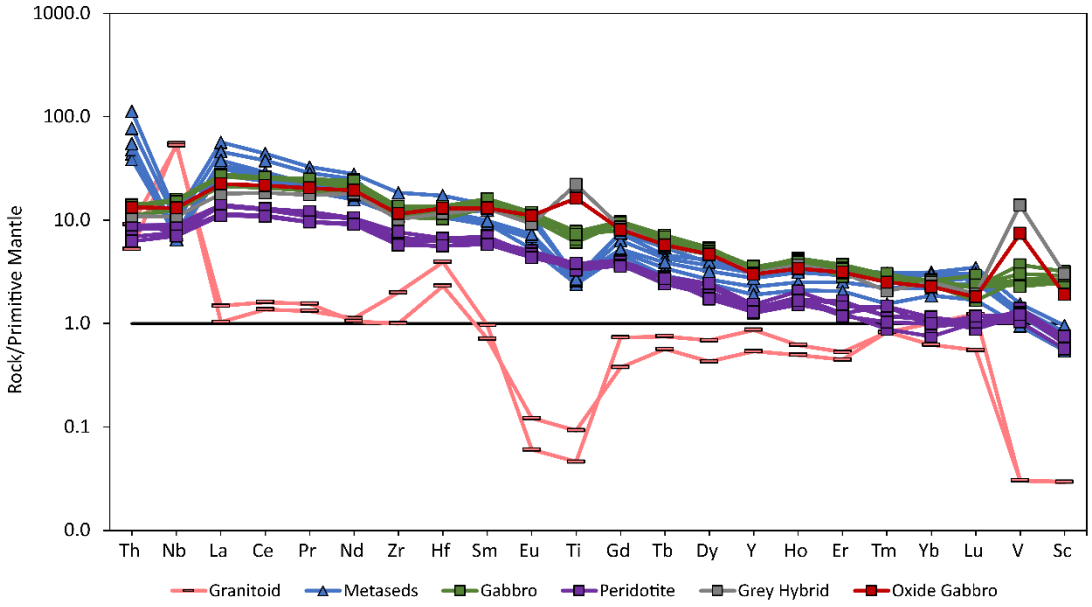

Figure 5.9: Primitive mantle-normalized spidergrams for Escape intrusive and country rocks. Normalizing values from Sun and McDonough (1989).

The Escape intrusive rocks lack the distinctive negative Nb anomaly (Fig. 5.9) seen in the metasedimentary rocks (or positive Nb anomaly in the case of the granitoids). This suggests that the Quetico metasedimentary rocks were not a significant contaminant of the Escape magma. However, Nb is depleted in the Escape intrusive rocks relative to typical OIB (Fig. 5.7). If the Escape parental magma was derived from a mantle plume with an OIB-like signature, it is possible that the parental magma was contaminated by limited quantities of crustal material to account for this decreased Nb abundance observed in the intrusive units.

5.2.2 R factor and S-isotopes

The sulfide mineralization within the Escape intrusion is characterized by high tenor PGE mineralization, with average metal grades around 6 g/t PGE within the ore horizon (Clark, 2020). A sulfide liquid that has segregated from a silicate melt (close to mantle composition) at cotectic proportions (that is 50–100:1, silicate to produced sulfide) will not be sufficiently enriched in PGE to generate economic concentrations that constitute an ore deposit (Naldrett, 2011; Godel et al., 2013; Barnes et al., 2015; Barnes and Ripley, 2016). To explain the high PGE metal tenors in

magmatic sulfide deposits (relative to most mafic magmas) such as those present in the Escape intrusion, the concept of R factor is explored. R factor refers to the volume of silicate magma that a given sulfide liquid has equilibrated with (Campbell and Naldrett, 1979). Due to the high partition coefficients of PGE between a silicate melt and sulfide liquid, PGE are expected to collect in the sulfide portion during interaction, depleting the silicate melt of metal (Naldrett, 2011; Barnes and Ripley, 2016). For a closed-system, the potential for upgrading of a sulfide liquid is limited to the volume of magma within the chamber. For an open-system where the injection of fresh, PGE-undepleted magma is possible, a sulfide liquid may scavenge PGE from the incoming melts, until magmatic activity terminates, and the sulfide liquid crystallizes.

The concept of magmatic upgrading has been applied to various magmatic deposits such as layered intrusions and komatiite flows, amongst others (Barnes and Ripley, 2016; Mungall, 2020). A unique subtype of magmatic sulfide deposits is known as "chonolith" or conduit-type magmatic sulfide deposits, which exhibit tubular morphologies, and are believed to form in high energy, dynamic environments in which prolonged flow-through of magma occurs (Barnes et al., 2015). Examples of this deposit subtype include Voisey's Bay in Newfoundland and Nebo-Babel in Western Australia (Evans-Lamswood, 2000; Seat et al., 2007). The Escape intrusion has previously been interpreted as a magma conduit (Clark, 2020), and geological modelling from drillhole logs illustrate that it has a tube-shaped geometry consistent with one (Fig. 2.5). Therefore, to account for the high concentration of PGE within the Escape sulfide mineralization, the application of a dynamic model in which successive pulses of magma were transported through a magma conduit, interacting with an immiscible sulfide liquid, is appropriate.

To assess the degree of PGE enrichment in sulfides during magmatic activity in the Escape conduit, numerical models were produced simulating the effect from sequential steps of batch equilibration between a sulfide liquid and fresh, PGE-undepleted silicate melt (utilizing equations from Ripley and Li, 2003). Figure 5.3 illustrates variations in S/Se sulfide trace-element

and Cu/Pd whole-rock geochemistry at increasing R factors. The model is consistent with Escape mineralization having formed at R factor values between 1,000 and 10,000 (~7500), which is indicative of a moderate degree of sulfide–silicate interaction when compared to other world-class Ni–Cu–PGE magmatic sulfide deposits, such as 1,000–10,000 R factor at Jinchuan, >10,000 R factor at Norilsk 1, and up to 1,000,000 R factor in the W Horizon at Marathon (Song et al., 2009; Duran et al., 2017; and Brzozowski et al., 2020).

The most common stable isotopes of S are ^{32}S, ^{33}S, ^{34}S, and ^{36}S. The relative abundance of each S-isotope in nature is governed by the mass differences in each isotope; the general process that creates this dependency is called mass-dependent fractionation (MDF; Farquhar and Wing, 2003). This is true for compounds in thermodynamic equilibrium and for some non-equilibrium processes in the present day (Farquhar and Wing, 2003). However, sediments from the Archean (~2.45 Ga) record signals of mass-independent fractionation (MIF), where the S-isotopes measured are governed by different fractionation processes unrelated to isotopic mass and have non-zero compositions for $\Delta^{33}S$ and $\Delta^{36}S$ (the terminology for reporting S-isotopes to the international reference standard V-CDT; Farquhar and Wing, 2003). A given S-isotope signature is preserved when passed from one reservoir to another, until there is addition of a different sulfur signature (Farquhar and Wing, 2003). It has been proposed that the MIF signal recorded in Archean rocks was the result of ancient volcanic activity, and that it has been preserved because bacterial sulfate reduction necessary to recycle the MDF S-isotopic signature did not operate at this time (Halevy et al., 2010). By measuring the respective S-isotopes in a sample, we can determine whether mass-dependent fractionation processes were responsible for the fractionation of S isotopes in the sample. This is particularly useful in studying magmatic sulfide systems, where addition of external sulfur is commonly invoked as the catalyst for driving sulfide saturation and generating mineralization from an ultramafic magma (Naldrett, 2011; Ripley and Li, 2013). If a given magmatic sulfide deposit is proximal to a S-rich source that records a MIF

signal, and the progenitor magma to the deposit could have assimilated bulk quantities of that source, then it follows that the MIF would have necessarily been transferred to the sulfur in the magma, and hence to the resulting sulfide minerals in the deposit. Therefore, if an MIF signal is measured in the sulfides from a deposit, it would be reasonable to conclude that addition of external sulfur played a role in the genesis of that deposit.

Pyrite measured from adjacent metasedimentary country rocks to Escape are characterized by groups of S-isotope values. For $\delta^{34}S$ in Quetico pyrite, there is one group around 0–0.5‰ that is within mantle range, and a single point around -3.0‰ which is outside the mantle range (Fig. 5.10a). For $\Delta^{33}S$ in Quetico pyrite, there is one group around 0–0.5‰ that records a MDF signal, and another around 0.25‰ which records a MIF signal (Fig. 5.10). All the $\Delta^{36}S$ measured from Quetico pyrite record a MDF signal (Fig. 5.10b). The fractionation signature of sulfur isotopes within Escape sulfides are such that values fall within a range (0 ± 0.2‰ for $\Delta^{33}S$ and 0 ± 0.4‰ for $\Delta^{36}S$) that indicates control by mass-dependent fractionation processes (Fig. 5.10). This is true except for a few outlier values of $\delta^{34}S$ in pentlandite, which fall outside the mantle range of values. With the significant overlap between Quetico pyrite and the Escape sulfide S-isotopic values, it is possible that country rock did contaminate the Escape parental magma, contributing to its resulting S-isotope signature.

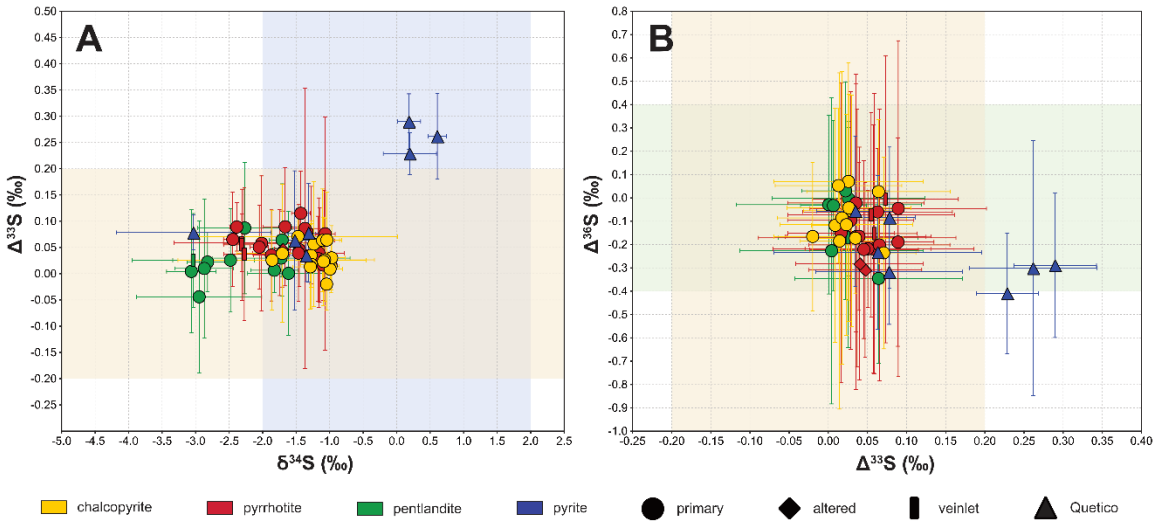

Figure 5.10: S isotope binary variation diagrams for Escape and Quetico sulfides. Error bars are two standard deviations from the mean (2σ). Coloured fields represent mantle ranges (the range in MDF signal) for each isotope, with values from Farquhar and Wing (2003) and Ripley and Li (2003).

However, this conclusion is not definitive, as both the Escape and Quetico values fall within mantle range, meaning that the signal recorded in Escape sulfides cannot distinguish between contamination or a mantle source of S. Moreover, the overlap in Escape pentlandite with a single Quetico $\delta^{34}S$ point constitutes minimal evidence in support of the addition of crustal S via contamination. The possibility remains that the Escape parental magma did assimilate bulk material from the Quetico and incorporate each of the S-isotope signatures shown in Figure 5.10. Ripley and Li (2003) have suggested that during interaction between a crustally-contaminated sulfide melt and successive pulses of uncontaminated silicate magma, that sulfur isotope exchange occurs whilst metal upgrading, and enrichment is underway. This process could lead to the erasure of the MIF isotopic signature contributed by Quetico sulfur within the Escape deposit, as the mantle signature that the segregated sulfide melt equilibrated with would become the dominant signal. To assess this possibility of S-isotope masking, numerical models were produced to simulate the effect of sequential steps of batch equilibration (using the same parameters as the previous S/Se versus Cu/Pd model) between a sulfide liquid contaminated by Quetico pyrite and successive pulses of uncontaminated silicate magma (as would be expected in the case of the dynamic conduit that the Escape deposit represents). The modelling assumes a constant rate of

sulfur isotope exchange. Four models illustrating the equilibration process at various R factors utilizing in situ S-isotope values, trace-element sulfide chemistry, and whole rock concentrations are shown in Figure 5.11.

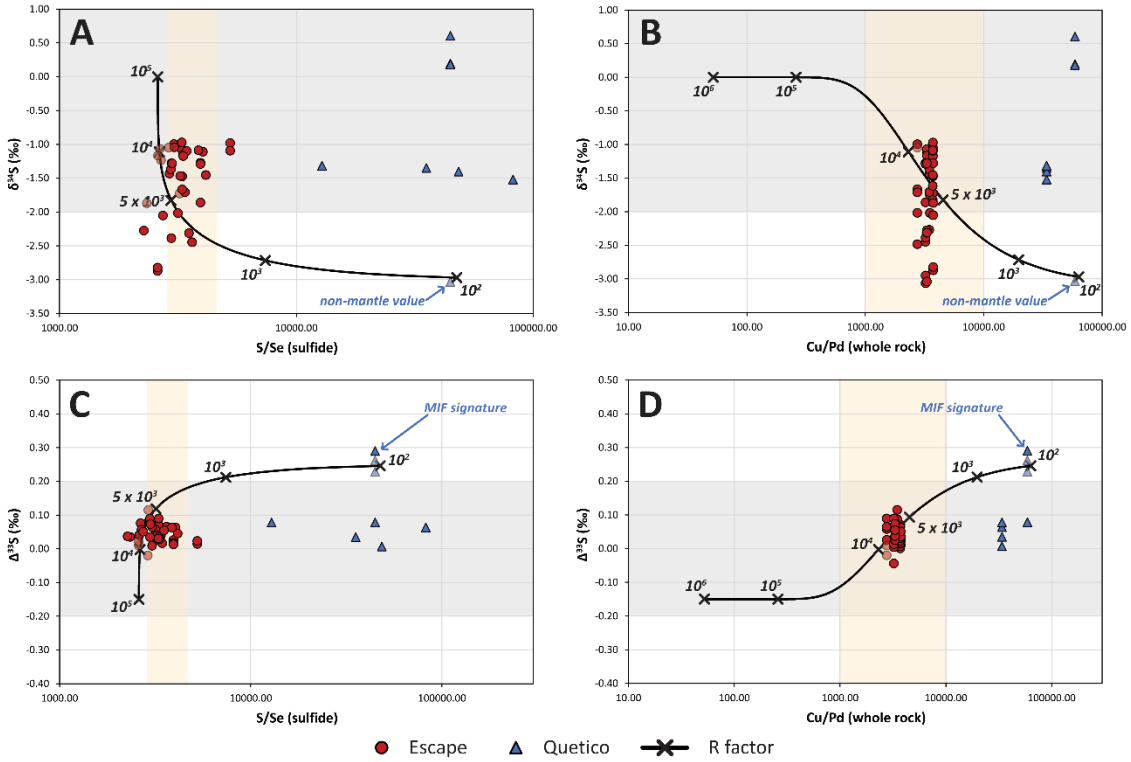

Figure 5.11: Binary variation diagrams for Escape intrusive and metasedimentary country rocks, with R factor model curves illustrating S-isotope exchange between an external sulfur contaminant and sulfide melt. Curves were modelled by using equations from Ripley and Li (2003).

For these models, a starting composition equivalent to the non-mantle signature measured in the country rock was used. Input parameters for each element or isotope were consistent for each calculation of batch equilibrium (e.g., starting composition for Cu is the same in both Fig. 5.11b and d). The values for Escape sulfides fall roughly along the curve at R factors between 5,000–10,000, consistent with the model in Figure 5.2. For the scenario modelled, repeated equilibration with successive batches of uncontaminated silicate melt at variations in R factor ~7,500, the MIF signal present in select pyrite from the country rock would be significantly exchanged to leave minimal record in the Escape sulfide liquid (Fig. 5.11). This provides a possible explanation for why most Escape sulfides have S-isotopic values that fall within the mantle range, as they were

continually refreshed by incoming silicate melt with mantle-derived sulfur. Given that $\Delta^{33}S$ values for Escape sulfides are entirely represented by mass-dependent fractionation, it follows that the other S-isotopes (^{33}S, ^{36}S) were sufficiently exchanged during equilibration as well. An important caveat to this model is that any Quetico country rock that was assimilated would have also contributed sulfur that recorded an MDF signal. Therefore, the Escape parental magma would have also been diluted with this sulfur, which would further mask the potential signature of MIF via crustal contamination. Another potential source of sulfur within the region are various forms of pyrite within the sedimentary rocks of the Animikie Group. Pufahl et al. (2010) reported $\delta^{34}S$ values of 8.4 ± 5.4‰ and 17.2 ± 5.1‰ for the Gunflint and Rove formations, respectively. It is unlikely that the parental Escape magmas assimilated much or any sulfur-rich material from these formations because the $\delta^{34}S$ for Escape is negative (values ranging from -3.07 to -0.97‰). It would be difficult to produce a signature such as this through magmatic mixing of repeated mantled-derived magmas with $\delta^{34}S$ values at 0 ± 2‰. The only scenario where this is possible is where the Escape sulfide liquid interacted with silicate melts with exceedingly high R factors at or greater than one million — which is not consistent with the findings of this thesis. In summary, it is possible that S-rich material from the adjacent Quetico metasedimentary country rock contaminated the Escape parental magma and contributed to S-saturation of the deposit, albeit the signature of which has been mostly eliminated.

5.3 Genetic model of the Escape intrusion

The results of this study have been integrated into a generalized model for the formation of the Escape intrusion. The Escape intrusive rocks are characterized by whole-rock trace element patterns similar to OIB. This pattern is shared amongst other MRS ultramafic intrusions and is supportive of their formation by partial melting of an upwelling mantle plume. Around 1107.6 ± 0.9 Ma, extensive magmatism during the early stage of Midcontinent rift formation occurred, during which the parental magma(s) for the Escape intrusion were generated. These parental

magmas were transported by crustal-scale faults (e.g., Lightfoot and Evans-Lamswood, 2014), and focused by the Quetico and Escape faults into the Thunder Bay North Intrusive Complex (Fig. 5.12a).

The results of this thesis are inconclusive as to when and what definitively caused the S-saturation of the Escape parental magma. During prolonged flow through in the dynamic conduit system, minor Quetico metasedimentary country rock was thermally eroded and digested, but the isotopic signature expected from this contamination was mostly erased due to isotopic exchange (Fig. 5.12b). The inconsistent phase layering of plagioclase and wide range of olivine size throughout the intrusion suggests there were repeated injections of fractionated crystal mush in the conduit. This helped provide an abundance of silicate melt that the segregated sulfide liquid was able to interact with and scavenge PGE from, at moderate R factors around 7,500, resulting in high PGE tenors within the Escape deposit.

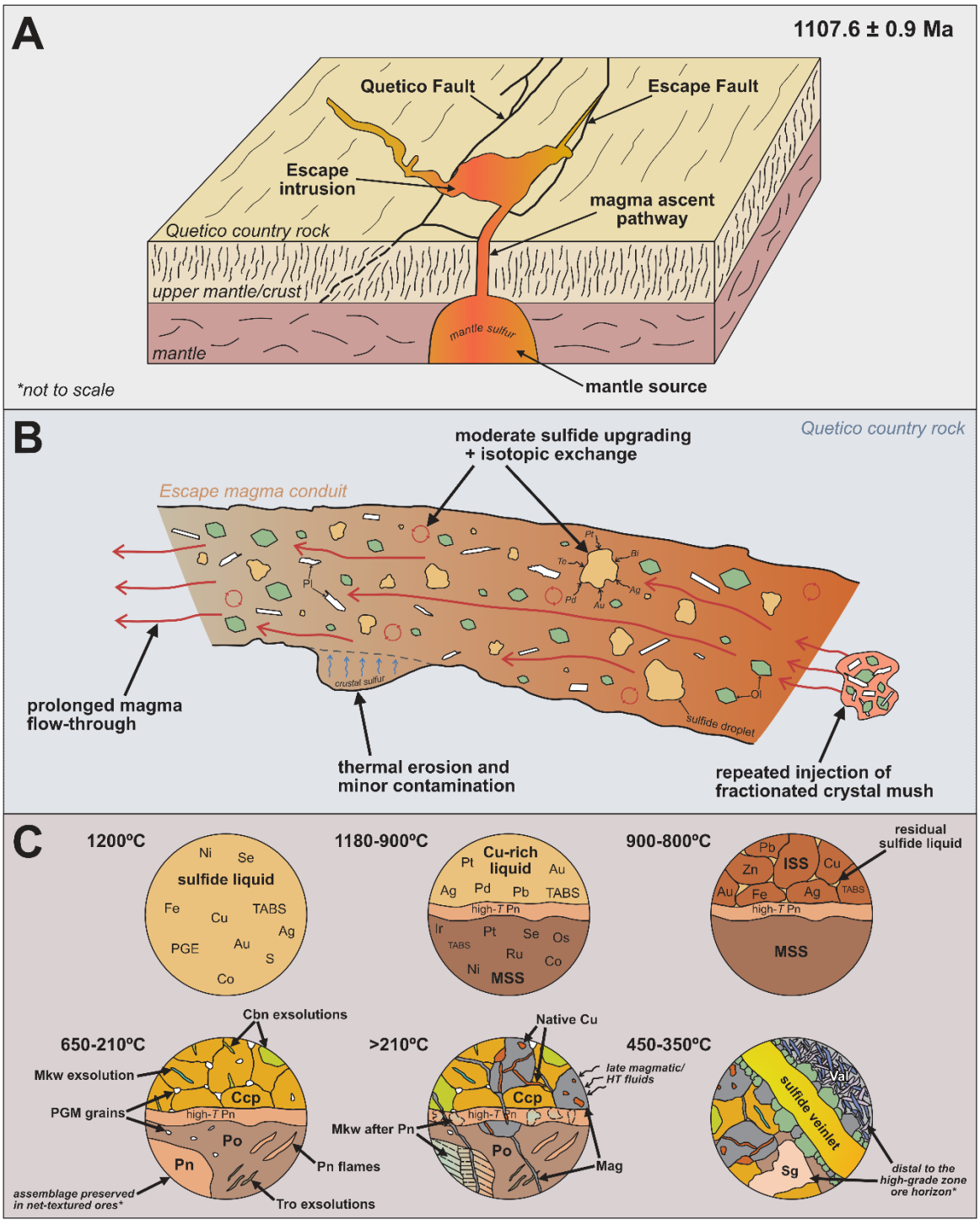

Figure 5.12: Schematic deposit model for the Escape intrusion at sequential stages in its formation. A – During Midcontinent rifting of the North American craton. Generation of high-degree partial melts from the upwelling mantle plume and subsequent ascent of magmas towards the Thunder Bay Intrusive Complex. B – Dynamic magmatism through the Escape conduit during which metal tenors were increased. C – Evolution of the sulfide liquid during crystallization and post-crystallization modification by hydrothermal fluids.

As energy in the conduit waned and the liquids started to cool, the sulfide liquid was trapped interstitial to the cumulates and fractionated in a manner broadly consistent with the empirically determined sulfide system behaviour (Mansur et al., 2021). The sulfide liquid was enriched in PGE and base metals at high temperatures (Fig. 5.12c). During progressive cooling, the primary mineral assemblage exsolved from MSS and ISS to form pyrrhotite + chalcopyrite + pentlandite + platinum-group minerals ± pyrite ± troilite ± cubanite ± mackinawite. After the formation of this assemblage, the Escape system underwent extensive alteration due to one or more hydrothermal fluids. The main, initial ore modifications included desulfurization of chalcopyrite to form native Cu + magnetite and replacement of pentlandite by mackinawite. This led to the local downgrading of the disseminated sulfides, with PGM apparently absent from the assemblage, and a lack of Pd in mackinawite (as well as a decrease in Pd within relict pentlandite). With Cu and sulfur remobilized, there was later alteration of hydrous minerals to valleriite, modification of pentlandite to sugakiite, and the emplacement of PGE-poor crosscutting sulfide veinlets (Fig. 5.12c).

6 Conclusions

The Escape deposit of the Thunder Bay North Intrusive Complex (TBNIC), part of the 1.1 Ga Midcontinent Rift System (MRS), is a mafic–ultramafic intrusion that hosts high-grade PGE–Cu–Ni magmatic sulfide mineralization. This study utilized detailed petrography, whole-rock geochemistry, sulfide geochemistry, mineral liberation analysis, and sulfur isotopes to investigate the formation of the Escape intrusion. The study investigated questions related to the deposit paragenesis, fractionation history of sulfide minerals, phases that hosted platinum-group elements (PGE), source and contamination history, the degree of metal upgrading, and modifications to primary mineralization post-magmatism. The answers to these research questions have been incorporated into a schematic model for the genesis of the Escape intrusion and its sulfide mineralization.

The magmatic sulfide mineralization is hosted within the peridotite unit, which is overlain by the weakly mineralized gabbroic, oxide gabbro, and hybrid units. The peridotite unit exhibits variable composition throughout the intrusion due to irregular phase layering of plagioclase, and ranges from wehrlite, to felspathic wehrlite, to melanocratic gabbro. The ore horizon of the high-grade zone of the Escape intrusion is chiefly characterized by net-textured (intercumulus) sulfide mineralization that is composed of pyrrhotite + chalcopyrite + pentlandite. Lesser disseminated sulfides mark the margins of the high-grade zone, which decrease in abundance with distance from the net-textured sulfides. Platinum-group elements are concentrated within the primary sulfides, and as discrete platinum-group minerals. The primary sulfides contain individual PGE concentrations ranging from 0.1–10 ppm, with IPGEs (Ir, Os, Ru) exhibiting preference for pyrrhotite. Palladium is strongly enriched in pentlandite from the primary assemblage, with concentrations around 100 ppm. Moreover, minerals such as sperrylite ($PtAs_2$) and michenerite

(PdBiTe) constitute some of the main PGM that exsolved during fractionation of the interstitial–primary mineralization.

The rocks within the peridotite unit have undergone hydrothermal alteration that resulted in a variable assemblage consisting of one or more of serpentine + biotite + amphibole + saussurite + chlorite + talc + carbonate + actinolite + clay minerals. Alteration during the hydrothermal phase also affected interstitial sulfides to varying degrees. Whereas the net-textured sulfides are effectively unaltered, the disseminated sulfides that surround the net-textured ores have been considerably modified. This alteration of disseminated sulfides is predominantly characterized by desulfurization of chalcopyrite (+ pyrrhotite) and replacement of pentlandite by nickeliferous mackinawite. The breakdown of chalcopyrite allowed for the remobilization of Cu locally and throughout the system, and is most obviously marked by the intergrowth of native copper and magnetite. The loss of S from this reaction is recorded by the depleted (relative to primary sulfides) S/Se signature in the relict sulfides of the altered ores. As a result of a change in redox conditions from reducing serpentinization to talc-carbonation, multiple secondary Cu-bearing phases were formed including: sugakiite, Cu-rich mackinawite, Cu-rich Po, and valleriite. Moreover, during desulfurization, PGE were also remobilized, as suggested by the decreased metal tenors of the sulfide minerals in the interstitial–altered assemblage, as well the absence of PGM. The PGE were transported by bisulfide complexes in the hydrothermal fluids and partially reprecipitated as As-rich PGM within sulfide veinlets. The crosscutting sulfide veinlets record an elevated S/Se signature relative to primary sulfides, and were emplaced within fractures in the peridotite groundmass during a secondary, hydrothermal mineralization event.

The primitive mantle-normalized trace element signatures of Escape intrusive rocks are characterized by a gently-sloping trend, similar to ocean island basalt (OIB), and numerous other ultramafic intrusions associated with the MRS. This signature and the elevated Gd/Yb_{cn} values for Escape rocks suggest its derivation from a mantle source, consistent with the mantle plume model

of MRS formation. The Escape intrusive rocks do not exhibit a pronounced Nb anomaly and Th enrichment characteristic of continental crust but are depleted in Nb relative to OIB. This may suggest that the Escape parental magma was contaminated by small amounts of country rock, possibly Quetico metasediments.

Numerical modelling of whole-rock, trace-element, and S-isotopic data of Escape rocks and sulfide minerals indicate that the deposit underwent moderate metal upgrading (~7,500 R factor) during prolonged flow-through in a dynamic magma conduit. This ratio between the Escape segregated sulfide liquid and silicate melt helps explain the high-PGE metal tenor of the deposit. Platinum-group elements were effectively concentrated in the sulfide liquid during interaction as the metals readily partitioned from silicate magma to the sulfide fraction. The sulfide liquid was provided with sufficient PGE to scavenge due to system replenishment by repeated injections of fractionated crystal mush.

The Escape sulfides are characterized by S-isotope values that are mostly within the mantle range. Pyrite measured from the country rock is characterized by groups of S-isotopes, some of which record a mass-independent fractionation signal. Comparison of these data in conjunction with isotopic exchange modelling suggests that the Escape parental magma was contaminated by minor Quetico metasediments, but the source of sulfur likely constitutes a mixture from mantle and country rock. It is possible that the predominantly mantle signature of Escape sulfides was the result of erasure during interaction with fresh mantle sulfur when the conduit was active.

In summary, the Escape parental magma was formed by partial melts from the mantle during MRS formation and exploited crustal-scale faults resulting in its emplacement along the boundary of the Quetico Basin. During flow-through in the TBNIC, minor contamination from country rock likely occurred adding sulfur to the system that possibly contributed to S-saturation. The immiscible sulfide liquid within the parental magma was enriched in PGE as it interacted

with injections of PGE-undepleted magmas during convection in the conduit. This process likely also contributed to the masking of the country rock S-isotope signature within the Escape rocks. Sulfide liquid trapped between cumulus minerals cooled to produce a primary mineralization assemblage rich in PGE, Cu, and Ni. Post-magmatism, the mineralization and host rocks in the peridotite unit underwent a complex history of hydrothermal modification. As a result of serpentinization and talc-carbonation of the Escape rocks, desulfurization of the primary disseminated assemblage occurred, decreasing the metal tenor in these ores. The hydrothermal phase remobilized base- and precious-metals throughout the system, and redeposited them primarily as As-rich, crosscutting sulfide veinlets.

References

Addison, W.D., Brumpton, G.R., Vallini, D.A., McNaughton, N.J., Davis, D.W., Kissin, S.A., Fralick, P.W., and Hammond, A.L., 2005, Discovery of distal ejecta from the 1850 Ma Sudbury impact event: Geology, v. 33, no. 3, p. 193.

Almeida, C.M., Olivo, G.R., and de Carvalho, S.G., 2007, The Ni–Cu–PGE Sulfide Ores of the Komatiite-hosted Fortaleza de Minas Deposit, Brazil: Evidence of Hydrothermal Remobilization: The Canadian Mineralogist, v. 45, no. 4, p. 751–773.

Andreani, M., Mével, C., Boullier, A.-M., and Escartín, J., 2007, Dynamic control on serpentine crystallization in veins: Constraints on hydration processes in oceanic peridotites: Geochemistry, Geophysics, Geosystems, v. 8, no. 2, p. 24.

Angus, D.A., Kendall, J.-M., Wilson, D.C., White, D.J., Sol, S., and Thomson, C.J., 2009, Stratigraphy of the Archean western Superior Province from P- and S-wave receiver functions: Further evidence for tectonic accretion? Physics of the Earth and Planetary Interiors, v. 177, nos. 3–4, p. 206–216.

Barnes, S.-J., and Lightfoot, P.C., 2005, Formation of Magmatic Nickel Sulfide Ore Deposits and Processes Affecting Their Copper and Platinum Group Element Contents: Economic Geology, v. One Hundredth Anniversary Volume, p. 35.

Barnes, S.-J., and Ripley, E.M., 2016, Highly Siderophile and Strongly Chalcophile Elements in Magmatic Ore Deposits: Reviews in Mineralogy and Geochemistry, v. 81, no. 1, p. 725–774.

Barnes, S.-J., Couture, J.F., Sawyer, E.W., and Bouchaib, C., 1993, Nickel-copper occurrences in the Belleterre-Angliers Belt of the Pontiac Subprovince and the use of Cu-Pd ratios in interpreting platinum-group element distributions: Economic Geology, v. 88, no. 6, p. 1402–1418.

Barnes, S.J., Cruden, A.R., Arndt, N., and Saumur, B.M., 2016, The mineral system approach applied to magmatic Ni–Cu–PGE sulphide deposits: Ore Geology Reviews, v. 76, p. 296–316.

Beard, J.S., Frost, B.R., Fryer, P., McCaig, A., Searle, R., Ildefonse, B., Zinin, P., and Sharma, S.K., 2009, Onset and Progression of Serpentinization and Magnetite Formation in Olivine-rich Troctolite from IODP Hole U1309D: Journal of Petrology, v. 50, no. 3, p. 387–403.

Behrendt, J.C., Green, A.G., Cannon, W.F., Hutchinson, D.R., Lee, M.W., Milkereit, B., Agena, W.F., and Spencer, C., 1988, Crustal structure of the Midcontinent rift system: Results from GLIMPCE deep seismic reflection profiles: Geology, v. 16, no. 1, p. 81.

Bleeker, W., Smith, J., Hamilton, M., Kamo, S., Liikane, D., Hollings, P., Cundari, R., Easton, M., and Davis, D., 2020, The Midcontinent Rift and its Mineral Systems: Overview and Temporal Constraints of Cu-Ni-PGE Mineralized Intrusions: Geological Survey of Canada Targeted Geoscience Initiative 5: Advances in the understanding of Canadian Ni-Cu-PGE and Cr ore systems - Examples from the Midcontinent Rift, the Circum-Superior Belt, the Archean Superior Province, and Cordilleran Alaskan-type intrusions: Report No. 8722.

Bollmann, T.A., Lee, S., Frederiksen, A.W., Wolin, E., Revenaugh, J., Wiens, D.A., Darbyshire, F.A., Stein, S., Wysession, M.E., and Jurdy, D., 2019, *P* Wave Teleseismic Traveltime Tomography of the North American Midcontinent: Journal of Geophysical Research: Solid Earth, v. 124, no. 2, p. 1725–1742.

Bradfield, A., Barry, J., Brown, F., Burga, D., Feasby, D.G., Kuchling, K., Mackie, B., Pitman, P., and Puritch, E., 2020, Technical Report, Updated Mineral Resource Estimate and Preliminary Economic Assessment of the Marathon Deposit, Thunder Bay Mining District Northwestern Ontario, Canada: P&E Mining Consultants Inc.

Brzozowski, M.J., Hollings, P., Zhu, J.-J., and Creaser, R.A., 2023, Osmium isotopes record a complex magmatic history during the early stages of formation of the North American Midcontinent Rift — Implications for rift initiation: Lithos, v. 436–437, p. 106966.

Brzozowski, M.J., Samson, I.M., Gagnon, J.E., Good, D.J., and Linnen, R.L., 2020, On the Mechanisms for Low-Sulfide, High-Platinum Group Element and High-Sulfide, Low-Platinum Group Element Mineralization in the Eastern Gabbro, Coldwell Complex, Canada: Evidence from Textural Associations, S/Se Values, and Platinum Group Element Concentrations of Base Metal Sulfides: Economic Geology, v. 115, no. 2, p. 355–384.

Calvert, A.J., and Ludden, J.N., 1999, Archean continental assembly in the southeastern Superior Province of Canada: Tectonics, v. 18, no. 3, p. 412–429.

Cannon, W.F., 1992, The Midcontinent rift in the Lake Superior Region with emphasis on its geodynamic evolution: Tectonophysics, v. II, no. 213, p. 41–48.

Cannon, W.F., and Hinze, W.J., 1992, Speculations on the origin of the North American Midcontinent rift (P.A. Ziegler, Ed.): Tectonophysics, v. II, no. 213, p. 49–55.

Card, K.D., and Ciesielski, A., 1986, DNAG #1. Subdivisions of the Superior Province of the Canadian Shield: Geoscience Canada, v. 13, no. 1, p. 5–13.

Chaffee, M., 2015, Petrographic and Geochemical Study of the Hybrid Rock Unit Associated with the Current Lake Intrusive Complex: University of Minnesota: unpublished MSc thesis.

Clark, J.G., 2020, Technical Report on the Thunder Bay North and Escape Lake Properties, Northern Ontario Canada: Internal Report: Clark Exploration Consulting.

Corfu, F., and Davis, D.W., 1992, U-Pb Geochronological Framework for the Western Superior Province, Ontario, in Geology of Ontario: Ontario Geological Survey, p. 1335–1346.

Corfu, F., Stott, G.M., and Breaks, F.W., 1995, U-Pb geoehronology and evolution of the English River Subprovince, an Archean low P-high T metasedimentary belt in the Superior Province: Tectonics, v. 14, no. 5, p. 1220–1233.

Corkery, M.T., Cameron, H.D.M., Lin, S., Skulski, T., Whalen, J.B., and Stern, R.A., 2000, Geological Investigations in the Knee Lake Belt (Parts of NTS 53L): Manitoba Geological Survey Report of Activities 2000, 129–136 p.

Craig, J.R., and Vaughan, D.J., 1994, Ore Microscopy and Ore Petrography: John Wiley & Sons, Inc.

Cundari, R.M., Puumala, M.A., Smyk, M.C., and Hollings, P., 2021, New and Compiled Whole-Rock Geochemical and Isotope Data of Midcontinent Rift–Related Rocks, Thunder Bay Area: Ontario Geological Survey: Miscellaneous Release—Data 308.

Daly, R.A., 1905, The Classification of Igneous Intrusive Bodies: The Journal of Geology, v. 13, no. 6, p. 485–508.

D'Angelo, M., 2013, Igneous textures and mineralogy of the Steepledge Intrusion, Northern Ontario: Lakehead University: unpublished HBSc thesis.

Davis, D.W., 1998, Speculations on the formation and crustal structure of the Superior province from U-Pb geochronology: University of British Columbia Western Superior Transect 4th Annual Workshop 65, 21–28 p.

Davis, D.W., Pezzutto, F., and Ojakangas, R.W., 1990, The age and provenance of metasedimentary rocks in the Quetico Subprovince, Ontario, from single zircon analyses: implications for Archean sedimentation and tectonics in the Superior Province: Earth and Planetary Science Letters, v. 99, no. 3, p. 195–205.

Delacour, A., Früh-Green, G.L., and Bernasconi, S.M., 2008, Sulfur mineralogy and geochemistry of serpentinites and gabbros of the Atlantis Massif (IODP Site U1309): Geochimica et Cosmochimica Acta, v. 72, no. 20, p. 5111–5127.

Ding, X., Li, C., Ripley, E.M., Rossell, D., and Kamo, S., 2010, The Eagle and East Eagle sulfide ore-bearing mafic-ultramafic intrusions in the Midcontinent Rift System, upper Michigan: Geochronology and petrologic evolution: Geochemistry, Geophysics, Geosystems, v. 11, no. 3.

Duran, C.J., Barnes, S.-J., Pleše, P., Kudrna Prašek, M., Zientek, M.L., and Pagé, P., 2017, Fractional crystallization-induced variations in sulfides from the Noril'sk-Talnakh mining district (polar Siberia, Russia): Ore Geology Reviews, v. 90, p. 326–351.

Evans, K.A., Frost, B.R., Reddy, S.M., and Brown, T.C., 2023, Causes, effects, and implications of the relationships amongst fluids, serpentinisation, and alloys: Lithos.

Farquhar, J., and Wing, B.A., 2003, Multiple sulfur isotopes and the evolution of the atmosphere: Earth and Planetary Science Letters, v. 213, nos. 1–2, p. 1–13.

Fralick, P., Davis, D.W., and Kissin, S.A., 2002, The age of the Gunflint Formation, Ontario, Canada: single zircon U–Pb age determinations from reworked volcanic ash: v. 39, p. 8.

Fralick, P., Purdon, R.H., and Davis, D.W., 2006, Neoarchean trans-subprovince sediment transport in southwestern Superior Province: sedimentological, geochemical, and geochronological evidence: Canadian Journal of Earth Sciences, v. 43, p. 1055–1070.

Frost, B.R., and Beard, J.S., 2007, On Silica Activity and Serpentinization: Journal of Petrology, v. 48, no. 7, p. 1351–1368.

Godel, B.M., Barnes, S.J., and Barnes, S.-J., 2013, Deposition Mechanisms of Magmatic Sulphide Liquids: Evidence from High-Resolution X-Ray Computed Tomography and Trace Element Chemistry of Komatiite-hosted Disseminated Sulphides: Journal of Petrology, v. 54, no. 7, p. 1455–1481.

Government of Canada, 2022, The Canadian Critical Minerals Strategy: Ottawa, Natural Resources Canada.

Halevy, I., Johnston, D.T., and Schrag, D.P., 2010, Explaining the Structure of the Archean Mass-Independent Sulfur Isotope Record: Science, v. 329, no. 5988, p. 204–207.

Hart, T.R., 2005, Precambrian Geology of the Southern Black Sturgeon River and Seagull Lake Area, Nipigon Embayment, Northwestern Ontario: Ontario Geological Survey 6165, 63p p.

Hart, T.R., and MacDonalds, C.A., 2007, Proterozoic and Archean geology of the Nipigon Embayment: implications for emplacement of the Mesoproterozoic Nipigon diabase sills and mafic to ultramafic intrusions: Canadian Journal of Earth Sciences, v. 44, p. 1021–1040.

Hart, T.R., Hollings, P., Heggie, G., and MacDonald, C.A., 2005, Proterozoic platinum group element mineralization of the Nipigon Embayment, northwest Ontario, in 10th International Platinum Symposium – Proceedings of the 10th International Platinum Symposium: Oulu, Finland, p. 362–364.

Heaman, L.M., Easton, R.M., Hart, T.R., Hollings, P., MacDonald, C.A., and Smyk, M., 2007, Further refinement to the timing of Mesoproterozoic magmatism, Lake Nipigon region, Ontario: Canadian Journal of Earth Sciences, v. 44, no. 8, p. 1055–1086.

Heggie, G., 2011, TBN Liquid Compositions: Lithogeochemical Compilation: Internal Report: Magma Metals Ltd.

Heggie, G.J., and Hollings, P., 2004, Controls on PGE mineralization in the Seagull Intrusion, northwestern Ontario, in Geological Association of Canada – Mineralogical Association of Canada – Program with Abstracts: p. 226.

Hinchey, J.G., and Hattori, K.H., 2005, Magmatic mineralization and hydrothermal enrichment of the High Grade Zone at the Lac des Iles palladium mine, northern Ontario, Canada: Mineralium Deposita, v. 40, no. 1, p. 13–23.

Hinze, W.J., and Chandler, V.W., 2020, Reviewing the configuration and extent of the Midcontinent rift system: Precambrian Research, v. 342.

Hollings, P., and Cundari, R., 2020, Ni-Cu-PGE mineralization of the 1.1Ga Midcontinent Rift of N. America: rethinking models for the rift and the implications for mineralization, in Mineral Deposits Studies Group Annual Meeting 2020 – Mineral Deposits Studies Group Annual Meeting 2020 Proceedings: p. 24.

Hollings, P., Smyk, M., Heaman, L.M., and Halls, H., 2010, The geochemistry, geochronology and paleomagnetism of dikes and sills associated with the Mesoproterozoic Midcontinent Rift near Thunder Bay, Ontario, Canada: Precambrian Research, v. 183, no. 3, p. 553–571.

Hollings, P., Smyk, M., Bleeker, W., Hamilton, M., Cundari, R., and Easton, M., 2021, Geology of the Mesoproterozoic Pillar Lake Volcanics and Inspiration Sill, Armstrong, Ontario: evidence of early Midcontinent Rift magmatism in the northwestern Nipigon Embayment: Canadian Journal of Earth Sciences, v. 58, no. 10, p. 1116–1131.

Holwell, D.A., and McDonald, I., 2010, A Review of the Behaviour of Platinum Group Elements within Natural Magmatic Sulfide Ore Systems: Platinum Metals Review, v. 54, no. 1, p. 26–36.

Holwell, D.A., Adeyemi, Z., Ward, L.A., Smith, D.J., Graham, S.D., McDonald, I., and Smith, J.W., 2017, Low temperature alteration of magmatic Ni-Cu-PGE sulfides as a source for hydrothermal Ni and PGE ores: A quantitative approach using automated mineralogy: Ore Geology Reviews, v. 91, p. 718–740.

Hrabi, R.B., and Cruden, A.R., 2006, Structure of the Archean English River subprovince: implications for the tectonic evolution of the western Superior Province, Canada: Canadian Journal of Earth Sciences, v. 43, p. 947–966.

Ikehata, K., and Hirata, T., 2012, Copper Isotope Characteristics of Copper-Rich Minerals from the Horoman Peridotite Complex, Hokkaido, Northern Japan: Economic Geology, v. 107, no. 7, p. 1489–1497.

Jayananda, M., Kano, T., Peucat, J., and Channabasappa, S., 2008, 3.35Ga komatiite volcanism in the western Dharwar craton, southern India: Constraints from Nd isotopes and whole-rock geochemistry: Precambrian Research, v. 162, nos. 1–2, p. 160–179.

Kato, T., Ringwood, A.E., and Irifune, T., 1988, Experimental determination of element partitioning between silicate perovskites, garnets and liquids: constraints on early differentiation of the mantle: Earth and Planetary Science Letters, v. 89, no. 1, p. 123–145.

Kiseleva, O., Airiyants, E., Belyanin, D., and Zhmodik, S., 2019, Hydrothermal remobilization platinum group elements and their secondary minerals in chromitite deposits of the Eastern Sayan ophiolites (Russia) (O. Chudaev, Y. Kharaka, R. Harmon, R. Millot, & O. Shouakar-Stash, Eds.): E3S Web of Conferences, v. 98.

Kitakaze, A., 2008, Sugakiite, Cu(Fe,Ni)8S8, A New Mineral Species from Hokkaido, Japan: The Canadian Mineralogist, v. 46, no. 1, p. 263–267.

LaFlamme, C., Martin, L., Jeon, H., Reddy, S.M., Selvaraja, V., Caruso, S., Bui, T.H., Roberts, M.P., Voute, F., Hagemann, S., Wacey, D., Littman, S., Wing, B., Fiorentini, M., et al., 2016, In situ multiple sulfur isotope analysis by SIMS of pyrite, chalcopyrite, pyrrhotite, and pentlandite to refine magmatic ore genetic models: Chemical Geology, v. 444, p. 1–15.

Li, C., Barnes, S.-J., Makovicky, E., Rose-Hansen, J., and Makovicky, M., 1996, Partitioning of nickel, copper, iridium, rhenium, platinum, and palladium between monosulfide solid solution and sulfide liquid: Effects of composition and temperature: Geochimica et Cosmochimica Acta, v. 60, no. 7, p. 1231–1238.

Lightfoot, P.C., and Evans-Lamswood, D., 2015, Structural controls on the primary distribution of mafic–ultramafic intrusions containing Ni–Cu–Co–(PGE) sulfide mineralization in the roots of large igneous provinces: Ore Geology Reviews, v. 64, p. 354–386.

Listerud, W.H., and Meineke, D.G., 1977, Mineral Resources of a Portion of the Duluth Complex and Adjacent Rocks in St. Louis and Lake Counties, Northeastern Minnesota: Minnesota Department of Natural Resources, Division of Minerals, n. 93.

Mansur, E.T., Barnes, S.-J., and Duran, C.J., 2021, An overview of chalcophile element contents of pyrrhotite, pentlandite, chalcopyrite, and pyrite from magmatic Ni-Cu-PGE sulfide deposits: Mineralium Deposita, v. 56, no. 1, p. 179–204.

Mavrogenes, J.A., and O'Neill, H.St.C., 1999, The relative effects of pressure, temperature and oxygen fugacity on the solubility of sulfide in mafic magmas: Geochimica et Cosmochimica Acta, v. 63, nos. 7–8, p. 1173–1180.

Meurer, W.P., and Boudreau, A.E., 1996, Compaction of Density-Stratified Cumulates: Effect on Trapped-Liquid Distribution: The Journal of Geology, v. 104, no. 1, p. 115–120.

Miller, J., 2021, Petrography and Lithostratigraphy of DDH ELR20-004: Internal Report: JDM GeoConsulting.

Mucke, A., 2017, Review on Mackinawite and Valleriite: Formulae, Localities, Associations and Intergrowths of the Minerals, Mode of Formation and Optical Features in Reflected Light: Journal of Earth Science & Climatic Change, v. 8, no. 11.

Mudd, G.M., and Jowitt, S.M., 2014, A Detailed Assessment of Global Nickel Resource Trends and Endowments: Economic Geology, v. 109, no. 7, p. 1813–1841.

Mudd, G.M., Jowitt, S.M., and Werner, T.T., 2018, Global platinum group element resources, reserves and mining – A critical assessment: Science of The Total Environment, v. 622–623, p. 614–625.

Mungall, J.E., 2014, Geochemistry of Magmatic Ore Deposits, in Treatise on Geochemistry: Elsevier, p. 195–218.

Mungall, J.E., Christopher Jenkins, M., Robb, S.J., Yao, Z., and Brenan, J.M., 2020, Upgrading of Magmatic Sulfides, Revisited: Economic Geology, v. 115, no. 8, p. 1827–1833.

Naldrett, A.J., 1997, Key factors in the genesis of Noril'sk, Sudbury, Jinchuan, Voisey's Bay and other world-class Ni-Cu-PGE deposits: Implications for exploration: Australian Journal of Earth Sciences, v. 44, no. 3, p. 283–315.

Naldrett, A.J., 1999, World-class Ni-Cu-PGE deposits: key factors in their genesis: Mineralium Deposita, v. 34, no. 3, p. 227–240.

Naldrett, A.J., 2004, Magmatic Sulfide Deposits: Berlin, Heidelberg, Springer Berlin Heidelberg.

Naldrett, A.J., 2011, Fundamentals of Magmatic Sulfide Deposits: Reviews in Economic Geology, v. 17, p. 1–50.

Nicholson, S.W., Schulz, K.J., Shirey, S.B., and Green, J.C., 1997, Rift-wide correlation of 1.1 Ga Midcontinent rift system basalts: implications for multiple mantle sources during rift development: Canadian Journal of Earth Sciences, v. 34, no. 4, p. 504–520.

O'Driscoll, B., Garwood, R., Day, J.M.D., and Wogelius, R., 2018, Platinum-group element remobilization and concentration in the Cliff chromitites of the Shetland Ophiolite Complex, Scotland: Mineralogical Magazine, v. 82, no. 3, p. 471–490.

Ohtani, E., Kawabe, I., Moriyama, J., and Nagata, Y., 1989, Partitioning of elements between majorite garnet and melt and implications for petrogenesis of komatiite: Contributions to Mineralogy and Petrology, v. 103, no. 3, p. 263–269.

Percival, J.A., 2007, Eo- to Mesoarchean Terranes of the Superior Province and Their Tectonic Context, in Kranendonk, M.J., Smithies, R.H., and Bennett, V.C. eds., Earth's Oldest Rocks: Elsevier B.V., p. 1065–1085.

Percival, J.A., and Easton, R.M., 2007, Geology of the Canadian Shield in Ontario: an update: no. 5511.

Percival, J.A., and Helmstaedt, H., 2006, The Western Superior Province Lithoprobe and NATMAP transects: introduction and summary: Canadian Journal of Earth Sciences, v. 43, p. 743–747.

Percival, J.A., and Williams, H.R., 1989, Late Archean Quetico accretionary complex, Superior province, Canada: Geology, v. 17, no. 1, p. 23.

Percival, J.A., McNicoll, V., and Bailes, A.H., 2006a, Strike-slip juxtaposition of ca. 2.72 Ga juvenile arc and >2.98 Ga continent margin sequences and its implications for Archean terrane accretion, western Superior Province, Canada: Canadian Journal of Earth Sciences, v. 43, no. 7, p. 895–927.

Percival, J.A., Sanborn-Barrie, M., Skulski, T., Stott, G.M., Helmstaedt, H., and White, D.J., 2006b, Tectonic evolution of the western Superior Province from NATMAP and Lithoprobe studies: Canadian Journal of Earth Sciences, v. 43, no. 7, p. 1085–1117.

Prichard, H.M., Knight, R.D., Fisher, P.C., McDonald, I., Zhou, M.-F., and Wang, C.Y., 2013, Distribution of platinum-group elements in magmatic and altered ores in the Jinchuan intrusion, China: an example of selenium remobilization by postmagmatic fluids: Mineralium Deposita, v. 48, no. 6, p. 767–786.

Pufahl, P.K., Hiatt, E.E., and Kyser, T.K., 2010, Does the Paleoproterozoic Animikie Basin record the sulfidic ocean transition? Geology, v. 38, no. 7, p. 659–662.

Queffurus, M., and Barnes, S.-J., 2015, A review of sulfur to selenium ratios in magmatic nickel–copper and platinum-group element deposits: Ore Geology Reviews, v. 69, p. 301–324.

Raič, S., and Mogessie, A., 2015, Arsenic-rich Cu-Ni-PGE Mineralization in Wetlegs, Duluth Complex, St. Louis County, Minnesota, USA: The Canadian Mineralogist, v. 53, p. 105–132.

Ripley, E.M., and Li, C., 2003, Sulfur Isotope Exchange and Metal Enrichment in the Formation of Magmatic Cu-Ni-(PGE) Deposits: Economic Geology, v. 98, no. 3, p. 635–641.

Ripley, E.M., and Li, C., 2013, Sulfide Saturation in Mafic Magmas: Is External Sulfur Required for Magmatic Ni-Cu-(PGE) Ore Genesis? Economic Geology, v. 108, no. 1, p. 45–58.

Sanborn-Barrie, M., and Skulski, T., 2006, Sedimentary and structural evidence for 2.7 Ga continental arc-oceanic-arc collision in the Savant-Sturgeon greenstone belt, western Superior Province, Canada: Canadian Journal of Earth Sciences, v. 43, p. 995–1030.

Schwarzenbach, E.M., Gazel, E., and Caddick, M.J., 2014, Hydrothermal processes in partially serpentinized peridotites from Costa Rica: evidence from native copper and complex sulfide assemblages: Contributions to Mineralogy and Petrology, v. 168, no. 5.

Schwarzenbach, E.M., Vrijmoed, J.C., Engelmann, J.M., Liesegang, M., Wiechert, U., Rohne, R., and Plümper, O., 2021, Sulfide Dissolution and Awaruite Formation in Continental Serpentinization Environments and Its Implications to Supporting Life: Journal of Geophysical Research: Solid Earth, v. 126, no. 5.

Seat, Z., Beresford, S.W., Grguric, B.A., Waugh, R.S., Hronsky, J.M.A., Gee, M.A.M., Groves, D.I., and Mathison, C.I., 2007, Architecture and emplacement of the Nebo–Babel gabbronorite-hosted magmatic Ni–Cu–PGE sulphide deposit, West Musgrave, Western Australia: Mineralium Deposita, v. 42, no. 6, p. 551–581.

Song, X.-Y., Keays, R.R., Zhou, M.-F., Qi, L., Ihlenfeld, C., and Xiao, J.-F., 2009, Siderophile and chalcophile elemental constraints on the origin of the Jinchuan Ni-Cu-(PGE) sulfide deposit, NW China: Geochimica et Cosmochimica Acta, v. 73, no. 2, p. 404–424.

Southwick, D.L., 1991, On the genesis of Archean granite through two-stage melting of the Quetico accretionary prism at a transpressional plate boundary: Geological Society of America Bulletin, v. 103, no. 11.

Stott, G.M., 1997, The Superior Province, Canada, in de Wit, M.J. and Ashwal, L.D. eds., Greenstone Belts: Oxford Clarendon Press, p. 480–507.

Stott, G.M., 2011, A revised terrane subdivision of the Superior Province in Ontario: Ontario Geological Survey: Miscellaneous Release—Data 278.

Stott, G.M., Corkery, M.T., Percival, J.A., Simard, M., and Goutier, J., 2010, A Revised Terrane Subdivision of the Superior Province: Ontario Geological Survey Summary of Field Work and Other Activities: no. 6260, p.20-1 to 20–10p.

Sun, S. -s., and McDonough, W.F., 1989, Chemical and isotopic systematics of oceanic basalts: implications for mantle composition and processes: Geological Society, London, Special Publications, v. 42, no. 1, p. 313–345.

Sutcliffe, R.H., 1991, Proterozoic Geology of the Lake Superior Area, in Geology of Ontario: Ontario Geological Survey, p. 627–658.

Swanson-Hysell, N.L., Ramezani, J., Fairchild, L.M., and Rose, I.R., 2019, Failed rifting and fast drifting: Midcontinent Rift development, Laurentia's rapid motion and the driver of Grenvillian orogenesis: GSA Bulletin, v. 131, nos. 5–6, p. 913–940.

Swanson-Hysell, N.L., Hoaglund, S.A., Crowley, J.L., Schmitz, M.D., Zhang, Y., and Miller, J.D., 2021, Rapid emplacement of massive Duluth Complex intrusions within the North American Midcontinent Rift: Geology, v. 49, no. 2, p. 185–189.

Sylvester, P.J., Cabri, L.J., Tubrett, M.N., McMahon, G., Laflamme, J.H.G., and Peregoedova, A., 2005, Synthesis and evaluation of a fused pyrrhotite standard reference material for platinum group element and gold analysis by laser ablation-ICPMS: International Platinum Symposium, 10th, Geological Survey of Finland, Oulu, August 8–11, Extended Abstracts, p. 16–20.

Tabelin, C.B., Igarashi, T., and Takahashi, R., 2012, Mobilization and speciation of arsenic from hydrothermally altered rock in laboratory column experiments under ambient conditions: Applied Geochemistry, v. 27, no. 1, p. 326–342.

Taranovic, V., Ripley, E.M., Li, C., and Rossell, D., 2015, Petrogenesis of the Ni–Cu–PGE sulfide-bearing Tamarack Intrusive Complex, Midcontinent Rift System, Minnesota: Lithos, v. 212–215, p. 16–31.

Thomas, D.G., Melnyk, J., Gormely, L., Searston, S., and Kulla, G., 2011, Magma Metals Limited, Thunder Bay North Polymetallic Project, Ontario, Canada, NI 43-101 Technical Report on Preliminary Assessment: Interal Report: amec.

Trevisan, B.E., 2015, The petrology, mineralization, and regional context of the Thunder mafic to ultramafic intrusion, Midcontinent Rift, Thunder Bay, Ontario: Lakehead University: unpublished MSc thesis.

Wang, C., Song, S., Wei, C., Su, L., Allen, M.B., Niu, Y., Li, X.-H., and Dong, J., 2019, Palaeoarchaean deep mantle heterogeneity recorded by enriched plume remnants: Nature Geoscience, v. 12, no. 8, p. 672–678.

Wang, S., Kuzmich, B., Hollings, P., Zhou, T., and Wang, F., 2020, Petrogenesis of the Dog Lake Granite Chain, Quetico Basin, Superior Province, Canada: Implications for Neoarchean crustal growth: Precambrian Research, v. 346.

Wang, S.-M., Wu, C.-Z., Muhtar, M.N., Lei, R.-X., and Brzozowski, M.J., 2021, Mobilization of ore-forming metals during post-magmatic hydrothermal overprinting of the Huangshandong Ni–Cu sulfide deposit, Eastern Tianshan, NW China: Ore Geology Reviews, v. 137.

Wedepohl, K.H., 1995, The composition of the continental crust: Geochimica et Cosmochimica Acta, v. 59, no. 7, p. 1217–1232.

White, A.J.R., and Chappell, B.W., 1983, Granitoid types and their distribution in the Lachlan Fold Belt, southeastern Australia, in Geological Society of America Memoirs: Geological Society of America, p. 21–34.

White, D.J., Musacchio, G., Helmstaedt, H.H., Harrap, R.M., Thurston, P.C., van der Velden, A., and Hall, K., 2003, Images of a lower-crustal oceanic slab: Direct evidence for tectonic accretion in the Archean western Superior province: Geology, v. 31, no. 11, p. 997.

Williams, H.R., 1991, Quetico Subprovince, in Geology of Ontario: Ontario Geological Survey, p. 383–403.

Williams, H.R., Stott, G.M., Thurston, P.C., Sutcliffe, R.H., Bennett, G., Easton, R.M., and Armstrong, D.K., 1992, Tectonic Evolution of Ontario: Summary and Synthesis, in Geology of Ontario: Ontario Geological Survey, p. 1255–1332.

Wilson, S.A., Ridley, W.I., and Koenig, A.E., 2002, Development of sulfide calibration standards for the laser ablation inductively-coupled plasma mass spectrometry technique: J. Anal. At. Spectrom., v. 17, no. 4, p. 406–409.

Winter, J.D., 2001, An Introduction to Igneous and Metamorphic Petrology: Prentice Hall.

Wood, S.A., Mountain, B.W., and Fenlon, B.J., 1989, Thermodynamic constraints on the solubility of platinum and palladium in hydrothermal solutions; reassessment of hydroxide, bisulfide, and ammonia complexing: Economic Geology, v. 84, no. 7, p. 2020–2028.

Wood, S.A., Pan, P., Zhang, Y., and Mucci, A., 1994, The solubility of Pt and Pd sulfides and Au in bisulfide solutions: I. Results at 25°–90°C and 1 bar pressure: Mineralium Deposita, v. 29, no. 4.

Woodruff, L.G., Schulz, K.J., Nicholson, S.W., and Dicken, C.L., 2020, Mineral deposits of the Mesoproterozoic Midcontinent Rift system in the Lake Superior region – A space and time classification: Ore Geology Reviews, v. 126, p. 103716.

Yahia, K., 2023, Geochemistry of Midcontinent Rift related intrusions near Thunder Bay: Lakehead University: unpublished MSc thesis.

Zhang, H., Lee, S., Wolin, E., Bollmann, T.A., Revenaugh, J., Wiens, D.A., Frederiksen, A.W., Darbyshire, F.A., Aleqabi, G.I., Wysession, M.E., Stein, S., and Jurdy, D.M., 2016, Distinct crustal structure of the North American Midcontinent Rift from *P* wave receiver functions: Journal of Geophysical Research: Solid Earth, v. 121, no. 11, p. 8136–8153.

Appendix A – Sample Information

*Depths in metres.

Sample ID	Hole ID	Location	From	To	Pd + Pt (ppm)	Lithology	Mineralization	Methods
CAM-21-CC-001	ELR20-025	High-grade zone	296.6	296.9	-	grey hybrid	-	whole-rock
CAM-21-CC-002	ELR20-025	High-grade zone	300.5	300.6	-	oxide gabbro	-	whole-rock
CAM-21-CC-003	ELR20-025	High-grade zone	315.7	315.9	-	gabbro	-	petrography
CAM-21-CC-005	ELR20-025	High-grade zone	358.1	358.5	2.50	feldspathic wehrlite	disseminated	petrography, LA–ICP–MS
CAM-21-CC-007	ELR20-025	High-grade zone	379.1	379.3	2.12	feldspathic wehrlite	disseminated + veinlet	petrography, LA–ICP–MS
CAM-21-CC-008	ELR20-025	High-grade zone	393.9	394.3	5.48	dunite	net-textured	petrography, LA–ICP–MS
CAM-21-CC-009	ELR20-025	High-grade zone	398.4	398.9	7.08	wehrlite	net-textured	petrography, LA–ICP–MS, SIMS, MLA
CAM-21-CC-011	ELR20-025	High-grade zone	403.6	404.0	12.01	dunite	net-textured	petrography, LA–ICP–MS, SIMS, MLA
CAM-21-CC-010	ELR20-025	High-grade zone	401.0	401.4	7.64	feldspathic wehrlite	net-textured	petrography; quick log
CAM-21-CC-012	ELR20-025	High-grade zone	416.2	416.6	1.69	wehrlite	strongly disseminated	petrography; quick log
CAM-21-CC-013	ELR20-025	High-grade zone	421.5	421.8	4.30	feldspathic wehrlite	net-textured	petrography
CAM-21-CC-014	ELR20-025	High-grade zone	431.6	432.1	0.82	wehrlite	disseminated	petrography; quick log
CAM-21-CC-015	ELR20-025	High-grade zone	441.0	441.3	0.80	wehrlite	disseminated	petrography; quick log
CAM-21-CC-016	ELR20-025	High-grade zone	452.5	452.9	0.03	melanocratic gabbro	trace	petrography; quick log
CAM-21-CC-019	ELR20-025	High-grade zone	489.2	489.4	0.03	melanocratic gabbro	trace	petrography, LA–ICP–MS
CAM-21-CC-020	ELR20-025	High-grade zone	501.0	501.2	0.00	metasedimentary schist	-	petrography, whole-rock, SIMS
CAM-21-CC-023	ELR20-002	High-grade zone	296.9	297.2	0.00	gabbro	-	petrography, whole-rock
CAM-21-CC-024	ELR20-002	High-grade zone	313.9	314.3	0.11	wehrlite	trace	petrography, whole-rock
CAM-21-CC-025	ELR20-002	High-grade zone	329.2	329.4	0.19	wehrlite	trace + veinlet	petrography
CAM-21-CC-026	ELR20-002	High-grade zone	331.4	331.7	0.18	wehrlite	trace	petrography
CAM-21-CC-027	ELR20-002	High-grade zone	336.0	336.1	0.32	wehrlite	trace	petrography, SIMS
CAM-21-CC-028	ELR20-002	High-grade zone	349.4	349.7	0.35	feldspathic wehrlite	weakly disseminated	petrography; quick log
CAM-21-CC-029	ELR20-002	High-grade zone	359.1	359.4	0.66	feldspathic wehrlite	weakly disseminated	petrography; quick log
CAM-21-CC-030	ELR20-002	High-grade zone	371.5	371.6	0.35	wehrlite	trace + veinlet	petrography, LA–ICP–MS
CAM-21-CC-032	ELR20-002	High-grade zone	389.0	389.3	3.53	feldspathic wehrlite	strongly disseminated	petrography; quick log
CAM-21-CC-033	ELR20-002	High-grade zone	400.1	400.4	11.71	feldspathic wehrlite	net-textured	petrography, LA–ICP–MS

Sample ID	Hole ID	Location	From	To	Pd + Pt (ppm)	Lithology	Mineralization	Methods
CAM-21-CC-034	ELR20-002	High-grade zone	414.0	414.3	2.21	feldspathic wehrlite	strongly disseminated	petrography; quick log
CAM-21-CC-035	ELR20-002	High-grade zone	426.0	426.1	0.31	olivine melagabbro	trace + veinlet	petrography, LA–ICP–MS, SIMS
CAM-21-CC-037	ELR20-002	High-grade zone	443.3	443.7	0.00	metasedimentary schist	-	petrography, whole-rock, LA–ICP–MS, SIMS
CAM-21-CC-038	ELR20-004	High-grade zone	300.8	301.4	0.00	gabbro	-	petrography, whole-rock
CAM-21-CC-039	ELR20-004	High-grade zone	321.3	321.7	0.19	wehrlite	trace	petrography, whole-rock
CAM-21-CC-041	ELR20-004	High-grade zone	344.0	344.3	0.27	wehrlite	weakly disseminated	petrography; quick log
CAM-21-CC-042	ELR20-004	High-grade zone	363.7	364.2	1.76	feldspathic wehrlite	weakly disseminated	petrography, LA–ICP–MS
CAM-21-CC-043	ELR20-004	High-grade zone	382.3	382.7	0.29	wehrlite	trace	petrography; quick log
CAM-21-CC-044	ELR20-004	High-grade zone	400.0	400.4	10.60	dunite	net-textured	petrography, LA–ICP–MS, SIMS, MLA
CAM-21-CC-045	ELR20-004	High-grade zone	404.3	404.7	9.53	dunite	net-textured	petrography, LA–ICP–MS, SIMS
CAM-21-CC-046	ELR20-004	High-grade zone	430.4	430.8	3.27	feldspathic wehrlite	strongly disseminated + veinlet	petrography, LA–ICP–MS, MLA
CAM-21-CC-047	ELR20-004	High-grade zone	452.8	453.2	0.05	feldspathic wehrlite	trace	petrography; quick log
CAM-21-CC-048	ELR20-004	High-grade zone	475.1	475.6	5.34	feldspathic wehrlite	net-textured + veinlet	petrography, LA–ICP–MS, MLA
CAM-21-CC-049	ELR20-004	High-grade zone	491.4	491.8	0.68	feldspathic wehrlite	weakly disseminated	petrography; quick log
CAM-21-CC-050	ELR20-004	High-grade zone	521.9	522.3	0.84	feldspathic wehrlite	weakly disseminated	petrography; quick log
CAM-21-CC-052	ELR20-004	High-grade zone	558.1	558.5	-	metasedimentary schist	-	petrography, whole-rock
CAM-21-CC-053	ELR20-015	N perimeter	307.7	308.0	0.08	gabbro	trace	petrography, whole-rock
CAM-21-CC-054	ELR20-015	N perimeter	317.8	318.2	0.18	wehrlite	trace	petrography, whole-rock
CAM-21-CC-055	ELR20-015	N perimeter	318.6	318.7	0.29	wehrlite	trace	petrography; quick log
CAM-21-CC-057	ELR20-015	N perimeter	352.0	352.5	0.31	wehrlite	weakly disseminated	petrography; quick log
CAM-21-CC-058	ELR20-015	N perimeter	371.0	371.5	0.47	wehrlite	weakly disseminated	petrography; quick log
CAM-21-CC-059	ELR20-015	N perimeter	387.8	388.1	1.04	wehrlite	weakly disseminated	petrography; quick log
CAM-21-CC-060	ELR20-015	N perimeter	396.3	396.5	4.89	wehrlite	weakly disseminated + veinlet	petrography, LA–ICP–MS, MLA
CAM-21-CC-061	ELR20-015	N perimeter	399.3	399.6	5.60	melanocratic gabbro	disseminated	petrography, LA–ICP–MS, MLA
CAM-21-CC-065	ELR20-015	N perimeter	432.0	432.3	-	metasedimentary schist	-	petrography, whole-rock
CAM-21-CC-066	ELR20-006	S perimeter	300.8	301.3	0.14	gabbro	trace	whole-rock
CAM-21-CC-068	ELR20-006	S perimeter	317.2	317.6	0.14	wehrlite	trace	whole-rock
CAM-21-CC-069	ELR20-006	S perimeter	343.1	343.5	0.12	wehrlite	trace	petrography; quick log
CAM-21-CC-070	ELR20-006	S perimeter	368.4	368.7	0.28	wehrlite	weakly disseminated	petrography; quick log
CAM-21-CC-071	ELR20-006	S perimeter	378.7	379.1	3.46	melanocratic gabbro	weakly disseminated	petrography, LA–ICP–MS, MLA

Sample ID	Hole ID	Location	From	To	Pd + Pt (ppm)	Lithology	Mineralization	Methods
CAM-21-CC-072	ELR20-006	S perimeter	383.0	383.3	4.30	melanocratic gabbro	weakly disseminated + veinlet	petrography, LA–ICP–MS, MLA
CAM-21-CC-074	ELR20-006	S perimeter	413.9	414.3	0.16	wehrlite	disseminated	petrography; quick log
CAM-21-CC-077	ELR20-006	S perimeter	450.9	451.0	0.05	wehrlite	disseminated	petrography; quick log
CAM-21-CC-079	ELR20-006	S perimeter	496.0	496.4	0.15	feldspathic wehrlite	weakly disseminated	petrography; quick log
CAM-21-CC-080	ELR20-006	S perimeter	521.0	521.4	-	granitoid	-	whole-rock
CAM-21-CC-081	ELR20-006	S perimeter	529.3	529.5	-	granitoid	-	whole-rock
CAM-21-CC-082	ELR20-018	W perimeter	298.1	298.5	0.13	gabbro	trace	whole-rock
CAM-21-CC-083	ELR20-018	W perimeter	317.3	317.6	0.17	wehrlite	trace	whole-rock
CAM-21-CC-087	ELR20-018	W perimeter	390.9	391.3	2.63	melanocratic gabbro	strongly disseminated	petrography, LA–ICP–MS, MLA
CAM-21-CC-088	ELR20-018	W perimeter	396.4	396.7	2.99	feldspathic wehrlite	weakly disseminated + veinlet	petrography, LA–ICP–MS
CAM-21-CC-089	ELR20-018	W perimeter	399.6	400.3	5.93	melanocratic gabbro	disseminated + veinlet	petrography, LA–ICP–MS, SIMS, MLA
CAM-21-CC-090	ELR20-018	W perimeter	425.1	425.3	-	metasedimentary schist	-	whole-rock
CAM-21-CC-092	ELR20-018	W perimeter	519.2	519.5	0.05	wehrlite	weakly disseminated	petrography; quick log
CAM-21-CC-094	ELR20-011	E perimeter	323.4	323.8	0.04	gabbro	trace	whole-rock
CAM-21-CC-095	ELR20-011	E perimeter	343.5	343.9	0.12	wehrlite	trace	whole-rock
CAM-21-CC-097	ELR20-011	E perimeter	380.2	380.5	0.21	wehrlite	trace	petrography; quick log
CAM-21-CC-098	ELR20-011	E perimeter	389.2	389.5	0.78	wehrlite	trace	petrography; quick log
CAM-21-CC-099	ELR20-011	E perimeter	398.0	398.3	4.48	feldspathic wehrlite	disseminated	petrography; quick log
CAM-21-CC-100	ELR20-011	E perimeter	399.0	399.4	5.60	feldspathic wehrlite	net-textured to strongly disseminated	petrography, LA–ICP–MS, SIMS
CAM-21-CC-101	ELR20-011	E perimeter	403.6	404.0	5.66	feldspathic wehrlite	strongly disseminated + veinlet	petrography, LA–ICP–MS, SIMS, MLA
CAM-21-CC-103	ELR20-011	E perimeter	440.6	440.8	-	metasedimentary schist	-	whole-rock
CAM-21-CC-116	ELR20-002	High-grade zone	392.1	392.6	6.03	feldspathic wehrlite	net-textured	petrography, LA–ICP–MS, SIMS, MLA
CAM-21-CC-117	ELR20-002	High-grade zone	399.3	399.5	10.64	wehrlite	net-textured + veinlet	petrography, LA–ICP–MS, MLA
CAM-21-CC-118	11CL0005	High-grade zone	380.0	380.1	0.14	wehrlite	trace	petrography; quick log
CAM-21-CC-119	11CL0005	High-grade zone	397.5	397.6	5.31	feldspathic wehrlite	strongly disseminated	petrography; quick log
CAM-21-CC-120	11CL0005	High-grade zone	401.1	401.2	13.18	feldspathic wehrlite	net-textured	petrography, LA–ICP–MS, MLA
CAM-21-CC-121	11CL0005	High-grade zone	403.2	403.6	13.07	feldspathic wehrlite	net-textured	petrography, MLA
CAM-21-CC-122	11CL0005	High-grade zone	411.4	411.5	4.74	dunite	disseminated	petrography, LA–ICP–MS
CAM-21-CC-124	12CL0012	High-grade zone	411.5	411.9	3.11	feldspathic wehrlite	disseminated	petrography, LA–ICP–MS, MLA

Appendix B – Petrographic Descriptions

*HGZ = high-grade zone, per. = perimeter

Sample ID: CAM-21-CC-003	***Depth:* 315.65 m**	***Location:* HGZ**	***CAM Code:* Mg**	***Rock Type:* Altered Gabbro**
Mineral	*Abundance*	*Habit*	*Grain Size*	*Comments*
Clinopyroxene	50%	Equant to elongate; subhedral	Fine to medium	Relatively fresh, unaltered with cumulus texture. Simple twinning is common. One to two cleavage planes often visible. Commonly exhibits undulatory extinction.
Plagioclase	40%	Interstitial; anhedral	Medium	Comprises the intercumulus mineralogy. Intensely altered to very fine-grained (gritty) sericite, with localized patches of fine-grained radial aggregates of chlorite.
Olivine	5%	Anhedral to subhedral	Fine	Completely pseudomorphed; no relict olivine apparent. Pervasive replacement is mostly by iddingsite; some grains do not display as advanced alteration and are serpentinized. Crystal faces preserved in some grains owing to identification as olivine.
Alteration assemblage	45%	Interstitial; anhedral to radial aggregates	Fine to very fine	Full assemblage includes iddingsite + serpentine, sericite + chlorite, with local talc alteration. Chiefly confined to interstices between clinopyroxene grains.
Fe-Ti oxides	2-3%	Intergranular, ameboid; locally boxwork/reticular; locally mottled	Fine to very fine	Strongly anisotropic ilmenite is the dominant oxide phase; displays reddish-grey colouration relative to dark grey-coloured magnetite. Magnetite occurs as mottled intergrowths with ilmenite in intergranular assemblage. Reticular ilmenite where present, was produced from magnetite exsolution, the latter of which was completely replaced by very fine-grained alteration (chlorite?).
Sulfides	1-2%	Interstitial, disseminated; anhedral to subhedral	Very fine to fine	Assemblage is mostly composed of chalcopyrite and lesser pyrite. Mackinawite occurs in trace abundance within the sulfide assemblage and exhibits a strongly blue to beige anisotropy.
Overall Comments: Strongly altered, homogeneous, fine-grained, weakly foliated, poikilitic, oxide- and sulfide-bearing, gabbro.				

Sample ID: CAM-21-CC-005	**Depth: 358.10 m**	**Location: HGZ**	**CAM Code: Upd**	**Rock Type: Feldspathic wehrlite**
Mineral	*Abundance*	*Habit*	*Grain Size*	*Comments*
Olivine	55-60%	Rounded to subrounded; subhedral to anhedral	Fine	Strongly to pervasively replaced by serpentine; highly fractured and occurs as chadacrysts within clinopyroxene.
Clinopyroxene	15-20%	Oikocrystic; anhedral	Medium to coarse	Relatively fresh with little to no alteration; encloses olivine grains.
Plagioclase	5-10%	Interstitial, anhedral	Fine to very fine	Intensely altered to variable, ultra fine-grained minerals; typically, v.f.g. sericite or a patchy intergrowth of chlorite ± biotite ± talc ± carbonate.
Oxides	3-5%	Multiple habits: (i) interstitial (intergranular) (ii) elongate laths (iii) anhedral chain aggregates	Fine to medium	(i) Constitutes the most abundant and coarsest oxide in the group; moderate anisotropy supportive of ilmenite identification. (ii) Magnetite occurs within the sulfide assemblage and with native copper; appears to be oriented along crystallographic planes; possible product of S-loss/oxidation of chalcopyrite. (iii) Magnetite occurs along fractures of olivine as a by-product of serpentinization.
Pyrrhotite	7-10%	Intergranular; massive or anhedral	Fine to very fine	Constitutes the most abundant sulfide mineral within the messy assemblage.
Chalcopyrite	1-3%	Intergranular; massive or anhedral	Fine to very fine	Tarnishes rapidly and does not show characteristic yellow colour (as seen elsewhere in Escape mineralization). Possibly altered to another Cu-bearing sulfide phase such as bornite, talnakhite or sugakiite.
Mackinawite	1-3%	Intergranular; anhedral to tabular	Fine to very fine	Relatively abundant within the sulfide assemblage; exhibits strong blue–beige anisotropy; possible pervasive replacement of granular pentlandite.
Pentlandite	<1%	Flamed; anhedral, granular	Fine to very fine	Mostly occurs as exsolution flames within pyrrhotite; trace amounts of relict pentlandite remains.
Native copper	<1%	Elongate, thin lenticular	Fine to very fine	Occurs within sulfide assemblage and with magnetite; appears to be oriented along crystallographic planes; possible product of S-loss/oxidation of chalcopyrite.
Overall Comments: Intensely altered, seriate, fine- to medium-grained, weakly foliated, poikilitic, disseminated sulfide-bearing, feldspathic wehrlite. Alteration phases constitute up to 60-80% of the mode. Within the sulfide assemblage commonly occurs an ultra fine-grained, gritty intergrowth of sulfides.				

Sample ID: CAM-21-CC-007	**Depth: 379.1 m**	**Location: HGZ**	**CAM Code: Upd**	**Rock Type: Feldspathic wehrlite**
Mineral	*Abundance*	*Habit*	*Grain Size*	*Comments*
Olivine	~50%	Rounded; occasionally elongate to prismatic	Fine to medium	Olivine exhibits variable intensity of alteration; in particular, the degree of alteration increases as proximity to the centre veinlet increases. Olivine alteration style ranges from strongly serpentinized along fractures to complete (pervasive) replacement. Some olivine grains enclose fine-grained, rounded (circular) pseudomorphs of indeterminate composition.
Clinopyroxene	~20%	Anhedral, oikocrystic	Coarse	Relatively unaltered; encloses olivine chadacrysts.
Plagioclase	~5%	Interstitial	Fine	Estimation of plagioclase mode is difficult due to the intense alteration of interstitial material. Plagioclase is variably altered with some grains exhibiting minor, patchy/gritty sericite; elsewhere plagioclase is altered to a variable assemblage of chlorite ± carbonate ± talc ± sericite.
Alteration assemblage	~10-15%	Interstitial; various habits	Fine to ultra fine	Chlorite is fine-grained, anhedral, and forms aggregates as well as rims on olivine along grain boundaries. Locally, chlorite is fibrous in habit. Calcite is fine- to very fine-grained and forms anhedral aggregates as well. Sericite is very fine-grained, gritty, and often intergrown with the previous two alteration phases. Biotite is also a relatively common phase (~2-5%) and occurs interstitially to olivine. It is fine to medium-grained and often exhibits characteristic basal cleavage in sheets.
Crosscutting veinlet	<5%	Anhedral; granular	Fine to ultra fine	The centre veinlet is composed of a mixture of calcite, magnetite, and serpentine.
Oxides	<2%	(i) Interstitial, rounded (ii) Interstitial, anhedral (iii) Anhedral, chain aggregates	(i) Fine (ii) Fine to medium (iii) Very fine to ultra fine	(i) Magnetite; discrete grains, often associated with sulfides. (ii) Magnetite; intergrown with sulfides; rims and embays sulfides. (iii) Linear magnetite chains within olivine fractures; by-product of serpentinization.
Ore assemblage	<8%	Interstitial; anhedral, massive	Fine to ultra fine	Assemblage is variably altered; assemblage is composed of Po >> Pn > Mkw > Cbn > Native Cu >> Ccp > Val.
Pentlandite	~1-2%	Anhedral to subhedral, fractured	Fine to ultra fine	Often exhibits and ocean-island texture with anastomosing Po ± Mkw running through the fractures.
Mackinawite	~1%	Anhedral, feathery, thin tabular	Very fine to ultra fine	Occurs within and amongst all sulfides. Does not exhibit clear grain boundaries. Light blue-grey in

				colouration; exhibits very strong yellow-beige to bluish anisotropy.
Native Cu	Trace	Anhedral, wispy, elongate	Ultra fine	Occurs along grain boundaries of Po, Mag, and Ccp (where present).
Valleriite	Trace	Platy, acicular, needle-like	Ultra fine	Associated with (trace) relict sulfides, magnetite, and alteration silicates. Strongly anisotropic.
Overall Comments: Moderately serpentinized, homogeneous, fine-grained, non-foliated, poikilitic, sulphide-bearing, feldspathic wehrlite, with a characteristic 2mm-wide crosscutting serpentine-carbonate veinlet.				

Sample ID: CAM-21-CC-008	**Depth: 393.87 m**	**Location: HGZ**	**CAM Code: MmgEL**	**Rock Type: Dunite**
Mineral	*Abundance*	*Habit*	*Grain Size*	*Comments*
Olivine	40-45%	Subhedral to euhedral	Medium to coarse	Weakly serpentinized along fractures. Most grains are altered along the rim to a fine- to ultra fine-grained assemblage of variable composition (mostly talc with ± serpentine ± chlorite ± biotite).
Clinopyroxene	~5%	Oikocrystic; massive, anhedral	Medium to coarse	Occurs in minor abundance compared to similar rocks in the Escape intrusion. Clinopyroxene is effectively unaltered where present. Diagnostic cleavage of clinopyroxene is commonly observed in grains.
Plagioclase	1-2%	Interstitial; pseudomorphic	Fine to very fine	Little to no fresh plagioclase remains; intensely altered to very fine-grained to microcrystalline intergrowth of sericite ± talc ± chlorite ± biotite. Biotite occurs along the interface between sulfides and silicates – it is readily identified by its brown colour in plane polarized light and platy, micaceous habit.
Oxides	2-5%	(i) Chadacrystic; anhedral to euhedral (ii) Interstitial; anhedral	(i) Very fine (ii) Fine to medium	(i) Ubiquitous chromite occurs throughout silicate minerals. (ii) Magnetite occurs as intergrowth with sulfide assemblage.
Pyrrhotite	~20%	Intergranular; massive, anhedral	Fine to medium	Constitutes majority of the net-textured sulfide assemblage. Appears anomalously isotropic in this sample.
Chalcopyrite	~10%	Intergranular; massive, anhedral	Fine to medium	Exhibits texture that is in equilibrium with pyrrhotite.
Pentlandite	3-5%	Two habits: (i) anhedral, granular aggregates (ii) flamed; dendritic	Fine to very fine	Aggregates are commonly found along grain boundaries between pyrrhotite and chalcopyrite. Exsolution flames are present in pyrrhotite and appear to cluster together.
Pyrite	<3%	Subhedral to anhedral cubic	Fine	Distinguished from pentlandite by its cubic habit and higher reflectance.
Cubanite	<1%	Anhedral to tabular	Fine	Occurs as trace exsolutions in chalcopyrite.
Mackinawite	<<1%	Anhedral	Very fine	Very low abundance, not readily located within the section; exhibits strong bluish anisotropy.
Overall Comments: Weakly altered, homogeneous, medium-grained, weakly foliated, poikilitic, sulfide-rich dunite. Alteration assemblage accounts for ~5-10% of the mode. Thin stringers of talc ± chlorite ± biotite cut through grains of the net-textured sulfides**.** Trace (<<1%) very fine-grained, sub hexagonal apatite grains occur within the sample.				

Sample ID: CAM-21-CC-009	**Depth: 398.41 m**	**Location: HGZ**	**CAM Code: MmgEL**	**Rock Type: Sulfidic wehrlite**
Mineral	*Abundance*	*Habit*	*Grain Size*	*Comments*
Olivine	~30-40%	Granular, rounded, subhedral, locally prismatic	Fine to medium	Olivine commonly displays zoned extinction under cross polarized light. Rim replacement is common in olivine grains by microcrystalline, anhedral talc ± chlorite ± sericite. Locally, olivine contains rounded, pseudomorphic inclusions, with are variably composed of ± chlorite ± sericite ± calcite.
Clinopyroxene	~20-30%	Anhedral, oikocrystic	Coarse	Clinopyroxene commonly shows zoned extinction under cross polarized light, and locally it is weakly altered to amphibole at grain boundaries. Diagnostic cleavage is present locally, as well as twinning down the centre of grains.
Plagioclase	~8-15%	Interstitial, anhedral	Very fine	Intensely altered to a variable assemblage consisting of very fine-grained to fibrous chlorite ± sericite ± talc ± very fine-grained anhedral to tabular biotite (commonly rims sulfides). Very few relict plagioclase cores remain in the sample.
Magnetite	~1-3%	(i) Interstitial, anhedral (ii) Anhedral, chain aggregates	(i) Fine (ii) Ultra fine	(i) Associated with sulfides, which are often grown around magnetite. (ii) Occurs within fractures in olivine; by-product of serpentinization.
Chromite	<1%	Subhedral	Very fine	Occurs as chadacrysts enclosed by both olivine and clinopyroxene.
Pyrrhotite	~10-20%	Interstitial, anhedral (massive)	Medium to fine	Occurs as the most abundant sulfide within the net-textured sulfide assemblage.
Chalcopyrite	~5-10%	Interstitial, anhedral	Fine to medium	Occurs interstitial to Po and is often found at the silicate-sulfide interface.
Pentlandite	~2-5%	(i) Interstitial; anhedral (granular) aggregates (ii) 'Flames'	(i) Fine to very fine (ii) Ultra fine	(i) Occur as clusters/veinlets within the sulfide assemblage, and commonly interface between Po and Ccp. (ii) Occur within Po; commonly emanates perpendicular to fractures.
Overall Comments: Variably altered, homogeneous, medium-grained, non-foliated, poikilitic, sulfidic wehrlite with interstitial sulfides in excess of 20-30% modally.				

Sample ID: CAM-21-CC-011	**Depth: 403.6 m**	**Location: HGZ**	**CAM Code: MmgEL**	**Rock Type: Dunite**
Mineral	*Abundance*	*Habit*	*Grain Size*	*Comments*
Olivine	~65%	Euhedral to prismatic; rounded	Fine to medium	Strongly serpentinized, particularly along fractures. Occurs as chadacrysts in Cpx.
Clinopyroxene	~5%	Anhedral, oikocrystic	Medium	Mostly fresh, minor serpentinization locally along fractures. Altered to amphibole locally.
Plagioclase	~5%	Interstitial; anhedral	Fine	Patchy alteration to chlorite, saussurite (+ actinolite?). Intergrown with biotite locally.
Oxides	~5%	(i) Subhedral chadacrysts (ii) Interstitial, rounded (i) Anhedral chain aggregates	(i) Fine to ultra fine (ii) Fine to very fine (iii) Ultra fine	(i) Chromite in silicates (ii) Fe-Ti oxides intergrown with sulfides (iii) Magnetite within olivine fractures; by-product of serpentinization
Pyrrhotite	~10%	Interstitial; anhedral	Fine	Troilite exsolutions abundant throughout section. Trace u.f.g. PGMs found within Po.
Chalcopyrite	5-7%	Interstitial; anhedral	Fine	Trace cubanite exsolutions.
Pentlandite	2-3%	(i) Granular aggregates (ii) Flames	Fine to ultra fine	Anhedral grains line interface between Po and Ccp, also commonly grown along fractures in Po. Flames occur within Po and are commonly orthogonal to fractures in Po.
Overall Comments: Moderately serpentinized, seriate, fine- to medium-grained, non-foliated, poikilitic, net-textured sulfide-bearing, dunite, with a characteristic (but subtle) talc-carbonate (± serpentine) veinlet crosscutting the groundmass.				

Sample ID: CAM-21-CC-013	**Depth: 421.5 m**	**Location: HGZ**	**CAM Code: Upd**	**Rock Type: Feldspathic wehrlite**
Mineral	*Abundance*	*Habit*	*Grain Size*	*Comments*
Olivine	~20-30%	Rounded, anhedral	Fine	Occurs as chadacrysts within clinopyroxene. Moderately serpentinized along fractures.
Clinopyroxene	~25-30%	Anhedral, oikocrystic	Coarse	Mostly unaltered, locally altered to amphibole along grain boundaries (amphibole alteration exhibits characteristic cleavage).
Plagioclase	~5-8%	Interstitial, anhedral	Fine to very fine	Often exhibits undulatory to zoned extinction. Variably altered (in both intensity and assemblage) throughout the section; ranges from almost fresh with minor gritty sericite to complete replacement.
Alteration assemblage	~15-20%	Various interstitial; anhedral, fibrous, aggregates	Fine to very fine	Consists of chlorite + sericite ± biotite ± calcite ± talc ± serpentine. Alteration (of chlorite in particular) is strongest along grain boundaries and where silicates interface with sulfides.
Oxides	~1-2%	(i) Rounded (ii) Subhedral (iii) Anhedral	(i) Very fine (ii) Medium to fine (iii) Very fine	(i) Chromite chadacrysts in silicates. (ii) Magnetite phenocrysts, often associated with sulfides which wrap around. Commonly exhibits ilmenite lamellae in a boxwork (reticular) fashion. (iii) Linear chain aggregates found within olivine fractures; by-product of serpentinization.
Pyrrhotite	~20%	Interstitial, anhedral	Medium	Strongly anisotropic; constitutes the majority of the interstitial sulfide assemblage.
Pentlandite	~5%	Interstitial, anhedral (granular) aggregates; flames	Fine to very fine	Granular aggregates often occur at the interface/boundary between Po and Ccp. Flame textures within pyrrhotite are abundant and tend to propagate outward (perpendicular) from fractures in Po.
Chalcopyrite	~4%	Interstitial, anhedral	Fine to medium	Often occurs at the edge of the sulfide assemblage and appears to wrap around and/or embay the other two sulfides.
Cubanite	~1%	Laths/lamellae	Fine	Occur as thin lamellae within Ccp. Appears greenish yellow in colouration when compared to Ccp.
Overall Comments: Strongly serpentinized, seriate, medium-grained, weakly to moderately foliated, poikilitic, sulphide-bearing, feldspathic wehrlite. This sample is characterized by net-textured (varies to intensely disseminated) sulphide minerals which occupy the interstitial space.				

Sample ID: CAM-21-CC-019	**Depth: 419.17 m**	**Location: HGZ**	**CAM Code: MmgEL**	**Rock Type: Altered melanocratic gabbro**
Mineral	*Abundance*	*Habit*	*Grain Size*	*Comments*
Olivine	40-45%	Rounded; subhedral to anhedral	Fine to very fine	Intensely altered along fractures and boundaries/rim; some crystals are completely pseudomorphed to ± serpentine ± talc.
Clinopyroxene	~10-15%	Oikocrystic; massive, anhedral	Medium to fine	Alteration varies through the thin section; some oikocrysts cores are still fresh. Some grained are uralitized. Original grain boundaries are obscured due to intense alteration of interstitial material.
Plagioclase	~10-15%	Interstitial/intergranular; anhedral	Fine to very fine	Intensely altered with distribution of alteration variable. Alteration is often microcrystalline (gritty) sericite, but elsewhere occurs talc ± chlorite ± sericite ± serpentine (see below). Polysynthetic twinning visible locally.
Alteration assemblage	~20-30%	Anhedral, polycrystalline aggregates; biotite is often micaceous	Very fine to ultra fine	The alteration assemblage constitutes the most dominant group of phases in the section. Composed of complex intergrowths of talc ± chlorite ± sericite ± serpentine ± biotite.
Oxides	~1%	(i) Subhedral (ii) Intergranular; rounded/anhedral (iii) Anhedral, chain aggregates	(i) Very fine to ultra fine (ii) Fine to very fine (iii) Very fine to ultra fine	(i) Chromite chadacrysts in silicates. (ii) Mottling of multiple Fe-Ti oxides; ilmenite positively identified due to strong anisotropy, also contains magnetite and possibly hematite; assemblage often associated/intergrown with sulfides. Locally intergranular oxides associated with sulfides exhibit thin oriented ilmenite exsolution lamellae with "boxwork" or reticular habit. (iii) Magnetite found in fractures of olivine; by-product of serpentinization.
Sulfides	~5-6%	-	-	-
Pyrite	~4%	Anhedral to euhedral; island mineral in an "island-ocean" texture	Very fine to fine	Most abundant sulfide in section and appears highly reflective and isotropic. Exhibits and angular, 'fractured'-like appearance by which pyrrhotite occupies the fractures.
Pyrrhotite	~1-2%	Anhedral, anastomosing; ocean mineral in an "island-ocean" texture	Very fine to fine	Moderately anisotropic. Resembles a "sea" of pyrrhotite with "islands" of pyrite.
Chalcopyrite	<<1%	Anhedral	Ultra fine	Trace wisps/blebs (disseminations) of chalcopyrite found in the section.
Overall Comments: Pervasively altered, seriate, fine-grained, non-foliated, poikilitic, melanocratic gabbro. Alteration is super intense which is reflected in the silicate, oxide, and sulfide phases.				

Sample ID: CAM-21-CC-020	**Depth: 501.0 m**	**Location: Country rock**	**CAM Code: Spt**	**Rock Type: Metasedimentary schist**
Mineral	*Abundance*	*Habit*	*Grain Size*	*Comments*
Feldspar	~70%	Anhedral, granular	Fine	Lithogeochemical data suggests that the main feldspar phase is albite. Feldspar is almost completely replaced by microcrystalline sericite.
Chlorite	~10%	Anhedral, platy	Very fine to ultra fine	Strongly anisotropic, and green colouration in plane polarized light.
Quartz	~20%	Rounded	Fine	Classic undulatory extinction; unaltered/fresh.
Pyrite	<1%	Anhedral	Fine to very fine	Fine disseminations found throughout the groundmass.
Overall Comments: Greenschist facies(?), homogeneous, fine-grained, well foliated, quartz, sericite, chlorite schist.				

Sample ID: CAM-21-CC-023	**Depth: 296.9 m**	**Location: HGZ**	**CAM Code: Mg**	**Rock Type: Altered gabbro**
Mineral	*Abundance*	*Habit*	*Grain Size*	*Comments*
Clinopyroxene	50-55%	Subrounded	Fine to medium	Clinopyroxene is commonly twinned and sometimes displays one or two cleavage planes. Locally Clinopyroxene appears irregularly chloritized, ranging from moderate to strong rim replacement, up to pervasive, intense alteration whereby the grain boundaries are obliterated and there are no relict grains remaining.
Plagioclase	40-45%	Interstitial, anhedral	Fine to very fine	Polysynthetic twinning is faintly recognizable in select relict grains. Plagioclase is strongly to intensely saussuritized with the assemblage being variable, in that some strongly altered crystals display blotchy epidote and pervasive carbonate – elsewhere there is a weaker degree of alteration which is very fine-grained, and with dull interference colours (possibly sericite).
Chlorite	-	Anhedral to radial fibrous/acicular	Very fine	Occurs interstitially to clinopyroxene.
Oxides	~5%	(i) Interstitial, mottled (ii) Interstitial, reticular	(i, ii) Fine	(i) Ilmenite that exhibits strong, mottled anisotropy. (ii) Ilmenite lamellae in a boxwork structure; host magnetite has been altered by chlorite, leaving behind trellis-like ilmenite.
Sulfides	<1%	Anhedral	Very fine to ultra fine	Predominantly composed of discrete Ccp grains. Local pentlandite aggregates which are associated with a grain or two of anisotropic pyrrhotite.
Overall Comments: Variably altered, seriate, fine- to medium-grained, non-foliated, poikilitic, gabbro.				

Sample ID: CAM-21-CC-024	**Depth: 314.0 m**	**Location: HGZ**	**CAM Code: Upd**	**Rock Type: Wehrlite**
Mineral	*Abundance*	*Habit*	*Grain Size*	*Comments*
Olivine	~60%	Rounded, occasionally prismatic	Fine to very fine	Variably serpentinized, with alteration ranging from moderate (along fractures) to complete replacement (pervasive).
Clinopyroxene	~20%	Anhedral, oikocrysts	Medium	Encloses olivine chadacrysts and is relatively fresh/unaltered in comparison.
Plagioclase	~1-3%	Interstitial, anhedral	Fine to very fine	Often intensely altered to saussurite. Difficult to estimate abundance of plagioclase due to irregular alteration, where some grains are intact, and others completely obliterated.
Biotite	~3-5%	Tabular, platy; locally anhedral	Fine to very fine	Associated with feldspar alteration assemblage; locally intergrown with magnetite.
Magnetite	~5%	(i) Interstitial (ii) Anhedral, chain aggregates	(i) Fine (ii) Very fine	(i) Intergrown with and/or rims sulfides. (ii) Occurs within fractures in olivine; by-product of serpentinization.
Sulfides	<1%	Anhedral, irregularly intergrown	Very fine to ultra fine	Ccp > Po >> Pn
Overall Comments: Strongly serpentinized, seriate, fine- to medium-grained, moderately foliated, poikilitic wehrlite, with olivine grains ranging from sub-mm scale up to >1mm.				

Sample ID: CAM-21-CC-025	**Depth: 329.2 m**	**Location: HGZ**	**CAM Code: Upd**	**Rock Type: Wehrlite**
Mineral	*Abundance*	*Habit*	*Grain Size*	*Comments*
Olivine	~40%	Rounded, chadacrystic	Fine	Olivine exhibits progressive alteration with proximity to the crosscutting veinlets. The majority of olivine is pseudomorphed to an assemblage of ultra fine-grained minerals, possibly an aggregate of clay minerals (iddingsite), talc, and serpentine. Distal to the crosscutting veinlets, olivine is completely replaced by serpentine, which accounts for about 20% of olivine in the section.
Clinopyroxene	~20%	Interstitial, oikocrystic	Coarse	Proximal to the crosscutting veinlets, clinopyroxene is replaced by aggregates of ultra fine-grained alteration phases. Distal to the veinlets, where olivine is only serpentinized, clinopyroxene is preserved.
Plagioclase	<5%	Interstitial, anhedral	Fine	Plagioclase is faintly recognizable in some grains with preserve polysynthetic twinning. It is difficult to estimate the true modal abundance of plagioclase due to its intense alteration to a combination of what appears to be sericite ± chlorite ± biotite ± talc.
Magnetite	<5%	(i) Interstitial, anhedral (ii) Anhedral, chain aggregates (iii) Anhedral to blebby	(i) Very fine (ii) Very fine to ultra fine (iii) Fine	(i) Faintly anisotropic; possibly due to minor amounts of ilmenite present as exsolutions. (ii) Occurs within fractures of olivine; by-product of serpentinization. (iii) Appears entrained within the calcite veinlet. Contains abundant specs/flecks of chalcopyrite, which together exhibit an emulsoid texture reminiscent of "chalcopyrite disease"; possibly the result of oxidation of the original sulfide grain(s).
Calcite veinlet	~20%	Anhedral	(i) Medium to fine (calcite) (ii) Ultra fine (serpentine)	The ~3mm-thick veinlet consists of an aggregate of calcite crystals with trace patches of serpentine, which crosscuts the groundmass.
Serpentine stringers	<3%	Radial clusters, fibrous	Fine to ultra fine	The stringers crosscut and displace the central calcite veinlet, doing so at roughly at 90°. The stringers are millimetre-sized and contain minor amounts of blebby/anhedral calcite, but are mostly composed of serpentine. At the margins of the stringers, serpentine is fibrous and aligned perpendicular to the stringer wall. Towards the centre of the stringers, serpentine forms radial aggregates.
Sulfides	<2%	Anhedral	Ultra fine to very fine	(i) Various proportions of Po, Pn, and Ccp occur as disseminations in the groundmass. (ii) Aggregates of Po and minor Mag are present within the main carbonate veinlet; Po here exhibits triple junctions (sub grains) when viewed under crossed nicols.

Overall Comments: Strongly altered, seriate, medium-grained, non-foliated, poikilitic, wehrlite, with a single crosscutting calcite veinlet cut by a series of serpentine stringers.

Sample ID: CAM-21-CC-026	**Depth: 331.4 m**	**Location: HGZ**	**CAM Code: Upd**	**Rock Type: Wehrlite**
Mineral	*Abundance*	*Habit*	*Grain Size*	*Comments*
Olivine	~40-50%	Rounded, chadacrystic	Fine	Intensely serpentinized along fractures, locally pervasively replaced.
Clinopyroxene	~20-25%	Interstitial, oikocrystic	Coarse	Relatively fresh. Commonly exhibits undulatory extinction.
Plagioclase	~5%	Interstitial, anhedral	Fine	Plagioclase exhibits moderate to strong, gritty sericite ± chlorite ± biotite alteration; difficult to estimate modal abundance due to alteration.
Serpentine stringers	~1-3%	Fibrous to anhedral	Fine to ultra fine	Composed of a variable mixture of serpentine ± magnetite ± calcite. Serpentine and magnetite occur normal to the stringer wall.
Oxides	<5%	(i) Interstitial, anhedral to subhedral (ii) Anhedral chain aggregates	(i) Ultra fine to fine (ii) Ultra fine	(i) Composed of both magnetite and ilmenite which are associated with sulfides where present. (ii) Occurs within olivine fractures; by-product of serpentinization.
Sulfides	Trace	Anhedral	Very fine to ultra fine	Too fine to properly identify. Po ± Ccp faintly recognizable.
Overall Comments: Intensely serpentinized, homogeneous, medium-grained, moderately foliated, poikilitic, wehrlite with multiple crosscutting, mm-thick serpentine stringers.				

Sample ID: CAM-21-CC-027	**Depth: 336.0 m**	**Location: HGZ**	**CAM Code: Upd**	**Rock Type: Wehrlite**
Mineral	*Abundance*	*Habit*	*Grain Size*	*Comments*
Olivine	~50-60%	Rounded, chadacrystic	Fine to medium	Intense serpentine alteration occurs along olivine fractures and is locally pervasive. Olivine commonly contains very fine-grained, rounded inclusions which are pseudomorphed.
Clinopyroxene	~30%	Interstitial, oikocrystic	Coarse	Encloses olivine grains and appears relatively unaltered.
Plagioclase	~8-10%	Interstitial, anhedral	Fine	Strongly altered to various phases; most commonly to sericite which occurs along fractures, which creates the appearance of a network of conjugate veinlet sets.
Alteration assemblage	~10-15%	Interstitial; anhedral, fibrous, tabular	Fine to ultra fine	Various assemblage consisting of sericite ± chlorite ± biotite ± calcite. Biotite is commonly tabular and recognizable as discrete crystals. Chlorite commonly forms clusters or aggregates of fibrous crystals.
Serpentine stringers	~1-3%	Fibrous, anhedral	Fine to ultra fine	Predominantly composed of serpentine, but also contain abundant oxides and variable carbonate. Serpentine is fibrous and occurs normal to the stringer walls. These stringers also contain an unidentified dark, yellow-brown mineral (viewed in transmitted light), which is interpreted as possible clay alteration.
Oxides	<5%	(i) Interstitial, anhedral (ii) Anhedral to subhedral, elongate (iii) Anhedral chain aggregates (iv) Subhedral to euhedral	(i, ii) Fine (iii) Very fine to ultra fine (iv) Fine to very fine	(i) Strongly anisotropic ilmenite (Ti-Mag?) occurs commonly with sulfides. (ii) Magnetite occurs alongside a bluish-grey, anisotropic mineral (possibly hematite) within the serpentine stringers, and are roughly oriented normal to the stringer walls. (iii) Occur within olivine fractures; by-product of serpentinization. (iv) Chromite chadacrysts present within silicates.
Ore assemblage	<1%	Interstitial	Fine to ultra fine	Disseminated sulfides are quite variable in assemblage and exhibit complex/chaotic intergrowths.
Pyrrhotite	~0.5%	Massive to subhedral	Fine	Constitutes the majority phase of the ore assemblage. Some cleavage planes visible. Copper minerals are present within Po fractures.
Pentlandite	Trace	Anhedral, granular aggregates	Fine to very fine	Strongly altered along grain boundaries to mackinawite.
Chalcopyrite	Trace	Anhedral	Fine to very fine	Readily tarnishes; commonly associated with Bn-Dg and Native Cu
Digenite-bornite	Trace	Blotchy, anhedral	Fine to very fine	Commonly found within Po and tarnished Ccp; Dg appears blue to bluish grey, whilst Bn appears brown to orange-brown. The two phases are intimately intergrown. Possibly misidentified; tarnished Ccp.
Native Cu	Trace	Disseminated	Very fine to ultra fine	Occurs as irregular disseminations in Po and Ccp.

Mackinawite	Trace	Anhedral, thin tabular	Very fine to ultra fine	Readily identifiable due it its strong blue-beige anisotropy.
Overall Comments: Intensely serpentinized, homogeneous, medium-grained, moderately foliated, poikilitic, weakly mineralized, wehrlite with sub-mm serpentine stringers.				

Sample ID: CAM-21-CC-030	**Depth: 371.5 m**	**Location: HGZ**	**CAM Code: Mgm**	**Rock Type: Wehrlite**
Mineral	*Abundance*	*Habit*	*Grain Size*	*Comments*
Olivine	~40-50%	Anhedral to subhedral; chadacrysts	Fine	Strongly serpentinized, with intensity ranging from moderate along fractures to locally pervasive, with talc (± chlorite) rim replacement. Locally, olivine grains are weakly serpentinized, but show moderately alteration to iddingsite.
Clinopyroxene	~20-30%	Anhedral; oikocrysts	Medium to coarse	Relatively unaltered except within proximity to central crosscutting vein; encloses olivine and orthopyroxene.
Orthopyroxene	~5-10%	Anhedral to subhedral; chadacrysts	Fine	Alteration pattern is same as clinopyroxene.
Plagioclase	~2-5%	Interstitial; anhedral to subhedral	Fine	Locally fresh, ranging to complete replacement by ± saussurite ± chlorite ± talc.
Crosscutting veinlet	-	Anhedral to subhedral	Medium to ultra fine	Predominantly composed of calcite, with lesser amounts of serpentine, chlorite, and talc. Calcite crystals are often subhedral and chlorite/serpentine/talc occur between carbonate grains. A handful of sulfide blebs (irregular, aggregate grains) occur within the veinlet.
Ore assemblage 1	~1-5%	Interstitial	Fine to ultra fine	Po >> Ccp > Pn > Bn(?) > Native Cu The size grain size of the interstitial sulfides ranges to a ultra fine-grained at which they become very difficult to identify. Original grain boundaries appear to be modified. Po is typically massive, but shows deformation twinning and triple junctions under cross nicols. Pentlandite forms anhedral (granular) aggregates where present, while Ccp is anhedral and commonly found at the silicate-sulfide interface. Native Cu is found disseminated within (possible) Bn in trace abundance.
Ore assemblage 2	~1%	Crosscutting (blebs)	Fine	Po >> Pn >> Cbn > Ccp Pyrrhotite occurs as very fine-grained aggregates of grains exhibiting triple junctions and undulatory extinction. Pentlandite occurs within pyrrhotite as clusters, lacks distinct grain boundaries, and is locally intergrown with cubanite (and trace chalcopyrite).
Oxides	~1-3%	(i) Interstitial (ii) Subhedral to anhedral (iii) Anhedral, chain aggregates	(i) Fine (ii) Very fine to ultra fine (iii) Very fine	(i) Ilmenite; moderately anisotropic. (ii) Chromite chadacrysts within silicates. (iii) Magnetite occurring within olivine fractures; by-product of serpentinization.
Overall Comments: Variably altered, homogeneous, fine-grained, non-foliated, poikilitic, wehrlite with a 2-3mm, sulphide-bearing, calcite + serpentine veinlet crosscutting the sample.				

Sample ID: CAM-21-CC-033	**Depth: 400.1 m**	**Location: HGZ**	**CAM Code: Mgm**	**Rock Type: Feldspathic wehrlite**
Mineral	*Abundance*	*Habit*	*Grain Size*	*Comments*
Olivine	30-35%	Rounded, subhedral to anhedral; occasionally prismatic, elongate	Very fine to medium	Strongly serpentinized along fractures. Some olivine cores are surrounded by intense alteration to microcrystalline aggregates of talc ± serpentine ± chlorite ± biotite. Occurs as chadacrysts in clinopyroxene.
Clinopyroxene	20-25%	Oikocrysts; massive, anhedral	Medium to coarse	Mostly fresh; local partial replacement by amphibole. Locally twinning down centre of grains apparent as well.
Plagioclase	5-7%	Interstitial; anhedral to lath-shaped, pseudomorphic	Fine to very fine	Some plagioclase is relatively intact with only weak, gritty microcrystalline sericitization present. Elsewhere, there is intense, complete replacement by sericite ± talc ± chlorite.
Alteration assemblage	~20-30%	(i) Anhedral (polycrystalline aggregates) (ii) Pseudomorphic (amphibole) (iii) Platy (biotite)	Fine to ultra fine	Alteration is variable in terms of mineralogy, but intense generally. Interstitial space is often pervasively replaced. Biotite constitutes ~2-3% of the total assemblage.
Oxides	~5%	(i) Subhedral (ii) Rounded to blocky (iii) Anhedral chain aggregates	(i) Very fine (ii) Fine (iii) Very fine to ultra fine	(i) Chromite chadacrysts in silicates; trace abundance, ~1%, mostly occurring within olivine grains. (ii) Intergranular/interstitial isotropic magnetite are associated (often enclosed) with sulfides. (iii) Occurs within fractures in olivine by-product of serpentinization.
Sulfides	~20%	Interstitial; net-textured	Very fine to medium	Assemblage consists of pyrrhotite > chalcopyrite > pentlandite, all of which appear to be strongly pitted. The assemblage ranges from "fresh" (primary) to "replaced" (secondary) within the section. Secondary assemblages are associated with intense silicate alteration (e.g., surrounded by micaceous biotite). Most intense expression of alteration consists of a messy intergrowth of cubanite + pyrrhotite with ± chalcopyrite ± pentlandite ± millerite. Possible presence of sugakiite in this section; single grain of anhedral native silver located into area composed of most altered sulfide assemblage.
Pyrrhotite	10-15%	Massive; anhedral	Fine to very fine	Most abundant sulfide in the mode. Exhibits strong anisotropism. Pyrrhotite is occasionally intergrown/found as inclusions in chalcopyrite.
Chalcopyrite	5-7%	Massive; anhedral	Fine to very fine	Typically exhibits textures in equilibrium with pyrrhotite. Often exsolved to cubanite in altered sections. Chalcopyrite rapidly tarnishes, which contrasts greatly with cubanite exsolutions.

Pentlandite	2-5%	(i) Anhedral granular aggregates (ii) Flames	Fine to ultra fine	(i) Forms chain aggregates/clusters that often marks the boundary (interfaces) between pyrrhotite and chalcopyrite. (ii) Occurs as exsolution flames in pyrrhotite; often orthogonal to grain boundaries and fractures.
Cubanite	1-3% of Ccp	Anhedral; mottled to lath-shaped exsolutions	Fine to very fine	Occurs both as irregular/massive exsolutions in chalcopyrite as well as blocky/lathed. Appears greenish in colouration when compared to chalcopyrite and does not readily tarnish.
Mackinawite	<<1%	Anhedral; stringers/sub veinlets	Very fine to ultra fine	Trace in abundance and difficult to locate in section.
Overall Comments: Variably altered, seriate, fine- to medium-grained, weakly to moderately foliated, poikilitic, net-textured sulfide-bearing, feldspathic wehrlite. Stringers of both alteration silicates and oxides (respectively) cut through the net-textured sulfides.				

Sample ID: CAM-21-CC-035	**Depth: 426.0 m**	**Location: HGZ**	**CAM Code: Mgm**	**Rock Type: Olivine melagabbro**
Mineral	*Abundance*	*Habit*	*Grain Size*	*Comments*
Olivine	~30%	Anhedral; chadacrystic	Fine	Olivine exhibits variable alteration in this section. Olivine grains (most distal from the central veinlet are weakly serpentinized along fractures. Close to ~5% of olivine elsewhere is altered to green saponite(?).
Clinopyroxene	~20-30%	Anhedral; oikocrystic	Medium	Encloses olivine crystals; often completely altered to amphibole.
Plagioclase	~10-20%	Interstitial; anhedral to tabular	Medium	Exhibits variable alteration; locally quite fresh, showing only minor, (gritty) sericite alteration. Elsewhere, alteration reflects the assemblage described below.
Alteration assemblage	~10-15%	Interstitial; anhedral aggregates	Fine to ultra fine	Assemblage consists of ± talc ± serpentine ± sericite ± chlorite ± biotite. Where present, biotite is fine-grained and anhedral to tabular in habit.
Crosscutting veinlet	-	Anhedral; bladed; fibrous; aggregates	Coarse (i.e., amphibole) to ultra fine (e.g., sericite)	The veinlet consists of (in order of decreasing abundance), talc, sericite, serpentine, chlorite, hornblende, calcite, and biotite (sulphide blebs are entrained as well). Within the veinlet, very fine-grained to microcrystalline talc + sericite + chlorite are intergrown, and occur as anhedral to fibrous aggregates. Hornblende is medium- to coarse-grained and bladed/elongate in habit. Calcite occurs as fine- to medium-grained, anhedral crystals. Biotite is fine-grained and typically anhedral but occasionally tabular.
Ore assemblage 1	<1-3%	Anhedral blebs in crosscutting veinlet	Medium to very fine	Po > Pn > Cbn > Ccp Pyrrhotite is generally massive in habit and often exhibits medium-grained, elongate deformation twins. Trace pentlandite exsolution flames occur within pyrrhotite. Locally, pyrrhotite forms very fine-grained, anhedral aggregates, which display triple junctions under crossed nicols. Pentlandite forms fine-grained, granular, anhedral aggregates, which are distributed throughout the blebs in a network-like fashion. Fine-grained, anhedral chalcopyrite is often confined to the margins of the blebs, and commonly displays thick lamellar (ranges to tabular and massive) cubanite exsolutions. Minor collections of chalcopyrite also occur intergrown with pentlandite aggregates, in between mineral boundaries.
Ore assemblage 2	~1%	Interstitial; anhedral	Fine	Chalcopyrite, often associated with magnetite.
Ore assemblage 3	<1%	Anhedral, linear aggregates	Very fine	Pyrrhotite occurs with this peculiar habit and is found throughout

				pseudomorphed phases (proximal to the veinlet) and within the groundmass.
Oxides	~1-3%	(i) Interstitial (ii) Subhedral	(i) Fine (ii) Fine to ultra fine	(i) Magnetite and ilmenite; commonly exhibit mottled intergrowths. Often associated with interstitial sulfides. (ii) Chromite chadacrysts in silicates.
Overall Comments: Strongly altered, homogeneous, fine- to medium-grained, non-foliated, poikilitic, sulphide-bearing, olivine melagabbro, with a 1.5cm-wide crosscutting carbonate, talc, serpentine, amphibole, chlorite veinlet				

Sample ID: CAM-21-CC-037	**Depth: 443.3 m**	**Location: Country rock**	**CAM Code: Spt**	**Rock Type: Metasedimentary schist**
Mineral	*Abundance*	*Habit*	*Grain Size*	*Comments*
Feldspar	~70%	Anhedral, granular	Fine	Strongly to completely altered by sericite and clay minerals.
Chlorite	~30%	Anhedral to platy	Fine to ultra fine	Spattered throughout the groundmass.
Quartz	~2-5%	Anhedral	Fine to medium	Occur as roughly linear aggregates.
Sillimanite(?)	~1-3%	Acicular	Fine	Forms aggregates of radial fans in the groundmass.
Pyrite	<1%	Anhedral	Ultra fine to medium	Disseminated throughout the groundmass.
Overall Comments: Greenschist facies(?), homogeneous, fine-grained, moderately to poorly foliated, muscovite (sericite), chlorite, quartz, sillimanite schist.				

Sample ID: CAM-21-CC-038	**Depth: 300.8 m**	**Location: HGZ**	**CAM Code: Mg**	**Rock Type: Altered gabbro**
Mineral	*Abundance*	*Habit*	*Grain Size*	*Comments*
Clinopyroxene	~45%	Subhedral to prismatic	Medium	It is commonly weakly altered at grain boundaries to amphibole, and often shows one or two cleavage planes.
Plagioclase	~10-20%	Anhedral, tabular	Fine	Alteration of plagioclase ranges from strong to pervasive with an assemblage of what appears to be chlorite + sericite ± calcite. Difficult to identify; only select altered grains exhibit original polysynthetic twinning.
Orthopyroxene	~5%	Subhedral to anhedral	Fine	Appears intergrown (interlocking grains) with clinopyroxene.
Chlorite; alteration assemblage	-	Anhedral, aggregates	Fine to ultra fine	Occurs as the predominant alteration phase (green in PPL, dark blueish anomalous interference colours in XPL) and may occur with ± talc ± serpentine. This alteration assemblage commonly occurs within the interstices between pyroxenes.
Oxides	~10-15%	(i) Interstitial, mottled (ii) Reticular, boxwork	Fine to very fine	(i) Ilmenite and magnetite; blotchy; ilmenite strongly anisotropic. (ii) Host magnetite altered to chlorite, leaving behind ilmenite in a trellis-like pattern.
Sulfides	~1%	Interstitial, anhedral disseminated; aggregates	Fine to very fine	Py > Ccp > Po Py and Ccp often occur as individual grains/droplets, but locally the three phases are associated together; Po is never found as an isolated phase. Very fine-grained cubanite lamellae are found in few chalcopyrite grains.
Overall Comments: Moderately to intensely altered, heterogenous, fine to medium-grained, non-foliated, intergranular, Ti-oxide-bearing, gabbro.				

Sample ID: CAM-21-CC-039	**Depth: 321.3 m**	**Location: HGZ**	**CAM Code: Upd**	**Rock Type: Wehrlite**
Mineral	*Abundance*	*Habit*	*Grain Size*	*Comments*
Olivine	~60%	Subrounded to subhedral; occasionally prismatic	Fine	Strongly altered; most grains show pervasive serpentinization.
Clinopyroxene	~30%	Interstitial, oikocrystic	Medium to coarse	Relatively unaltered and encloses olivine chadacrysts.
Alteration assemblage	~1-3%	Interstitial; subhedral to anhedral; aggregates	Fine to ultra fine	Biotite is associated with chlorite and trace relict plagioclase.
Magnetite	~10%	(i) Interstitial, anhedral (ii) Anhedral, chain aggregates	(i) Fine (ii) Very fine to ultra fine	(i) Most abundant style of Mag; occurs between silicate grains. (ii) Occurs within olivine fractures; by-product of serpentinization.
Overall Comments: Strongly serpentinized, seriate, fine-grained, moderately foliated, sulfide-barren, poikilitic, magnetite-bearing, wehrlite.				

Sample ID: CAM-21-CC-042	**Depth: 363.7 m**	**Location: HGZ**	**CAM Code: Upd**	**Rock Type: Feldspathic wehrlite**
Mineral	*Abundance*	*Habit*	*Grain Size*	*Comments*
Olivine	50-55%	Rounded granular to prismatic	Very fine to fine	Moderately serpentinized along fractures; occurs as chadacrysts in clinopyroxene. A few grains are almost completely replaced by serpentine with their original grain boundaries obliterated.
Clinopyroxene	15-20%	Oikocrystic; anhedral	Medium to coarse	Occurs as mostly fresh oikocrysts enclosing olivine. Some edges/rims exhibit uralitization to amphibole – possible pervasive replacement in some grains by serpentine (difficult to distinguish).
Plagioclase	5-10%	Interstitial; intergranular	Fine to very fine	Weakly to moderately altered by microcrystalline (gritty) sericite. Polysynthetic twinning is still visible despite alteration. Plagioclase is locally altered to chlorite ± serpentine ± biotite.
Alteration assemblage	10-20%	Interstitial; anhedral, polycrystalline granular aggregates, locally fibrous; biotite platy	Very fine to ultra fine	Interstitial alteration assemblage is abundant modally; composition varies from ± serpentine ± chlorite ± biotite ± talc. It is difficult to distinguish what altered from olivine vs. plagioclase vs. clinopyroxene.
Opaques	~10%	-	-	Oxides + sulfides
Oxides	<2%	(i) Granular; subhedral (ii) Intergranular; anhedral (iii) Anhedral masses/clusters and/or chain aggregates	(i) Very fine to ultra fine (ii) Very fine to fine (iii) Very fine to ultra fine	(i) Chromite chadacrysts in silicates; trace abundant overall. (ii) Interstitial assemblage is often associated with sulfides. Some grains are isotropic, others are anisotropic, indicative of both magnetite and ilmenite, respectively (~60/40 split between the two phases). This style constitutes the most abundant occurrence of oxide in the section. (iii) Trace abundance; magnetite in and around olivine due to serpentinization.
Sulfides	5-10%	Interstitial; intergranular	Fine to ultra fine	Assemblage is intensely altered with relict primary mineralization minimal. Messy sulfide intergrowths consist of pyrrhotite ± cubanite (chalcopyrite?) ± mackinawite ± native copper. Pyrrhotite exhibits mottled colouration and anisotropy (indicative of solid solution?). Mackinawite and native copper are crystallographically oriented with an angular trellis-like arrangement. Pn cleavage planes
Pyrrhotite	~4-7%	Interstitial; anhedral	Fine to very fine	Exhibits weak anisotropism; very difficult to distinguish from possible cubanite. Most abundant sulfide in assemblage.
Cubanite	~2-3%	Interstitial; anhedral	Fine to very fine	Often intergrown with pyrrhotite. Possible solid solution?

Mackinawite	~2-3%	Interstitial; somewhat fibrous or with platy orientation; occasionally elongate to tabular	Fine to ultra fine	High relative abundance when compared to other thin sections studied. Appears pleochroic (or just variable colour?) ranging from olive-beige to more brown-olive in colouration; strong anisotropy. Sometimes tarnished to a purplish hue?
Native Cu	<1%	Anhedral; fracture-filling, vermicular, elongate	Very fine to ultra fine	-
Overall Comments: Intensely altered, seriate, fine-grained, weakly to moderately foliated, poikilitic, sulfidic, feldspathic wehrlite.				

Sample ID: CAM-21-CC-044	**Depth: 400.0 m**	**Location: HGZ**	**CAM Code: Mgm**	**Rock Type: Dunite**
Mineral	*Abundance*	*Habit*	*Grain Size*	*Comments*
Olivine	~65%	Granular, rounded, subhedral	Medium to fine	Weakly to moderately serpentinized along fractures and altered to talc commonly around the margin of grains.
Clinopyroxene	~5%	Interstitial; anhedral	Medium	Occurs as oikocrysts enclosing olivine. Trace amphibole alteration at margins.
Plagioclase	2-5%	Interstitial; anhedral	Fine to very fine	Variably altered to chlorite ± saussurite ± biotite?
Oxides	~3%	(i) Subhedral chadacrysts (ii) Interstitial, rounded (i) Anhedral chain aggregates	(i) Fine to ultra fine (ii) Fine to very fine (iii) Ultra fine	(i) Chromite in silicates (ii) Fe-Ti oxides intergrown with sulfides (iii) Magnetite within olivine fractures; by-product of serpentinization
Pyrrhotite	~15%	Interstitial; anhedral	Fine to medium	Interstitial to cumulates, associated with Ccp, Pn, Mag and a few tiny PGM
Chalcopyrite	~5%	Interstitial; anhedral	Fine	Trace Cbn exsolutions.
Pentlandite	~3%	(i) Granular aggregates (ii) Flames	Fine to ultra fine	Anhedral grains line interface between Po and Ccp, also commonly occur along fractures in Po. Flames occur within Po and are commonly orthogonal to fractures in Po.
Overall Comments: Moderately altered, seriate, medium-grained, non-foliated, poikilitic, net-textured sulfide-bearing, dunite.				

Sample ID: CAM-21-CC-045	**Depth: 404.3 m**	**Location: HGZ**	**CAM Code: Mgm**	**Rock Type: Dunite**
Mineral	*Abundance*	*Habit*	*Grain Size*	*Comments*
Olivine	30-35%	Ranges from practically euhedral to rounded, anhedral; larger grains tend to be more intact	Medium to fine	Occurs as highly fractured chadacrysts in clinopyroxene. Moderate serpentinization along fractures; ~5-20% of olivine are almost completely replaced by serpentine ± talc. All grains exhibit intense alteration along boundaries to a very fine-grained to microcrystalline aggregate of (mostly) talc ± serpentine ± (fibrous, acicular) chlorite ± sericite.
Clinopyroxene	~5-7%	Interstitial; oikocrysts surrounding olivine; anhedral with no visible crystal faces	Medium	Moderate alteration apparent at margins of oikocrysts to a variable mixture of uralite + talc ± serpentine ± chlorite; minor patchy talc alteration presents within grains. Oikocrysts exhibit undulose extinction.
Plagioclase	<3%	Interstitial; stubby tabular to anhedral habit	Fine to very fine	Overall minor in abundance. Plagioclase exhibits minor to trace microcrystalline (gritty) sericite alteration. Polysynthetic twinning common.
Alteration assemblage	10-20%	Interstitial; complex polycrystalline aggregates; micaceous, fibrous	Very fine to ultra fine	Consists of talc ± chlorite ± sericite ± serpentine ± biotite. Ol -> Srp -> Tlc Cpx -> Amp -> Chl
Opaques	~30-35%	-	-	-
Oxides	1-3%	(i) Subhedral to euhedral (ii) Interstitial; anhedral (iii) Anhedral, chain aggregates	(i) Very fine to ultra fine (ii) Fine (iii) Ultra fine	(i) Chromite chadacrysts in silicates (<1% in total). (ii) Isotropic magnetite is often associated with sulfides; constitutes the most abundant oxide at ~1-3%. (iii) Magnetite occurring in trace amounts within fractures of olivine as a by-product of serpentinization (<<1%).
Sulfides	27-32%	Interstitial; net-textured	-	-
Pyrrhotite	~20-25%	Massive; anhedral	Fine to medium	Constitutes the most abundant sulfide phase and is often shown in equilibrium with chalcopyrite. Exhibits strong anisotropy under cross polars.
Chalcopyrite	~5%	Massive; anhedral	Fine to medium	Intergrown (interfingered) with pyrrhotite and is occasionally found as inclusions within pyrrhotite (and vice versa). Occasional weak mottled anisotropy visible under cross polars.
Pentlandite	~3-5%	Anhedral, granular aggregates; sub veinlets to clusters; 'flames'	Fine to ultra fine	Appears creamy in colouration and isotropic with cross polars. Linear chain aggregates commonly occur along silicate rims. Granular aggregates often "cross cuts" pyrrhotite as sub veinlets. Aggregates also commonly occur along the boundary (interface) between pyrrhotite and chalcopyrite. 'Flames' occur as exsolutions in

				pyrrhotite and are oriented perpendicular to fractures, grain boundaries, or silicate crystal faces.
Pyrite	~1%	Subhedral; rounded	Fine	Overall minor in abundance, with only a few solitary grains visible. Pyrite is more reflective when trying to distinguish between pentlandite in this thin section.
Overall Comments: Variably altered, bimodal, medium-grained, non-foliated, poikilitic, net-textured sulfidic dunite.				

Sample ID: CAM-21-CC-046	**Depth: 430.4 m**	**Location: HGZ**	**CAM Code: Mgm**	**Rock Type: Feldspathic wehrlite**
Mineral	*Abundance*	*Habit*	*Grain Size*	*Comments*
Olivine	50-60%	Rounded to prismatic	Fine to very fine	Strongly serpentinized along fractures and replaced by talc along margins of grains. Occurs as chadacrysts in Cpx.
Clinopyroxene	7-15%	Interstitial; oikocrystic	Medium to fine	Weak alteration to serpentine along fractures; local trace amphibole alteration at margins.
Plagioclase	5-8%	Interstitial, anhedral	Fine to very fine	Exhibits variable, patchy alteration. Commonly find clusters of nasty intergrowths consisting of chlorite, talc, carbonate, biotite, serpentine(?), and actinolite(?).
Oxides	3-5%	(i) subhedral chadacrysts (ii) Interstitial, rounded (i) Anhedral chain aggregates	(i) Fine to ultra fine (ii) Fine to very fine (iii) Ultra fine	(i) Chromite in silicates (ii) Fe-Ti oxides intergrown with sulfides. Local symplectite textures. (iii) Magnetite within olivine fractures; by-product of serpentinization
Pyrrhotite	~5%	(i) Interstitial, anhedral (ii) Fracture-fill, anhedral	(i) Fine (ii) Very fine to ultra fine	(i) Primary, associated with Pn, Ccp, Mag. Troilite exsolutions lamellae present. (ii) Occurs in an anastomosing fashion within fractures in pyrite from central veinlet.
Chalcopyrite	~3-5%	Interstitial, anhedral	Fine	Trace alteration (exsolution?) to cubanite.
Pentlandite	~1-3%	(i) Anhedral, granular aggregates (ii) Flames	Fine to ultra fine	(i) Occurs with primary sulfide assemblage. (ii) Occurs as exsolutions in Po, commonly perpendicular to fractures.
Pyrite	~3-5%	Anhedral; crosscutting + interstitial	Fine	Appears to replace Po in both a thin sulfide veinlet and adjacent net-textured sulfides.
Overall Comments: Strongly altered, homogeneous, fine-grained, non-foliated, poikilitic, strongly disseminated to net-textured sulfide-bearing feldspathic wehrlite, with two crosscutting veinlets. The main veinlet is predominantly composed of pyrite with lesser Po + Pn + Ccp, and the second veinlet contains sulfides also, but contains abundant talc and chlorite. Margins of interstitial sulfides are commonly replaced by biotite (+ actinolite?), with clear sulfur loss/destruction of original boundaries.				

Sample ID: CAM-21-CC-048	**Depth: 475.1 m**	**Location: Lower min. zone**	**CAM Code: Mgm**	**Rock Type: Feldspathic wehrlite**
Mineral	*Abundance*	*Habit*	*Grain Size*	*Comments*
Olivine	55-60%	Subhedral, rounded	Medium to fine	Strongly serpentinized along fractures. Margins of crystals commonly altered to talc. Occurs as chadacrysts in Cpx.
Clinopyroxene	~10%	Interstitial, anhedral	Medium	Relatively fresh, minor alteration to amphibole locally.
Plagioclase	~5%	Interstitial, anhedral	Fine	Locally intensely altered to complex intergrowth of chlorite, talc, biotite, actinolite, and serpentine(?). Trace saussuritization.
Oxides	~3%	(i) Subhedral chadacrysts (ii) Interstitial, rounded (i) Anhedral chain aggregates	(i) Fine to ultra fine (ii) Fine to very fine (iii) Ultra fine	(i) Chromite in silicates (ii) Magnetite with ilmenite exsolution lamellae associated with sulfides (iii) Magnetite within olivine fractures; by-product of serpentinization
Pyrrhotite	~10-15%	Interstitial, anhedral; massive	Fine to medium	Occurs with Ccp + Pn + Mag/Ilm interstitial to cumulus olivine. Possibly replaced by subhedral pyrite at single location in section.
Pentlandite	~5%	(i) Anhedral, granular (i) Flames	Fine to ultra fine	(i) Occurs amongst interstitial assemblage (ii) Occurs as exsolutions in Po
Chalcopyrite	~5-10%	Interstitial, anhedral; massive	Fine	-
Overall Comments: Strongly altered, seriate, medium-grained, weakly foliated, poikilitic, net-textured sulfide-bearing feldspathic wehrlite, with a thin massive sulfide layer near the bottom of the section. Sulfide textures in the massive sulfide lens interpreted as pattern from fractionation of classic MSS/ISS from sulfide liquid; Pn clearly lines the interface between Po and Ccp, but also occurs within Po as flames and clusters of grains.				

Sample ID: CAM-21-CC-052	Depth: 558.1 m	Location: Country rock	CAM Code: Spt	Rock Type: Metasedimentary schist
Overall Comments: Greenschist facies(?), homogeneous, fine-grained, moderately foliated, quartz, chlorite, muscovite (sericite) schist.				

Sample ID: CAM-21-CC-053	**Depth: 307.7 m**	**Location: N per.**	**CAM Code: Mgol**	**Rock Type: Altered gabbro**
Mineral	*Abundance*	*Habit*	*Grain Size*	*Comments*
Clinopyroxene	~60%	Anhedral to euhedral (prismatic)	Medium	Commonly twinned down the grain midline. Occurs as phenocrysts.
Olivine	-	Rounded	Fine	Under PPL, pseudomorphic olivine is identified due to preservation of original grain boundaries. Challenging to estimate modal abundance due to intense alteration blending in with associated interstitial alteration assemblage.
Alteration assemblage	~30%	Anhedral, aggregates	Fine to ultra fine	The alteration assemblage is variable and consists of sericite + chlorite ± calcite. The intensity of alteration renders it difficult to identify relict feldspar grains within the interstitial space.
Ilmenite	~1-2%	(i) Interstitial, mottled (ii) Reticular, boxwork	(i) Fine to medium (ii) Fine to very fine	(i) Strongly anisotropic; mottling potentially result of alteration along grain boundaries. (ii) Host magnetite altered to chlorite, leaving behind ilmenite in a trellis-like pattern.
Chalcopyrite	Trace	Anhedral disseminations	Ultra fine	Occurs interstitially.
Overall Comments: Strongly altered, homogeneous, medium-grained, non-foliated, poikilitic, Ti-oxide bearing, gabbro.				

Sample ID: CAM-21-CC-054	**Depth: 317.8 m**	**Location: N per.**	**CAM Code: Upd**	**Rock Type: Wehrlite**
Mineral	*Abundance*	*Habit*	*Grain Size*	*Comments*
Olivine	55-60%	Rounded; chadacrystic	Fine to medium	Intensity of serpentinization ranges from pervasive to strong; often minimal relict olivine remains.
Clinopyroxene	15-20%	Interstitial, oikocrystic	Medium	Encloses olivine grains. Relatively unaltered; serpentine runs through fractures which connect between olivine crystals.
Plagioclase	5-10%	Interstitial, anhedral	Fine	Strong patchy alteration; messy intergrowths of chlorite, biotite, talc, carbonate, and actinolite(?).
Oxides	~5-10%	(i) Interstitial, anhedral (ii) Anhedral (iii) Anhedral, chain aggregates	(i) Fine (ii) Fine (iii) Very fine	(i) Ilmenite; strongly anisotropic. (ii) Magnetite intergrown with sulfides. (iii) Magnetite occurs within fractures of olivine; by-product of serpentinization.
Sulfides	Trace	Interstitial, anhedral	Very fine	Complex intergrowths of Po + Ccp + Mag + Pn.
Overall Comments: Strongly serpentinized, seriate, medium-grained, moderately foliated, poikilitic, wehrlite.				

Sample ID: CAM-21-CC-060	**Depth: 396.3 m**	**Location: N per.**	**CAM Code: MmgEL**	**Rock Type: Feldspathic wehrlite**
Mineral	*Abundance*	*Habit*	*Grain Size*	*Comments*
Olivine	~40%	Subhedral, locally prismatic	Fine to medium	Serpentine alteration ranges from strong along olivine fractures, to pervasive with complete grain replacement. Serpentine crystals occur perpendicular to the fracture walls. Along grain boundaries near clinopyroxene, olivine rims are replaced with very fine-grained, anhedral talc. Locally, finer olivine grains are completely pseudomorphed by talc.
Clinopyroxene	~15-20%	Interstitial, oikocrystic	Medium to coarse	Encloses olivine chadacrysts. Clinopyroxene is often unaltered, but local exhibits serpentine alteration along fractures which connect between olivine grains. Clinopyroxene is locally twinned down the centre of the grain.
Plagioclase	<10%	Interstitial, anhedral	Fine	Often weakly to moderately altered to ultra fine-grained, dusty sericite (saussurite?). Locally where less altered, polysynthetic twinning is still visible.
Alteration assemblage	~15%	Interstitial, anhedral; aggregates	Fine to ultra fine	Chlorite occurs as the most abundant alteration mineral in the assemblage (~5-10%). Chlorite is anhedral with irregular (patchy) distribution, and sometimes occurs as very fine-grained, anhedral aggregates. Chlorite is often associated with anhedral to subhedral, fine-grained biotite ± sericite (altered plagioclase) ± talc; it occurs rarely with anhedral grains of calcite.
Sulfide veinlet	~15%	Crosscutting; massive and anhedral aggregates within the veinlet	Fine to ultra fine	Crosscutting veinlet appears to be fractionated along the length of the veinlet. The mineralogy transitions from dominantly Ccp, to a Pn interface near the middle of the veinlet, which is followed by predominantly Po intergrown with Pn. Chalcopyrite is visibly massive in habit, whilst both pyrrhotite and pentlandite occur as fine-grained, anhedral aggregates. The composition of the veinlet is approximately 60% Ccp, 20-30% Po, and 10-20% Pn. This veinlet contains microcrystalline to medium-grained inclusions of alteration phases (i.e., talc, carbonate, and biotite). There are also <1mm crosscutting stringers of chlorite ± carbonate throughout
Disseminated sulfides	~1-2%	Interstitial; anhedral	Fine to ultra fine	Mottled intergrowths of Ccp + Po + Sg(?) + Mkw + Mag ± Val.
Oxides	~1%	(i) Rounded to subhedral droplets (ii) Interstitial, anhedral (iii) Anhedral,	(i) Very fine (ii) Fine (iii) Very fine to ultra fine	(i) Chromite chadacrysts in silicates. (ii) Strongly anisotropic ilmenite; often associated with sulfides. (iii) Magnetite occurs within fractures of olivine; by-product of serpentinization.

		chain aggregates		
Overall Comments: Intensely altered, hiatal, medium-grained, non-foliated, poikilitic, wehrlite with a 5mm-wide crosscutting sulphide veinlet.				

Sample ID: CAM-21-CC-061	**Depth: 399.3 m**	**Location: N per.**	**CAM Code: MmgEL**	**Rock Type: Melanocratic gabbro**
Mineral	*Abundance*	*Habit*	*Grain Size*	*Comments*
Olivine	~40%	Rounded; anhedral	Fine	Strongly serpentinized along fractures, trace talc alteration along grain boundaries. Local pervasive (complete) replacement to serpentine.
Clinopyroxene	~15-20%	Interstitial; oikocrystic, anhedral	Coarse	Moderate serpentinization along thin fractures. Local twinning down centre of grain. Locale replacement to amphibole, along grain boundaries ranging to pervasive.
Plagioclase	10-15%	Interstitial; anhedral to tabular; polysynthetic twinning easily visible	Fine to medium	Strongly to intensely saussuritized throughout; commonly along fractures. Alteration ranges from ultra fine-grained to coarser. High interference-coloured epidote masses. Locally altered to intergrowth assemblage of saussurite + chlorite + carbonate + serpentine with irregular, patchy anhedral habit.
Biotite	~1-2%	Platy, tabular; micaceous with obvious basal cleavage	Fine	Occurs interstitially and often at the interface with sulfides.
Opaques	~10-15%	-	-	-
Oxides	3-5%	(i) Chadacrysts; subhedral (ii) Interstitial; anhedral, rounded (iii) Gashes + rim replacement, occurring with sulfides (iv) Anhedral chain aggregates	Fine to ultra fine	(i) Chromite in silicates (ii) Ilmenite ± magnetite (iii) Oxidation; associated with sulfides (iv) Occurs within silicate (mostly olivine) fractures; by-product of serpentinization
Ore assemblage	~10-12%	Interstitial; anhedral	Fine to ultra fine	Ccp (± Cbn) > Sg > Mag > Po > Pn > Cu > Ag > Val
Chalcopyrite	-	Anhedral; mottled intergrowths with Cbn	-	Variably tarnished from light yellow to orangey-yellow.
Sugakiite	-	Anhedral; anastomosing, "island-ocean" texture with Pn	-	Isotropic to faintly anisotropic; reddish brownish in colouration and Po is whiter, creamy in comparison. Shares grain boundaries with Ccp + Po. Irregularly intergrown often with mottled textures.
Native Cu	-	Lenticular to anhedral	Ultra fine	Occurs as fracture-fill in both sulfides and oxides.
Native Ag	Trace	Anhedral to cuspate	Ultra fine	Occurs as inclusions in mostly Ccp.
Valleriite	Trace	Interstitial, gritty to fibrous	Ultra fine	-

Overall Comments: Strongly altered, homogeneous, fine-grained, weakly foliated, poikilitic, sulfide-bearing melagabbro.

Sample ID: CAM-21-CC-065	**Depth: 432.0 m**	**Location: Country rock**	**CAM Code: SIc**	**Rock Type: Metasedimentary schist**
Mineral	*Abundance*	*Habit*	*Grain Size*	*Comments*
Pyrite	~1%	Anhedral, disseminated	Very fine	Occurrence of Py in the sample varies; some grains are randomly distributed, others are foliation-controlled, and locally, grains are aligned perpendicular to the sample's fabric as a chain aggregate resembling a "string of pearls".
Overall Comments: Homogeneous, fine-grained, moderately to poorly foliated, feldspar (sericite-altered), biotite, quartz schist.				

Sample ID: CAM-21-CC-071	**Depth: 378.7 m**	**Location: S per.**	**CAM Code: Upd**	**Rock Type: Melanocratic gabbro**
Mineral	*Abundance*	*Habit*	*Grain Size*	*Comments*
Olivine	~60-70%	Rounded; granular to prismatic	Fine to very fine	Occurs as chadacrysts in Cpx. Strongly serpentinized along fractures; pervasive locally. Rims commonly replaced by talc.
Clinopyroxene	10-15%	Interstitial, anhedral, oikocrystic	Medium	Moderately serpentinized along fractures; local replacement along margins to amphibole.
Plagioclase	10-15%	Interstitial, anhedral	Fine	Patchy alteration to f.g. saussurite common; alteration intergrowths of chlorite, talc, carbonate, actinolite intermittent.
Oxides	~3-5%	(i) Anhedral, rounded (ii) Anhedral, pseudomorphic (iii) Interstitial, anhedral (iv) Anhedral, chain aggregates	(i) Fine to ultra fine (ii) Fine to ultra fine (iii) Fine (iv) Ultra fine	(i) Chromite chadacrysts throughout the groundmass (ii) Magnetite replacement; associated with sulfide assemblage, but also found as almost complete replacement of olivine (iii) Ilmenite is commonly interstitial to olivine (iv) Magnetite occurring as linear arrangements within olivine fractures
Sulfides	~5-7%	Interstitial, intergrown	Fine to ultra fine	Ccp + Cbn > Po > Sg > Pn ~ Mkw > Cu > Val Primary assemblage has been intensely altered. Sulfides exhibit complex intergrowths and disequilibrium textures. "Island-ocean" texture observed with Pn in Sg. Ccp strongly tarnished to Bn-like colours. Po exhibits triple junctions under cross-polars; Mkw + Val very strongly anisotropic. S-loss apparent in that original boundaries of sulfides appear to be significantly reduced and replaced by hydrous silicates.
Overall Comments: Strongly altered, homogeneous, fine-grained, non-foliated, poikilitic, melanocratic gabbro.				

Sample ID: CAM-21-CC-072	**Depth: 383.0 m**	**Location: S per.**	**CAM Code: Upd**	**Rock Type: Melanocratic gabbro**
Mineral	*Abundance*	*Habit*	*Grain Size*	*Comments*
Olivine	60-65%	Rounded, granular	Fine to very fine	Intensely serpentinized along fractures; finer crystals are pervasively replaced. Patchy rim replacement by talc.
Clinopyroxene	10-15%	Interstitial, anhedral	Medium to fine	Oikocrysts enclose olivine chadacrysts. Weakly serpentinized along fractures. Commonly replaced by amphibole along margins of grains.
Plagioclase	10-15%	Interstitial, anhedral	Fine	Patchy alteration is common with some Pl appearing relatively fresh. Elsewhere Pl is intensely replaced by intergrowths of talc, chlorite, biotite, actinolite, carbonate, and saussurite.
Oxides	3-5%	(i) Rounded, granular, anhedral (ii) Anhedral (iii) Interstitial, rounded (iv) Anhedral linear chain aggregates	(i) Very fine to ultra fine (ii) Very fine to ultra fine (iii) Fine (iv) Ultra fine	(i) Chromite chadacrysts in the groundmass (ii) Magnetite associated with sulfides (iii) Fe-Ti oxides (mostly ilmenite?) (iv) Magnetite occurring within fractures in olivine due to serpentinization
Sulfides	3-5%	Interstitial, anhedral	Fine to ultra fine	Ccp + Cbn > Pn + Mkw > Sg(?) > Po > Cu >> Val Primary assemblage has been strongly modified during hydrothermal alteration. Patches and wisps of mackinawite common in Ccp, as well as oriented cubanite lamellae. Ccp is easily tarnished (to blue colours) and strongly altered locally (looks brownish similar to Bn). Po exhibits triple junctions under cross polars. Relict Pn is commonly fractured, possible Sg occupies between the fractures. Native Cu often occurs as thin lines at the boundaries of sulfides. Magnetite gashes occurs commonly between sulfides.
Sulfide blebs in veinlet	10%	Crosscutting	Fine to medium	Cu-Fe sulfides occur within an apparently felsic veinlet. Cu-Fe sulfides are mostly Cbn exsolutions in Ccp, but a fine-grained, isolated chalcocite grain occurs within the felsic veinlet as well. Small patch of an anhedral Pn aggregate is intergrown with Cbn + Ccp in one of the blebs. Possible discrete PGM are present within Ccp (appears strongly reflective). The felsic veinlet is possibly feldspar-dominant.
Overall Comments: Strongly altered, homogeneous, fine-grained, non-foliated, poikilitic, melanocratic gabbro with a characteristic crosscutting sulfide-bearing felsic veinlet.				

Sample ID: CAM-21-CC-087	**Depth: 390.9 m**	**Location: W per.**	**CAM Code: MmgEL**	**Rock Type: Melanocratic gabbro**
Mineral	*Abundance*	*Habit*	*Grain Size*	*Comments*
Olivine	55-65%	Rounded to subhedral	Medium	Intensely serpentinized along fractures, local talc alteration at the interface between plagioclase. Occurs as chadacrysts in clinopyroxene.
Clinopyroxene	20%	Interstitial, oikocrystic	Coarse to medium	Relatively fresh, but moderately serpentinized along fractures (fewer fractures than olivine) and locally replaced by amphibole at margins of oikocrysts.
Plagioclase	~10%	Interstitial, anhedral to tabular	Fine	Strongly saussuritized along fractures. Local patches of alteration intergrowths that consist of talc, chlorite, actinolite(?), serpentine, and saussurite.
Oxides	5-7%	(i) Rounded to anhedral (ii) Bladed, tabular to granular (iii) Anhedral to gashed (iv) Linear chain aggregates, locally cuspate	(i) Fine to ultra fine (ii) Fine (iii) Fine to ultra fine (iv) Fine to ultra fine	(i) Chromite chadacrysts throughout the groundmass. (ii) Ilmenite occurring within (mostly) plagioclase. (iii) Magnetite intergrown with sulfides. (iv) Magnetite occurring within fractures in olivine, associated with serpentine. Also occurs as symplectite-like textures intergrown with hydrous silicates replacing olivine.
Sulfides	~5%	Interstitial; various	Fine to ultra fine	Po > Ccp + Cbn > Pn + Mkw > Cu > Val Po is relatively preserved compared to the other sulfides. Ccp + Cbn + Mkw exhibit complex mottled to tabular intergrowth/exsolution relationships. Pn is commonly fractured with Mkw and Mag replacing between fractures. Pn also occurs as flames in Po. Abundant fractures throughout Po that are commonly Cu-rich (both native and sulfides). Native copper occurs intermittently throughout the groundmass. Cu is often intergrown with hydrous silicates with a jagged, wispy habit. Native Cu is also observed to occur within serpentine fractures in Olivine.
Overall Comments: Strongly altered, homogeneous, medium-grained, non-foliated, poikilitic, melanocratic gabbro.				

Sample ID: CAM-21-CC-088	**Depth: 396.4 m**	**Location: W per.**	**CAM Code: Mmg**	**Rock Type: Feldspathic wehrlite**
Mineral	*Abundance*	*Habit*	*Grain Size*	*Comments*
Olivine	~50-60%	Rounded	Medium	Strongly altered to serpentine along abundant fractures. Anhedral, microcrystalline talc alteration is found along the boundaries of olivine (sub-mm rims) and is associated with serpentine. Near the main sulphide veinlet, olivine grains are completely pseudomorphed by serpentine.
Clinopyroxene	~10-20%	Anhedral, oikocrysts	Medium to coarse	Encloses olivine chadacrysts. Grains locally exhibit twinning down the centre of the crystal. Mostly unaltered, except for a few grains. Altered clinopyroxene grains are pseudomorphed to amphibole which exhibit brown to light beige pleochroism and characteristic 120-60° cleavage plane angles.
Plagioclase	~5-10%	Interstitial; anhedral to tabular	Fine	Exhibits variable alteration; ranges from microcrystalline (gritty) sericite to aggregates of chlorite, sericite and ± talc. Relict grains that are most intact preserve characteristic polysynthetic twinning.
Oxides	~1%	(i) Subangular (ii) Interstitial, anhedral (iii) Anhedral, chain aggregates	(i) Very fine (ii) Fine (iii) Ultra fine	(i) Chromite chadacrysts within silicates. (ii) Magnetite, locally associated with sulfides. Some grains exhibit ilmenite lamellae, which range from a few lamellae to boxwork (reticular) habit. Elsewhere, mottled textures at grain boundaries (partial rim replacement?) are apparent. (iii) Magnetite occurs within fractures of olivine; by-product of serpentinization.

Sulfide veinlet	~10%	Crosscutting; complex intergrowths	Fine to ultra fine	Po > Pn >> Ccp Po occurs as fine-grained, polygonal mosaic aggregates (abundant triple junctions clearly observed due to strong anisotropy under crossed-nicols). Pn occurs as fine-grained, anhedral, granular aggregates that appear as "belts" which run along the centre of the veinlet. These bands/belts/veinlet-parallel aggregates are less than a mm-thick and are often discontinuous throughout the veinlet. Trace Ccp occurs along the boundaries/rim of the veinlet and along the fractures of Po. Minor Ccp occurs parallel to the vein wall, similar to the Pn aggregates. In some of the olivine pseudomorphs near the vein contact, thin, wispy aggregates of microcrystalline sulfides occur along boundaries and within fractures of the altered grains. The sulfides in this occurrence are composed of Po and Pn with trace Dg/Cct ± Ccp (possibly just tarnished Ccp that was not effectively polished due to its extremely small size). Towards the main sulphide vein selvedge, alteration becomes pervasive and chaotic; the vein margin is almost entirely lined with talc and chlorite. Interstitial material within the main sulfide vein is composed of chlorite and carbonate. A fibrous chlorite (serpentine?) veinlet runs perpendicular to the main sulphide vein (the chlorite fibres are roughly normal to the veinlet walls).
Disseminated sulfides	~5%	Interstitial; anhedral	Fine	Po >> Ccp >> Pn Variable assemblage; pentlandite is mostly absent. Often intergrown with magnetite.
Overall Comments: Strongly altered, seriate, fine- to medium-grained, non-foliated, poikilitic, sulphide veinlet-bearing, feldspathic wehrlite.				

Sample ID: CAM-21-CC-089	**Depth: 399.6 m**	**Location: W per.**	**CAM Code: Mmg**	**Rock Type: Melanocratic gabbro**
Mineral	*Abundance*	*Habit*	*Grain Size*	*Comments*
Olivine	~40-50%	Subhedral	Fine	Weakly serpentinized along fractures. Locally, contains very fine-grained, rounded, pseudomorphed inclusions, which are variably altered to ± chlorite ± sericite ± serpentine.
Clinopyroxene	~20-30%	Anhedral, oikocrystic	Fine to medium	Encloses olivine chadacrysts. Local alteration to amphibole, ranging from partial to complete replacement.
Plagioclase	~20%	Interstitial, tabular to anhedral	Medium	Polysynthetic twinning common. Moderately altered to very fine-grained, anhedral (gritty) sericite; patchy distribution, occurs along fractures.
Alteration assemblage	~20%	Interstitial, anhedral, aggregates	Fine to ultra fine	The degree of alteration in the sample increases with proximity to the central sulfide veinlet. The sulfide veinlet selvedge is lined with biotite, chlorite, and serpentine. A few chlorite stringers run through the sulphide veinlet, with orientation parallel to the veinlet. Interstitial biotite (<1%) is fine-grained, and anhedral to tabular in habit.
Oxides	~1%	(i) Anhedral to subhedral (ii) Interstitial, anhedral to subhedral (iii) Anhedral, chain aggregates	(i) Ultra fine (ii) Fine (iii) Very fine	(i) Chromite chadacrysts in silicates. (ii) Ilmenite and magnetite. Ilmenite is bluish-grey in colouration and exhibits strong, mottled anisotropy. Magnetite is brownish-grey in colouration and is clearly anisotropic. (iii) Trace magnetite occurs within fractures of olivine; by-product of serpentinization.
Sulfide veinlet	~8-10%	Crosscutting; various textures	Fine to ultra fine	Po > Pn > Ccp > Cbn Composed of four phases; differentiated along the length of the veinlet. Po occurs as fine-grained, anhedral/polygonal aggregates with triple junctions between grains. Pn occurs as fine-grained, anhedral (granular) aggregates that tend to occur in linear chains (sub-veinlets), which are aligned to the veinlet's orientation. Ccp occurs sparsely as anhedral patches/interstitially to the other sulfides, and exhibits an exsolution relationship with Cbn, which is lamellar in form. Minor, fine-grained, anhedral magnetite occurs along the margins of the veinlet as well.
Disseminated sulfides	~5%	Interstitial; anhedral aggregates	Fine to ultra fine	Individual sulfide disseminations are variable. Locally, grains are composed of Po, while elsewhere are almost entirely Ccp ± Cbn. However, in all disseminations, Pn occurs in minor to trace abundance. Commonly associated (surround) intergranular ilmenite. Magnetite exsolution gashes are very common in the sulfide grains and are

				oriented along cleavage planes. Ultrafine/microcrystalline, chain aggregates and discrete sulfide disseminations commonly occur in the sulfide veinlet selvedge. These disseminations are composed of Ccp, and are associated with strong silicate alteration.
Overall Comments: Weakly serpentinized, seriate, fine- to medium-grained, poorly foliated, poikilitic, melagabbro with a mm-sized crosscutting sulfide veinlet.				

Sample ID: CAM-21-CC-100	**Depth: 399.0 m**	**Location: E per.**	**CAM Code: Mgm**	**Rock Type: Feldspathic wehrlite**
Mineral	*Abundance*	*Habit*	*Grain Size*	*Comments*
Olivine	~50%	Granular; subhedral to euhedral	Fine	Occurs as chadacrysts in Cpx. Strongly serpentinized along fractures, local talc alteration along rims of crystals.
Clinopyroxene	20-30%	Interstitial; oikocrystic	Medium	Moderately serpentinized along fractures.
Plagioclase	~5-8%	Interstitial, anhedral	Fine	Variably altered, patchy, saussurite, chlorite, etc.
Oxides	~5-10%	(i) Anhedral to subhedral (ii) Interstitial; anhedral, shares cuspate boundaries with sulfides (iii) Anhedral, linear aggregates	(i) Fine to ultra fine (ii) Fine (iii) Ultra fine	(i) Chromite chadacrysts within the silicate groundmass. (ii) Fe-Ti oxides intergrown with sulfides. (iii) Magnetite occupying fractures in olivine associated with serpentinization.
Sulfides	~20%	Interstitial, anhedral	Fine to ultra fine	Po >> Ccp > Pn > Cbn >> Mkw Sulfides are weakly altered in this sample compared to pristine net-textured assemblage. Cbn exsolutions in Ccp are abundant, typically as oriented laths, but also rounded in shape. Pn occurs as granular aggregates at the interface between Po and Cu-Fe sulfides. Pn also occurs as abundant exsolution flames in Po, which often emanate from fractures. Trace Mkw intergrown with Pn (replaces Pn?).
Overall Comments: Strongly serpentinized, homogeneous, fine-grained, weakly foliated, poikilitic, feldspathic wehrlite with strongly disseminated to semi-net-textured sulfide mineralization.				

Sample ID: CAM-21-CC-101	**Depth: 403.6 m**	**Location: E per.**	**CAM Code: Mgm**	**Rock Type: Feldspathic wehrlite**
Mineral	*Abundance*	*Habit*	*Grain Size*	*Comments*
Olivine	~40-50% *normalized	Rounded	Fine to medium	Moderately serpentinized along fractures. Locally, olivine cores are partially replaced with yellowish green colouration, and marshy olivine green interference coloured, saponite(?). Some olivine grains adjacent to the main veinlet are completely (pervasively) altered to serpentine (± chlorite).
Clinopyroxene	~40% *normalized	Anhedral; oikocrystic	Medium to coarse	Encloses olivine chadacrysts. Exhibits undulatory extinction locally.
Plagioclase	~5-9% *normalized	Interstitial; anhedral	Fine	Exhibits patchy, but strong to intense sericite alteration. Associated with (altered to?) aggregates of microcrystalline chlorite (<<1% abundance).
Biotite	~1-3% *normalized	Interstitial; anhderal to stacked sheets (platy)	Fine	Associated with plagioclase, chlorite; often occurs between sulfide-silicate interface.
Oxides	~1-3%	(i) Subhedral (ii) Interstitial; anhedral (iii) Anhedral, chain aggregates	(i) Very fine to ultra fine (ii) Fine to very fine (iii) Ultra fine	(i) Chromite chadacrysts in silicates. (ii) Magnetite ± ilmenite; commonly associated with disseminated sulfides. (iii) Magnetite occurs within olivine fractures; by-product of serpentinization.
Sulfide veinlet	~20-25%	Crosscutting; various textures	Medium to ultra fine	Po > Pn > Ccp Po occurs as a mosaic aggregate of crystals (exhibiting triple junctions) that are anhedral to subhedral, and medium-grained. Running through the fractures (perhaps grain boundaries) of the Po is a network of fine-grained, anhedral (granular) pentlandite aggregates (sub-veinlets). Locally, a single larger Pn aggregate (~0.5-1mm wide) runs linearly parallel to the veinlet's orientation. This larger Pn veinlet is associated with several other fine-grained Pn aggregate veinlets which splay off (usually shoot out perpendicular) from it. These splays propagate through the overall sulphide veinlet, forming a network or stockwork-like texture through Po. Pn "flames" are commonly found throughout the veinlet – some are contained within Po grains, but most often occur perpendicular to the smaller Pn aggregate veinlet splays. Ccp occurs in minor abundance throughout the veinlet. It is often tarnished blue (may require a more thorough polish). Ccp occurs interstitial to both Po and Pn. Ccp's distribution is patchy, but most often occurs in close proximity to the veinlet wall.

Disseminated sulfides	~1-2%	Interstitial; anhedral	Fine to ultra fine	Ccp > Po > Pn Assemblage often surrounded oxides, and composition varies between the above sulfide phases. Also occurs as anhedral, chain aggregates associated with silicate alteration; mimics magnetite from serpentinization.
Overall Comments: Moderately serpentinized, homogeneous, medium-grained, non-foliated, poikilitic, feldspathic wehrlite with a 3-4mm thick, sulfide veinlet that crosscuts the sample.				

Sample ID: CAM-21-CC-116	**Depth: 392.1 m**	**Location: HGZ**	**CAM Code: Mgm**	**Rock Type: Feldspathic wehrlite**
Mineral	*Abundance*	*Habit*	*Grain Size*	*Comments*
Olivine	55-65%	Rounded; subhedral to prismatic	Fine	Moderately to weakly serpentinized along fractures. Local alteration of rims to talc, typically were in contact with altered plagioclase. Occurs as chadacrysts in clinopyroxene.
Clinopyroxene	~10%	Interstitial; oikocrystic	Medium	Relatively fresh compared to Ol and Pl; weakly serpentinized along a few fractures; locally altered to amphibole (characteristic ~120/60 cleavage visible) at margins of oikocrysts.
Plagioclase	5-7%	Interstitial, anhedral	Fine	Exhibits messy, patchy alteration to fibrous intergrowths of chlorite, talc, biotite, serpentine, carbonate, and another unknown phase.
Oxides	3-5%	(i) Granular; euhedral to rounded (ii) Rounded, anhedral (iii) Anhedral, linear chain aggregates	(i) Very fine to ultra fine (ii) Fine (iii) Ultra fine	(i) Chromite chadacrysts in silicates. (ii) Magnetite intergrown with sulfides; shares cuspate boundaries. (iii) Magnetite occurring with serpentine within fractures in olivine.
Pyrrhotite	10-15%	Interstitial; anhedral, massive	Fine	Troilite exsolution lamellae abundant throughout. Trace reflective, greyish PGM identified amongst the sulfide assemblage; elongate to angular in habit.
Chalcopyrite	~5%	Interstitial; anhedral, massive	Fine	Contains trace cubanite exsolution lamellae.
Pentlandite	2-4%	(i) Anhedral, granular aggregates (ii) Flames	(i) Fine to very fine (ii) Ultra fine	(i) Occurs at the interface between Po and Ccp, and also lines fractures in Po (ii) Occurs as exsolutions in Po, typically emanating from fractures or grain boundaries.
Overall Comments: Moderately altered, seriate, fine-grained, non-foliated, poikilitic, feldspathic wehrlite with primary net-textured sulfide mineralization.				

Sample ID: CAM-21-CC-117	**Depth: 399.3 m**	**Location: HGZ**	**CAM Code: Mgm**	**Rock Type: Wehrlite**
Mineral	*Abundance*	*Habit*	*Grain Size*	*Comments*
Olivine	~50-60%	Rounded to subhedral; chadacrystic	Fine	Extent of serpentinization is inconsistent; locally it is weak to moderate occurring within fractures. Extensive replacement to serpentine ± talc ± clay minerals increasingly occurs with proximity to crosscutting veinlet.
Clinopyroxene	~20%	Anhedral; oikocrystic	Coarse to medium	Fresh, unaltered; encloses olivine crystals.
Plagioclase	~2-5%	Interstitial, anhedral	Medium	Relatively unaltered; locally sericitized.
Biotite	~1%	Anhedral to tabular	Very fine	Found interstitially often associated with plagioclase; commonly found in interface between silicates and sulfides.
Ore assemblage 1	~5%	Interstitial	Medium to ultra fine	Mag >> Po > Ccp ~ Cbn >> Pn. This assemblage exhibits chaotic, mottled intergrowths. Original grain boundaries appear to be disturbed/obliterated. Po exhibits sub grains/triple junctions when viewed under cross nicols. Pentlandite appears trace in abundance.
Ore assemblage 2	~15%	Crosscutting	Medium to ultra fine	Po > Ccp ~ Cbn >> Pn > Py. Sulfide aggregate grains occur as blebs within the alteration veinlet. Composition and texture of the blebs is inconsistent from bleb to bleb. Within the blebs, Po commonly occurs as abundant sub hexagonal, sub grains (which exhibit triple junctions) with Ccp occupying the space between sub grains, in a loop-texture fashion. Pyrite occurs as angular, disaggregated grains within the blebs. Pentlandite is present as discrete granular aggregates (clusters) within the assemblage. In the larger blebs (where Po is more massive), Ccp occurs as "scars" or gashes through Po.
Overall Comments: Variably altered, seriate, fine- to medium-grained, non-foliated, poikilitic, wehrlite with an intense crosscutting sulfide, serpentine, carbonate, talc veinlet.				

Sample ID: CAM-21-CC-120	**Depth: 401.1 m**	**Location: HGZ**	**CAM Code: Upd**	**Rock Type: Feldspathic wehrlite**
Mineral	*Abundance*	*Habit*	*Grain Size*	*Comments*
Olivine	60-65%	Subhedral to prismatic	Fine	Occur as chadacrysts in Cpx. Strongly serpentinized along fractures; locally altered to talc along crystal margins.
Clinopyroxene	10-15%	Interstitial; oikocrystic	Medium	Weakly serpentinized along fractures. Minor alteration of margin to amphibole, locally.
Plagioclase	~5%	Interstitial, anhedral to tabular	Fine	Strong to intense, patchy alteration to clusters of chlorite, carbonate, talc, biotite, saussurite. Some patches are intensely altered to an unknown assemblage.
Oxides	~3-5%	(i) Rounded to subhedral (ii) Anhedral, chain aggregates (iii) Anhedral, sub veinlets	(i) Fine to ultra fine (ii) Ultra fine (iii) Very fine to ultra fine	(i) Chromite chadacrysts throughout the entire groundmass. (ii) Magnetite occurring within fractures of olivine associated with serpentine. (iii) Minor magnetite occupies fractures through sulfides, particularly in Pn.
Pyrrhotite	~10%	Interstitial, anhedral	Fine	Troilite exsolution lamellae abundant in Po. Po is locally intergrown with Ccp with a spotty, mottled pattern. There is also trace valleriite amongst the sulfide assemblage.
Chalcopyrite	5-7%	Interstitial, anhedral	Fine	Cbn exsolutions are common; occur as oriented laths and in rounded, anhedral form. Mkw exsolution worms occur in minor abundance.
Pentlandite	2-3%	(i) Anhedral, granular aggregates (ii) Flames	(i) Fine to very fine (ii) Ultra fine	(i) Occurs at the interface between Po and Ccp, as well as clustered around fractures in Po. (ii) Occurs as exsolutions in Po, typically emanating orthogonally from fractures and grain boundaries.
Galena	Trace	Interstitial, anhedral	Very fine	A lone, rounded galena grain was identified in the sulfide assemblage; shares grain boundary in equilibrium with Ccp.
Overall Comments: Serpentinized, homogeneous, fine-grained, non-foliated, poikilitic, feldspathic wehrlite with net-textured sulfide mineralization.				

Sample ID: CAM-21-CC-121	**Depth: 403.2 m**	**Location: HGZ**	**CAM Code: Upd**	**Rock Type: Feldspathic wehrlite**
Mineral	*Abundance*	*Habit*	*Grain Size*	*Comments*
Olivine	60-65%	Subrounded to subhedral	Fine to very fine	Occurs as chadacrysts in Cpx. Moderately to strongly serpentinized along fractures. Trace talc alteration locally on rims.
Clinopyroxene	10-15%	Interstitial; oikocrystic	Medium	Relatively fresh, weakly altered to serpentine along few fractures.
Plagioclase	5-7%	Interstitial, anhedral	Fine	Exhibits patchy, intermittent alteration to aggregates of talc, chlorite, biotite, and possibly another unidentified phase.
Oxides	2-4%	(i) Subrounded (ii) Linear, chain aggregates (iii) Anhedral, sub veinlets	(i) Fine to ultra fine (ii) Ultra fine (iii) Very fine to ultra fine	(i) Chromite chadacrysts throughout the groundmass. (ii) Magnetite occupying fractures in olivine; by-product of serpentinization. (iii) Minor magnetite occupies fractures through sulfides.
Pyrrhotite	8-12%	Interstitial, anhedral	Fine	Possible PGM present within the sulfide assemblage due to observation of highly reflective inclusions.
Chalcopyrite	~7%	Interstitial, anhedral	Fine	Cubanite exsolution lamellae common.
Pentlandite	2-3%	(i) Anhedral, granular aggregates (ii) Flames	(i) Fine to very fine (ii) Ultra fine	(i) Occurs at the interface between Po and Ccp, as well as clustered around fractures in Po. (ii) Occurs as exsolutions in Po, typically emanating orthogonally from fractures and grain boundaries.
Galena	Trace	Interstitial, anhedral	Very fine	A few rounded galena grains were identified in the sulfide assemblage; shares grain boundary in equilibrium with Ccp + Po. Found at the interface between silicates and sulfides.
Overall Comments: Altered, homogeneous, fine-grained, weakly foliated, poikilitic, feldspathic wehrlite, with fine, net-textured sulfide mineralization.				

Sample ID: CAM-21-CC-122	**Depth: 411.4 m**	**Location: HGZ**	**CAM Code: Upd**	**Rock Type: Dunite**
Mineral	*Abundance*	*Habit*	*Grain Size*	*Comments*
Olivine	60-70%	Granular, rounded	Fine to very fine	Strongly serpentinized along fractures; local talc alteration at margins of crystals.
Clinopyroxene	5-10%	Interstitial, anhedral	Fine to medium	Occurs as oikocrysts enclosing olivine. Moderately serpentinized along fractures.
Plagioclase	~3%	Interstitial, anhedral to tabular	Fine to very fine	Patchy alteration to saussurite, chlorite, talc, biotite, and actinolite(?).
Oxides	1-3%	(i) Granular, subhedral (ii) Interstitial, anhedral (iii) Anhedral, chain aggregates	(i) Very fine to ultra fine (ii) Very fine (iii) Ultra fine	(i) Chromite chadacrysts in silicates and sulfides. (ii) Magnetite intergrown with sulfides; shares cuspate grain boundaries, and also crosscuts as gashes/sub veinlets. (iii) Magnetite occurs within fractures in olivine with serpentine.
Sulfides	20-25%	Interstitial, various	Fine to ultra fine	Ccp + Cbn > Po > Pn + Mkw >> Val Sulfides exhibit mottled intergrowths, particularly with Ccp, Cbn, Pn, and Mkw. Mkw occur as elongate to tabular exsolutions(?) typically. Ccp occurs within fine fractures in Po. Val appears to overgrow sulfides and is intermittent. Loss of sulfide apparent as original grain boundaries are visibly replaced by hydrous silicates.
Overall Comments: Serpentinized, homogeneous, fine-grained, non-foliated, poikilitic, sulfide-bearing dunite.				

Sample ID: CAM-21-CC-124	**Depth: 411.5 m**	**Location: HGZ**	**CAM Code: MmgEL**	**Rock Type: Feldspathic wehrlite**
Mineral	*Abundance*	*Habit*	*Grain Size*	*Comments*
Olivine	50-55%	Granular, rounded, pseudomorphic	Fine to very fine	Intensely serpentinized along fractures, common pervasive replacement as well. Biotite often occurs interstitial to olivine. Trace apatite(?) grains as well.
Clinopyroxene	15-20%	Interstitial; anhedral	Medium to fine	Occurs as oikocrysts enclosing olivine. Moderately serpentinized along fractures. Commonly replaced by amphibole which may show characteristic ~120/60 cleavage planes.
Plagioclase	5-9%	Interstitial; anhedral	Fine	Exhibits patchy alteration with some areas relatively fresh, and elsewhere altered to complex intergrowths of hydrous phases (e.g., chlorite, biotite, serpentine, talc).
Oxides	3-5%	(i) Rounded to subhedral (ii) Interstitial, anhedral (iii) Linear chain aggregates; anhedral	(i) Very fine to ultra fine (ii) Fine to ultra fine (iii) Ultra fine	(i) Chromite chadacrysts predominantly occurring within silicates. (ii) Fe(-Ti?) oxides intergrown with the sulfide assemblage. Typically shares grain boundaries or occurs within fractures. (iii) Magnetite present within olivine fractures with serpentine.
Pyrrhotite	5-10%	Interstitial; anhedral	Fine	-
Chalcopyrite	~5%	Interstitial; anhedral	Fine	Oriented Cbn and Mkw exsolution lamellae common. Easily tarnished.
Pentlandite	2-3%	(i) Anhedral, granular aggregates (ii) Flames	(i) Fine to very fine (ii) Ultra fine	(i) Occurs at the interface between Po and Ccp, as clustered around fractures in Po, and as aggregates within Po. (ii) Occurs as exsolutions in Po, typically emanating orthogonally from fractures and grain boundaries.
Overall Comments: Strongly altered, homogeneous(?), fine-grained, non-foliated, poikilitic, feldspathic wehrlite.				

Quick Logs				
Section ID	*Depth (m)*	*Location*	*Mineralization*	*Comments*
CAM-21-CC-010	401.0	High-grade zone	net-textured Po > Ccp > Pn	Pn granular + flames; Po + Tro exs. tr. Mkw exs. in Po; no Cbn
CAM-21-CC-012	416.2	High-grade zone	disseminated Po > Ccp > Pn > Mkw	- oxide gashes - readily tarnished Ccp - possible native Cu, but tarnished - Fe-Ox associated with tarnished Ccp - weak anisotropy in Po; local "electric texture" w/ Cu-rich selvages along fractures; Ccp local fracture fill in Po
CAM-21-CC-014	431.6	High-grade zone	weakly disseminated to trace Po > Ccp > Pn ~ Mag	- intensely altered - abundant Pl; possibly melagabbro - deformation twins in Po - possible sulfide oxidation to Mag - appears to be just starting to alter; trace Mkw, Val - grain boundaries have been affected
CAM-21-CC-015	441.0	High-grade zone	disseminated Po > Ccp > Cbn > Pn	- intense silicate alteration - Cbn occurs as exs. laths in Ccp - abundant Pn flames in Po - ores appear to be somewhat deformed; deformation twins in Po + possible kink bands - Ccp appears to be starting to tarnish - Pn boundaries appear to be affected - Val and Mkw absent - trace native Ag - oxidized Pn ??
CAM-21-CC-016	452.5	High-grade zone	trace Po > Ccp	- sample is very altered
CAM-21-CC-028	349.4	High-grade zone	weakly disseminated Po > Pn > Val > Ccp > Mkw > Cu	- Mkw occurs with trellis-like habit - Fe-Ox ± Cu ± Ccp fill fractures along ~120-60° cleavage planes(?) in sulfides - abundant valleriite present in this section
CAM-21-CC-029	359.1	High-grade zone	weakly disseminated Po ~ Mag > Pn > Val > Mkw > Cu	- sample is strongly to intensely altered - valleriite is abundant
CAM-21-CC-032	389.0	High-grade zone	strongly disseminated Po > Ccp >> Pn > Mkw	- original sulfide grain boundaries modified - trace Mkw exs. in Ccp; - abundant Pn flames + Tro exs. in Po
CAM-21-CC-034	414.0	High-grade zone	strongly disseminated Po > Cbn > Ccp ~ Mag > Pn > Mkw > Val	- very intense serpentine alteration, w/ abundant amphibole, biotite alteration - "sample shows intermediate alteration" - Ccp is fully oxidized in some areas while Cbn remains clean; but native Cu is absent - Val and Mkw constitute only a minor amount of the ore assemblage - appears to be Cu-diffusion into Po crystal lattice; creates a halo effect along fracture selvages - Pn grain boundaries are affected; irregular

				- deformation twins in Po; local undulatory extinction
CAM-21-CC-041	344.0	High-grade zone	weakly disseminated Po > Mag > Pn > Mkw > Val > Ccp > Cu	- intensely serpentinized sample - "electric" Po w/ Cu-rich fracture selvages
CAM-21-CC-043	382.3	High-grade zone	trace Po + Ccp + Pn + Val + Mkw + Cu	- strongly serpentinized sample - difficult to accurately estimate modal abundance due to fine-grained nature, and complex intergrowths
CAM-21-CC-047	452.8	High-grade zone	trace indistinguishable	-
CAM-21-CC-049	491.4	High-grade zone	weakly disseminated Po > Ccp > Pn	- moderate serpentine alteration - amphibole, talc, and chlorite alteration is stronger - lots of pitting apparent throughout the section - abundant troilite exsolutions in Po - sulfide grain boundaries somewhat affected by alteration
CAM-21-CC-050	521.9	High-grade zone	weakly disseminated Po > Ccp > Py > Pn > Val > Mkw	- Po commonly appears recrystallized - trace Cbn lamellae in Ccp - no native Cu
CAM-21-CC-055	318.6	N perimeter	trace indistinguishable	- completely altered - sample shows carbonate tension gashes(?) - abundant Srp, Tlc ± Idd ± Sap alteration - sulfide mineralization is in too low abundance to identify
CAM-21-CC-057	352.0	N perimeter	weakly disseminated Po > Mag > Pn > Val > Mkw > Cu	- intensely serpentinized + additional interstitial alterations - very little Ccp remaining - "false" bornite associated with Cu (altered Ccp?) - Cu-rich haloes in Po present (diffusion into fracture selvages)
CAM-21-CC-058	371.0	N perimeter	weakly disseminated Po > Ccp > Pn >> Mkw > Val > Cu	- intensely serpentinized, talc-altered, etc. - Ccp is strongly tarnished - Po is recrystallized in some grains w/ obvious triple junctions
CAM-21-CC-059	387.8	N perimeter	weakly disseminated Po > Pn > Cu > Mkw > Val >> Ccp	- intensely altered throughout to an assemblage of Srp ± Chl ± Tlc ± etc. - native Cu stands out as abundant - possible presence of "false" bornite
CAM-21-CC-069	343.1	S perimeter	trace Cu + ?	- silicates are completely replaced; strong interference colours observed in

				Srp - very little sulfide remaining; renders it difficult to positively identify phases and their abundances
CAM-21-CC-070	368.6	S perimeter	weakly disseminated Po > Cu > Ccp ~ Fe-Ox ± Mkw	- very messy intergrowths; no primary textures remain - highly tarnished Ccp anastomoses through/entangled with Po - oriented Fe-Ox laths - abundant native Cu - Pn effectively absent
CAM-21-CC-074	413.9	S perimeter	disseminated Po > Ccp ± Cbn > Pn >> Mkw > Val > Cu	- strongly serpentinized + interstitial Pl alteration - abundant Po remaining - abundant Cu-diffusion into fracture selvages in Po - mottled textures common
CAM-21-CC-077	450.9	S perimeter	disseminated Po > Cbn > Ccp > Pn > Cu	- intensely altered; Cpx strongly altered to amphibole - sample shows primary assemblages intact in the larger grains, but in smaller grains alteration is variable
CAM-21-CC-079	496.0	S perimeter	weakly disseminated Po > Ccp > Cbn >> Pn	- intensely altered sample - abundant Pn flames in Po - Cbn occurs as exs. laths in Ccp - only change to sulfides are that their original grain boundaries have been destroyed/modified
CAM-21-CC-092	390.9	W perimeter	weakly disseminated Py > Po	- intensely Tlc+ altered - Py "islands" in Po "oceans" (anastomosing texture through Py fractures) - sample is barren of both Cu- and Ni-sulfide minerals; "depleted"
CAM-21-CC-097	380.2	E perimeter	trace Po ~ Mag > Pn > Mkw ~ Val > Cu	- intense serpentinization + other alteration - dark Ccp (or Po?) associated with native Cu gives consideration for classification as bornite
CAM-21-CC-098	389.2	E perimeter	trace Po > Val > Mkw ~ Cu ~ Pn > Ccp	- silicates are intensely altered to Srp + Chl + Tlc + etc.
CAM-21-CC-099	398.0	E perimeter	disseminated Po > Ccp ~ Mag > Pn	- intensely altered to dominantly Tlc - appears to be an intermediate sulfide assemblage - Ccp strongly tarnishes - appears to be abundant associated Mag; possible oxidation (of Po?)
CAM-21-CC-118	380.0	High-grade zone	trace Pn + Ccp + Cu + Val	- moderately serpentinized - "vermicular" Ccp occupying fractures of Po - highly tarnished Ccp + associated w/ Fe-Ox
CAM-21-CC-119	397.5	High-grade zone	strongly disseminated Mag > Ccp > Pn >> Po > Mkw	- intensely serpentinized (most dominant style of alteration) - Ccp + Pn largely unaffected - Po appears to have been extremely oxidized to Mag throughout the sample - trace amounts of Mkw - Mag exhibits mottled/messy

				intergrowths with the remaining sulfides

Appendix C – Whole-rock Geochemistry

*All values are reported anhydrous. Major element oxides reported in weight percent. Trace elements reported in parts per million. Sample IDs are shortened. Ti and P values derived from their major element oxides.

Method	Sample ID Analyte	CC-023 Gabbro	CC-038 Gabbro	CC-053 Gabbro	CC-066 Gabbro	CC-082 Gabbro
ICP-AES	SiO_2	50.37	49.76	50.11	50.52	51.53
ICP-AES	TiO_2	1.67	1.67	1.32	1.68	1.41
ICP-AES	Al_2O_3	6.83	5.57	5.42	6.35	6.60
ICP-AES	Fe_2O_3	11.39	13.19	9.95	11.89	10.47
Calculated	FeO_T	10.25	11.87	8.95	10.70	9.42
ICP-AES	MnO	0.22	0.22	0.30	0.29	0.26
ICP-AES	MgO	13.95	14.48	15.04	13.88	14.13
ICP-AES	CaO	13.38	13.91	15.87	13.98	13.47
ICP-AES	K_2O	0.48	0.16	0.30	0.28	0.41
ICP-AES	Na_2O	1.52	0.93	1.50	0.96	1.51
ICP-AES	P_2O_5	0.20	0.11	0.18	0.18	0.20
Calculated	Mg#	0.73	0.71	0.77	0.72	0.75

Method	Sample ID Analyte	CC-094 Gabbro	CC-024 Peridotite	CC-039 Peridotite	CC-054 Peridotite	CC-068 Peridotite
ICP-AES	SiO_2	51.15	41.82	41.46	41.81	41.59
ICP-AES	TiO_2	1.58	0.75	0.78	0.82	0.80
ICP-AES	Al_2O_3	5.46	3.16	3.29	3.47	3.59
ICP-AES	Fe_2O_3	10.83	17.54	17.78	17.47	17.98
Calculated	FeO_T	9.75	15.78	15.99	15.72	16.18
ICP-AES	MnO	0.22	0.23	0.23	0.22	0.24
ICP-AES	MgO	14.34	32.64	32.49	32.05	31.63
ICP-AES	CaO	14.70	3.13	3.26	3.36	3.47
ICP-AES	K_2O	0.61	0.24	0.26	0.32	0.28
ICP-AES	Na_2O	0.99	0.38	0.36	0.35	0.32
ICP-AES	P_2O_5	0.12	0.11	0.10	0.11	0.10
Calculated	Mg#	0.74	0.80	0.80	0.80	0.79

Method	Sample ID Analyte	CC-083 Peridotite	CC-095 Peridotite	CC-001 Hybrid Grey	CC-002 Oxide Gabbro	CC-020 Schist
ICP-AES	SiO_2	41.75	41.10	37.51	43.56	64.18
ICP-AES	TiO_2	0.71	0.83	4.79	3.54	0.55
ICP-AES	Al_2O_3	3.69	3.30	5.64	13.12	17.26
ICP-AES	Fe_2O_3	17.36	18.29	28.69	19.55	5.77

Calculated	**FeO_T**	15.62	16.45	25.81	17.59	5.19
ICP-AES	**MnO**	0.22	0.23	0.40	0.21	0.08
ICP-AES	**MgO**	32.88	32.27	10.24	6.60	2.63
ICP-AES	**CaO**	2.53	3.30	11.51	9.39	2.85
ICP-AES	**K_2O**	0.36	0.24	0.10	0.82	1.49
ICP-AES	**Na_2O**	0.40	0.34	1.01	3.08	5.04
ICP-AES	**P_2O_5**	0.11	0.09	0.12	0.13	0.16
Calculated	**Mg#**	0.81	0.80	0.44	0.43	0.50

Method	Sample ID Analyte	CC-037 Schist	CC-52 Schist	CC-065 Schist	CC-090 Schist	CC-103 Schist
ICP-AES	**SiO_2**	64.39	59.68	65.32	62.12	61.42
ICP-AES	**TiO_2**	0.60	0.52	0.57	0.60	0.59
ICP-AES	**Al_2O_3**	17.15	14.56	16.18	17.76	19.14
ICP-AES	**Fe_2O_3**	5.14	7.53	6.05	7.08	5.73
Calculated	**FeO_T**	4.62	6.78	5.44	6.37	5.16
ICP-AES	**MnO**	0.04	0.10	0.04	0.05	0.07
ICP-AES	**MgO**	2.54	9.02	2.72	3.64	2.78
ICP-AES	**CaO**	2.65	2.46	2.03	1.64	2.95
ICP-AES	**K_2O**	2.20	1.87	2.01	3.42	2.07
ICP-AES	**Na_2O**	5.08	4.10	4.77	3.55	5.08
ICP-AES	**P_2O_5**	0.21	0.16	0.32	0.12	0.17
Calculated	**Mg#**	0.52	0.72	0.50	0.53	0.52

Method	Sample ID Analyte	CC-080 Granitoid	CC-081 Granitoid
ICP-AES	**SiO_2**	74.79	74.14
ICP-AES	**TiO_2**	0.02	0.01
ICP-AES	**Al_2O_3**	14.32	15.26
ICP-AES	**Fe_2O_3**	1.23	1.20
Calculated	**FeO_T**	1.11	1.08
ICP-AES	**MnO**	0.01	0.08
ICP-AES	**MgO**	0.17	0.16
ICP-AES	**CaO**	0.96	0.69
ICP-AES	**K_2O**	4.33	3.80
ICP-AES	**Na_2O**	3.96	4.43
ICP-AES	**P_2O_5**	0.21	0.22
Calculated	**Mg#**	0.23	0.23

Method	Sample ID Analyte	CC-023 Gabbro	CC-038 Gabbro	CC-053 Gabbro	CC-066 Gabbro	CC-82 Gabbro
Calculated	**Ti**	9854.60	9995.45	7838.79	10189.54	8535.49
Calculated	**P**	851.86	497.12	763.82	809.17	894.00
ICP-MS	**Cr**	482.87	248.54	2450.38	1679.07	1597.90
ICP-AES	**Co**	67.81	81.81	64.86	76.23	54.29
ICP-AES	**Ni**	244.52	225.76	296.52	326.54	319.58
ICP-MS	**Rb**	7.71	2.59	3.91	4.33	6.66
ICP-MS	**Sr**	67.19	89.58	71.14	59.75	66.58
ICP-MS	**Cs**	0.10	0.13	0.16	0.10	0.09
ICP-MS	**Ba**	37.60	22.37	24.71	27.19	35.13
ICP-AES	**Sc**	46.23	54.89	43.24	43.26	43.02
ICP-MS	**V**	228.08	309.64	199.74	222.50	191.54
ICP-MS	**Ta**	0.72	0.62	0.72	0.72	0.72
ICP-MS	**Nb**	11.30	8.91	10.71	10.61	10.76
ICP-MS	**Zr**	137.67	119.09	127.67	143.18	151.60
ICP-MS	**Hf**	3.60	3.52	3.81	3.91	4.20
ICP-MS	**Th**	1.18	1.14	1.19	1.21	1.18
ICP-MS	**U**	0.39	0.36	0.42	0.42	0.40
ICP-MS	**Y**	15.51	16.05	15.13	15.66	16.18
ICP-MS	**La**	18.60	14.81	18.94	17.92	18.44
ICP-MS	**Ce**	46.44	37.49	46.33	45.12	46.20
ICP-MS	**Pr**	6.65	5.51	6.40	6.50	6.89
ICP-MS	**Nd**	33.08	25.48	28.11	30.49	32.47
ICP-MS	**Sm**	7.07	6.69	7.13	6.66	7.14
ICP-MS	**Eu**	1.93	1.65	1.72	1.98	2.00
ICP-MS	**Gd**	5.78	5.37	5.62	5.29	5.55
ICP-MS	**Tb**	0.77	0.67	0.69	0.68	0.74
ICP-MS	**Dy**	3.99	3.91	3.92	3.71	3.88
ICP-MS	**Ho**	0.70	0.68	0.64	0.67	0.66
ICP-MS	**Er**	1.78	1.78	1.64	1.36	1.53
ICP-MS	**Tm**	0.21	0.22	0.21	0.21	0.22
ICP-MS	**Yb**	1.17	1.20	1.31	1.11	1.29
ICP-MS	**Lu**	0.12	0.17	0.16	0.18	0.22
ICP-AES	**Cu**	438.69	471.19	14.41	776.70	452.74
ICP-AES	**Zn**	70.89	85.95	915.29	82.41	86.04
ICP-AES	**Mo**	1.03	1.04	1.03	2.06	2.05
ICP-AES	**Ag**	0.26	0.26	0.26	0.26	0.26
ICP-MS	**Tl**	0.32	0.32	0.10	0.24	0.15
ICP-AES	**Pb**	14.38	11.39	27.80	37.08	5.12
ICP-MS	**Sn**	1.03	1.04	1.03	1.03	1.02
ICP-MS	**Sb**	0.03	0.06	0.03	0.05	0.03
ICP-MS	**Ga**	12.53	12.94	10.60	11.95	11.98
ICP-MS	**Ge**	0.26	0.26	0.26	0.26	0.26

ICP-MS	**As**	1.34	1.86	11.63	14.83	3.07
ICP-MS	**W**	0.51	0.52	1.03	2.06	1.02
ICP-MS	**Bi**	0.04	0.05	0.06	0.11	0.05

Method	Sample ID Analyte	CC-094 Gabbro	CC-024 Peridotite	CC-039 Peridotite	CC-054 Peridotite	CC-068 Peridotite
Calculated	**Ti**	9503.93	4427.48	4624.27	4815.18	4842.83
Calculated	**P**	535.61	473.96	426.70	473.67	428.75
ICP-MS	**Cr**	1196.65	2986.70	3389.61	3809.77	3253.08
ICP-AES	**Co**	75.69	170.51	171.65	175.84	157.20
ICP-AES	**Ni**	290.47	1330.44	1450.36	1411.02	1189.89
ICP-MS	**Rb**	9.21	5.65	5.43	8.68	6.88
ICP-MS	**Sr**	64.44	155.31	192.30	192.66	173.57
ICP-MS	**Cs**	0.15	0.31	0.24	0.76	0.53
ICP-MS	**Ba**	206.60	83.08	84.85	105.72	95.30
ICP-AES	**Sc**	50.12	11.95	11.95	13.02	10.92
ICP-MS	**V**	252.63	101.00	111.90	117.22	106.98
ICP-MS	**Ta**	0.51	0.43	0.33	0.43	0.33
ICP-MS	**Nb**	8.90	5.43	5.43	5.97	6.22
ICP-MS	**Zr**	120.69	68.42	65.18	75.98	75.32
ICP-MS	**Hf**	3.17	1.95	1.74	1.95	1.96
ICP-MS	**Th**	0.95	0.79	0.59	0.69	0.69
ICP-MS	**U**	0.36	0.25	0.18	0.24	0.26
ICP-MS	**Y**	13.91	6.19	5.76	6.40	6.44
ICP-MS	**La**	14.63	9.45	7.93	9.33	9.39
ICP-MS	**Ce**	36.62	23.02	19.77	23.12	22.38
ICP-MS	**Pr**	5.30	3.10	2.66	3.19	2.98
ICP-MS	**Nd**	25.98	13.90	12.60	14.22	14.19
ICP-MS	**Sm**	5.88	2.90	2.74	2.82	2.87
ICP-MS	**Eu**	1.76	0.73	0.80	0.85	0.80
ICP-MS	**Gd**	4.76	2.38	2.22	2.44	2.36
ICP-MS	**Tb**	0.62	0.30	0.26	0.30	0.31
ICP-MS	**Dy**	3.66	1.50	1.41	1.47	1.68
ICP-MS	**Ho**	0.64	0.28	0.25	0.28	0.29
ICP-MS	**Er**	1.60	0.75	0.61	0.79	0.60
ICP-MS	**Tm**	0.23	0.09	0.07	0.09	0.11
ICP-MS	**Yb**	1.20	0.58	0.37	0.54	0.46
ICP-MS	**Lu**	0.17	0.07	0.08	0.07	0.08
ICP-AES	**Cu**	443.89	238.94	469.33	272.44	251.08
ICP-AES	**Zn**	67.50	114.04	123.85	123.74	108.07
ICP-AES	**Mo**	1.02	0.54	0.54	0.54	3.27
ICP-AES	**Ag**	0.26	0.27	0.27	0.27	0.27
ICP-MS	**Tl**	0.20	0.04	0.03	0.05	0.03
ICP-AES	**Pb**	5.11	3.26	3.26	3.26	3.27

ICP-MS	**Sn**	1.02	1.09	0.54	1.09	1.09
ICP-MS	**Sb**	0.03	0.03	0.03	0.03	0.03
ICP-MS	**Ga**	10.23	5.86	6.52	7.16	6.77
ICP-MS	**Ge**	0.26	0.27	0.27	0.27	0.27
ICP-MS	**As**	1.02	0.22	0.22	0.33	0.33
ICP-MS	**W**	1.02	1.09	1.09	0.54	0.55
ICP-MS	**Bi**	0.04	0.08	0.12	0.05	0.08

Method	Sample ID Analyte	CC-083 Peridotite	CC-095 Peridotite	CC-001 Hybrid Grey	CC-002 Oxide Gabbro	CC-020 Schist
Calculated	**Ti**	4299.05	4899.17	28919.74	21068.47	3259.12
Calculated	**P**	474.16	380.41	534.08	584.68	671.45
ICP-MS	**Cr**	3476.88	2963.75	20.40	10.31	133.35
ICP-AES	**Co**	177.10	178.70	122.38	87.60	20.51
ICP-AES	**Ni**	1570.03	1590.84	159.10	35.04	61.54
ICP-MS	**Rb**	7.82	5.56	1.73	13.91	37.64
ICP-MS	**Sr**	214.05	155.27	70.78	212.30	614.41
ICP-MS	**Cs**	0.58	0.44	0.16	0.12	2.14
ICP-MS	**Ba**	115.71	78.34	23.56	176.23	445.17
ICP-AES	**Sc**	9.78	13.08	52.01	32.98	11.28
ICP-MS	**V**	86.92	102.42	1167.75	623.51	100.52
ICP-MS	**Ta**	0.43	0.33	0.61	0.52	0.31
ICP-MS	**Nb**	6.41	5.01	7.75	9.38	4.72
ICP-MS	**Zr**	85.84	64.29	114.23	128.82	124.11
ICP-MS	**Hf**	2.06	1.74	3.57	4.02	3.28
ICP-MS	**Th**	0.76	0.53	0.93	1.12	3.74
ICP-MS	**U**	0.23	0.20	0.33	0.35	1.05
ICP-MS	**Y**	6.95	5.88	13.97	13.60	10.36
ICP-MS	**La**	9.67	7.63	12.34	15.46	21.75
ICP-MS	**Ce**	22.93	19.29	32.64	38.44	45.44
ICP-MS	**Pr**	3.32	2.64	4.85	5.64	5.35
ICP-MS	**Nd**	14.23	12.31	24.37	26.38	22.87
ICP-MS	**Sm**	3.07	2.59	5.73	5.80	3.99
ICP-MS	**Eu**	0.78	0.73	1.55	1.87	1.12
ICP-MS	**Gd**	2.17	2.12	5.12	4.84	2.93
ICP-MS	**Tb**	0.30	0.29	0.60	0.62	0.37
ICP-MS	**Dy**	1.80	1.27	3.42	3.45	1.96
ICP-MS	**Ho**	0.34	0.27	0.60	0.56	0.41
ICP-MS	**Er**	0.70	0.57	1.49	1.50	1.21
ICP-MS	**Tm**	0.11	0.08	0.15	0.19	0.16
ICP-MS	**Yb**	0.56	0.49	1.23	1.12	1.09
ICP-MS	**Lu**	0.08	0.09	0.14	0.13	0.18
ICP-AES	**Cu**	758.39	493.59	288.62	79.36	57.44
ICP-AES	**Zn**	119.52	130.75	90.77	98.94	53.34

ICP-AES	**Mo**	0.54	0.54	1.02	1.03	2.05
ICP-AES	**Ag**	0.27	0.27	0.25	0.26	0.26
ICP-MS	**Tl**	0.07	0.03	0.05	0.07	0.05
ICP-AES	**Pb**	5.43	4.36	11.22	8.24	10.26
ICP-MS	**Sn**	1.09	1.09	2.04	1.03	1.03
ICP-MS	**Sb**	0.03	0.03	0.03	0.03	0.03
ICP-MS	**Ga**	6.85	5.99	21.42	22.78	21.44
ICP-MS	**Ge**	0.27	0.27	0.25	0.26	0.26
ICP-MS	**As**	0.43	0.33	0.51	0.62	1.74
ICP-MS	**W**	0.54	0.54	0.51	0.52	1.03
ICP-MS	**Bi**	0.22	0.09	0.04	0.01	0.40

Method	**Sample ID** **Analyte**	**CC-037** **Schist**	**CC-52** **Schist**	**CC-065** **Schist**	**CC-090** **Schist**	**CC-103** **Schist**
Calculated	**Ti**	3636.26	3128.55	3432.11	3644.40	3512.07
Calculated	**P**	942.14	683.22	1427.64	539.57	762.49
ICP-MS	**Cr**	174.77	709.73	173.79	154.55	164.44
ICP-AES	**Co**	22.62	51.14	21.47	22.67	21.58
ICP-AES	**Ni**	75.05	327.73	80.76	94.79	76.06
ICP-MS	**Rb**	80.60	59.07	176.86	107.16	74.72
ICP-MS	**Sr**	521.22	530.21	467.20	450.26	706.08
ICP-MS	**Cs**	1.74	2.06	26.17	4.49	2.43
ICP-MS	**Ba**	449.26	459.24	337.36	1027.26	489.22
ICP-AES	**Sc**	12.34	9.39	14.31	16.49	12.33
ICP-MS	**V**	100.75	79.32	115.52	129.82	107.92
ICP-MS	**Ta**	0.51	0.31	0.31	0.41	0.41
ICP-MS	**Nb**	8.02	5.11	4.60	7.01	5.34
ICP-MS	**Zr**	206.64	123.16	142.10	131.88	137.72
ICP-MS	**Hf**	5.35	3.44	3.78	3.71	3.60
ICP-MS	**Th**	9.58	3.28	4.09	6.57	4.68
ICP-MS	**U**	2.42	1.00	1.23	1.83	1.25
ICP-MS	**Y**	14.08	8.66	14.01	15.04	12.54
ICP-MS	**La**	38.96	18.89	23.41	31.63	26.00
ICP-MS	**Ce**	78.23	42.06	48.15	66.97	51.59
ICP-MS	**Pr**	9.05	5.24	5.82	7.90	6.17
ICP-MS	**Nd**	37.73	21.40	23.82	33.80	26.21
ICP-MS	**Sm**	6.24	4.11	4.41	5.52	4.37
ICP-MS	**Eu**	1.66	0.89	1.17	1.85	1.23
ICP-MS	**Gd**	4.40	2.74	3.79	4.52	3.11
ICP-MS	**Tb**	0.49	0.31	0.46	0.59	0.42
ICP-MS	**Dy**	3.05	1.80	2.68	2.87	2.36
ICP-MS	**Ho**	0.52	0.34	0.59	0.64	0.51
ICP-MS	**Er**	1.52	0.98	1.48	1.61	1.40
ICP-MS	**Tm**	0.20	0.11	0.20	0.23	0.21
ICP-MS	**Yb**	1.23	0.92	1.46	1.55	1.48
ICP-MS	**Lu**	0.21	0.13	0.19	0.26	0.23

ICP-AES	**Cu**	32.90	61.58	59.29	10.30	10.28
ICP-AES	**Zn**	25.70	72.02	23.51	32.97	20.56
ICP-AES	**Mo**	2.06	1.04	2.04	2.06	1.03
ICP-AES	**Ag**	0.26	0.26	0.26	0.26	0.26
ICP-MS	**Tl**	0.05	0.09	0.78	0.11	0.06
ICP-AES	**Pb**	8.22	7.31	8.18	10.30	5.14
ICP-MS	**Sn**	1.03	1.04	5.11	2.06	1.03
ICP-MS	**Sb**	0.03	0.03	0.03	0.03	0.03
ICP-MS	**Ga**	21.28	17.22	21.26	23.70	22.41
ICP-MS	**Ge**	0.26	0.26	0.26	0.26	0.26
ICP-MS	**As**	1.75	1.25	0.51	0.82	1.23
ICP-MS	**W**	3.08	1.04	1.02	2.06	1.03
ICP-MS	**Bi**	0.22	0.30	0.24	0.13	0.15

Method	**Sample ID** **Analyte**	**CC-080** **Granitoid**	**CC-081** **Granitoid**
Calculated	**Ti**	122.29	60.81
Calculated	**P**	934.70	973.91
ICP-MS	**Cr**	20.40	20.29
ICP-AES	**Co**	1.02	0.51
ICP-AES	**Ni**	6.12	3.04
ICP-MS	**Rb**	309.04	278.96
ICP-MS	**Sr**	113.72	115.64
ICP-MS	**Cs**	4.27	2.96
ICP-MS	**Ba**	146.87	100.33
ICP-AES	**Sc**	0.51	0.51
ICP-MS	**V**	2.55	2.54
ICP-MS	**Ta**	4.69	7.30
ICP-MS	**Nb**	37.64	39.36
ICP-MS	**Zr**	11.22	22.32
ICP-MS	**Hf**	0.71	1.22
ICP-MS	**Th**	0.78	0.45
ICP-MS	**U**	7.36	11.82
ICP-MS	**Y**	2.45	3.96
ICP-MS	**La**	1.02	0.71
ICP-MS	**Ce**	2.86	2.43
ICP-MS	**Pr**	0.43	0.37
ICP-MS	**Nd**	1.43	1.52
ICP-MS	**Sm**	0.32	0.43
ICP-MS	**Eu**	0.02	0.01
ICP-MS	**Gd**	0.22	0.44
ICP-MS	**Tb**	0.06	0.08
ICP-MS	**Dy**	0.32	0.51
ICP-MS	**Ho**	0.08	0.10
ICP-MS	**Er**	0.21	0.25
ICP-MS	**Tm**	0.06	0.06

ICP-MS	**Yb**	0.31	0.50
ICP-MS	**Lu**	0.04	0.09
ICP-AES	**Cu**	5.10	4.06
ICP-AES	**Zn**	7.14	33.48
ICP-AES	**Mo**	1.02	1.01
ICP-AES	**Ag**	0.25	0.25
ICP-MS	**Tl**	0.07	0.06
ICP-AES	**Pb**	6.12	16.23
ICP-MS	**Sn**	4.08	5.07
ICP-MS	**Sb**	0.03	0.03
ICP-MS	**Ga**	23.97	29.21
ICP-MS	**Ge**	0.25	0.25
ICP-MS	**As**	0.31	0.41
ICP-MS	**W**	2.04	2.03
ICP-MS	**Bi**	0.83	0.93

Appendix D – Sulfide Geochemistry

*Co in Sg obtained from LA–ICP–MS

Analysis ID	Sample ID	Unit Mineralization	SEM wt.% S	SEM wt.% S_2σ	SEM wt.% Fe	SEM wt.% Fe_2σ	SEM wt.% Cu	SEM wt.% Cu_2σ	SEM wt.% Ni	SEM wt.% Ni_2σ	SEM wt.% Co	SEM wt.% Co_2σ
Py 1	CAM-21-CC-008	Net-textured	52.42	0.32	47.76	0.46						
Po 2	CAM-21-CC-008	Net-textured	37.69	0.28	62.38	0.52						
Ccp 3	CAM-21-CC-008	Net-textured	33.67	0.28	30.67	0.38	35.61	0.56				
Pn 4	CAM-21-CC-008	Net-textured	32.36	0.26	30.62	0.38			34.34	0.48	2.30	0.24
Po 5	CAM-21-CC-008	Net-textured	37.78	0.28	62.11	0.52						
Ccp 6	CAM-21-CC-008	Net-textured	33.49	0.28	30.72	0.38	35.34	0.56				
Ccp 7	CAM-21-CC-008	Net-textured	33.79	0.28	30.88	0.38	35.89	0.56				
Po 8	CAM-21-CC-008	Net-textured	37.70	0.28	62.44	0.52						
Pn 9	CAM-21-CC-008	Net-textured	32.56	0.26	31.15	0.38			34.38	0.48	2.23	0.24
Ccp 10	CAM-21-CC-008	Net-textured	33.83	0.28	30.54	0.38	35.30	0.56				
Po 11	CAM-21-CC-008	Net-textured	38.14	0.28	62.14	0.52						
Ccp 12	CAM-21-CC-009	Net-textured	33.59	0.28	30.66	0.38	35.37	0.56				
Po 13	CAM-21-CC-009	Net-textured	37.66	0.28	62.20	0.52						
Ccp 14	CAM-21-CC-009	Net-textured	33.85	0.28	30.56	0.38	35.81	0.56				
Po 15	CAM-21-CC-009	Net-textured	37.88	0.28	62.57	0.52						
Ccp 16	CAM-21-CC-009	Net-textured	33.59	0.28	30.59	0.38	35.81	0.56				
Po 17	CAM-21-CC-009	Net-textured	37.95	0.28	62.03	0.52						
Ccp 18a	CAM-21-CC-009	Net-textured	33.61	0.28	30.54	0.38	35.88	0.56				
Po 18b	CAM-21-CC-009	Net-textured	37.84	0.28	62.22	0.52						
Ccp 19	CAM-21-CC-009	Net-textured	33.79	0.28	30.67	0.38	35.99	0.56				
Po 20	CAM-21-CC-009	Net-textured	37.85	0.28	62.67	0.52						
Ccp 21	CAM-21-CC-011	Net-textured	34.23	0.28	30.60	0.38	35.18	0.54				
Po 22	CAM-21-CC-011	Net-textured	35.92	0.28	63.85	0.52						
Ccp 23	CAM-21-CC-011	Net-textured	34.02	0.28	30.70	0.38	34.99	0.54				
Po 24	CAM-21-CC-011	Net-textured	36.22	0.28	63.90	0.52						
Ccp 25	CAM-21-CC-011	Net-textured	34.23	0.28	30.59	0.38	34.97	0.54				
Po 26	CAM-21-CC-011	Net-textured	38.17	0.28	61.61	0.52						
Ccp 27	CAM-21-CC-011	Net-textured	33.78	0.28	30.44	0.36	35.32	0.54				
Po 28	CAM-21-CC-011	Net-textured	37.75	0.28	62.67	0.52						

Analysis ID	Sample ID	Unit Mineralization	SEM wt.% S	SEM wt.% S_2σ	SEM wt.% Fe	SEM wt.% Fe_2σ	SEM wt.% Cu	SEM wt.% Cu_2σ	SEM wt.% Ni	SEM wt.% Ni_2σ	SEM wt.% Co	SEM wt.% Co_2σ
Ccp 29	CAM-21-CC-011	Net-textured	34.22	0.28	30.63	0.38	35.54	0.54				
Po 30	CAM-21-CC-011	Net-textured	36.71	0.28	63.60	0.52						
Ccp 31	CAM-21-CC-035	Veinlet	34.29	0.28	30.61	0.36	35.28	0.54				
Po 32	CAM-21-CC-035	Veinlet	35.97	0.28	64.07	0.52						
Cbn 33	CAM-21-CC-035	Veinlet	35.21	0.28	41.29	0.42	23.28	0.46				
Po 34	CAM-21-CC-035	Veinlet	36.17	0.26	63.44	0.52						
Pn 35	CAM-21-CC-035	Veinlet	33.51	0.26	36.86	0.40			29.87	0.46		
Ccp 36	CAM-21-CC-035	Veinlet	34.55	0.28	30.66	0.36	35.01	0.54				
Po 37	CAM-21-CC-035	Veinlet	36.13	0.28	63.82	0.52						
Ccp 41a	CAM-21-CC-044	Net-textured	34.40	0.28	30.79	0.38	35.14	0.54				
Po 41b	CAM-21-CC-044	Net-textured	38.31	0.28	61.85	0.52			0.36	0.16		
Ccp 42	CAM-21-CC-044	Net-textured	34.70	0.28	30.95	0.38	34.80	0.54				
Po 43	CAM-21-CC-044	Net-textured	38.45	0.28	61.59	0.52						
Ccp 44	CAM-21-CC-044	Net-textured	34.40	0.28	30.64	0.38	34.69	0.54				
Po 45	CAM-21-CC-044	Net-textured	38.22	0.28	61.51	0.52			0.46	0.16		
Ccp 46	CAM-21-CC-044	Net-textured	34.39	0.28	30.78	0.38	34.84	0.54				
Po 47	CAM-21-CC-044	Net-textured	38.37	0.28	61.33	0.52			0.69	0.16		
Ccp 48	CAM-21-CC-045	Net-textured	34.26	0.28	30.85	0.38	34.86	0.54				
Po 49	CAM-21-CC-045	Net-textured	38.07	0.28	62.23	0.52						
Ccp 50a	CAM-21-CC-045	Net-textured	34.16	0.28	30.69	0.38	35.08	0.54				
Po 50b	CAM-21-CC-045	Net-textured	38.18	0.28	61.74	0.52						
Pn 50c	CAM-21-CC-045	Net-textured	32.88	0.28	31.17	0.38			34.54	0.48	1.90	0.22
Ccp 51	CAM-21-CC-045	Net-textured	34.63	0.28	30.83	0.38	34.59	0.54				
Po 52	CAM-21-CC-045	Net-textured	37.39	0.28	62.55	0.52			0.40	0.16		
Py 53	CAM-21-CC-045	Net-textured	52.86	0.32	47.46	0.46						
Ccp 54	CAM-21-CC-045	Net-textured	34.13	0.28	30.79	0.38	34.94	0.54				
Po 55	CAM-21-CC-045	Net-textured	38.02	0.28	61.59	0.52						
Po 56	CAM-21-CC-045	Net-textured	38.31	0.28	61.81	0.52						
Ccp 57	CAM-21-CC-045	Net-textured	34.38	0.28	30.65	0.38	34.62	0.54				
Po 58	CAM-21-CC-045	Net-textured	38.25	0.28	61.87	0.52						
Ccp 59	CAM-21-CC-048	Semi-n.t.	34.52	0.28	30.78	0.38	35.11	0.54				
Po 60	CAM-21-CC-048	Semi-n.t.	38.12	0.28	62.09	0.52						
Ccp 61	CAM-21-CC-048	Semi-n.t.	34.51	0.28	31.09	0.38	34.80	0.54				

Analysis ID	Sample ID	Unit Mineralization	SEM wt.% S	SEM wt.% S_2σ	SEM wt.% Fe	SEM wt.% Fe_2σ	SEM wt.% Cu	SEM wt.% Cu_2σ	SEM wt.% Ni	SEM wt.% Ni_2σ	SEM wt.% Co	SEM wt.% Co_2σ
Po 62	CAM-21-CC-048	Semi-n.t.	38.23	0.28	61.53	0.52						
Ccp 63	CAM-21-CC-048	Veinlet	34.45	0.28	30.68	0.38	35.02	0.54				
Po 64	CAM-21-CC-048	Veinlet	38.04	0.28	61.54	0.52						
Pn 65	CAM-21-CC-048	Veinlet	32.97	0.28	30.87	0.38			33.96	0.48	1.79	0.22
Po 66	CAM-21-CC-048	Veinlet	38.47	0.28	61.65	0.52						
Ccp 67	CAM-21-CC-048	Veinlet	34.34	0.28	30.60	0.38	35.03	0.54				
Po 68	CAM-21-CC-048	Veinlet	38.20	0.28	61.63	0.52						
Ccp 69	CAM-21-CC-048	Semi-n.t.	34.40	0.28	30.59	0.38	34.99	0.54				
Po 70	CAM-21-CC-100	Semi-n.t.	35.93	0.28	63.90	0.52						
Po 71	CAM-21-CC-100	Semi-n.t.	36.18	0.28	64.15	0.52						
Po 72	CAM-21-CC-100	Semi-n.t.	36.04	0.28	63.76	0.52						
Cbn 73	CAM-21-CC-100	Semi-n.t.	33.02	0.28	38.01	0.40	28.81	0.50				
Ccp 74	CAM-21-CC-100	Semi-n.t.	32.06	0.28	28.74	0.36	38.86	0.56				
Po 75	CAM-21-CC-100	Semi-n.t.	36.08	0.28	64.23	0.52						
Po 76	CAM-21-CC-101	Disseminated	35.80	0.26	64.09	0.50						
Po 77	CAM-21-CC-101	Veinlet	36.08	0.26	64.29	0.50						
Po 78	CAM-21-CC-101	Veinlet	36.04	0.26	63.99	0.50						
Cbn 79	CAM-21-CC-101	Veinlet	34.57	0.26	40.99	0.40	24.55	0.46				
Po 80	CAM-21-CC-101	Veinlet	36.02	0.26	63.99	0.50						
Po 81	CAM-21-CC-101	Veinlet	36.00	0.26	64.10	0.50						
Ccp 82	CAM-21-CC-116	Net-textured	34.41	0.26	30.42	0.36	35.31	0.52				
Pn 83	CAM-21-CC-116	Net-textured	32.78	0.26	31.62	0.36			32.92	0.46	2.18	0.22
Ccp 84	CAM-21-CC-116	Net-textured	34.26	0.26	30.83	0.36	35.14	0.52				
Po 85	CAM-21-CC-116	Net-textured	38.23	0.26	61.57	0.50						
Ccp 86	CAM-21-CC-116	Net-textured	34.66	0.26	30.50	0.36	34.58	0.52				
Po 87	CAM-21-CC-116	Net-textured	38.44	0.26	61.90	0.50						
Ccp 88	CAM-21-CC-116	Net-textured	34.46	0.26	30.81	0.36	34.67	0.52				
Po 89	CAM-21-CC-116	Net-textured	38.39	0.26	61.97	0.50						
Po 90	CAM-21-CC-116	Net-textured	38.25	0.26	61.46	0.50						
Ccp 91	CAM-21-CC-116	Net-textured	34.82	0.26	30.81	0.36	34.77	0.52				
Po 92	CAM-21-CC-116	Net-textured	38.33	0.26	61.99	0.50						
Po 93	CAM-21-CC-005	Disseminated	35.60	0.28	64.11	0.54						
Po 94	CAM-21-CC-005	Disseminated	35.69	0.28	64.47	0.54						

Analysis ID	Sample ID	Unit Mineralization	SEM wt.% S	SEM wt.% S_2σ	SEM wt.% Fe	SEM wt.% Fe_2σ	SEM wt.% Cu	SEM wt.% Cu_2σ	SEM wt.% Ni	SEM wt.% Ni_2σ	SEM wt.% Co	SEM wt.% Co_2σ
Po 95	CAM-21-CC-005	Disseminated	35.18	0.26	63.96	0.52	0.53	0.20				
Mkw 96	CAM-21-CC-005	Disseminated	34.99	0.28	60.80	0.52	1.34	0.22	2.46	0.20		
Po 97	CAM-21-CC-005	Disseminated	35.54	0.28	64.40	0.54						
Po 98	CAM-21-CC-005	Disseminated	35.68	0.28	64.45	0.54						
Ccp 99	CAM-21-CC-005	Disseminated	30.31	0.26	34.42	0.40	35.14	0.56				
Cu 100	CAM-21-CC-005	Disseminated					99.84	0.82				
Mkw 101	CAM-21-CC-005	Disseminated	35.20	0.28	60.59	0.52	1.72	0.22	2.27	0.20		
Po 102	CAM-21-CC-005	Disseminated	35.75	0.28	64.43	0.54						
Ccp 103	CAM-21-CC-060	Disseminated	32.47	0.26	32.84	0.38	34.47	0.54				
Po 104	CAM-21-CC-060	Disseminated	35.41	0.26	64.25	0.52	0.57	0.20				
Mkw 105	CAM-21-CC-060	Disseminated	35.82	0.28	59.16	0.52	0.83	0.22	3.74	0.22		
Mkw 106a	CAM-21-CC-060	Disseminated	35.79	0.28	60.64	0.52	1.16	0.22	2.68	0.20		
Mkw 106b	CAM-21-CC-060	Disseminated	36.00	0.28	60.93	0.52			3.00	0.22		
Ccp 107	CAM-21-CC-060	Disseminated	32.58	0.26	32.93	0.38	34.18	0.54				
Ccp 108	CAM-21-CC-060	Veinlet	32.03	0.26	31.72	0.38	36.61	0.56				
Pn 109	CAM-21-CC-060	Veinlet	32.96	0.26	39.17	0.42			27.44	0.44		
Pn 110	CAM-21-CC-060	Veinlet	33.12	0.26	39.48	0.42			27.62	0.44		
Cbn 111	CAM-21-CC-060	Veinlet	34.22	0.28	41.59	0.42	23.95	0.48				
Ccp 112	CAM-21-CC-060	Veinlet	32.04	0.26	29.95	0.36	37.18	0.56	0.93	0.16		
Ccp 113	CAM-21-CC-060	Disseminated	34.29	0.28	34.35	0.40	31.61	0.52				
Mkw 114	CAM-21-CC-060	Disseminated	36.30	0.28	61.02	0.52			2.56	0.22		
Po 115	CAM-21-CC-060	Disseminated	35.75	0.28	64.61	0.54						
Cu 116	CAM-21-CC-087	Disseminated					99.65	0.82				
Po 117	CAM-21-CC-087	Disseminated	35.39	0.28	64.27	0.54						
Cbn 118	CAM-21-CC-087	Disseminated	32.33	0.26	37.30	0.40	30.00	0.52				
Po 119	CAM-21-CC-087	Disseminated	35.50	0.26	64.64	0.54						
Mkw 120a	CAM-21-CC-087	Disseminated	35.45	0.28	60.60	0.52	1.07	0.22	2.85	0.22		
Mix 120b	CAM-21-CC-087	Disseminated	34.80	0.28	56.34	0.50	5.70	0.30	2.87	0.22		
Po 121	CAM-21-CC-087	Disseminated	35.56	0.26	64.35	0.52						
Po 122	CAM-21-CC-087	Disseminated	35.86	0.28	64.49	0.54						
Cu 123	CAM-21-CC-087	Disseminated			0.78	0.12	98.64	0.82				
Ccp 124	CAM-21-CC-087	Disseminated	31.75	0.26	32.42	0.38	36.35	0.56				
Po 125	CAM-21-CC-087	Disseminated	35.42	0.26	64.12	0.52						

Analysis ID	Sample ID	Unit Mineralization	SEM wt.% S	SEM wt.% S_2σ	SEM wt.% Fe	SEM wt.% Fe_2σ	SEM wt.% Cu	SEM wt.% Cu_2σ	SEM wt.% Ni	SEM wt.% Ni_2σ	SEM wt.% Co	SEM wt.% Co_2σ
Po 126	CAM-21-CC-087	Disseminated	35.59	0.28	64.40	0.54						
Mix 127a	CAM-21-CC-087	Disseminated	34.84	0.28	57.08	0.50	5.04	0.28	2.68	0.20		
Mkw 127b	CAM-21-CC-087	Disseminated	35.94	0.28	61.46	0.52			3.09	0.22		
Po 128	CAM-21-CC-072	Disseminated	35.61	0.26	64.87	0.52						
Ccp 130	CAM-21-CC-072	Disseminated	31.61	0.26	32.13	0.38	36.29	0.56				
Ccp 131	CAM-21-CC-072	Disseminated	31.25	0.26	35.31	0.40	33.34	0.54				
Ccp 132	CAM-21-CC-072	Veinlet	32.15	0.26	29.72	0.36	37.84	0.56				
Ccp 133	CAM-21-CC-072	Veinlet	32.27	0.26	30.08	0.36	37.65	0.56				
Cbn 134	CAM-21-CC-072	Veinlet	34.25	0.26	41.42	0.42	24.33	0.48				
Ccp 135	CAM-21-CC-072	Veinlet	32.17	0.26	29.47	0.36	38.44	0.56				
Cct 136	CAM-21-CC-072	Veinlet	19.25	0.22			80.74	0.76				
Cbn 137	CAM-21-CC-072	Veinlet	34.45	0.26	41.56	0.42	24.03	0.48				
Ccp 138	CAM-21-CC-072	Veinlet	32.92	0.26	30.16	0.36	37.13	0.56				
Ccp 140	CAM-21-CC-061	Disseminated	31.53	0.26	31.74	0.38	36.41	0.56				
Sg 141a	CAM-21-CC-061	Disseminated	31.93	0.26	43.77	0.44	9.42	0.36	14.93	0.34	0.24	0.06
Ccp 141b	CAM-21-CC-061	Disseminated	31.81	0.26	32.17	0.38	35.92	0.56				
Ccp 142	CAM-21-CC-061	Disseminated	32.47	0.26	33.04	0.38	34.22	0.54				
Sg 143	CAM-21-CC-061	Disseminated	32.52	0.26	43.65	0.44	8.73	0.34	15.15	0.34	0.37	0.05
Po 144	CAM-21-CC-061	Disseminated	35.54	0.26	64.80	0.52						
Ccp 145	CAM-21-CC-061	Disseminated	31.78	0.26	32.52	0.38	36.17	0.56				
Ccp 146	CAM-21-CC-061	Disseminated	31.48	0.26	32.03	0.38	36.03	0.54				
Po 147	CAM-21-CC-089	Disseminated	35.48	0.26	64.31	0.52						
Mix 148	CAM-21-CC-089	Disseminated	33.40	0.26	33.50	0.38	33.63	0.54				
Po 149	CAM-21-CC-089	Disseminated	35.41	0.26	64.03	0.52						
Po 150	CAM-21-CC-089	Veinlet	35.88	0.26	64.11	0.52						
Po 151	CAM-21-CC-089	Veinlet	35.96	0.28	64.60	0.52						
Ccp 152	CAM-21-CC-089	Veinlet	32.63	0.26	33.25	0.38	34.47	0.54				
Pn 153	CAM-21-CC-089	Veinlet	32.47	0.26	41.20	0.44			23.58	0.42	2.21	0.24
Cbn 154	CAM-21-CC-089	Veinlet	34.26	0.28	41.28	0.42	24.45	0.48				
Cbn 155	CAM-21-CC-089	Veinlet	34.38	0.28	41.57	0.42	24.46	0.48				
Po 156	CAM-21-CC-089	Veinlet	35.47	0.26	64.31	0.52						
Cbn 157	CAM-21-CC-089	Veinlet	34.50	0.28	41.44	0.42	24.05	0.48				
Cbn 158	CAM-21-CC-089	Disseminated	34.12	0.26	41.40	0.42	24.03	0.48				

Analysis ID	Sample ID	Unit Mineralization	SEM wt.% S	SEM wt.% S_2σ	SEM wt.% Fe	SEM wt.% Fe_2σ	SEM wt.% Cu	SEM wt.% Cu_2σ	SEM wt.% Ni	SEM wt.% Ni_2σ	SEM wt.% Co	SEM wt.% Co_2σ
Po 159	CAM-21-CC-089	Disseminated	35.66	0.26	64.36	0.52						
Ccp 160	CAM-21-CC-089	Disseminated	31.43	0.26	32.09	0.38	36.60	0.56				
Po 161	CAM-21-CC-071	Disseminated	35.61	0.26	64.30	0.52	0.49	0.20				
Ccp 162	CAM-21-CC-071	Disseminated	32.02	0.26	32.49	0.38	35.85	0.54				
Po 163	CAM-21-CC-071	Disseminated	35.25	0.26	63.71	0.52	0.75	0.20				
Ccp 164	CAM-21-CC-071	Disseminated	31.28	0.26	31.59	0.38	36.63	0.56				
Ccp 165	CAM-21-CC-071	Disseminated	32.36	0.26	32.79	0.38	34.78	0.54				
Po 166	CAM-21-CC-071	Disseminated	35.52	0.26	64.71	0.52						
Ccp 167	CAM-21-CC-117	Disseminated	33.93	0.28	30.78	0.36	35.50	0.54				
Po 168	CAM-21-CC-117	Disseminated	35.45	0.26	64.42	0.52						
Ccp 169	CAM-21-CC-117	Disseminated	33.47	0.28	30.88	0.36	35.60	0.54				
Pn 170	CAM-21-CC-117	Veinlet	32.53	0.26	34.94	0.40			30.22	0.46	1.91	0.24
Pn 171	CAM-21-CC-117	Veinlet	32.45	0.26	35.12	0.40			30.59	0.46	1.90	0.24
Po 172	CAM-21-CC-117	Veinlet	35.55	0.26	64.38	0.52						
Ccp 173	CAM-21-CC-117	Veinlet	34.01	0.28	30.80	0.38	35.42	0.54				
Po 174	CAM-21-CC-117	Veinlet	35.46	0.26	64.35	0.52						
Cbn 175	CAM-21-CC-117	Veinlet	34.45	0.28	41.39	0.42	23.78	0.48				
Pn 176	CAM-21-CC-117	Veinlet	32.19	0.26	34.63	0.40			30.92	0.46	1.93	0.22
Pn 177	CAM-21-CC-117	Veinlet	32.36	0.26	33.85	0.40			31.08	0.46	2.21	0.24
Pn 178	CAM-21-CC-117	Veinlet	32.28	0.26	35.44	0.40			29.99	0.46	2.21	0.24
Po 179	CAM-21-CC-117	Veinlet	35.77	0.26	64.30	0.52						
Py 180	CAM-21-CC-117	Veinlet	52.41	0.32	47.63	0.46						
Po 181	CAM-21-CC-117	Veinlet	35.56	0.26	64.48	0.52						
Ccp 184	CAM-21-CC-117	Disseminated	33.77	0.28	31.07	0.38	35.28	0.54				
Po 185	CAM-21-CC-117	Disseminated	35.21	0.26	64.52	0.52						
Ccp 186	CAM-21-CC-120	Net-textured	33.77	0.26	30.55	0.36	35.94	0.54				
Po 187	CAM-21-CC-120	Net-textured	35.94	0.26	64.59	0.52						
Ccp 188	CAM-21-CC-120	Net-textured	33.67	0.26	30.78	0.36	35.83	0.54				
Ccp 189	CAM-21-CC-120	Net-textured	33.25	0.26	30.98	0.36	35.34	0.54				
Po 190	CAM-21-CC-120	Net-textured	35.71	0.26	64.31	0.52						
Tro 191a	CAM-21-CC-120	Net-textured	35.52	0.26	64.39	0.52						
Po 191b	CAM-21-CC-120	Net-textured	37.67	0.28	61.98	0.52						
Ccp 192	CAM-21-CC-120	Net-textured	33.63	0.28	30.86	0.36	35.87	0.54				

Analysis ID	Sample ID	Unit Mineralization	SEM wt.% S	SEM wt.% S_2σ	SEM wt.% Fe	SEM wt.% Fe_2σ	SEM wt.% Cu	SEM wt.% Cu_2σ	SEM wt.% Ni	SEM wt.% Ni_2σ	SEM wt.% Co	SEM wt.% Co_2σ
Ccp 193b	CAM-21-CC-120	Net-textured	33.58	0.26	30.78	0.36	35.98	0.54				
Tro 194a	CAM-21-CC-120	Net-textured	35.73	0.26	63.79	0.52						
Po 194b	CAM-21-CC-120	Net-textured	37.76	0.28	62.43	0.52						
Ccp 195	CAM-21-CC-120	Net-textured	33.84	0.26	30.80	0.36	35.28	0.54				
Tro 196a	CAM-21-CC-120	Net-textured	35.63	0.26	64.23	0.52						
Po 196b	CAM-21-CC-120	Net-textured	37.51	0.28	62.18	0.52						
Cbn 197	CAM-21-CC-007	Disseminated	32.21	0.26	36.17	0.40	31.59	0.54				
Mkw 198	CAM-21-CC-007	Disseminated	35.58	0.28	61.26	0.52	0.86	0.20	2.20	0.20		
Mkw 199	CAM-21-CC-007	Disseminated	35.64	0.28	61.44	0.52	0.82	0.20	2.29	0.20		
Cbn 200	CAM-21-CC-007	Disseminated	31.98	0.26	35.94	0.40	31.81	0.54				
Po 201a	CAM-21-CC-007	Disseminated	35.59	0.28	64.54	0.54						
Pn 201b	CAM-21-CC-007	Disseminated	32.80	0.26	41.83	0.44			23.08	0.42	2.64	0.24
Cbn 202	CAM-21-CC-007	Disseminated	31.55	0.26	36.10	0.40	32.51	0.54				
Pn 203	CAM-21-CC-007	Disseminated	32.61	0.26	41.48	0.44			23.51	0.42	2.79	0.24
Po 204	CAM-21-CC-007	Disseminated	35.59	0.28	64.28	0.54						
Mkw 205	CAM-21-CC-007	Disseminated	36.03	0.28	61.09	0.52	0.31	0.20	2.09	0.20		
Cbn 206	CAM-21-CC-007	Disseminated	31.29	0.26	35.69	0.40	32.49	0.54				
Po 207	CAM-21-CC-007	Disseminated	35.57	0.28	64.13	0.54						
Po 208a	CAM-21-CC-007	Disseminated	35.57	0.28	64.55	0.54						
Pn 208b	CAM-21-CC-007	Disseminated	32.51	0.26	42.05	0.44			22.35	0.42	2.65	0.24
Pn 209	CAM-21-CC-007	Disseminated	32.45	0.26	40.37	0.42			23.38	0.42	3.91	0.26
Po 210	CAM-21-CC-007	Disseminated	35.66	0.28	64.60	0.54						
Po 211	CAM-21-CC-007	Disseminated	35.47	0.28	64.79	0.54						
Pn 212	CAM-21-CC-007	Disseminated	32.62	0.26	42.21	0.44			23.76	0.42	1.96	0.24
Po 213a	CAM-21-CC-007	Disseminated	35.38	0.28	64.55	0.54						
Pn 213b	CAM-21-CC-007	Disseminated	32.27	0.26	41.38	0.44			23.18	0.42	2.89	0.26
Po 214	CAM-21-CC-122	Disseminated	35.56	0.28	64.65	0.54						
Po 216	CAM-21-CC-122	Disseminated	35.77	0.28	64.36	0.54						
Cbn 217	CAM-21-CC-122	Disseminated	34.11	0.28	41.65	0.42	24.00	0.48				
Po 218	CAM-21-CC-122	Disseminated	35.24	0.26	64.44	0.54						
Ccp 219	CAM-21-CC-122	Disseminated	31.86	0.26	35.83	0.40	32.81	0.54				
Po 220	CAM-21-CC-122	Disseminated	35.80	0.28	64.27	0.54						
Cbn 221	CAM-21-CC-122	Disseminated	34.43	0.28	41.36	0.42	24.61	0.48				

Analysis ID	Sample ID	Unit Mineralization	SEM wt.% S	SEM wt.% S_2σ	SEM wt.% Fe	SEM wt.% Fe_2σ	SEM wt.% Cu	SEM wt.% Cu_2σ	SEM wt.% Ni	SEM wt.% Ni_2σ	SEM wt.% Co	SEM wt.% Co_2σ
Po 223	CAM-21-CC-122	Disseminated	35.65	0.28	64.30	0.54						
Ccp 224	CAM-21-CC-124	Disseminated	33.67	0.28	33.51	0.38	33.15	0.54				
Po 225	CAM-21-CC-124	Disseminated	35.29	0.26	64.33	0.52						
Po 226a	CAM-21-CC-124	Disseminated	35.41	0.28	64.58	0.54						
Pn 226b	CAM-21-CC-124	Disseminated	33.16	0.26	40.09	0.42			26.77	0.44		
Pn 227	CAM-21-CC-124	Disseminated	33.22	0.26	39.46	0.42			27.20	0.44		
Po 228	CAM-21-CC-124	Disseminated	35.56	0.28	64.84	0.54						
Po 229	CAM-21-CC-124	Disseminated	35.39	0.26	64.37	0.54						
Ccp 231	CAM-21-CC-124	Disseminated	32.16	0.26	31.92	0.38	35.89	0.56				
Ccp 232	CAM-21-CC-124	Disseminated	33.00	0.28	31.38	0.38	35.32	0.56				
Po 233	CAM-21-CC-124	Disseminated	35.69	0.28	64.48	0.54						
Po 234	CAM-21-CC-124	Disseminated	35.51	0.28	64.05	0.52						
Ccp 236	CAM-21-CC-124	Disseminated	32.98	0.26	32.79	0.38	33.73	0.54				
Po 237	CAM-21-CC-046	Disseminated	36.37	0.28	63.39	0.52						
Ccp 238	CAM-21-CC-046	Disseminated	33.75	0.28	30.58	0.38	35.53	0.56				
Ccp 239	CAM-21-CC-046	Disseminated	33.81	0.28	31.05	0.38	35.43	0.56				
Po 240	CAM-21-CC-046	Disseminated	35.67	0.28	64.87	0.54						
Py 241	CAM-21-CC-046	Disseminated	52.80	0.32	47.71	0.48						
Py 242	CAM-21-CC-046	Veinlet	52.46	0.32	47.48	0.48						
Py 243	CAM-21-CC-046	Veinlet	52.83	0.32	47.13	0.48						
Po 244	CAM-21-CC-046	Veinlet	35.70	0.28	64.51	0.54						
Py 245	CAM-21-CC-046	Veinlet	52.30	0.32	47.30	0.48						
Ccp 246	CAM-21-CC-046	Disseminated	33.95	0.28	30.94	0.38	35.42	0.56				
Po 247	CAM-21-CC-046	Disseminated	35.55	0.28	64.56	0.54						
Po 248	CAM-21-CC-088	Disseminated	35.76	0.28	64.58	0.54						
'Pn' 249	CAM-21-CC-088	Disseminated	33.17	0.26	44.33	0.44	6.42	0.32	16.16	0.36		
Pn 250	CAM-21-CC-088	Disseminated	32.83	0.26	40.35	0.44			24.39	0.42	2.93	0.26
Po 251	CAM-21-CC-088	Veinlet	35.84	0.28	64.65	0.54						
Cbn 252	CAM-21-CC-088	Veinlet	34.30	0.28	41.57	0.42	24.26	0.48				
Pn 253	CAM-21-CC-088	Veinlet	32.64	0.26	41.82	0.44			23.88	0.42	1.46	0.24
Po 254	CAM-21-CC-088	Veinlet	35.71	0.28	64.51	0.54						
Pn 255	CAM-21-CC-088	Veinlet	32.56	0.26	41.50	0.44			24.40	0.42	1.85	0.24
Po 256a	CAM-21-CC-088	Veinlet	35.62	0.28	64.59	0.54						

Analysis ID	Sample ID	Unit Mineralization	SEM wt.% S	SEM wt.% S_2σ	SEM wt.% Fe	SEM wt.% Fe_2σ	SEM wt.% Cu	SEM wt.% Cu_2σ	SEM wt.% Ni	SEM wt.% Ni_2σ	SEM wt.% Co	SEM wt.% Co_2σ
Ccp 256b	CAM-21-CC-088	Veinlet	33.33	0.28	33.11	0.38	33.85	0.54				
Mkw 257	CAM-21-CC-088	Disseminated	35.77	0.28	61.30	0.52	0.12	0.18	2.04	0.20		
Po 258	CAM-21-CC-088	Disseminated	35.69	0.28	64.48	0.54						
Ccp 259	CAM-21-CC-088	Disseminated	31.48	0.26	32.23	0.38	36.57	0.56				
Po 260	CAM-21-CC-030	Veinlet	35.58	0.28	64.21	0.54						
Pn 261	CAM-21-CC-030	Veinlet	32.46	0.26	40.27	0.42			24.85	0.42	2.49	0.24
Po 262	CAM-21-CC-030	Veinlet	35.59	0.28	64.14	0.54						
Po 263	CAM-21-CC-030	Veinlet	35.58	0.28	64.01	0.54						
Cbn 264	CAM-21-CC-030	Veinlet	34.07	0.28	39.30	0.42	27.11	0.50				
Pn 265	CAM-21-CC-030	Veinlet	32.61	0.26	40.44	0.44			24.80	0.42	2.66	0.24
Po 266	CAM-21-CC-030	Veinlet	35.79	0.28	64.16	0.54						
Po 267	CAM-21-CC-030	Veinlet	35.77	0.28	64.51	0.54						
Po 268	CAM-21-CC-030	Veinlet	35.60	0.28	64.46	0.54						
Po 270	CAM-21-CC-033	Net-textured	35.35	0.26	64.40	0.52	0.69	0.20				
Po 271	CAM-21-CC-033	Net-textured	35.52	0.26	64.38	0.52						
Ccp 272	CAM-21-CC-033	Net-textured	32.40	0.26	30.07	0.36	37.35	0.56				
Cbn 273	CAM-21-CC-033	Net-textured	34.28	0.28	41.11	0.42	24.38	0.48				
Po 274	CAM-21-CC-033	Net-textured	35.45	0.26	64.24	0.52						
Ccp 275	CAM-21-CC-033	Net-textured	31.83	0.26	30.13	0.36	37.62	0.56				
Po 276	CAM-21-CC-033	Net-textured	35.59	0.26	64.65	0.52						
Ccp 277	CAM-21-CC-033	Net-textured	32.38	0.26	30.22	0.36	37.60	0.56				
Ccp 278	CAM-21-CC-033	Net-textured	32.34	0.26	30.15	0.36	37.64	0.56				
Po 279	CAM-21-CC-033	Net-textured	35.85	0.26	64.33	0.52						
Po 280	CAM-21-CC-033	Net-textured	35.49	0.26	64.91	0.52						
Ccp 281	CAM-21-CC-033	Net-textured	32.37	0.26	30.08	0.36	37.20	0.56				
Po 282	CAM-21-CC-042	Disseminated	35.62	0.28	64.88	0.54						
Mlr 283	CAM-21-CC-042	Disseminated	35.88	0.28	61.32	0.52	1.55	0.22	1.78	0.18		
Cu 284	CAM-21-CC-042	Disseminated					99.52	0.82				
Po 285	CAM-21-CC-042	Disseminated	35.85	0.28	64.59	0.54						
Po 286	CAM-21-CC-042	Disseminated	35.81	0.28	64.06	0.54	0.31	0.18				
Po 287	CAM-21-CC-042	Disseminated	35.76	0.28	64.55	0.54						
Po 288	CAM-21-CC-042	Disseminated	35.75	0.28	64.38	0.54						
Pn 289	CAM-21-CC-042	Disseminated	32.78	0.26	42.87	0.44			22.22	0.40	2.18	0.24

Analysis ID	Sample ID	Unit Mineralization	SEM wt.% S	SEM wt.% S_2σ	SEM wt.% Fe	SEM wt.% Fe_2σ	SEM wt.% Cu	SEM wt.% Cu_2σ	SEM wt.% Ni	SEM wt.% Ni_2σ	SEM wt.% Co	SEM wt.% Co_2σ
Cu 291	CAM-21-CC-042	Disseminated					99.91	0.82				
Cu 292	CAM-21-CC-042	Disseminated					99.86	0.84				
Po 293	CAM-21-CC-019	Disseminated	35.69	0.26	64.61	0.52						
Po 294	CAM-21-CC-019	Disseminated	35.58	0.26	64.08	0.52						
Py 295	CAM-21-CC-019	Disseminated	52.63	0.32	47.74	0.46						
Py 296	CAM-21-CC-019	Disseminated	52.63	0.32	47.60	0.46						
Py 297	CAM-21-CC-019	Disseminated	52.41	0.32	47.30	0.46						
Py 298	CAM-21-CC-019	Disseminated	52.80	0.32	47.51	0.46						
Cob 299	CAM-21-CC-088	Veinlet	12.48	0.2	21.95	0.32			33.08	0.46	1.43	0.22
Mkw 24	CAM-21-CC-057	Disseminated	35.17	0.14	59.32	0.26			3.03	0.11		
Mkw 25	CAM-21-CC-057	Disseminated	35.41	0.14	58.92	0.26			2.95	0.10		
Mkw 27	CAM-21-CC-057	Disseminated	34.41	0.13	58.03	0.25			3.20	0.11		
Mkw 28	CAM-21-CC-057	Disseminated	34.44	0.13	58.27	0.25			3.22	0.11		
Mkw 29	CAM-21-CC-057	Disseminated	35.04	0.14	58.60	0.26			3.75	0.11		
Mkw 34	CAM-21-CC-005	Disseminated	35.46	0.14	60.66	0.26	1.76	0.11	2.41	0.10		
Mkw 35	CAM-21-CC-005	Disseminated	35.25	0.14	60.52	0.26	1.36	0.11	2.45	0.10		
Mkw 36	CAM-21-CC-005	Disseminated	35.46	0.14	60.79	0.26	1.91	0.12	2.28	0.10		
Mkw 37	CAM-21-CC-005	Disseminated	35.56	0.14	60.52	0.26	1.67	0.11	2.22	0.10		
Mkw 38	CAM-21-CC-005	Disseminated	35.12	0.14	60.87	0.26	1.10	0.11	2.51	0.10		
Mkw 39	CAM-21-CC-005	Disseminated	35.25	0.14	60.81	0.26	1.34	0.11	2.47	0.10		
Mkw 40	CAM-21-CC-005	Disseminated	35.35	0.14	61.22	0.26	1.20	0.11	2.70	0.10		
Mkw 44	CAM-21-CC-005	Disseminated	35.06	0.14	60.73	0.26	1.57	0.11	2.16	0.10		
Mkw 45	CAM-21-CC-005	Disseminated	35.41	0.14	60.82	0.26	1.79	0.11	2.22	0.10		
Mkw 52	CAM-21-CC-005	Disseminated	34.83	0.13	59.64	0.26	1.58	0.11	1.95	0.10		
Mkw 53	CAM-21-CC-005	Disseminated	35.04	0.14	59.72	0.26	2.47	0.12	2.20	0.10		
Mkw 54	CAM-21-CC-005	Disseminated	35.02	0.14	59.27	0.26	3.12	0.13	2.43	0.10		
Mkw 59	CAM-21-CC-005	Disseminated	34.49	0.14	58.85	0.26	2.56	0.12	2.65	0.10		
Mkw 61	CAM-21-CC-005	Disseminated	34.58	0.13	59.79	0.26	1.73	0.11	2.11	0.10		
Mkw 62	CAM-21-CC-005	Disseminated	35.41	0.14	60.62	0.26	1.38	0.11	2.46	0.10		
Mkw 63	CAM-21-CC-005	Disseminated	34.70	0.13	60.37	0.26	1.49	0.11	2.28	0.10		
Mkw 64	CAM-21-CC-005	Disseminated	35.34	0.14	60.47	0.26	1.38	0.11	2.31	0.10		
Mkw 65	CAM-21-CC-005	Disseminated	35.27	0.14	61.02	0.26	0.89	0.11	2.45	0.10		
Mkw 96	CAM-21-CC-005	Disseminated	34.99	0.14	60.80	0.26	1.34	0.11	2.46	0.10		

Analysis ID	Sample ID	Unit Mineralization	SEM wt.% S	SEM wt.% S_2σ	SEM wt.% Fe	SEM wt.% Fe_2σ	SEM wt.% Cu	SEM wt.% Cu_2σ	SEM wt.% Ni	SEM wt.% Ni_2σ	SEM wt.% Co	SEM wt.% Co_2σ
Mkw 101	CAM-21-CC-005	Disseminated	35.20	0.14	60.59	0.26	1.72	0.11	2.27	0.10		

*All LA–ICP–MS sulfide trace element data reported in ppm. Sample IDs are shortened.

Sample ID	CC-008	CC-008	CC-008	CC-008	CC-008	CC-008	CC-008
Mineralization	NT	NT	NT	NT	NT	NT	NT
Analysis ID	Py 1	Po 2	Ccp 3	Pn 3.1	Pn 4	Po 5	Ccp 6
^{34}S	410739.68	349209.67	377483.13	302008.47	452262.81	343114.13	376942.75
^{51}V	0.58	0.74	0.44		1.97	0.74	0.46
^{59}Co	6634.22	87.53	0.39	48773.36	66672.34	122.85	1.10
^{61}Ni	184.36	9044.02	31.12	588939.33	802209.33	12047.12	
^{63}Cu	0.15	0.78	311581.26	529.76	147.79	1.12	319130.07
^{66}Zn	0.88	1.35	1453.04	525.16	32.65		1462.01
^{75}As	30.43						
^{77}Se	132.69	105.26	74.01	70.77	110.46	108.97	83.94
^{101}Ru		0.16		1.76	1.91		
^{103}Rh	0.18	0.38	2.03		0.20	0.42	0.98
^{108}Pd	0.89	3.03		105.40	108.77	2.03	2.75
^{109}Ag		0.68	0.65	2.16	4.10	0.35	0.35
^{111}Cd			29.02	6.58			35.15
^{118}Sn			1.05				2.56
^{123}Sb	0.05						0.25
^{125}Te	3.09	7.46	1.98	3.14	4.35	9.95	4.94
^{189}Os	0.24						
^{193}Ir	0.27	0.15				0.29	
^{194}Pt	0.69	0.20				0.37	0.01
^{197}Au	0.03						
^{208}Pb	0.46	2.87	5.72	2.04	25.05	5.93	3.19
^{209}Bi	0.54	2.19	0.52		5.21	2.41	3.65
S/Se	3950.43	3580.52	4549.21	4572.25	2929.56	3467.16	3989.75

Sample ID	CC-008	CC-008	CC-008	CC-008	CC-008	CC-009	CC-009
Mineralization	NT	NT	NT	NT	NT	NT	NT
Analysis ID	Ccp 7	Po 8	Pn 9	Ccp 10	Po 11	Ccp 12	Po 13
^{34}S	405398.88	389285.64	300778.03	378354.47	374235.78	368102.09	354407.69
^{51}V	0.60	0.70	0.76	0.54	0.64	0.50	0.43
^{59}Co	0.33	81.57	50733.49	0.55	99.59		24.45
^{61}Ni	34.61	8936.17	580946.10	19.23	11000.05		4189.14
^{63}Cu	318982.48	0.61	15.18	305976.72	1.79	305786.24	2.17
^{66}Zn	443.99		872.90	1338.06		998.98	
^{75}As							
^{77}Se	81.93	103.07	70.79	73.68	117.66	63.93	97.42
^{101}Ru	0.08		1.54			0.32	
^{103}Rh	1.54	0.82		2.12	0.42	2.09	0.63
^{108}Pd	1.10	1.37	122.92	0.95	1.95		0.61
^{109}Ag	0.24	1.13	0.71	0.32	0.56	0.90	2.28
^{111}Cd	17.97		7.76	26.05		49.06	

^{118}Sn				2.39			
^{123}Sb							0.26
^{125}Te	3.11	9.11	0.84	4.80	7.02		10.75
^{189}Os							1.66
^{193}Ir		0.20			0.21		1.63
^{194}Pt							1.84
^{197}Au						0.10	
^{208}Pb	3.69	2.52	3.30	1.61	3.94	1.38	2.04
^{209}Bi	1.78	1.13	0.19	1.84	2.71	0.13	1.84
S/Se	4124.29	3657.78	4599.27	4591.30	3241.56	5254.32	3865.78

Sample ID	CC-009	CC-009	CC-009	CC-009	CC-009	CC-009	CC-009
Mineralization	NT	NT	NT	NT	NT	NT	NT
Analysis ID	Ccp 14	Po 15	Ccp 16	Po 17	Ccp 18	Po 18.1	Ccp 19
^{34}S	392126.72	362305.90	404952.08	369772.70	423317.08	374324.90	402564.42
^{51}V	0.43	0.50	0.58	0.46	0.72	0.58	0.72
^{59}Co		45.01		48.19	1.60	44.37	
^{61}Ni		6049.98		4947.97	83.25	5575.92	
^{63}Cu	315332.11	4.31	313788.10	5.36	296977.35	10.17	302018.97
^{66}Zn	1792.40		944.63	1.75	517.08		320.32
^{75}As							
^{77}Se	98.45	114.20	90.85	96.21	100.42	107.16	97.77
^{101}Ru					0.34	0.40	0.26
^{103}Rh	1.59	0.64	0.87	0.73	0.81	0.42	0.80
^{108}Pd	0.48	0.31		1.17			1.00
^{109}Ag	2.22	0.61	1.85	0.96	8.19	0.77	2.32
^{111}Cd	59.00		47.38		34.73		29.15
^{118}Sn	7.35		0.78		0.95		2.62
^{123}Sb		0.32		0.30			
^{125}Te	7.05	10.28	2.11	7.84	5.00	5.43	13.49
^{189}Os		0.95		2.35		3.34	
^{193}Ir	0.13	3.09		2.96		2.68	0.22
^{194}Pt	1.54	1.55		1.28	2.25	1.07	5.09
^{197}Au	0.12				0.55		
^{208}Pb	2.72	1.62	2.91	2.00	12.61	1.48	7.28
^{209}Bi	2.18	1.73	0.20	1.95	1.82	0.97	4.44
S/Se	3438.22	3317.03	3697.47	3944.70	3346.82	3531.06	3456.02

Sample ID	CC-009	CC-011	CC-011	CC-011	CC-011	CC-011	CC-011
Mineralization	NT	NT	NT	NT	NT	NT	NT
Analysis ID	Po 20	Ccp 21	Po 22	Ccp 23	Po 24	Ccp 25	Po 26
^{34}S	366480.85	387346.96	326644.71	383801.74	364231.86	372477.24	373104.77
^{51}V	0.42	0.41	0.54	0.41	0.80	0.73	
^{59}Co	56.92		35.46		57.63		40.64

^{61}Ni	5739.41		1107.47		3131.47		3759.21
^{63}Cu	6.64	306872.72	8.55	297881.68	3.10	286587.66	4.42
^{66}Zn		236.09		583.96	1.75	241.08	
^{75}As							
^{77}Se	108.09	118.30	113.61	111.72	109.74	104.53	122.08
^{101}Ru							
^{103}Rh	0.55	0.63	1.96	1.17	1.42	1.62	0.30
^{108}Pd		0.07	3.59	0.82	1.17	1.45	3.09
^{109}Ag	0.45	14.35	11.65	27.67	1.66	20.46	13.00
^{111}Cd		23.18		42.45		20.83	
^{118}Sn		0.75		1.77		1.45	
^{123}Sb		0.26	0.81	0.71			0.94
^{125}Te	6.67	12.79	28.42	27.33	16.31	24.69	16.92
^{189}Os	3.86		1.86		5.12		3.30
^{193}Ir	2.59		3.72	0.11	4.56		4.34
^{194}Pt	2.38	1.17	0.34	1.68	0.89		
^{197}Au		0.16		0.13			
^{208}Pb	2.22	5.50	3.78	5.15	2.67	3.51	3.30
^{209}Bi	2.23	0.57	5.24	1.19	1.20	0.91	5.33
S/Se	3501.75	2893.49	3161.64	3045.05	3300.49	3274.79	3126.66

Sample ID	CC-011	CC-011	CC-011	CC-011	CC-035	CC-035	CC-035
Mineralization	NT	NT	NT	NT	GV	GV	GV
Analysis ID	Ccp 27	Po 28	Ccp 29	Po 30	Ccp 31r	Po 32r	Cbn 33r
^{34}S	388042.50	361408.04	409544.51	407511.06	267112.11	267513.45	266334.80
^{51}V	0.48	0.56	0.44	0.57	0.37	0.40	0.49
^{59}Co		40.01		52.71	0.49	4.06	0.28
^{61}Ni		2216.43		3710.01	54.64		24.41
^{63}Cu	313569.26	3.82	319539.37	4.00	330115.49	6.02	237988.54
^{66}Zn	278.06		469.07		4497.18	1.03	7.89
^{75}As						0.52	0.40
^{77}Se	103.62	118.86	110.19	118.65	115.36	131.49	150.16
^{101}Ru							
^{103}Rh	0.73	1.98	1.51	0.30	0.06	0.02	0.36
^{108}Pd		4.16	1.18		0.35	0.12	0.27
^{109}Ag	16.33	26.12	24.79	1.70	1.18	12.28	3.85
^{111}Cd	23.00		32.32		18.77		1.74
^{118}Sn					1.54	0.00	0.77
^{123}Sb	0.24	0.72	0.60			1.14	0.46
^{125}Te	17.62	38.51	25.27	9.16	1.72	4.14	3.74
^{189}Os		2.41		3.31			0.41
^{193}Ir		3.25		4.03	0.04		
^{194}Pt							
^{197}Au	0.26		0.23		0.09	0.01	0.45

^{208}Pb	6.65	4.70	7.40	1.03	5.27	10.48	24.98
^{209}Bi	0.17	5.08	1.23	0.53	0.02	0.36	0.05
S/Se	3260.14	3175.98	3105.45	3093.95	2972.45	2735.53	2344.88

Sample ID	CC-035	CC-035	CC-035	CC-035	CC-037	CC-037	CC-037
Mineralization	GV	GV	GV	GV	D	D	D
Analysis ID	Po 34r	Pn 35r	Ccp 36r	Po 37r	Py 38r_1	Py 38r_2	Py 39r_1
^{34}S	268142.58	244421.91	279286.94	253399.38	384011.35	388859.05	385502.16
^{51}V	0.56	0.08	0.61	0.36	0.31	0.32	0.34
^{59}Co	4.63	16579.33	0.07	7.98	34.57	4141.54	143.68
^{61}Ni	24.79	414906.07	65.92		149.56	3488.45	166.47
^{63}Cu	13.51	15.50	355128.21	6.34	3.08	3.46	1.55
^{66}Zn	1.17	0.69	2273.51	0.48	0.55	0.76	0.73
^{75}As		1.86		0.27	0.39	23.30	0.78
^{77}Se	154.67	129.20	125.92	126.20	14.94	41.18	10.89
^{101}Ru		0.63	0.12				0.03
^{103}Rh			0.08				
^{108}Pd		23.43	1.20				0.01
^{109}Ag	3.27	3.11	0.64	1.52	0.01		0.00
^{111}Cd		0.97	4.26				
^{118}Sn		0.38	0.38	0.46	0.03	0.01	0.12
^{123}Sb	0.21	0.23		0.19	0.01		
^{125}Te	2.06	1.98	1.81	1.81			0.03
^{189}Os	0.03			0.16			
^{193}Ir			0.08				
^{194}Pt							0.01
^{197}Au	0.04		0.31		0.00	0.01	
^{208}Pb	1.28	4.10	4.53	1.33		0.02	0.01
^{209}Bi			0.04	0.09			
S/Se	2338.55	2593.75	2743.79	2862.82	35411.79	12848.10	48473.87

Sample ID	CC-037	CC-037	CC-037	CC-044	CC-044	CC-044	CC-044
Mineralization	D	D	D	NT	NT	NT	NT
Analysis ID	Py 39r_2	Py 40r_1	Py 40r_2	Ccp 41r	Po 41.1r	Ccp 42r	Po 43r
^{34}S	383757.15	401800.02	401259.85	281772.36	292105.29	303075.41	269002.75
^{51}V	0.37	0.38	0.18	0.24	0.04	0.27	0.06
^{59}Co	413.47	30.82	4237.74	0.27	37.75	1.01	53.15
^{61}Ni	884.84	408.66	2467.57	47.41	5996.87		6325.97
^{63}Cu	0.88	5.34	1.32	329599.95	3.64	310962.65	1.10
^{66}Zn	0.56	0.66	0.67	218.54	2.02	357.70	0.63
^{75}As	1.49	0.90	8.32			2.81	
^{77}Se	12.80	6.45	26.64	101.53	129.75	129.39	131.95
^{101}Ru				0.31			
^{103}Rh					0.09	0.22	

^{108}Pd	0.03				0.15		0.32
^{109}Ag	0.02			0.57	0.59	0.21	0.42
^{111}Cd			0.09	22.01		24.38	
^{118}Sn	0.02	0.05	0.02			2.78	0.34
^{123}Sb			0.04	0.25	0.68	0.16	0.11
^{125}Te	0.07		0.08	4.56	11.44	9.26	5.39
^{189}Os			0.06		0.69		0.14
^{193}Ir				0.26	0.40		0.03
^{194}Pt	0.03			4.17	5.84	4.15	1.43
^{197}Au						0.12	
^{208}Pb	0.04		0.03	2.56	3.17	3.39	2.73
^{209}Bi			0.25	1.74	3.31	3.09	0.97
S/Se	41249.15	82248.95	19924.17	3388.02	2952.69	2681.82	2914.01

Sample ID	CC-044	CC-044	CC-044	CC-044	CC-044	CC-045	CC-045
Mineralization	NT	NT	NT	NT	NT	NT	NT
Analysis ID	Ccp 44r	Po 45r_1	Po 45r_2	Ccp 46r	Po 47r	Ccp 48r	Po 49r
^{34}S	270510.98	324970.91	303814.00	298350.40	277064.28	286713.24	296377.14
^{51}V	0.12			0.23	0.28	0.13	0.23
^{59}Co	0.39	53.81	38.50	0.41	74.88	0.38	59.02
^{61}Ni	3.59	8313.47	6158.60	5.08	8150.54	29.73	7519.98
^{63}Cu	313904.96	2.18	2.46	323807.80	2.00	314545.86	1.86
^{66}Zn	303.92	2.20		362.74	1.00	386.49	
^{75}As	0.39		7.38				0.20
^{77}Se	109.22	140.37	107.21	99.32	120.45	84.99	146.20
^{101}Ru							
^{103}Rh	0.50	0.34		0.20	0.36		0.17
^{108}Pd		0.31	0.49		1.00		
^{109}Ag		0.95	0.14	0.40	0.28	0.83	0.22
^{111}Cd	21.27			23.55	0.84	17.34	0.65
^{118}Sn	0.74		0.38	2.77	0.14	1.73	0.47
^{123}Sb	0.16	0.29	0.39	0.33	0.11	0.13	0.12
^{125}Te		7.94	5.90	5.86	8.18		
^{189}Os		1.53	0.50		0.16		
^{193}Ir			0.42		0.18		0.18
^{194}Pt		1.57	7.63	2.39	5.21	0.76	0.69
^{197}Au	0.07			0.02	0.02	0.16	0.04
^{208}Pb	1.24	4.66	4.44	2.24	4.13	4.78	2.57
^{209}Bi	0.05	2.84	5.96	3.29	3.27	0.76	1.25
S/Se	3149.56	2722.87	3564.82	3462.62	3185.68	4031.05	2603.99

Sample ID	CC-045	CC-045	CC-045	CC-045	CC-045	CC-045	CC-045
Mineralization	NT	NT	NT	NT	NT	NT	NT
Analysis ID	Ccp 50r	Ccp 51r	Po 52r	Py 53r_1	Py 53r_2	Ccp 54r	Po 55r
^{34}S	302381.32	302970.11	290363.34	412023.04	435565.17	272111.94	281274.09
^{51}V	0.20	0.35	0.11	0.26	0.26	0.05	0.18
^{59}Co	0.39	0.36	83.22	142.14	760.00	0.73	41.82
^{61}Ni		22.13	8571.55	4.14	52.21	7.98	7669.11
^{63}Cu	324812.85	327405.86	1.71	1.09	0.62	302651.51	1.47
^{66}Zn	603.31	632.67	0.99	0.70	0.86	463.57	1.36
^{75}As	0.69	1.27		3.62	36.44		
^{77}Se	88.98	102.52	141.05	320.86	289.88	83.50	129.99
^{101}Ru		0.23	0.21				
^{103}Rh	0.33	0.02	0.70			0.30	0.10
^{108}Pd					0.26		0.21
^{109}Ag	0.24	0.15	0.24			0.06	1.27
^{111}Cd	22.63	28.23				10.93	
^{118}Sn	5.01	0.55	0.01			0.41	1.24
^{123}Sb		0.04	0.45		0.12	0.10	0.67
^{125}Te	1.49	0.64	3.95	1.37	1.17		2.95
^{189}Os			0.22				
^{193}Ir			0.28				0.04
^{194}Pt	0.43	0.51	6.92		0.03	0.49	5.28
^{197}Au			0.04		0.02	0.11	
^{208}Pb	1.25	5.43	6.15	0.13	4.13	1.87	3.35
^{209}Bi	0.36	0.93	4.00	0.08	1.78	0.31	1.22
S/Se	3839.26	3377.93	2650.78	1647.45	1823.51	4087.66	2924.75

Sample ID	CC-045	CC-045	CC-045	CC-048	CC-048	CC-048	CC-048
Mineralization	NT	NT	NT	NT	NT	NT	NT
Analysis ID	Po 56r	Ccp 57r	Po 58r	Ccp 59	Po 60	Ccp 61	Po 62
^{34}S	312074.21	272345.68	289547.48	323520.83	296207.48	328375.13	294683.30
^{51}V	0.38	0.18	0.39	0.23	0.47	0.31	0.51
^{59}Co	62.20	0.55	51.52	0.34	53.51	0.16	58.80
^{61}Ni	9191.29	8.87	7244.59	15.00	4862.88	20.06	5118.67
^{63}Cu	1.21	293450.25	3.60	305753.69	2.04	309504.34	1.42
^{66}Zn	1.61	346.73	0.60	1155.83	0.36	719.20	0.80
^{75}As	1.54		1.66	1.37		0.21	
^{77}Se	129.91	92.83	137.15	110.77	129.56	160.47	196.73
^{101}Ru				0.43		0.38	0.50
^{103}Rh	0.30	0.05		0.84	0.48	0.79	1.30
^{108}Pd							4.21
^{109}Ag	0.24	0.94	0.24	0.39	0.11	0.61	0.41
^{111}Cd		18.35		57.89		44.36	

^{118}Sn	1.00	0.83		2.56		2.37	
^{123}Sb		0.02	0.32	0.18	0.17	0.09	0.31
^{125}Te	7.49	1.83	6.17	1.02		2.95	13.07
^{189}Os	0.97						4.28
^{193}Ir	0.59		0.47		0.45		5.25
^{194}Pt	3.49	0.16	5.67	0.06	0.30	0.16	1.41
^{197}Au	0.03	0.17	0.04	0.05	0.12		
^{208}Pb	3.08	1.94	6.08	2.26	1.13	3.01	3.27
^{209}Bi	1.94	0.26	5.59	0.63	0.46	0.64	5.01
S/Se	2949.04	3703.55	2788.86	3116.23	2942.29	2150.58	1943.25

Sample ID	CC-048	CC-048	CC-048	CC-048	CC-048	CC-048	CC-048
Mineralization	MS	MS	MS	MS	MS	MS	NT
Analysis ID	Ccp 63	Po 64	Pn 65	Po 66	Ccp 67	Po 68	Ccp 69
^{34}S	333701.36	309920.00	309984.73	346788.34	346043.29	319969.20	343029.98
^{51}V	0.46	0.40	0.35	0.25	0.94	1.29	0.35
^{59}Co	0.22	40.93	40200.83	53.46	0.18	68.03	0.38
^{61}Ni	15.22	6314.25	574495.26	8349.50	14.74	7598.72	9.86
^{63}Cu	302784.98	2.25	3.65	0.61	301355.98	2.56	308896.00
^{66}Zn	724.36	0.28	0.67	0.04	806.95		1209.59
^{75}As			0.37	0.80	1.39		
^{77}Se	143.95	175.67	155.38	130.31	135.90	166.00	83.44
^{101}Ru	0.01		1.71		0.78		0.03
^{103}Rh	0.87	0.00	0.06	0.53	0.81	0.76	0.41
^{108}Pd		0.09	199.82	0.21		0.11	
^{109}Ag	0.55	0.94	2.02	0.37	0.18	0.38	0.59
^{111}Cd	52.98	0.35			70.16		75.18
^{118}Sn	0.68		0.25	0.11	1.33		2.49
^{123}Sb			0.20	0.03	0.01	0.01	0.09
^{125}Te	4.19	1.44	0.95	0.83	1.55	3.06	2.27
^{189}Os				2.10	0.58	0.35	
^{193}Ir				0.88	0.92	0.68	0.01
^{194}Pt	1.07	0.06		1.77	0.83	0.82	0.43
^{197}Au			0.04		0.04		
^{208}Pb	4.11	24.42	1.12	2.14	6.98	2.28	2.91
^{209}Bi	0.60	0.92	0.02	0.61	0.35	0.24	0.32
S/Se	2393.19	2165.44	2121.95	2952.10	2526.83	2301.19	4122.60

Sample ID	CC-100	CC-100	CC-100	CC-100	CC-100	CC-100	CC-101
Mineralization	NT	NT	NT	NT	NT	NT	D
Analysis ID	Po 70	Po 71	Po 72	Cbn 73	Ccp 74	Po 75	Po 76
^{34}S	284789.87	303331.40	273831.21	304073.06	292508.26	276839.60	284399.00
^{51}V	0.37	0.53	0.36	0.31	0.33	0.32	0.20
^{59}Co	13.94	15.89	14.56	0.30	0.54	14.95	31.58

^{61}Ni	13.95	42.14	40.47		8269.85	28.05	3.31
^{63}Cu	6.49	8.92	14.74	209479.17	315114.63	9.75	8.78
^{66}Zn	0.84	2.95	0.64	79.48	84.48	1.32	1.88
^{75}As					1.89		0.68
^{77}Se	99.03	121.91	102.80	74.80	81.39	107.66	157.76
^{101}Ru				0.14	0.20		0.33
^{103}Rh	0.14	0.04	0.15	0.48	0.52	0.05	0.05
^{108}Pd				3.12	0.60		1.07
^{109}Ag	0.78	1.34	1.13	2.04	6.54	1.26	13.54
^{111}Cd				4.95	2.31	0.30	0.33
^{118}Sn	0.30	0.38	0.39	1.35	0.17	0.22	0.20
^{123}Sb	0.16		0.09		0.02	0.12	0.73
^{125}Te	8.04	9.12	7.33	2.41	1.24	6.21	16.51
^{189}Os	0.57	0.06	0.26		0.28	0.29	0.18
^{193}Ir	0.55	0.51	0.51			0.06	0.40
^{194}Pt	4.60	2.80	5.35	4.52	1.25	4.40	5.24
^{197}Au			0.08				0.06
^{208}Pb	4.46	2.87	3.69	5.31	9.99	3.22	3.81
^{209}Bi	2.49	1.49	2.46	3.08	0.44	0.74	5.49
S/Se	3628.10	2967.66	3505.70	4414.42	3939.13	3351.14	2269.28

Sample ID	CC-101	CC-101	CC-101	CC-101	CC-101	CC-116	CC-116
Mineralization	SV	SV	SV	SV	SV	NT	NT
Analysis ID	Po 77	Po 78	Cbn 79	Po 80	Po 81	Ccp 82	Pn 83
^{34}S	292999.91	267239.31	315554.66	313454.60	296429.01	365173.75	329794.86
^{51}V	0.33	0.15	0.08	0.45	0.30	0.49	
^{59}Co	11.59	11.34	0.21	6.18	7.21	0.24	33961.89
^{61}Ni	27.16		8968.91		1.99		436949.64
^{63}Cu	18.39	3.78	340627.30	24.18	15.41	325024.42	42747.46
^{66}Zn		0.51	57.18	1.01	0.39	1426.63	2947.50
^{75}As	0.33	1.32		1.45	4.95	0.94	
^{77}Se	102.47	120.69	149.88	129.19	120.70	104.83	101.97
^{101}Ru						0.31	0.70
^{103}Rh			0.32			0.43	0.01
^{108}Pd	0.25		2.65				125.30
^{109}Ag	0.60	0.61	0.77	0.12	0.37	0.40	28.77
^{111}Cd			4.38			53.11	55.14
^{118}Sn	0.07		2.17	0.12	0.32	0.44	0.67
^{123}Sb	0.27		0.14		0.12	0.06	
^{125}Te	4.39	0.85	6.10	0.18		5.73	5.52
^{189}Os							
^{193}Ir	0.20	0.29	0.06	0.11	0.15		0.09
^{194}Pt	2.88	0.81	1.59			1.54	0.68
^{197}Au							

^{208}Pb	2.87	2.48	11.21	6.88	6.47	2.93	37.87
^{209}Bi	1.76	0.94	1.70	0.28	0.51	1.59	1.93
S/Se	3521.14	2986.06	2306.58	2788.23	2982.55	3282.50	3214.76

Sample ID	CC-116	CC-116	CC-116	CC-116	CC-116	CC-116	CC-116
Mineralization	NT	NT	NT	NT	NT	NT	NT
Analysis ID	Ccp 84	Po 85	Ccp 86	Po 87	Ccp 88	Po 89	Po 90
^{34}S	367497.86	352105.42	516478.58	279452.26	378796.95	362355.89	370871.85
^{51}V	0.39	0.22	0.77	0.52	0.25	0.34	0.28
^{59}Co	0.13	42.48	0.35	27.04		23.03	32.14
^{61}Ni	23.22	4846.45	9.98	3453.35		4471.58	4939.51
^{63}Cu	322150.72	1.59	345170.42	1.37	332564.87	2.78	3.26
^{66}Zn	928.99	1.09	305.40	0.64	723.51	1.65	1.28
^{75}As			2.14	0.11			
^{77}Se	103.88	118.21	113.65	92.67	104.93	111.46	114.77
^{101}Ru	0.07	0.69	0.42			0.02	
^{103}Rh	0.99	1.30	0.50	0.10	0.97	0.58	0.71
^{108}Pd		0.10	0.18	0.17			0.25
^{109}Ag	0.76	0.42	0.90	0.24	0.82	1.03	0.25
^{111}Cd	48.10		29.88		37.14		
^{118}Sn	0.77	0.06	0.26	0.31	0.46	0.44	0.29
^{123}Sb	0.13	0.17	0.03	0.12		0.11	0.29
^{125}Te	7.86	10.19	5.23	2.47	3.76	6.52	10.87
^{189}Os		3.00				1.06	3.23
^{193}Ir		4.27		0.32		2.39	2.80
^{194}Pt	2.34	1.91	2.73	0.33	1.32	1.05	2.00
^{197}Au	0.07		0.22			0.00	
^{208}Pb	2.92	2.27	4.48	2.35	2.07	2.20	3.54
^{209}Bi	2.96	1.47	2.50	0.36	0.72	0.89	1.35
S/Se	3298.01	3234.19	3049.69	4148.22	3283.98	3444.20	3332.87

Sample ID	CC-116	CC-116	CC-005	CC-005	CC-005	CC-005	CC-005
Mineralization	NT	NT	D	D	D	D	D
Analysis ID	Ccp 91	Po 92	Po 93	Po 95	Mkw 96	Po 97	Po 98
^{34}S	362295.71	341117.87	330446.15	336163.51	339650.25	318455.71	331191.91
^{51}V	0.42	0.37	0.06	0.61	0.51	0.03	0.25
^{59}Co		40.57	20.71	26.85	23914.63	27.54	24.08
^{61}Ni		5677.02			48470.93		
^{63}Cu	337860.01	16.83	16.95	268.63	65096.38	13.04	13.64
^{66}Zn	1180.77	2.38	0.21		4.23	0.47	
^{75}As	0.79	0.91		0.03			
^{77}Se	95.71	137.35	141.57	119.15	128.97	120.05	134.39
^{101}Ru		0.43			0.20		0.04
^{103}Rh	1.05	0.44	0.41	1.07	2.51	0.34	1.21

^{108}Pd			3.05	3.05		0.86	0.78
^{109}Ag	0.86	0.33	15.38	12.48	31.36	8.45	12.71
^{111}Cd	50.22				4.62	0.69	
^{118}Sn	3.12	0.83			0.73	0.34	
^{123}Sb	0.15	0.06		0.22			0.22
^{125}Te	7.10	8.40	18.22	24.48	2.42	17.54	21.41
^{189}Os		2.15		0.67	0.20	1.44	1.12
^{193}Ir	0.07	5.26	0.35	1.98	3.31	2.63	2.93
^{194}Pt	2.23	0.97		0.90			
^{197}Au	0.00						
^{208}Pb	2.74	1.79	6.43	3.66	30.83	2.42	2.00
^{209}Bi	2.21	0.83	6.55	6.29	0.34	1.84	2.30
S/Se	3638.02	2790.72	2514.65	2952.52	2713.01	2960.46	2655.02

Sample ID	CC-005	CC-060	CC-060	CC-060	CC-060	CC-060	CC-060
Mineralization	D	WD	WD	WD	SV	SV	SV
Analysis ID	Po 102	Ccp 103	Mkw 106	Ccp 107	Ccp 108	Pn 109_1	Pn 109_2
^{34}S	560608.68	317623.29	333706.96	341769.87	308290.87	342477.68	327176.43
^{51}V		0.29	0.29		0.15		0.21
^{59}Co	28.72	1.71	29351.44	2.67	0.26	34559.44	34008.08
^{61}Ni		4919.78	52534.12	5677.14	6219.15	462021.45	431807.96
^{63}Cu	15.19	317319.08	1463.41	315374.35	325350.22	135.59	385.71
^{66}Zn		6.07	5.10	6.46	2.10	0.06	
^{75}As	5.27	0.42			0.44		11.75
^{77}Se	182.99	175.84	101.81	115.76	85.37	38.29	28.31
^{101}Ru			0.68				0.42
^{103}Rh	0.39	0.11		0.83	0.28		
^{108}Pd	5.91	0.77		0.11	1.29	0.24	
^{109}Ag	17.56	2.22	17.79	4.45	0.58	4.22	15.64
^{111}Cd			17.73	9.29	0.29		1.00
^{118}Sn		0.74			0.50		1.13
^{123}Sb							0.60
^{125}Te	14.47	1.46	0.00		2.91		0.68
^{189}Os							
^{193}Ir	1.96						0.16
^{194}Pt							
^{197}Au							
^{208}Pb	9.64	1.38	6.93	2.09	7.27	0.75	3.46
^{209}Bi	17.27	0.81	1.61		0.38		0.24
S/Se	1953.71	1846.61	3515.24	2814.34	3751.92	8608.17	11644.50

Sample ID	CC-060	CC-060	CC-060	CC-060	CC-060	CC-060	CC-087
Mineralization	SV	SV	SV	SV	WD	WD	SD
Analysis ID	Pn 110_1	Pn 110_2	Cbn 111	Ccp 112	Ccp 113	Po 115	Cu 116
^{34}S	352410.76	333625.64	335994.75	326336.87	381726.79	338888.31	33766.19
^{51}V	0.16	0.11	0.36	0.28	0.32	0.18	0.58
^{59}Co	33597.76	31375.17		0.28	1.48	9.55	1.64
^{61}Ni	439201.33	443585.18		12812.15	6049.80	15.47	60.25
^{63}Cu	86.26	50.92	221305.06	351539.58	295866.71	11.42	
^{66}Zn	2.69	0.66	0.49	7.72	129.56	0.60	9.44
^{75}As	2.93	1.41		2.33		0.23	8.18
^{77}Se	41.04	43.42	102.80	176.22	125.10	298.10	29.71
^{101}Ru	0.01						0.19
^{103}Rh			0.01	0.42	0.41	1.65	13.09
^{108}Pd	0.69	0.34		2.77	2.30	11.16	1.46
^{109}Ag	1.47	1.11	0.06	0.20	23.94	10.39	8.23
^{111}Cd	0.04	0.18		0.65	2.31	0.62	7.98
^{118}Sn	0.87		0.32	1.76	1.76	1.15	6.24
^{123}Sb	0.98					0.20	3.38
^{125}Te			1.82	2.82	1.96	22.25	7.37
^{189}Os	0.01			0.13			
^{193}Ir							1.02
^{194}Pt	0.56				0.07		3.28
^{197}Au						0.09	1.84
^{208}Pb	0.21	0.46	0.14	2.49	0.93	7.11	1.36
^{209}Bi				0.02	0.14	18.87	0.46
S/Se	8070.26	7627.76	3328.89	1818.22	2741.03	1199.25	

Sample ID	CC-087	CC-087	CC-087	CC-087	CC-087	CC-087	CC-072
Mineralization	SD	SD	SD	SD	SD	SD	WD
Analysis ID	Po 117	Po 119	Po 121	Po 122	Po 125	Po 126	Po 128_1
^{34}S	355283.11	351586.04	322077.88	341620.37	327794.49	341462.66	552907.97
^{51}V	0.12	0.44	0.34	0.20	0.21	0.28	0.34
^{59}Co	7.15	36.13	32.94	48.92	37.27	46.76	6.57
^{61}Ni	2.62	1.54		17.90			
^{63}Cu	49.34	10.14	7.92	4.36	4.63	5.55	351.04
^{66}Zn	51.46	0.72	1.09	1.00	0.79	1.13	
^{75}As			0.93	1.28		0.86	6.96
^{77}Se	171.36	140.44	126.16	142.48	127.37	150.52	316.78
^{101}Ru					0.27	0.18	
^{103}Rh			0.02	0.10	0.03	0.05	
^{108}Pd	0.55	0.62	1.18	2.21	1.08		
^{109}Ag	0.22	1.69	2.26	5.89	3.34	9.96	0.52

^{111}Cd	0.52	0.92			0.49	1.20	
^{118}Sn	0.10	0.38	0.26	0.56	0.66	0.01	
^{123}Sb		0.14	0.21	0.35	0.37	0.10	1.42
^{125}Te	4.53	9.43	9.74	8.02	13.05	8.12	69.19
^{189}Os		0.33	0.03		0.27	0.03	1.46
^{193}Ir		0.31	0.01	0.24	0.07	0.32	
^{194}Pt	0.15		0.03	0.14		0.03	
^{197}Au		0.05		0.06	0.04		
^{208}Pb	14.97	4.79	9.33	5.08	8.66	3.14	1514.52
^{209}Bi		2.25	2.54	4.67	2.63	0.41	
S/Se	2065.23	2527.69	2818.69	2516.88	2780.81	2364.52	1124.14

Sample ID	CC-072	CC-072	CC-072	CC-072	CC-072	CC-072	CC-072
Mineralization	WD	WD	WD	GV	GV	GV	GV
Analysis ID	Po 128_2	Ccp 130	Ccp 131	Ccp 132	Ccp 133	Cbn 134	Ccp 135
^{34}S	633523.79	350441.00	343586.81	363221.01	351162.22	371402.79	373558.05
^{51}V	0.77	0.13	0.01	0.09	0.28	0.29	0.32
^{59}Co	11.20	0.43	0.52	0.20		0.69	0.30
^{61}Ni		3790.83	252.94	8231.60	8252.72	33.56	8462.11
^{63}Cu	649.68	317067.02	300028.30	341266.42	342670.40	239478.46	375334.50
^{66}Zn	3281.21	60.59		81.00	4.60		13.19
^{75}As				0.40	1.81	2.60	0.02
^{77}Se	401.46	207.01	180.56	219.78	208.59	262.62	215.18
^{101}Ru			0.22				0.17
^{103}Rh	0.49	0.60	0.30	0.36			0.08
^{108}Pd		0.61		0.55		0.19	0.00
^{109}Ag	2.20	0.95	3.37	34.80	59.01	46.61	18.87
^{111}Cd	255.31	2.35	2.43	16.28	0.18	1.47	2.70
^{118}Sn		0.82	0.80	28.86	24.44	2.49	24.14
^{123}Sb	2.57	1.49	1.38	1.32	2.05	1.23	1.84
^{125}Te	69.62	31.92	43.31	48.89	55.92	43.47	67.27
^{189}Os	0.21		0.25				0.36
^{193}Ir		0.07				0.06	
^{194}Pt	2.53	0.50		0.13	0.22		
^{197}Au	1.03	0.02		0.01	0.07		
^{208}Pb	1472.51	42.94	34.38	3.05	27.89	5.31	2.74
^{209}Bi		0.07		0.10	0.01	0.03	
S/Se	887.01	1527.02	1730.71	1462.84	1547.03	1304.18	1495.02

Sample ID	CC-072	CC-072	CC-072	CC-072	CC-061	CC-061	CC-061
Mineralization	GV	GV	GV	WD	D	D	D
Analysis ID	Cct 136	Cbn 137	Ccp 138	Cbn 139	Ccp 140	Sg 141	Ccp 141
^{34}S	214510.54	402797.76	400417.79	263524.20	359822.20	356008.93	359934.09
^{51}V		0.05	0.19	0.02		0.05	0.20

^{59}Co	0.04	0.19	0.16	1.02	2.15	2366.67	3.01
^{61}Ni	4.08		9499.71	264.71	3591.80	216437.71	3848.05
^{63}Cu		225285.04	345584.18	202066.93	324602.17	100320.48	327737.31
^{66}Zn			47.09	433.68		0.56	0.92
^{75}As	0.01	0.00	0.46	1.36	7.95		
^{77}Se	323.34	263.02	244.34	179.18	157.47	182.86	234.10
^{101}Ru	0.06		0.13			0.11	
^{103}Rh	0.51	0.25	0.08		0.54	0.42	0.36
^{108}Pd		23.38			0.01		0.70
^{109}Ag	0.39	112.92	6.12	22.65	0.16	346.46	0.17
^{111}Cd			5.39	18.69	0.87	205.72	
^{118}Sn	0.12	38.60	30.90	0.31	0.51	0.77	2.99
^{123}Sb		2.60	1.36	0.69	0.73	0.27	0.22
^{125}Te	0.22	89.93	42.99	45.00	4.75	1.76	7.38
^{189}Os		0.48	0.26	0.25			
^{193}Ir		0.03		0.10		0.15	
^{194}Pt							
^{197}Au		0.10					
^{208}Pb	34.49	41.66	1.77	79.44	30.50	445.20	67.64
^{209}Bi		3.22	0.01	0.01		0.33	
S/Se	595.35	1309.79	1347.32	1479.56	2002.26	1746.11	1358.84

Sample ID	CC-061	CC-061	CC-061	CC-061	CC-061	CC-089	CC-089
Mineralization	D	D	D	D	D	D	D
Analysis ID	Ccp 142	Sg 143	Po 144	Ccp 145	Ccp 146	Po 147	Po 149
^{34}S	371066.24	360072.45	379769.76	349896.18	356061.51	375475.22	352440.03
^{51}V	0.14	0.17	0.44	0.18	0.18	0.27	0.28
^{59}Co	1.95	3692.59	52.05	0.47	1.90	6.07	7.90
^{61}Ni	3204.18	218747.62		3798.21	4668.17		31.58
^{63}Cu	320343.57	89045.10	12.66	325909.42	329783.66	130.39	145.30
^{66}Zn	5.00			2.50	0.56	996.79	
^{75}As	0.86	0.35	0.79	0.24	1.25		2.19
^{77}Se	213.83	190.99	223.48	198.17	211.71	231.53	261.70
^{101}Ru		0.49		0.22			
^{103}Rh	0.03	0.36	0.15		0.14	0.11	
^{108}Pd	0.00						
^{109}Ag	0.36	338.76	2.34	1.91	0.41	0.39	0.09
^{111}Cd	0.31	53.71		0.95		50.21	
^{118}Sn	0.35	0.48	0.29	0.16	0.29	1.52	
^{123}Sb	0.08	0.13		0.07		0.12	1.02
^{125}Te	3.44	5.34	7.22	3.20	4.33	24.23	27.81
^{189}Os					0.06		0.22
^{193}Ir	0.02		0.14			0.06	0.29
^{194}Pt	0.08	0.10	0.86		0.12	0.10	0.12

^{197}Au				0.04	0.02		
^{208}Pb	8.55	6.80	1.74	9.36	24.18	329.49	104.53
^{209}Bi		0.15	0.62				0.02
S/Se	1518.53	1702.74	1590.27	1603.69	1486.92	1532.40	1353.07

Sample ID	CC-089	CC-089	CC-089	CC-089	CC-089	CC-089	CC-089
Mineralization	SV	SV	SV	SV	SV	SV	SV
Analysis ID	Po 150	Po 151	Ccp 152	Pn 153	Cbn 154	Cbn 155	Po 156
^{34}S	384949.18	413872.85	354547.92	343769.90	369167.05	381253.34	380515.86
^{51}V	0.23		0.05	0.14	0.06	0.10	0.13
^{59}Co	7.94	6.01	0.40	51035.87		0.04	16.95
^{61}Ni			2614.75	316736.52	9.68	10.90	9.08
^{63}Cu	7.70	678.79	330406.12	698.37	230196.25	233542.75	13.23
^{66}Zn			78.40	2.31	2125.87	0.48	
^{75}As			1.90				
^{77}Se	88.34	71.29	90.34	122.59	183.97	149.93	113.84
^{101}Ru		1.39		0.16	0.20	0.11	
^{103}Rh			0.47	0.07		0.05	
^{108}Pd	8.58	2.81	3.60			0.11	
^{109}Ag	2.38	0.89	0.16	0.49	3.09	0.48	0.10
^{111}Cd		26.98	9.05	2.91	119.20		
^{118}Sn	4.41		2.40		2.06	0.87	0.65
^{123}Sb	0.11	0.90			0.41	0.25	0.28
^{125}Te	6.72	6.17	0.11	3.73	22.54	25.97	7.04
^{189}Os							
^{193}Ir							0.05
^{194}Pt	2.38	0.13	0.24		0.10		1.32
^{197}Au	0.21	0.30		0.15			
^{208}Pb	11.56	148.88	40.61	4.06	59.48	48.28	22.94
^{209}Bi	0.53		0.26		0.10	0.01	0.97
S/Se	4061.81	5044.31	3611.79	2648.76	1862.24	2293.00	3115.84

Sample ID	CC-089	CC-089	CC-089	CC-089	CC-089	CC-071	CC-071
Mineralization	SV	D	D	D	WD	WD	WD
Analysis ID	Cbn 157	Cbn 158	Po 159	Ccp 160	Po 161	Ccp 162	Po 163
^{34}S	401939.14	493017.32	374153.96	333250.54	379636.47	366226.12	355568.00
^{51}V	0.22	0.27	0.23	0.05		0.14	0.01
^{59}Co		0.19	19.73	0.05	33.99	0.94	7.48
^{61}Ni		22.85		3279.57	26.26	4447.15	
^{63}Cu	250008.35	242063.05	8.92	345378.59	39.16	337650.57	155.53
^{66}Zn	13.72	61.26	2.02	6.78		15.08	
^{75}As			0.21		2.65		
^{77}Se	191.42	189.25	225.05	233.70	215.16	198.32	70.45
^{101}Ru	0.32						

^{103}Rh	0.25		0.16	0.14	0.25		0.17
^{108}Pd		0.33	0.19	0.08	2.69	0.03	0.19
^{109}Ag	0.12	0.15	20.43	0.78	63.42	4.06	0.04
^{111}Cd		6.17		0.20		2.48	
^{118}Sn		0.54	0.40	0.47	0.39		
^{123}Sb		0.55	0.72	0.74	1.52	1.36	0.21
^{125}Te	1.44	15.49	33.14	37.30	51.66	32.42	3.47
^{189}Os			0.35		0.85	0.23	
^{193}Ir	0.07		0.32	0.04	0.55	0.06	0.05
^{194}Pt	0.17		4.12	0.05		0.10	
^{197}Au			0.36			0.03	
^{208}Pb	2.09	22.78	14.10	23.38	14.91	11.32	10.89
^{209}Bi			3.22	0.01	6.58	0.02	
S/Se	1802.35	1802.93	1584.54	1344.89	1655.04	1614.54	5003.58

Sample ID	CC-071	CC-071	CC-071	CC-117	CC-117	CC-117	CC-117
Mineralization	WD	WD	WD	SD	SD	SD	SV
Analysis ID	Ccp 164	Ccp 165	Po 166	Ccp 167	Po 168	Ccp 169	Pn 170
^{34}S	345743.76	358613.54	384470.69	353781.55	334616.21	328643.60	323917.78
^{51}V	0.21	0.13	0.20	0.01	0.11	0.19	0.02
^{59}Co	0.52	0.84	49.26	0.29	11.13	0.26	39308.19
^{61}Ni	4379.46	4113.28		702.96	19.00	702.29	394740.04
^{63}Cu	339352.76	322262.75	15.52	339649.25	4.33	323216.05	13.44
^{66}Zn	70.89	25.91	0.94	2303.56	78.40	1346.20	1.75
^{75}As		0.72		0.03	4.93	0.93	204.46
^{77}Se	208.74	206.19	238.52	99.32	93.16	86.47	71.91
^{101}Ru	0.26	0.22	0.13	0.36		0.34	0.38
^{103}Rh	0.02		0.27	0.63			
^{108}Pd		0.15	0.42		0.46		22.52
^{109}Ag	2.30	7.15	49.97	5.44	0.33	4.05	11.18
^{111}Cd	2.68			67.93	0.97	38.13	1.04
^{118}Sn	0.12	0.95	0.67	0.20	0.26	0.48	0.65
^{123}Sb	1.09	1.37	0.72	0.07	0.08		0.19
^{125}Te	41.37	46.51	50.71	3.36		0.03	0.49
^{189}Os		0.20	0.14		0.20		1.23
^{193}Ir	0.07	0.05	0.81		0.16		
^{194}Pt	0.07			0.06			1.35
^{197}Au	0.01			0.08		0.11	0.07
^{208}Pb	10.17	6.07	3.82	12.02	6.76	8.57	11.73
^{209}Bi			1.02		0.21	0.03	1.74
S/Se	1498.51	1569.46	1489.20	3416.26	3805.39	3870.92	4523.79

Sample ID	CC-117	CC-117	CC-117	CC-117	CC-117	CC-117	CC-117
Mineralization	SV	SV	SV	SV	SV	SV	SV
Analysis ID	Pn 171	Po 172	Ccp 173	Po 174	Cbn 175	Pn 176	Pn 177
^{34}S	442569.70	324394.95	352881.54	327803.02	343084.08	352876.91	305618.42
^{51}V	0.05	0.01		0.16	0.24	0.06	0.32
^{59}Co	52508.99	10.51		7.49		45329.43	43471.73
^{61}Ni	524882.84	4.91	601.14		11.70	465781.18	380278.17
^{63}Cu	43.00	4.86	332490.03	3.45	226884.62	8.55	21.02
^{66}Zn	1.89	1.04	75.99	0.91	1.28	0.36	2.01
^{75}As	780.12	2.00		1.68	1.14	161.39	33.60
^{77}Se	176.15	16.30	22.27	33.71	12.35	37.90	68.58
^{101}Ru	0.21			0.10	0.33		0.39
^{103}Rh	0.09				0.28	0.10	
^{108}Pd	47.75		0.05			46.27	15.54
^{109}Ag	56.82	0.97	776.41	1.30	1204.20	33.82	41.78
^{111}Cd			2.64	0.47	0.58	1.21	1.44
^{118}Sn	1.11	0.40	0.07	0.37		0.38	0.39
^{123}Sb	0.79		0.04	0.05			
^{125}Te	31.98		0.11	0.24		5.10	1.54
^{189}Os						0.28	0.07
^{193}Ir					0.08	0.28	0.02
^{194}Pt							0.42
^{197}Au	0.16		0.06	0.04		0.02	0.10
^{208}Pb	11.66	1.89	3.99	1.04	4.19	15.42	278.79
^{209}Bi	5.19					3.29	2.65
S/Se	1842.21	21810.11	15271.18	10518.34	27896.23	8492.80	4718.35

Sample ID	CC-117	CC-117	CC-117	CC-117	CC-117	CC-117	CC-120
Mineralization	SV	SV	SV	SV	SD	SD	NT
Analysis ID	Pn 178	Po 179	Py 180	Po 181	Ccp 184	Po 185	Ccp 186
^{34}S	327308.14	485414.50	505034.22	343956.14	357191.78	340693.11	354931.43
^{51}V	0.05		0.09				0.01
^{59}Co	44088.21	9.71	53.77	4.08		4.77	
^{61}Ni	396218.43		213.12	3.76	896.33	43.50	0.03
^{63}Cu	136.03	5.26	1.71	5.05	330779.29	67.90	322592.55
^{66}Zn	1.16		0.56	0.88	133.66	8.46	267.12
^{75}As	9.94	0.35	167.23	33.74	2.42		0.22
^{77}Se	78.09	29.34	122.25	356.90	119.65	120.66	135.37
^{101}Ru	1.39					0.31	
^{103}Rh	0.06	0.26			0.11	0.27	
^{108}Pd	13.22		0.02	6.49		0.10	1.64
^{109}Ag	58.91	2.12	0.06	141.16	10.11	4.69	4.46
^{111}Cd					5.83	0.95	30.44
^{118}Sn	0.35		0.01	1.84	0.34	0.60	3.95

^{123}Sb		0.16	0.43	1.09		0.13	0.18
^{125}Te	2.49		19.48	56.34	1.17	0.51	8.53
^{189}Os		0.02					
^{193}Ir	0.22						
^{194}Pt		0.22					2.17
^{197}Au					0.26	0.05	0.03
^{208}Pb	25.97	4.97		15.18	14.93	2.24	4.77
^{209}Bi	0.63		0.00	5.02		0.02	2.73
S/Se	4133.93	12190.68	4286.99	996.37	2822.45	2918.00	2494.56

Sample ID	CC-120	CC-120	CC-120	CC-120	CC-120	CC-120	CC-120
Mineralization	NT	NT	NT	NT	NT	NT	NT
Analysis ID	Po 187	Ccp 188	Ccp 189	Po 190	Po 191	Ccp 192	Ccp 193
^{34}S	353369.25	364274.87	415350.40	352645.87	347794.10	372809.09	358677.06
^{51}V	0.05	0.16	0.13	1.76	0.19	0.03	0.05
^{59}Co	16.90		0.22	5.34	9.09	0.04	
^{61}Ni	1355.65	6.38	1.01	103.51	340.10	5.58	
^{63}Cu	0.96	342105.77	343263.09	1.78	1.18	342911.53	316471.08
^{66}Zn	0.33	130.17	104.94	1.10	0.25	135.87	124.49
^{75}As			3.64	0.63			
^{77}Se	156.83	127.18	162.22	149.94	148.99	141.64	152.68
^{101}Ru	0.14	0.23		0.20			
^{103}Rh	0.64	0.05		0.09	0.08		
^{108}Pd	5.45	0.49	0.70		0.21	0.94	1.42
^{109}Ag	12.36	11.08	9.40	4.71	11.70	15.03	7.76
^{111}Cd	0.75	21.06	24.80			8.72	16.33
^{118}Sn		1.20	1.42	0.82	0.05	4.16	1.00
^{123}Sb	0.85	0.05	0.22	0.48	0.17	0.20	0.55
^{125}Te	31.73	4.01	0.67	8.17	12.68	6.63	3.04
^{189}Os	0.18	0.21		0.74	1.13		
^{193}Ir	0.64			0.89	0.78		0.05
^{194}Pt	6.98	1.46		2.44	1.31		0.27
^{197}Au	0.09	0.03		0.19			0.04
^{208}Pb	8.17	4.85	11.10	2.18	2.23	3.75	29.06
^{209}Bi	14.78	1.67	0.49	1.79	0.95	0.44	1.30
S/Se	2291.58	2647.50	2049.65	2381.65	2384.04	2374.31	2199.31

Sample ID	CC-120	CC-120	CC-120	CC-007	CC-007	CC-007	CC-007
Mineralization	NT	NT	NT	D	D	D	D
Analysis ID	Po 194	Ccp 195	Po 196	Cbn 197	Cbn 200	Pn 201	Cbn 202
^{34}S	402742.37	384986.47	403955.59	372404.72	332670.53	327496.49	323255.38
^{51}V	0.29	0.07		0.03	0.22	0.27	0.03
^{59}Co	13.53		19.82	3.22	0.62	53634.38	0.50
^{61}Ni	1247.73	14.47	915.12	1022.21	129.17	256394.91	93.44

^{63}Cu	1.63	324806.29	1.46	326878.89	317599.14	376.23	309476.53
^{66}Zn	1.16	183.81	1.51	42.01	1549.88	1.04	477.56
^{75}As	0.24			1.51	0.52		0.58
^{77}Se	177.14	144.11	167.17	76.35	101.80	282.29	99.69
^{101}Ru		0.21	0.08			1.56	0.29
^{103}Rh	0.01	0.25	0.33	0.09		2.61	
^{108}Pd	0.32	0.10	0.54			0.22	0.24
^{109}Ag	5.35	7.05	16.62	4.31	2.63	4.17	5.34
^{111}Cd		41.42	0.28		28.58	0.38	5.08
^{118}Sn		1.64		0.30	0.21	0.21	0.87
^{123}Sb	0.24		0.35			0.51	
^{125}Te	12.94	4.84	17.76	3.01	1.23	9.25	3.44
^{189}Os	0.87		0.49		0.08	10.02	
^{193}Ir	0.50		1.46			9.99	
^{194}Pt	0.96	0.30	4.47	0.17	0.04	0.28	
^{197}Au			0.01	0.27	0.05		2.19
^{208}Pb	3.75	2.32	4.52	6.74	9.56	4.17	10.16
^{209}Bi	1.90	0.45	4.35	0.05		0.39	
S/Se	2017.10	2348.15	2131.34	4218.68	3141.51	1161.94	3164.68

Sample ID	CC-007	CC-007	CC-007	CC-007	CC-007	CC-007	CC-007
Mineralization	D	D	D	D	D	D	D
Analysis ID	Pn 203	Po 204	Cbn 206	Po 207	Pn 211	Po 211	Pn 212
^{34}S	344877.12	351108.02	356818.32	344764.86	310524.58	352622.31	679106.86
^{51}V		0.07	0.47	0.13	0.09	0.34	
^{59}Co	42059.22	9.09	0.70	12.88	29387.96	18.32	71652.85
^{61}Ni	259754.67	14.21	104.76		197906.79		492092.75
^{63}Cu	2821.96	15.47	338133.00	9.05	177.14	8.68	263.02
^{66}Zn	1.92	0.52	0.71	0.56	0.13	0.68	0.44
^{75}As	0.15			0.07	2.51		14.41
^{77}Se	125.04	155.03	101.10	305.57	246.60	295.20	488.52
^{101}Ru		0.33		0.96	1.57		4.58
^{103}Rh	3.37	0.07		0.79	5.12	0.68	8.12
^{108}Pd		1.25			2.39	5.86	1.30
^{109}Ag	15.02	7.80	4.32	0.22	5.64	4.36	
^{111}Cd	2.38	0.48	4.43			0.45	
^{118}Sn	0.61					0.50	1.52
^{123}Sb	0.26	0.33	0.14	0.54		0.73	
^{125}Te	10.71	14.43	0.55	20.02	24.88	22.50	23.35
^{189}Os			0.36	8.05	4.92	4.13	8.80
^{193}Ir	0.12	0.08		12.63	3.06	5.68	8.67
^{194}Pt		2.29	0.50	0.31		0.56	
^{197}Au	0.09	0.03	0.08				0.71
^{208}Pb	40.69	2.50	6.83	4.45	27.32	3.94	4.99

^{209}Bi	3.65	4.42	0.04	4.88	3.59	12.21	
S/Se	2608.00	2295.74	3095.06	1164.05	1322.81	1201.55	667.73

Sample ID	CC-122	CC-122	CC-122	CC-122	CC-122	CC-122	CC-122
Mineralization	SD	SD	SD	SD	SD	SD	SD
Analysis ID	Po 214	Po 216	Cbn 217	Po 218	Ccp 219	Po 220	Cbn 221
^{34}S	373421.40	372529.82	401210.18	388643.10	341020.23	357643.70	377080.99
^{51}V	0.13	0.04	0.01	0.29		0.37	0.02
^{59}Co	18.95	5.15	0.15	18.66	0.18	14.68	1.68
^{61}Ni	17.48		5.99	8.27	3.17	21.58	6.76
^{63}Cu	7.83	10.23	241490.15	4.52	294963.42	18.77	230397.93
^{66}Zn	1.63	1.31	1.81	0.35	1.65		536.47
^{75}As	1.57	0.16			1.71	0.61	
^{77}Se	148.89	158.02	129.10	146.90	129.75	132.69	140.96
^{101}Ru	0.66			0.07	0.53	0.41	0.34
^{103}Rh	0.28		0.69	0.01	1.36	0.04	0.20
^{108}Pd			0.31	0.05	0.09		1.45
^{109}Ag	0.54	0.21	17.37	1.37	4.01		7.13
^{111}Cd			2.42			4.49	12.68
^{118}Sn	0.34		0.72	0.77	0.32	0.24	0.53
^{123}Sb	0.77		0.17	0.66	0.35	0.51	0.26
^{125}Te	13.35	4.41	16.90	11.45	7.63	4.91	1.87
^{189}Os	3.03	1.83		2.86	0.90	3.42	8.51
^{193}Ir	4.00	6.40		3.88	3.84	6.97	7.63
^{194}Pt				1.07	0.08		
^{197}Au			0.36	0.01	0.17		0.03
^{208}Pb	0.41	2.36	20.80	0.45	5.16	1.17	16.99
^{209}Bi				0.30	2.67	0.15	0.44
S/Se	2388.33	2263.62	2642.08	2398.98	2455.55	2697.99	2442.46

Sample ID	CC-122	CC-122	CC-124	CC-124	CC-124	CC-124	CC-124
Mineralization	SD	SD	D	D	D	D	D
Analysis ID	Po 221	Po 223	Ccp 224	Po 225	Po 226	Pn 226	Pn 227
^{34}S	378792.86	405259.01	282089.99	296435.00	278877.81	278020.83	279710.59
^{51}V	0.16	0.00	0.15	0.17	0.13	0.27	
^{59}Co	9.76	12.42	0.73	9.41	10.77	31989.38	33671.78
^{61}Ni	0.42	68.23	5915.44	22.97	16.76	363530.18	374106.11
^{63}Cu	74.53	2677.18	314067.78	4.31	5.14	64.71	1335.78
^{66}Zn	0.56	3.17	71.27	1.00	0.71	0.88	3.90
^{75}As		0.09		0.99	2.09	2.65	3.06
^{77}Se	132.47	124.87	101.04	168.49	118.60	108.68	102.95
^{101}Ru	0.55					1.04	0.44
^{103}Rh		0.01	0.93	0.06	0.09	6.83	0.15
^{108}Pd	0.02	0.14	1.28			57.17	39.25

^{109}Ag	0.63	1.15	2.24	1.98	0.79	2.55	5.71
^{111}Cd	1.49		4.31				
^{118}Sn	0.45	0.56			0.78	0.27	1.97
^{123}Sb	0.26		0.04	0.17		0.04	
^{125}Te	10.89	9.86	1.97	5.36	1.25	2.11	
^{189}Os	7.69	2.10		1.42	0.99	1.51	
^{193}Ir	7.52	3.24		0.45	1.27	1.01	
^{194}Pt	0.04	0.15	0.36	2.04	0.37		0.28
^{197}Au	0.01			0.06			
^{208}Pb	1.64	3.43	5.48	3.04	1.58	36.78	8.09
^{209}Bi	0.28	0.35	0.81	2.17	1.46	2.11	0.35
S/Se	2702.40	2855.07	3332.39	2094.46	2985.68	3051.18	3226.65

Sample ID	CC-124	CC-124	CC-124	CC-124	CC-124	CC-124	CC-124
Mineralization	D	D	D	D	D	D	D
Analysis ID	Po 228	Po 229	Ccp 231	Ccp 232	Po 233	Po 234	Ccp 236
^{34}S	276029.08	271799.81	289660.82	317470.78	277670.88	289700.32	317955.34
^{51}V	0.24	0.12	0.17	0.11	0.20	0.48	0.05
^{59}Co	8.32	10.10	0.87	0.12	11.77	9.78	0.81
^{61}Ni	19.84	40.58	5140.20	7800.20	30.51		5435.50
^{63}Cu	8.58	10.30	346791.26	353060.85	7.21	11.81	321970.38
^{66}Zn	2.21	2.47	103.93	98.69	0.85	0.08	122.22
^{75}As	1.85		4.79	0.35	0.95		
^{77}Se	116.70	117.21	85.88	135.58	167.69	169.32	118.49
^{101}Ru			0.23		0.57		
^{103}Rh	0.03		0.43	1.52	0.16		0.61
^{108}Pd		0.28	0.38	2.57		0.27	1.07
^{109}Ag	6.76	4.73	6.81	3.51	3.28	3.87	2.57
^{111}Cd		1.22	3.86	12.22			9.94
^{118}Sn		0.17		2.50	0.60		
^{123}Sb	0.43	0.11	0.38	0.28	0.36	0.75	
^{125}Te	6.50	9.88	0.95	2.95	7.67	5.34	4.21
^{189}Os						1.01	
^{193}Ir	0.91	0.23		0.05	0.71	1.67	
^{194}Pt	0.81	7.00	0.43	0.50	2.06	2.25	1.43
^{197}Au	0.06		0.50				
^{208}Pb	3.82	4.34	8.31	4.31	2.88	3.57	4.80
^{209}Bi	4.37	6.11	1.21	2.41	1.90	1.34	1.81
S/Se	3047.13	3019.34	3744.93	2433.95	2128.28	2097.16	2783.38

Sample ID	CC-046	CC-046	CC-046	CC-046	CC-046	CC-046	CC-046
Mineralization	SD	SD	SD	SD	SD	SV	SV
Analysis ID	Po 237	Ccp 238	Ccp 239	Po 240	Py 241	Py 242	Py 243
^{34}S	293041.07	299365.73	291373.22	298534.56	400885.88	418881.90	456557.08

^{51}V		0.09	0.04	0.26	0.20	0.15	0.19
^{59}Co	11.68	0.21	0.12	6.11	405.90	850.64	5050.04
^{61}Ni	1428.15	11.72		49.25	57.49	150.99	407.94
^{63}Cu	6.46	346569.59	341776.17	7.96	3.32	1.92	2.03
^{66}Zn	0.28	169.61	559.86	0.69	0.30	0.67	0.56
^{75}As			0.64		5.48	7.91	13.47
^{77}Se	172.90	105.87	147.35	125.19	149.71	117.60	87.58
^{101}Ru		0.18	0.35				
^{103}Rh		0.87	1.30	0.09			
^{108}Pd			0.28				0.02
^{109}Ag	0.86	2.03	1.56	2.82	0.02		
^{111}Cd		16.40	22.43				0.07
^{118}Sn		0.61	0.33	0.33		0.04	
^{123}Sb			0.28		0.00	0.04	0.00
^{125}Te	5.62	1.39	1.39		1.67	1.09	2.07
^{189}Os							0.10
^{193}Ir		0.04			0.01		0.02
^{194}Pt					0.01		
^{197}Au		0.04	0.13			0.03	0.01
^{208}Pb	3.84	4.67	2.66	2.62	0.10	0.06	1.08
^{209}Bi	3.58	0.47	0.28	0.26	0.26		3.37
S/Se	2103.55	3187.78	2294.60	2849.29	3526.73	4460.88	6032.23

Sample ID	CC-046	CC-046	CC-046	CC-046	CC-088	CC-088	CC-088
Mineralization	SV	SV	SD	SD	D	SV	SV
Analysis ID	Po 244	Py 245	Ccp 246	Po 247	Po 248	Po 251	Cbn 252
^{34}S	319419.10	453187.04	325487.24	302602.95	297335.09	292122.88	300854.18
^{51}V	0.30	0.18	0.21	0.21	0.12	0.54	0.34
^{59}Co	29.68	32459.25	0.03	3.94	7.58	6.78	0.23
^{61}Ni	7348.37	8044.87		19.45	52.20		15.28
^{63}Cu	6.22	6.53	364427.72	16.97	17.67	3.68	239729.42
^{66}Zn	1.13	0.86	212.74	0.90	4.13	0.87	2.12
^{75}As	5.00	37.37				3.75	6.87
^{77}Se	81.90	169.46	169.35	109.69	142.64	27.65	98.61
^{101}Ru	0.09						0.14
^{103}Rh	0.01	0.32	0.33	0.04			0.14
^{108}Pd	0.01	0.03					
^{109}Ag	2.70		4.17	3.39	1.00		0.50
^{111}Cd	1.35		22.44			0.67	1.34
^{118}Sn			0.20	0.97	0.70		
^{123}Sb	0.07	0.03	0.05	0.01			0.16
^{125}Te	0.36	0.13	4.90	1.46	0.96		1.10
^{189}Os	0.44	0.66					
^{193}Ir		0.82			0.11		0.05

^{194}Pt	2.51	22.21	0.88	0.66			0.09
^{197}Au	0.06	0.13		0.33	0.02		
^{208}Pb	38.07	1.36	3.75	2.95	6.23	1.41	7.91
^{209}Bi	1.16	1.58	0.48	0.72	0.26		
S/Se	4358.72	3086.24	2004.76	3240.86	2507.04	12963.53	3478.32

Sample ID	CC-088	CC-088	CC-088	CC-088	CC-088	CC-088	CC-030
Mineralization	SV	SV	SV	SV	D	D	GV
Analysis ID	Pn 253	Po 254	Pn 255	Po 256	Po 258	Ccp 259	Po 260
^{34}S	296707.02	294759.92	282810.24	297735.31	296369.35	278836.13	235773.81
^{51}V	0.60	0.16	0.11	0.03	0.49	0.32	0.06
^{59}Co	32080.30	4.36	35740.58	6.79	9.49	0.75	10.01
^{61}Ni	322958.59	60.21	316452.38	6.79		3521.93	
^{63}Cu	500.87	14.57	487.28	8.10	7.58	377854.31	4.55
^{66}Zn	6.32	1.41	976.84	0.90	0.20	13.57	2.12
^{75}As	164.21	17.19	76.40	10.34	0.70	0.73	1.58
^{77}Se	210.86	31.94	23.76	83.58	249.95	183.66	29.47
^{101}Ru	0.31		1.28			0.62	
^{103}Rh	0.77		0.53		0.06	0.88	
^{108}Pd	0.87				0.48		0.02
^{109}Ag	3.54		1.91	0.10	11.07	1.72	0.10
^{111}Cd	2.43		101.30	0.98		4.06	
^{118}Sn	0.04		1.24	0.18	0.66	0.99	
^{123}Sb	1.33	0.30					0.01
^{125}Te	24.35		2.99	0.31	9.27	1.11	
^{189}Os			0.29				
^{193}Ir	0.63				0.38	0.06	
^{194}Pt	109.92		2.51		0.19		
^{197}Au	0.66		0.28		0.12		0.11
^{208}Pb	102.12	8.50	175.44	2.76	4.22	1.59	1.56
^{209}Bi	4.86	0.06	1.16	0.01	0.26	0.00	0.02
S/Se	1547.95	11179.37	13706.23	4261.94	1427.87	1714.07	12074.03

Sample ID	CC-030	CC-030	CC-030	CC-030	CC-030	CC-030	CC-030
Mineralization	GV	GV	GV	GV	GV	GV	GV
Analysis ID	Pn 261	Po 262_1	Po 262_2	Po 263	Pn 265	Po 266	Po 268
^{34}S	240374.34	243577.75	239769.78	299553.31	428540.68	246997.84	252709.30
^{51}V	0.39	0.18	0.25		0.17		
^{59}Co	61081.36	9.99	8.09	9.80	105731.52	8.90	8.64
^{61}Ni	328951.41	0.70			574078.76		
^{63}Cu	294.91	3.68	5.97	3.52	2386.14	5.25	2.85
^{66}Zn	15.04	2.18	3.89	1.92	1.83	2.69	1.13
^{75}As	0.31	5.97	4.66		13.18		
^{77}Se	50.70	22.86	28.58	20.15	293.36	31.60	37.81

^{101}Ru	1.48	0.12	0.42				
^{103}Rh						0.08	
^{108}Pd		0.09					0.11
^{109}Ag	0.40	0.03	0.11		3.80	0.05	
^{111}Cd							
^{118}Sn	0.35	0.10	0.73		1.32		
^{123}Sb	0.50	0.09				0.01	
^{125}Te		0.36			38.39		0.17
^{189}Os							0.08
^{193}Ir	0.15				0.89		0.05
^{194}Pt				0.66	1.64	0.18	
^{197}Au							
^{208}Pb	76.72	1.42	10.34	2.57	263.95	2.69	3.21
^{209}Bi	2.67	0.15	0.34	0.20	0.17	0.02	0.01
S/Se	6402.98	15567.64	12451.97	17654.20	1111.61	11326.88	9416.20

Sample ID	**CC-033**	**CC-033**	**CC-033**	**CC-033**	**CC-033**	**CC-033**	**CC-033**
Mineralization	**NT**	**NT**	**NT**	**NT**	**NT**	**NT**	**NT**
Analysis ID	**Po 270**	**Po 271**	**Ccp 272**	**Cbn 273**	**Po 274**	**Ccp 275**	**Po 276**
^{34}S	247345.29	245919.03	251779.68	261712.69	254737.10	290517.32	278936.37
^{51}V	0.06	0.09	0.16		0.11		
^{59}Co	11.41	14.78	0.21	0.03	17.18		10.89
^{61}Ni			6865.49	34.08	31.83	7105.66	21.53
^{63}Cu	328.21	19.71	318709.24	216604.43	43.90	324207.42	120.71
^{66}Zn	0.83	0.48	47.57	10.36	1.10	24.80	1.73
^{75}As	3.18		0.37	1.37			5.69
^{77}Se	132.18	131.19	124.20	91.97	131.22	137.53	138.09
^{101}Ru	1.71		0.17		0.23	0.33	
^{103}Rh	0.01	0.50		0.61	0.84	0.07	
^{108}Pd		0.40	0.73	11.91	0.52	3.77	0.14
^{109}Ag	0.26	18.12	4.12	10.56	11.21	6.45	7.11
^{111}Cd	0.24	0.45	5.17	22.05	0.47	6.77	
^{118}Sn	0.08	0.19	1.41	4.45	1.16	2.80	
^{123}Sb	0.17	0.28	0.02	1.35	0.85	0.82	
^{125}Te	12.48	16.94	10.72	21.16	27.50	15.98	9.94
^{189}Os	26.77	1.00			1.60		3.78
^{193}Ir	13.44	1.89			2.16	0.08	4.40
^{194}Pt		1.66	0.71	3.38	3.05	0.44	0.99
^{197}Au		0.02	0.02	0.21		0.07	
^{208}Pb	3.30	3.60	9.08	53.27	5.11	9.53	2.95
^{209}Bi	0.28	2.95	1.52	3.05	5.67		1.59
S/Se	2674.34	2707.49	2608.61	3727.31	2701.57	2314.45	2577.31

Sample ID	CC-033	CC-033	CC-033	CC-033	CC-033	CC-042	CC-042
Mineralization	NT	NT	NT	NT	NT	D	D
Analysis ID	Ccp 277	Ccp 278	Po 279	Po 280	Ccp 281	Po 282	Cu 284
^{34}S	252504.34	253184.00	260725.18	273168.27	257908.42	261398.05	
^{51}V	0.08	0.20	0.38			0.36	0.59
^{59}Co	0.08	0.28	24.09	12.74	0.05	60.53	1.56
^{61}Ni	7484.71	7290.68	29.33	7.83	7063.89		429.61
^{63}Cu	341637.38	323148.93	28.84	44.53	330069.71	393.09	
^{66}Zn	26.79	48.20	0.95	1.14	19.74	3.53	14.87
^{75}As	5.23	0.58	2.26		0.01	0.75	
^{77}Se	112.84	116.70	155.06	137.62	117.62	107.28	33.34
^{101}Ru	0.25	0.32		0.43		0.77	
^{103}Rh		0.14	0.30	0.16		1.37	
^{108}Pd	2.46	7.27				0.49	
^{109}Ag	4.41	8.57	0.98	6.29	2.60	0.61	21.49
^{111}Cd	3.61	9.51	1.16		3.52	0.39	
^{118}Sn	1.42	6.19	0.56			0.95	
^{123}Sb	0.20	0.43	0.24	0.50	0.17	0.63	
^{125}Te	5.52	18.82	2.72	21.57	4.10	8.71	
^{189}Os			1.21			1.75	
^{193}Ir	0.06		2.83	2.99		2.61	
^{194}Pt		0.67	0.32	2.87		0.17	1.48
^{197}Au	0.05	0.20	0.12		0.23	0.18	0.25
^{208}Pb	8.11	5.15	4.82	2.86	7.69	3.85	0.30
^{209}Bi		0.49	0.78	3.20		4.41	
S/Se	2869.65	2771.20	2312.04	2578.87	2752.03	3320.19	

Sample ID	CC-042	CC-042	CC-042	CC-042	CC-042	CC-042	CC-042
Mineralization	D	D	D	D	D	D	D
Analysis ID	Po 285	Po 286	Po 288	Pn 289	Ccp 290	Cu 291	Cu 292
^{34}S	272417.16	287704.28	256275.88	280990.51	185586.20		
^{51}V			0.04	0.01	0.15		
^{59}Co	45.28	51.25	20.09	44002.49	3.63	0.99	
^{61}Ni				328224.05	85.37	255.07	
^{63}Cu	154.65	590.35	12.51	148.56	276800.34		
^{66}Zn	1.47	0.31	0.82	5.17	11.84	13.99	10.08
^{75}As	0.06	0.33	0.74	1.34			
^{77}Se	105.85	134.39	102.81	138.52	70.58	17.25	44.73
^{101}Ru	0.62	0.25		1.76		0.82	0.72
^{103}Rh	0.87	0.87	0.67	1.46	0.23		9.54
^{108}Pd	3.75	1.32	3.37		0.07		
^{109}Ag	0.64	0.39	5.55	0.49	40.12	11.86	13.55
^{111}Cd	0.33	0.38	0.32				3.86
^{118}Sn	0.58	0.32		0.84	0.62	0.28	3.02

^{123}Sb	1.36	0.18	0.39		0.21	1.06	1.37
^{125}Te	20.86	17.05	25.92	10.72	4.61		
^{189}Os	3.23	1.20	0.66	2.55			
^{193}Ir	2.52	1.95	2.25	2.71	0.03	0.60	
^{194}Pt			0.19			1.61	1.74
^{197}Au	0.03	0.13			0.03		0.47
^{208}Pb	13.89	7.11	9.57	8.35	10.97	0.46	0.99
^{209}Bi	8.84	4.72	8.74	0.95			
S/Se	3386.73	2664.56	3477.29	2366.48	3782.86		

S. ID	CC-019	CC-019	CC-019	CC-019	CC-019	CC-019	CC-019	CC-019
Min.	T	T	T	T	T	T	T	T
A. ID	Po 293	Po 294	Py 295.1	Py 295.2	Py 296	Py 297.1	Py 297.2	Py 298
^{34}S	282759.48	304911.20	451708.98	411399.88	429586.33	402061.60	403126.19	446673.53
^{51}V	0.12		0.37	0.11	0.06	0.10	0.14	0.04
^{59}Co	10.88	22.66	609.09	304.19	6726.49	2687.52	614.63	851.14
^{61}Ni	11.19	108.63	881.59	65.20	4830.82	3937.52	1888.37	4633.28
^{63}Cu	6.26	13.52	1.27	0.03	42.40	0.46	0.17	0.34
^{66}Zn		1.74	1.03	0.56	0.65	0.82	0.89	0.50
^{75}As	0.79	1.72	1.29	1.33	1.69	1.64	0.63	1.87
^{77}Se	36.73	53.27	38.31	55.20	29.66	61.05	53.71	53.42
^{101}Ru	0.22				0.08	0.01		
^{103}Rh		0.08			0.00	0.01	0.01	
^{108}Pd			0.04			0.01		0.02
^{109}Ag	1.38	0.57				0.00	0.01	
^{111}Cd	1.56	0.17	0.14	0.15	0.04			
^{118}Sn	0.52	0.07		0.01	0.04	0.05	0.01	0.12
^{123}Sb			0.07			0.01		
^{125}Te			0.59					0.06
^{189}Os				0.04		0.03	0.02	0.04
^{193}Ir							0.01	
^{194}Pt					0.20	0.01		
^{197}Au			0.02					
^{208}Pb	5.84	27.85	0.24		0.01	0.08	0.03	0.00
^{209}Bi	0.06	1.04	0.78		0.01	0.00	0.00	0.01
S/Se	9717.83	6679.61	13737.18	9534.82	17743.83	8584.46	9758.65	9883.13

Std.	UQAC FeS-1				MSS1	
N = 16	Mean	2σ	Ref	2σ Ref.	Mean	Ref.
^{34}S	467704.51	116707.12	407320.60	92052.40	376012.55	390000.00
^{51}V	17.32	1.75	21.20	1.20		
^{59}Co	866.98	120.02	643.10	38.80		
^{61}Ni	33123.07	6444.87	25680.30	3538.20	15373.81	11791.00
^{63}Cu	19304.25	1830.61	22541.90	1804.80	2476.82	4976.00
^{66}Zn	197.38	96.16	259.70	63.80		
^{75}As	860.36	242.75	1055.60	232.40	43.64	70.00
^{77}Se	261.55	45.17	345.80	84.00		
^{101}Ru	75.13	8.94	65.90	16.40	22.64	30.00
^{103}Rh	53.44	7.38	61.40	13.60	69.17	75.33
^{108}Pd	29.75	7.16	50.90	18.00		
^{109}Ag	140.24	17.45	175.90	39.20	58.50	54.80
^{118}Sn	137.87	19.71	183.40	36.60		
^{123}Sb	56.42	17.51	92.60	30.60	42.40	52.50
^{125}Te	115.25	19.83	151.00	49.40		
^{189}Os	82.03	15.08	83.80	23.80	52.59	71.00
^{193}Ir	46.82	4.95	61.70	19.40	37.18	54.00
^{194}Pt	32.95	9.23	59.60	25.00	35.54	43.03
^{197}Au	55.77	14.54	66.20	19.40	34.46	37.29
^{208}Pb	82.52	10.62	91.10	14.74	49.27	49.70
^{209}Bi	113.95	26.16	119.60	33.20	54.96	40.00

*R^2 = 0.99 between measured and reference values for all analytes.

Appendix E – Sulfur Isotopes

*All SIMS S-isotope data reported in per mille. Sample IDs shortened. Note: SIMS IDs are unique from LA–ICP–MS analysis IDs.

Sample ID	SIMS ID	N	$\delta^{34}S$	$\delta^{34}S$ 2σ	$\delta^{33}S$	$\delta^{33}S$ 2σ	$\delta^{36}S$	$\delta^{36}S$ 2σ	$\Delta^{33}S$	$\Delta^{33}S$ 2σ	$\Delta^{36}S$	$\Delta^{36}S$ 2σ
CC-009	Ccp 9	6	-1.09	0.14	-0.54	0.11	-2.19	0.53	0.02	0.08	-0.12	0.47
CC-009	Pn 10	8	-1.62	0.61	-0.83	0.26	-3.10	1.16	0.00	0.12	-0.03	0.38
CC-009	Po 11	8	-1.09	0.16	-0.50	0.11	-2.13	0.43	0.06	0.10	-0.06	0.27
CC-009	Ccp 12	5	-0.98	0.12	-0.49	0.07	-2.05	0.81	0.01	0.05	-0.19	0.72
CC-009	Pn 13	5	-1.83	0.35	-0.93	0.20	-3.50	0.92	0.01	0.04	-0.03	0.36
CC-009	Po 14	7	-1.15	0.16	-0.56	0.14	-2.36	0.75	0.04	0.09	-0.17	0.65
CC-011	Pn 15	2	-2.48	0.86	-1.25	0.35	-4.71	1.30	0.03	0.10	0.00	0.33
CC-011	Po 16	5	-2.02	0.57	-0.98	0.18	-4.05	1.44	0.06	0.13	-0.22	0.53
CC-011	Ccp 17	6	-1.05	0.07	-0.56	0.07	-2.16	0.28	-0.02	0.05	-0.17	0.32
CC-011	Pn 18	3	-1.71	0.19	-0.82	0.06	-3.60	0.39	0.06	0.11	-0.35	0.36
CC-011	Po 19	7	-1.67	0.32	-0.77	0.28	-3.21	1.20	0.09	0.11	-0.05	0.72
CC-011	Ccp 20	7	-1.00	0.19	-0.50	0.08	-2.01	0.64	0.01	0.03	-0.12	0.50
CC-027	Po 25	5	-1.71	0.12	-0.83	0.09	-3.55	0.21	0.05	0.07	-0.31	0.37
CC-027	Po 26	5	-1.75	0.16	-0.86	0.10	-3.61	0.72	0.04	0.08	-0.28	0.50
CC-035	Pn 27	8	-2.82	0.31	-1.43	0.16	-5.33	0.71	0.02	0.06	0.03	0.47
CC-035	Po 28	8	-2.05	0.14	-1.01	0.06	-4.11	0.20	0.05	0.08	-0.22	0.25
CC-035	Ccp 29	10	-1.28	0.22	-0.62	0.14	-2.60	0.39	0.03	0.06	-0.17	0.24
CC-035	Pn 30	7	-2.87	0.44	-1.47	0.22	-5.34	1.38	0.01	0.13	0.11	0.81
CC-035	Po 31	7	-1.87	0.26	-0.93	0.16	-3.57	0.91	0.04	0.09	-0.02	0.55
CC-044	Ccp 32	7	-1.71	0.68	-0.84	0.41			0.04	0.13		
CC-044	Pn 33	6	-2.27	0.71	-1.08	0.45			0.09	0.13		
CC-044	Po 34	13	-1.37	0.31	-0.62	0.16			0.09	0.27		
CC-044	Ccp 35	8	-1.24	0.15	-0.58	0.10			0.06	0.12		
CC-044	Po 36	2	-1.43	0.14	-0.62	0.01			0.12	0.08		
CC-045	Po 38	7	-1.17	0.18	-0.56	0.17			0.04	0.10		
CC-045	Ccp 39	14	-1.11	0.25	-0.51	0.14			0.06	0.10		
CC-045	Po 40	8	-1.07	0.15	-0.47	0.20			0.08	0.22		
CC-089	Po 61	14	-2.31	1.01	-1.13	0.51	-4.54	2.10	0.06	0.05	-0.15	0.60
CC-100	Pn 62	7	-2.95	0.93	-1.56	0.54			-0.04	0.14		
CC-100	Ccp 63	5	-1.27	0.17	-0.64	0.15	-2.50	0.77	0.02	0.08	-0.09	0.63
CC-100	Pn 64	8	-3.07	0.37	-1.58	0.22	-6.04	0.76	0.00	0.12	-0.23	0.66
CC-100	Po 65	7	-2.45	0.14	-1.20	0.12	-4.85	0.58	0.07	0.09	-0.20	0.58
CC-100	Ccp 66	5	-1.86	1.40	-0.93	0.74	-3.46	3.08	0.03	0.10	0.07	0.51
CC-100	Ccp 67	5	-1.29	0.26	-0.65	0.10	-2.40	0.60	0.01	0.08	0.05	0.33
CC-100	Po 68	8	-2.39	0.10	-1.14	0.06	-4.72	0.46	0.09	0.05	-0.19	0.45
CC-101	Po 69	5	-1.28	0.24	-0.59	0.13	-2.44	0.86	0.07	0.09	-0.01	0.62
CC-101	Pn 70	14	-3.04	0.91	-1.54	0.42	-5.94	1.93	0.03	0.09	-0.17	0.47
CC-101	Po 71	15	-2.31	0.26	-1.14	0.15	-4.46	0.48	0.06	0.11	-0.07	0.44
CC-101	Po 72	15	-2.27	0.31	-1.14	0.16	-4.49	0.95	0.04	0.13	-0.17	0.55
CC-116	Po 74	14	-1.17	0.12	-0.58	0.08	-2.32	0.57	0.03	0.08	-0.10	0.55
CC-116	Ccp 75	15	-0.97	0.20	-0.47	0.12	-1.90	0.47	0.03	0.06	-0.06	0.50
CC-116	Pn 76	3	-1.73	1.03	-0.86	0.50	-3.38	1.98	0.03	0.04	-0.11	1.31
CC-116	Po 77	10	-1.10	0.21	-0.55	0.13	-2.24	0.70	0.02	0.07	-0.15	0.64
CC-116	Ccp 78	10	-1.04	0.22	-0.47	0.08	-1.95	0.57	0.06	0.09	0.03	0.31

Sample ID	SIMS ID	N	$\delta^{34}S$	$\delta^{34}S$ 2σ	$\delta^{33}S$	$\delta^{33}S$ 2σ	$\delta^{36}S$	$\delta^{36}S$ 2σ	$\Delta^{33}S$	$\Delta^{33}S$ 2σ	$\Delta^{36}S$	$\Delta^{36}S$ 2σ
CC-116	Po 80	10	-1.45	0.18	-0.70	0.13	-2.98	0.54	0.05	0.07	-0.22	0.38
CC-116	Ccp 81	8	-1.47	1.49	-0.69	0.78	-3.03	2.90	0.07	0.04	-0.24	0.41
CC-116	Po 83	11	-1.47	0.68	-0.72	0.37	-2.95	1.28	0.04	0.09	-0.17	0.32
CC-116	Ccp 84	9	-1.08	0.74	-0.53	0.36	-2.09	1.32	0.03	0.08	-0.04	0.49
CC-027	Po 24	4	-2.02	0.04	-1.03	0.09	-4.29	0.33	0.01	0.10	-0.46	0.39
CC-020	Py 86	3	-3.03	1.15	-1.48	0.60	-5.84	2.06	0.08	0.03	-0.08	0.30
CC-020	Py 87	3	0.60	0.13	0.57	0.14	0.85	0.44	0.26	0.08	-0.30	0.55
CC-020	Py 88	2	0.19	0.40	0.33	0.24	-0.04	1.01	0.23	0.04	-0.41	0.26
CC-020	Py 89	2	0.18	0.17	0.38	0.14	0.06	0.64	0.29	0.05	-0.29	0.31
CC-037	Py 90	4	-1.35	0.39	-0.66	0.24	-2.62	0.92	0.03	0.05	-0.06	0.32
CC-037	Py 91	3	-1.31	0.32	-0.60	0.09	-2.81	0.43	0.08	0.09	-0.32	0.23
CC-037	Py 92	4	-1.40	0.13	-0.72	0.04	-3.19	0.52	0.01	0.11	-0.53	0.35
CC-037	Py 94	3	-1.52	0.23	-0.72	0.12	-3.12	0.76	0.06	0.13	-0.23	0.33

N	68		70		16		81	
	Ccp	Nifty-b	Pn	VMSO	Py	Sierra	Po	Alexo
	Measured	*Ref.*	*Measured*	*Ref.*	*Measured*	*Ref.*	*Measured*	*Ref.*
$\delta^{33}S$	-1.79	-1.78	1.61	1.66	1.09	1.09	1.72	1.73
$\delta^{33}S$ (2σ)	0.24	0.21	0.48	0.24	0.15	0.15	0.28	0.20
$\delta^{34}S$	-3.59	-3.58	3.10	3.22	2.17	2.17	5.20	5.23
$\delta^{34}S$ (2σ)	0.31	0.44	0.95	0.51	0.25	0.28	0.47	0.40
$\delta^{36}S$	-7.10	-7.15	6.09	6.37	3.98	3.96	10.92	10.98
$\delta^{36}S$ (2σ)	2.00	0.63	2.44	0.83	0.92	0.60	1.26	0.59
$\Delta^{33}S$	0.06	-0.06	0.01	0.00	-0.03	-0.02	-0.96	-0.96
$\Delta^{33}S$ (2σ)	0.16	0.03	0.13	0.02	0.06	0.01	0.13	0.04
$\Delta^{36}S$	-0.29	-0.36	0.19	0.24	-0.16	-0.18	1.01	1.02
$\Delta^{36}S$ (2σ)	2.04	0.45	1.18	0.35	0.62	0.15	0.96	0.27

*Comparison between measured reference standards for analyses used in this study, and published values of the reference standards. References values for sulfide standards are from LaFlamme et al. (2016).

Appendix F – Numerical Modelling Parameters

Equations used in modelling were from Ripley and Li (2003). To calculate R factor curves for sequential steps of batch equilibration in a closed-system exchange of metals between sulfide and silicate, the following equation was used:

$$C_{sul,f}^{Me} = \frac{C_{sul,i}^{Me} + RC_{sil,i}^{Me}}{1 + \frac{R}{D_{sul-sil}^{Me}}}$$

C represents the initial (*i*) or final (*f*) concentration of a given metal (*Me*), in the sulfide liquid (*sul*) and silicate melt (*sil*), respectively. *R* represents the ratio of the mass of silicate melt to sulfide liquid for the interaction, and *D* is the partition coefficient between the sulfide liquid and silicate liquids for the given metal.

An analogous expression was used to calculate R factor curves for the same hypothetical system but for a different equilibration process. The following equation was used to model the sulfur isotopic exchange of a sulfide mass and silicate melt:

$$S_{sul,f} = \frac{S_{sul,i} + R^{\star}\left(S_{sil,i} + d\right)}{1 + R^{\star}}$$

S represents the sulfur isotope composition of a sulfide mass (for either $\delta^{34}S$, $\Delta^{33}S$, or $\Delta^{36}S$). The variable *d* represents the isotopic difference between sulfur in the sulfide mass and the sulfur in the silicate melt (which is expected to be around 0‰ for magmatic systems; Ripley and Li, 2003). Lastly, $R^{\star}$ is the mass ratio of sulfur contributed by the silicate magma to that contributed by the sulfide mass. The following table summarizes the various parameters used in modelling and corresponding rationale.

Parameter	Variable	Value	Reference
Initial concentration of Cu in the sulfide liquid	$C_{sul,i}^{Cu}$	250,000 ppm	Close to deposit metal tenors.
Initial concentration of Cu in the silicate melt	$C_{sil,i}^{Cu}$	100 ppm	Close to calculated TBNIC parental liquid from Heggie (2012).
Partition coefficient for Cu	$D_{sul-sil}^{Cu}$	2,130	From Barnes and Ripley (2016).
Initial concentration of Pd in the sulfide liquid	$C_{sul,i}^{Pd}$	3 ppm	Close to deposit metal tenors.
Initial concentration of Pd in the silicate melt	$C_{sil,i}^{Pd}$	0.009 ppm	Close to calculated TBNIC parental liquid from Heggie (2012).
Partition coefficient for Pd	$D_{sul-sil}^{Pd}$	536,000	From Barnes and Ripley (2016).

Parameter	Variable	Value	Reference
Initial concentration of Se in the sulfide liquid	$C_{sul,i}^{Se}$	2 ppm	Chosen from within whole-rock values of other Ni–Cu–PGE deposits globally (Queffurus and Barnes, 2015).
Initial concentration of Se in the silicate melt	$C_{sil,i}^{Se}$	0.06 ppm	Close to calculated value using S/Se mantle range (2632) and S content of unmineralized dykes and volcanic rocks in the Lake Superior Region (250 ppm; Queffurus and Barnes, 2015; Cundari et al., 2021).
Partition coefficient for Se	$D_{sul-sil}^{Se}$	2,339	From Barnes and Ripley (2016).
Concentration of S (constant)	C_{sul}^{S}	365,000 ppm	Accepted concentration of sulfur in pure sulfides (i.e., S concentration in pyrrhotite).
Ratio of silicate mass to sulfide mass	R	100	Low R factor chosen for modelling successive batches.
Initial $\delta^{34}S$ composition in the sulfide liquid/contaminant	$\delta^{34}S_{sul,i}$	-3‰	Non-mantle value from Quetico pyrite from this study.
Initial $\delta^{34}S$ sulfur composition in the silicate melt	$\delta^{34}S_{sil,i}$	0‰	Within mantle range (Ripley and Li, 2003).
Initial $\Delta^{33}S$ sulfur composition in the sulfide liquid/contaminant	$\Delta^{33}S_{sul,i}$	0.25‰	MIF value from Quetico pyrite from this study.
Initial $\Delta^{33}S$ sulfur composition in the silicate melt	$\Delta^{33}S_{sil,i}$	-0.15‰	Within mantle range (Farquhar and Wing, 2003).
Isotopic difference	d	0	From Ripley and Li (2003).
Mass ratio of sulfur	$R^{\star}$	0.01	From Ripley and Li (2003).